# Microstructural sensitive model for plastic deformation of Ti-6Al-4V

Marco A. Galindo Fernandez

A thesis submitted for the degree of
Doctor of Philosophy

The University of Sheffield
Department of Mechanical Engineering

March 2019

# Abstract


The present work focuses on the so-called Ti-6Al-4V (Ti-64) which is the most widely produced and represents around 60% of total global production. As result of the high costs involved during conventional production of titanium components, Additive Manufacturing (AM) have shown a promising route for reducing production costs for Ti-alloys.

AM is relatively a new manufacturing technique that can be used to manufacture fully dense components with complex geometries reducing material waste, production time and costs. Despite the AM benefits, the produced parts by AM technologies are affected by poor surface finish that makes subtractive operations essential for finishing components. Therefore, work on describing the material behaviour during machining operations of additively manufactured Ti-alloy is becoming critically important.

The aim of this study is to present a new physically based model capable of describing the deformation response of additively manufactured Ti-64 and contribute to the current knowledge in cast wrought (C&W) technology under various deformation conditions.

The new proposed model was used to predict deformation behaviour, irrespective of the processing route, via linking relevant microstructural features with the strengthening mechanisms; grain shape, grain size, volume fraction and chemical composition for a wide range of deformation conditions (temperature and strain rate effects) suitable for studying hot forming and machining processes. Therefore, this study makes a major contribution to the understanding of processing routes in Ti-64. The new proposed model was implemented in a user subroutine VUMAT in commercial software Abaqus based on the Finite Element Method (FEM) and was compared with experimental data produce in this research and within literature.

To validate the new proposed model, two set of experiments were developed, including mechanical testing and orthogonal machining tests. The aim of mechanical testing was to study the mechanical properties of Ti-64 AM built components at various deformations conditions suitable for machining and hot forming conditions, whereas the orthogonal machining tests aimed to compare the cutting forces and the produced chip morphologies against the numerical simulations.

# Acknowledgments

This thesis would not have been possible without the support and help of many people, to whom I would like to express my sincere gratitude. Special thanks are extended to my supervisor Dr. Hassan Ghadbeigi, who provided me with invaluable suggestions, advice and feedback. I appreciate his enormous efforts and time spent to make this project valuable not only for academia but for industry. What I am the most grateful is his patience when I started exploring new research areas and still he always provided me with great feedback. Thank you Hassan!

I would also like to thank my second supervisor Dr. Kamran Mumtaz, who always was available for any project's discussion and also always helpful in terms of experimental work making possible this project. I would like to thank Dr. Enrique Galindo-Nava for his invaluable modelling contribution to this project, without his enormous efforts and time spent this project could not been so motivating, thanks cousin!

Also, I would like to thank Roger Fairclough and Tomaso Maccio from TWI Sheffield, for their help and materials support. A special thanks goes for Mr Jamie Booth for his advice and recommendations for the machining trials but even more his patience during the long days of machining trials. I want to thank all the technician staff at the mechanical engineering workshop for their support and advice, Special thanks goes to Gareth Barker and Dave Webster.

I would like to thank Dr Samuel Rigby and Dr Andrew Barr from the blast and impact research group at the Civil & Structural Engineering department at The University of Sheffield for their support, knowledge and jokes during one week of impact tests, it was a great experience. I would also like to thank Mr Dean Haylock and Dr. Nicholas Hughes who ran the hot deformation tests.

I want to thank the Mexican Council of Science and Technology (CONACyT) for financial support during my PhD course. I also want to thank the Roberto Rocca Education Program for awarding me a fellowship to complete my last year of PhD.

Special mention goes to my friends; Dr Behrooz Tafazzolimoghaddam, Jordan Cadd, Valentina Tu and Sara Kopecsni. I really appreciate your friendship during these years, especially during the bad days and always encourage me to keep going, thank you guys!

Also, would like to thank my colleagues and officemates at Sheffield, Haider Ali, Rafael Martinez, Luis Urena, Fernando Cepero, Jack Palmer and Ian Ericovich for their friendship and support during these years.

Last but not least, I want to thank my parents, my sister Nelly and brother Diego for their love and support all my life, without them I would not have been able to get this far. I always will be grateful to my parents for showing that impossible only requires more work, patience and time, I love you family!

*"Success is not final, failure is not fatal. It is the courage to continue that counts"*

-Winston Churchill

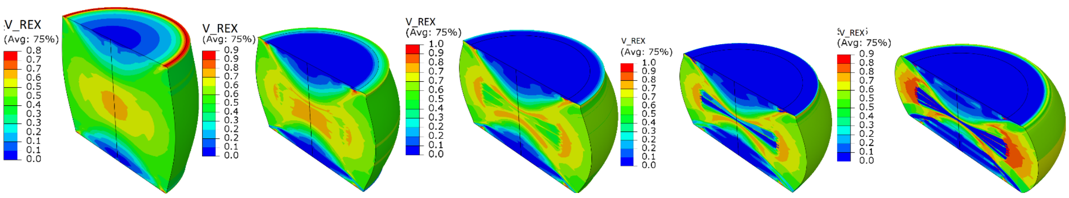


Hot forming

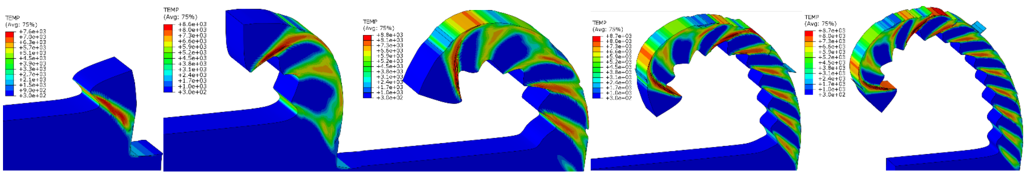

Machining

# Contents

# List of Figures

# Abbreviations

| | |
|---|---|
| AIT | Artificial Intelligence Techniques |
| ALE | Arbitrary Lagrangian-Eulerian |
| AM | Additive Manufacturing |
| ANN | Artificial Neural Networks |
| ASB | Adiabatic Shear Band |
| BCC | Body Centred Cubic |
| CA | Cellular Automata |
| CAD | Computer Aided Design |
| CAM | Computer Aided Manufacturing |
| CBN | Cubic Boron Nitride |
| C&W | Cast and Wrought |
| CP | Commercial Pure Titanium |
| CNC | Computer Numerical Control |
| CVD | Chemical Vapour Deposition |
| DGB | Dynamic Globularisation |
| DMLS | Direct Metal Laser Sintering |
| DRV | Dynamic Recovery |
| DRX | Dynamic Recrystallization |
| EBM | Electron Beam Melting |
| FCC | Face Centred Cubic |
| FE | Finite Element |
| FNN | Fuzzy Neural Networks |
| HAGBs | High-angle Grain Boundaries |
| HCP | Hexagonal Closed Packed |
| HIP | High Isostatic Pressing |
| HRC | Rockwell Hardness on the C scale |
| HSM | High Speed Machining |
| JC | Johnson Cook model |
| JMAK | Johnson Mehl Avrami Kolmogorov |
| PBF | Powder Bed Fusion |
| PLD | Powder Layer Deposition |
| RMS | Root Mean Square |
| SEM | Selective Electron Microscopy |
| SHPB | Split Hopkinson Pressure Bar testing |
| SLM | Selective Laser Melting |
| Tanh | Hyperbolic tangent model |
| Ti-64 | Ti-6Al-4V alloy |
| TMC | Thermomechanical Compression testing |
| VUMAT | Vectorised User Material subroutine |

# Nomenclature

| | |
|---|---|
| $\alpha_p$ | Alpha globular phase |
| $\alpha_s$ | Secondary alpha phase |
| $\sigma_Y$ | Yield strength |
| $\alpha'$ | Martensite |
| $k_{HP}$ | Hall-Petch coefficient |
| $D_\alpha$ | Mean grain size of α phase |
| $W_\alpha$ | α phase width's lath |
| $\sigma_0$ | Friction stress |
| $V_{\alpha s}$ | Volume fraction of secondary α phase |
| $D_{\alpha s}$ | Secondary α grain size |
| $\sigma_\alpha$ | Friction stress in α |
| $V_\alpha$ | Volume fraction of α phase |
| $\sigma_\beta$ | Friction stress in in β |
| $V_\beta$ | Volume fraction of β phase |
| $\sigma^{\alpha}_{prism}$ | Stress required activating prismatic slip |
| $G$ | Activation Energy |
| $T$ | Temperature |
| $\varepsilon$ | Applied strain |
| $\dot{\varepsilon}$ | Strain rate |
| $\eta$ | Material's constant |
| $\kappa$ | Material's constant |
| $\mu$ | Shear modulus |
| $k_B$ | Boltzmann constant |
| $\overline{\sigma}$ | Flow stress |
| $M$ | Taylor's factor |
| $b$ | Burgers vector |
| $\rho$ | Average dislocation density |
| $k_1$ | Dislocation generation coefficient |
| $f_{DRV}$ | Dynamic recovery coefficient |
| $\rho_0$ | Initial dislocation density |
| $\varepsilon_{trans}$ | Transformation strain |
| $\rho_{\alpha\prime}$ | Initial dislocation density in a single martensite lath |
| $d_{\alpha'}$ | Mean lamellar spacing |
| $W_{\alpha'}$ | Martensitic lamellar thickness |
| $E$ | Young's Modulus |
| $\rho_{0\alpha'}$ | Martensitic initial dislocation density |
| $\sigma_{DRV}$ | Stress due to dynamic recovery |

| | |
|---|---|
| $V_{REX}$ | Volume recrystallised of alpha phase |
| $\sigma_{DRX}$ | Stress due to forest hardening |
| $\sigma_{dis}$ | Stress due to forest hardening |
| $G_{\alpha}$ | Activation energy of beta phase |
| $G_{\beta}$ | Activation energy of beta phase |
| $T_{\beta}$ | $\beta$ transus temperature |
| $\rho_{DRX}$ | Dislocation evolution due to recrystallization |
| $f_{DRX}$ | Dynamic recrystallization coefficient |
| $Q_{DRX}$ | Energy barrier to induce grain growth |

# 1. Introduction

Titanium alloys have outstanding properties such as corrosion resistance, high strength-to-weight ratio even at high temperatures, that makes them a suitable candidate for high demanding applications such as the ones in aerospace industry. Among the Ti-alloys, Ti-6Al-4V (Ti-64) is the most widely produced and represents around 60% of total global production. Due to the importance of Ti-64 alloy modelling its mechanical properties has been a relevant topic for materials scientists and engineers. In this context, constitutive equations are highly used to describe flow stress of materials during plastic deformation and are commonly implemented into Finite Element (FE) techniques to simulate manufacturing processes such as forming and metal cutting.

As result of the high costs involved during conventional production of titanium components, special efforts are required to produce titanium closer to the final shape before machining operations in order to reduce costs and material waste. Additive Manufacturing (AM) is relatively a new manufacturing technique that can be used to manufacture fully dense components with complex geometries reducing material waste, production time and costs, hence the desirability of AM of Ti-alloys.

Despite the AM benefits explained earlier, the produced parts by AM technologies are affected by poor surface finish and geometrical accuracy that makes subtractive operations essential for finishing components. The hybrid (additive-subtractive) manufacturing strategy could aid reducing the associated cost / time in fabrication of Ti-based components. Therefore, work on describing the material behaviour during machining operations of additively manufactured Ti-alloy is becoming critically important.

The aim of this study is to present a new physically based model capable of describing the deformation response of additively manufactured Ti-64 and contribute to the current knowledge in cast wrought (C&W) technology. The new proposed model was used to predict deformation behaviour within a wide range of deformation conditions (high temperature and high strain rate) suitable for studying hot forming and machining processes, via linking relevant microstructural features, including; grain shape, grain size, volume fraction and chemical composition. In addition, the present work makes a major contribution to understanding the role of initial microstructure within C&W and those produced by AM and its strengthening mechanisms during processing routes such as forging and machining of Ti-64.

The new proposed model was implemented in a user subroutine VUMAT in commercial software Finite Element Abaqus and was compared with experimental data produce in this research and within literature.

To validate the new proposed model, two set of experiments were developed, including mechanical testing and orthogonal machining tests. The aim of mechanical testing was to study the mechanical properties of Ti-64 AM built components at various deformations conditions suitable for machining and hot forming conditions, whereas the orthogonal machining tests aimed to compare the cutting forces and the produced chip morphologies against the numerical simulations.

# 2. Background

## 2.1 Introduction

The following chapter aims to provide a summary of the state of art in titanium and its alloys. Starting from production of pure titanium, followed by the alloying elements and commercial titanium alloys. This work is focused in the so-called Ti-6Al-4V alloy (Ti-64), therefore special attention will be put on its production methods ranging from conventional processing and more recent Additive Manufacturing (AM) techniques. Also, it will be presented the most suitable AM techniques for manufacture Ti-64 alloy. Furthermore, it will be reviewed the effect on Ti-64's mechanical properties due to processing history. Subsequently, it will be covered the general concepts of machining mechanics, and machining of titanium alloys. The final section will review the constitutive material models commonly used for Finite Element (FE) techniques. It will be divided into the two studied manufacturing processes; hot deformation and chip formation.

## 2.2 Titanium and its alloys

Titanium is a transitional metal and can be as strong as steel, but with weights as much as 45% lighter than the former [1]. Despite titanium has the highest strength to density ratio for structural metals, it is been limited to specific applications due to its high production price. Titanium is highly reactive with oxygen making it difficult to obtain it in pure form, hence; the use of inert atmosphere or vacuum is required during the production process. Additional major cost elements are energy and the initial high cost of titanium tetrachloride [2].

It was until the years 1937-1940 that titanium was successfully isolated by Kroll, this process became famous and still remains essentially the same in the present, making it the most used process for titanium production. The Kroll process consists in three main steps; 1) Chlorination, 2) Reduction of TiCl4 and 3) Electrolysis, additional distillation and purification processes could be added depending on the purpose of the titanium alloy. After these processes, the resulted material has the shape of a sponge that is why this product is refer as titanium "sponge" (Figure 2.1).

Figure 2.1 Titanium sponge [3].

After taking the “titanium sponge” out of the Kroll process, the sponge is chipped into small pieces in sizes of around 100 mm (Figure 2.2, step 1), subsequently, these pieces are compacted and prepared for Vacuum Arc Remelting (VAR) where they are melted into ingots (step 2). After repeating three times the VAR process, bigger ingots are achieved (step 3), subsequently is ready for open die forging (step 4) where the main purpose is to break down the β grain size (which is commonly within 250 μm size) into smaller sizes ranging from 10 up to 30 μm. Finally, it is cut and forged (step 5) ready for machining process.

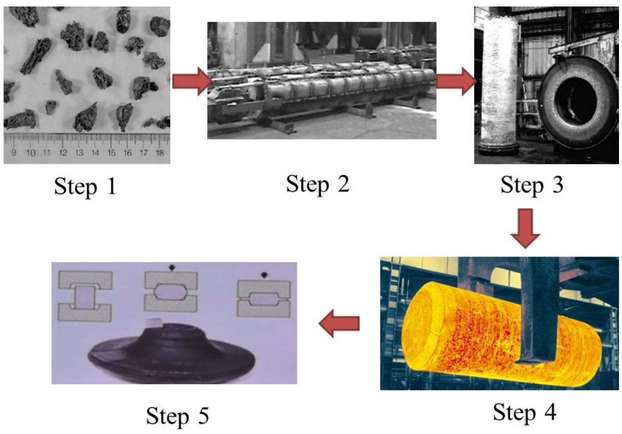


Figure 2.2 Titanium production, adapted from [1].

A Crystalline material is considered a material which contains atoms situated in a repeating pattern over large atomic distances. Atoms will position themselves in a repetitive three-dimensional pattern and each atom is bonded to its closest neighbour atoms. All metals, some polymers and many ceramic materials create crystalline structures during solidification [4].

When describing crystal structures, the term lattice is used and it refers to a three-dimensional array of atom positions. The manner of the atoms is arranged indicates that small groups of atoms form a repetitive pattern, therefore it is often convenient to subdivide the structure into several repeated entities called unit cells. Hence, the unit cell is the basic structural unit of the crystal structure and it is defined by its geometry and the atom positions within.

Mechanical properties of metallic systems depend on the crystal structure of the material. The atomic bonding of this materials is metallic, consequently there are minimal restrictions in number and position of closest neighbour atoms, this leads to dense atomic packings for most metallic systems. For most metals, there are three crystal structures named, Face-Centred Cubic (FCC), Body-Centred Cubic (BCC) and, Hexagonal Closed-Packed (HCP).

Crystalline materials are formed by small crystals (also referred as grains), hence the term polycrystalline is frequently used. During solidification process, grains have random crystallographic orientations, creating atomic mismatch from grain to grain, called grain boundary. However, in some cases polycrystalline materials possesses a preferential crystallographic orientation, in which case is called texture.

Pure titanium is a polycrystalline material which displays an allotropic transformation at 882 °C, from β phase which is a BCC structure (Figure 2.3a), at higher temperatures to an HCP structure α phase, (Figure 2.3b). Therefore, during hot forming processes, it is fundamental to have a good understanding on the deformation temperature and the effect on the resulted constitutive phases. For instance, if pure titanium is forged below the transus temperature (882 °C), the predominant constitutive phase will be α phase, whereas above the transus temperature will produce predominantly β phase.

According to the crystallographic orientation relationship (Burgers relationship) between α and β, α crystal can transform to 12 hexagonal variants orientations with respect to the original β crystal [1].

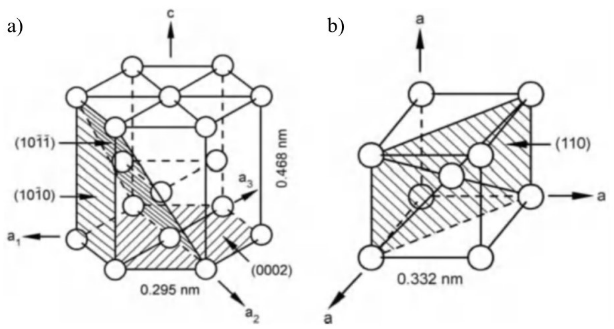


Figure 2.3 Crystal structure in Titanium alloys, a) α phase and b) β phase [1].

Transformation of β phase to α phase in titanium alloys can occur either by diffusion-controlled-nucleation and growth process or martensitically. The first one occurs, if the material is cooled at sufficiently at low rates from the β phase field to the (α+β) phase field. The α phase, first nucleates preferentially at β grain boundaries leading to continuous α lamellae along β grain boundaries. The α lamellae continue to grow inside the β grain interior until they meet other α colonies nucleated at other grain boundary areas of the β grain and belonging to other variants of the Burgers relationship. The individual α plates are separated within the α colonies by the retained β matrix, which are commonly called β plates[2].

Whereas, martensite transformation consists in movements of atoms by shear process which will lead in a microscopically homogenous transformation of the BCC into the hexagonal crystal lattice over a given volume[5]. This hexagonal martensite is designated as α' and is observed in two arrangements; massive martensite and acicular martensite. Large martensite grains are only observed in pure titanium, it consists of large irregular regions (about 20-100 µm) without any clear internal feature visible by light microscopy, but these regions contain packets of small, almost parallel α plates[6]. Acicular martensite occurs in alloys with higher solute content (lower martensite transformation temperature), consists of a mixture of individual α plates, each having different variant of the Burgers relationship [1].

Alloying elements are added to pure titanium to stabilise α or β phases in order to increase or decrease the phase transformation temperature of 882 ºC of pure titanium. These are categorised in four types (Figure 2.4). The α stabilisers; Al, O, N, and C, increase the transition temperature with solute content. Al is the most widely used due to large solubility in both α and β phases and is the only common metal that can reach the transition temperature. The β stabilisers are divided in β isomorphous such as V, Mo, and Nb, and β eutectoid elements; Cr, Fe, and Si. The neutral stabilisers such as Zr, Sn, which behave in a certain neutral way depending in their concentrations.

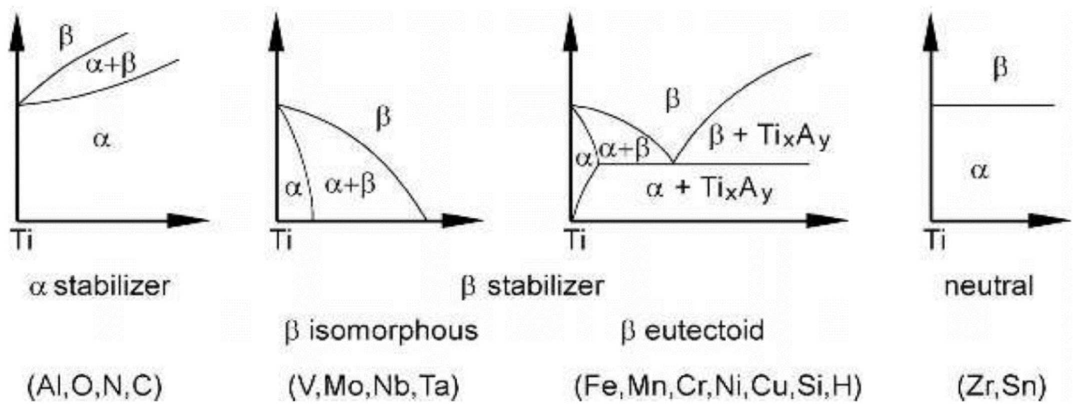


Figure 2.4 Effect of alloying elements on phase diagrams of titanium (schematically) [1].

For practical and commercial approach, titanium alloys are classified into three categories; near-α, α+β, and near-β alloys, according on the composition of the alloy and the room temperature constituent phase. It is worth to mention that this classification could misinform that α alloys do not contain β phase, which is not true, all α alloys contain certain percentage of β phase [1].

Near- α alloys consists in Commercial Pure (CP) titanium with low oxygen and iron as alloying elements and alloys with α-stabilisers such as Al, and Sn. In some cases, β stabilisers are added in very low quantities in order to facilitate forging. Some of the characteristics of these alloys are; good formability, excellent corrosion resistance, however they possess a lack of response to heat treatments.

The group of α+β alloys covers a range in the phase diagram (Figure 2.5) from the α/α+β phase boundary up to the intersection of the martensitic start temperature (Ms) line with room temperature, thus α+β alloys transform martensitically upon fast cooling from the β field to room temperature. Examples of these alloys are Ti-6Al-4V (Ti-6-4), Ti-6Al-6V-2Sn (Ti-6-6-2) and Ti-6Al-2Sn-4Zr-6Mo (Ti-6-2-4-6). Some characteristics of these alloys are higher strength compared to their near-α counterparts, and as it is shown in Figure 2.5, α+β alloys possess a wider temperature processing window compared to near-α and near-β alloys.

Within the commercial near-β alloys, there are two main classification; metastable and stable β alloys. Most of the commercial β alloys are metastable, because they contain certain amount of α phase, therefore, they are located in the equilibrium (α+β) phase region of the phase diagram (Figure 2.5). Although, stable β alloys allocated in the single β phase field do not exist as commercial materials, the expression “stable β alloys” is commonly used for practical purposes. Some examples of metastable β alloys are Ti-6246, Ti-17, SP-700, Beta-CEZ which can achieve strengths of the order of 1380 MPa. A manufacturing advantage is that they are easier to process at low temperatures such as cold rolling and forging, due to the fact that increasing temperature in these alloys, will enhance their strength.

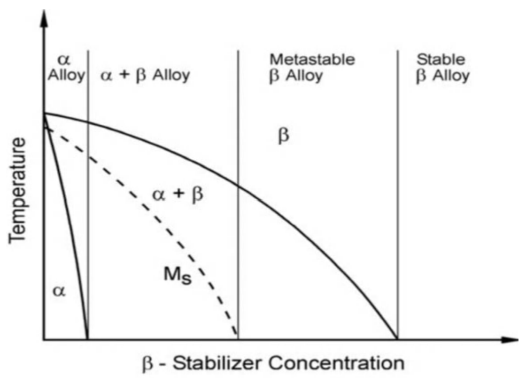


Figure 2.5 Schematic pseudo-binary section through β isomorphous phase diagram [1].

## 2.3 Production of α+β titanium alloys

As discussed in previous section, Ti-64 is part of the α+β alloys, Therefore, this thesis will only treat production of α+β alloys processing routes, which display diverse mechanical properties due to broad type of microstructural achieved.

### 2.3.1 Conventional processing route: Cast and Wrought

As mentioned in previous section during melting process (Figure 2.2), β grains crystallise very fast creating large grains (around 250 μm). For instance, Figure 2.6 depicts an image of these typical β grains before post processing, where small colonies of α phase (white plates) grew between the β grain boundaries. Depending on the conventional thermo-mechanical processing route, three types of Ti-64 of microstructures are commercially produced named: lamellar, bimodal and equiaxed.

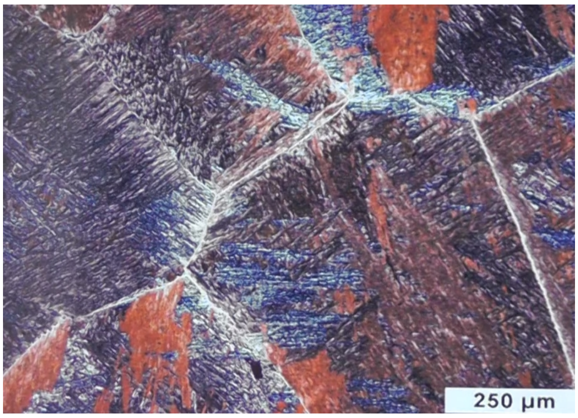


Figure 2.6 Typical β grains after Vacuum Arc Remelting process, adapted from [7]

Lamellar microstructures can be obtained by following the processing route schematically presented in Figure 2.7a, this route comprises four steps; Firstly, homogenisation of microstructure is performed above the transition temperature then, it is cooled down; depending on the cooling rate, different length scales of α grains can be achieved. Secondly, it is deformed, either below or above transus temperature which is 1263 K for Ti-64 (dotted line in Figure 2.7a).

Afterwards, recrystallization takes place above the transus temperature (third step in Figure 2.7a), then it is cooled down; if it is cooled down quickly, alpha grains will be finer, and if it is cooled down slowly alpha grains will be coarser. It is worth to mention that during the step 3, the cooling rate will define the final lamellar microstructure size [8]. The final step is annealing to relieve any stresses created during the process, and aloud any partition of elements to occur. A typical microstructure produced through this route is presented in Figure 2.7a.

Bimodal structures contain three constitutive phases; primary alpha $\alpha_p$ having a globular shape, secondary alpha $\alpha_s$ (which has the shape of plates that grew in between two β grains) and the β phase. The steps to produce these microstructures are represented in Figure 2.7b schematically.

First step is to homogenise the microstructure above the transus temperature, then cooling followed by subsequent deformation below the transus temperature (step two in Figure 2.7b), where the material is deformed, increasing the dislocation density due to plastic deformation.

Then, recrystallization process (step 3 in Figure 2.7b) occurs at a temperature below the transus; this temperature will set the final volume fraction of primary alpha, whereas the cooling rate in this step will determine the volume fraction of secondary alpha [8]. Finally annealing (fourth step in Figure 2.7b) is performed to relief stress generated during the process.

The equiaxed microstructures are formed by two phases, fully equiaxed α phase grains and β phase between the grains. The processing route is identical to the one described in bimodal microstructures up to the recrystallization process. In step three (Figure 2.7c), the cooling rate is sufficiently slow that allows only primary $\alpha_p$ grains to grow during the cooling process, inhibiting α lamellae formation inside β grains resulting in an equiaxed structure [9]. Finally, stress-relieving treatment is performed.

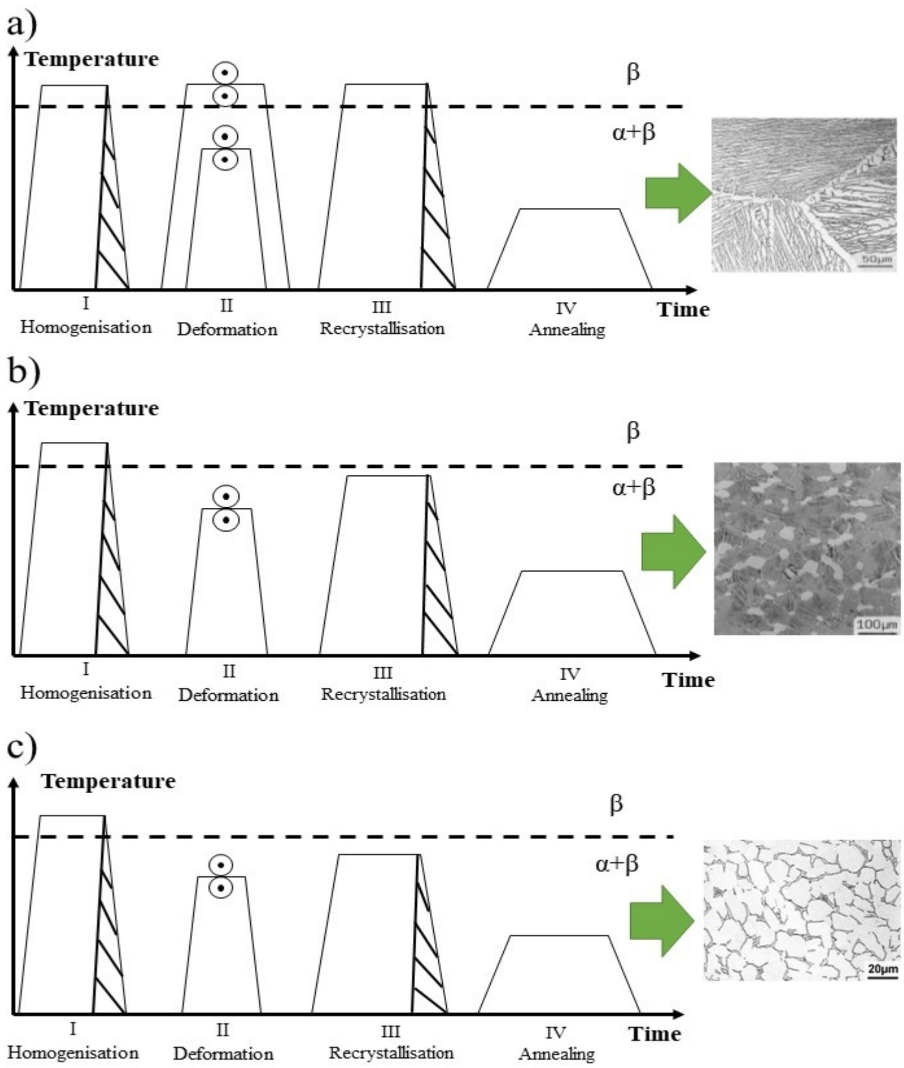


Figure 2.7 Processing routes of α+β alloys.

### 2.3.2 Kinetics of hot deformation in Ti-64

Previous section treated the hot working routes to produce Ti-64 different microstructures. In order to tailor them, its required good understanding of how the grain shape and size and constitutive phases evolve. The microstructure evolution will highly be affected by key parameters such as, temperature and strain rate during thermomechanical work [10-12].

While there is a competence between temperature and strain rate effects at the macroscale level, simultaneously complex phenomena occur at the microscale level. During plastic deformation some of the fraction of energy used during the hot working process is maintained by the metal as strain energy, which is associated to tensile, compressive and shear zones around the freshly generated dislocations [13]. The ability of a metal to release this strain energy during high temperatures is through two competing restoration processes including recovery and recrystallization, and if it is applied the appropriate heat treatment may lead in grain growth [14].

Dynamic Recovery (DRV) and Dynamic Recrystallization (DRX) terms are widely used due to the fact that hot deformation involves the application of different deformation speeds and temperatures hence, the recovery and recrystallization can occur as dynamic processes [15]. Added to these phenomena, it is shown that Ti-64 during hot working owns an additional mechanism called globularisation [13, 16-18]. This phenomenon only occurs with the initial lamellar type and consists in coarsening or transformation to a globular shape. In the following sections, firstly it will be treated DRV and DRX and secondly dynamic globularisation.

#### 2.3.2.1 Dynamic Recovery & Recrystallization

Dynamic Recovery (DRV) consists in releasing the stored strain energy by means of rearrangement of dislocations to lower their energy and annihilation of dislocations by the encounter of dislocations with opposite signs. Whereas, Dynamic Recrystallization (DRX) comprises the formation and migration of high-angle grain boundaries, driven by the stored energy due to plastic deformation. Moreover, DRX can occur either at high temperatures or low strain rates, decreasing the dislocation density as dislocation-free grains nucleate and consequently grow from highly dislocated sub-grains.

Figure 2.8 shows a schematic of a flow tress curve accompanied of the structure transition during DRV (a) and DRX (b) processes; (1) the initial microstructure is subjected to elastic strains, after the material has yielded, (2) the original grains get increasingly strained and dislocations start to pile up, (3) generation/annihilation of dislocations take place and sub-boundaries of grains start to form.

Until this point, both processes act similarly, (4) the sub-boundaries remain more or less equiaxed which implies that the new structure is “dynamic” and re-adapts continuously during increasing the strain. Afterwards, during DRV, recrystallised grains are formed at the original grain boundaries, whereas DRX, dislocation-free grains are formed producing the so-called “necklace structure”.

In the last stage (5), with further deformation, potential of nucleation increases and new recovered/recrystallised grains appear, at the same time the old grains that had already recovered/recrystallised in previous stage, are deformed again, until an equilibrium is reached. At this stage, the flow curve reaches a plateau and the microstructure consist of a dynamic mixture of grains with various dislocation densities. As for a macroscale point view, equilibrium is reached between the hardening due to dislocation accumulation and the softening due to dynamic recrystallization.

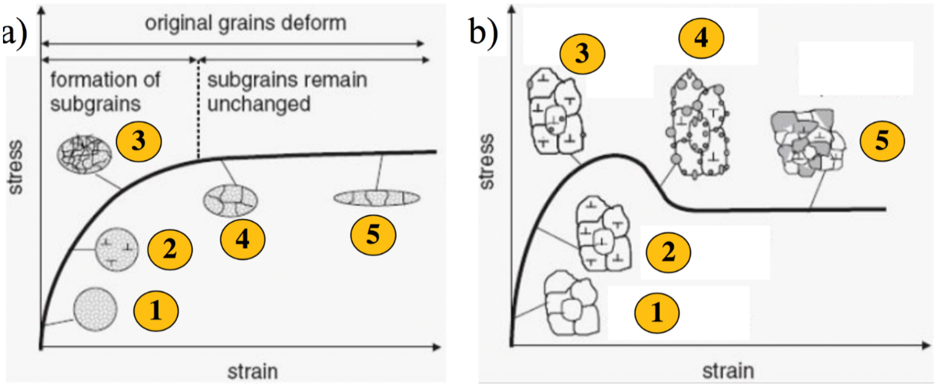


Figure 2.8 Dynamic recovery during hot deformation, adapted from [19].

2.3.2.2 Dynamic Globularisation

It has been reported that during hot deformation of Ti-64 is liable to undergo both DRV (predominant in β-phase) and DRX (in α-phase) mechanisms [17, 20, 21]. Adding to these mechanisms, dynamic globularisation could take place with the right conditions. This mechanism consists by split an alpha lath (grain) into several globular shaped grains.

Figure 2.9 shows the sequence of the process as follows; the initial α-laths are surrounded by β phase grains and both are delimited by pre-existing grains creating grain clusters (Figure 2.9a), after applying deformation and temperature, boundary splitting occurs within the lamellar phase (Figure 2.9b), such boundary creates a freshly unstable boundary that is temporally maintained by the diffusion of interlamellar phase into the boundaries (Figure 2.9c). Finally, the new second alpha phase ($\alpha_s$) diffuses into the grain boundary resulting in a "pinch off" generating new globular grains due to the elimination of the old lamella boundary [13].

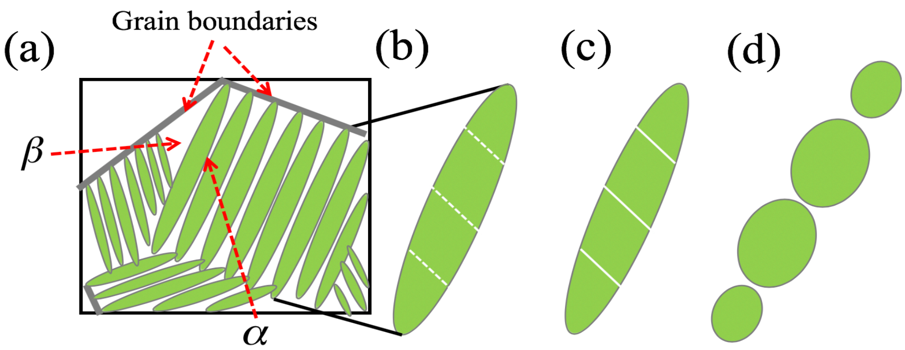


Figure 2.9 globularisation; a) initial microstructure, b) initial split of alpha/alpha boundaries, c) diffusion of alpha of interlamellar phase and) final globular grains.

Extensive research has been carried out in order to study the conditions in which this globularisation take place. Studies have focussed in two main fields; static globularisation occurring by post deformation annealing [13, 22, 23] and during deformation [9, 12, 13, 23-25]. Both methods had found that the lath thickness is the most relevant factor affecting the boundary splitting, hence the flow stress. Figure 2.10 shows a schematic of a generic flow curves of a Ti-64 alloy with lamellar microstructure at α-β transus temperature. Both plots (thin and thick lamellas) exhibit a peak stress ($\sigma_p$) followed by a severe drop in strength and eventually reach the steady-state stress ($\sigma_{ss}$), additionally it is presented $\varepsilon_p$ and $\varepsilon_{ss}$ which are the strains corresponding to $\sigma_p$ and $\sigma_{ss}$. It can be seen that decreasing the lath thickness, the yield strength increases, however a drastic softening occurs due to dynamic globularisation.

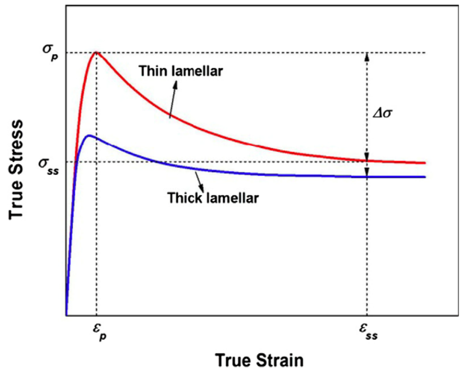


Figure 2.10 Diagram illustrating the flow curves of hot deformation in a typical Ti-64 alloy with different lath thickness, adapted from [17].

### 2.3.3 Constitutive equations for hot deformation of Ti-64

Numerous constitutive equations for describing the flow stress of Ti-64 during hot deformation have been proposed. Early work by Follansbee & Gray [26] studied the behaviour of Ti-64 in a wide range of temperatures (73 up to 1073 K) and strain rates (0.001 up to 3000 $s^{-1}$). Authors proposed a constitutive equation centred on the phenomenological form of Kocks-Mecking [27] formulation. The model explained the kinetics of dislocation/obstacle interactions and the evolution. Equations 2.1 to 2.4 describe their model as follows;

$$\frac{\sigma}{\mu} = \frac{\sigma_a}{\mu} + s_I \frac{\hat{\sigma}_I}{\mu} + s_S \frac{\hat{\sigma}_S}{\mu} + s_D \frac{\hat{\sigma}_D}{\mu}$$

Equation 2.1

$$s_I = \left[1 - \left(\frac{kT}{g_{0I}\mu b^3} ln\left(\frac{\dot{\gamma_{OI}}}{\dot{\gamma}}\right)\right)^{1/q_I}\right]^{1/PI}$$

Equation 2.2

$$s_S = \left[1 - \left(\frac{kT}{g_{0S}\mu b^3} ln\left(\frac{\dot{\gamma_{Os}}}{\dot{\gamma}}\right)\right)^{1/q_S}\right]^{1/PS}$$

Equation 2.3

$$s_D = \left[1 - \left(\frac{kT}{g_0\mu b^3} ln\left(\frac{\dot{\varepsilon_{OD}}}{\dot{\varepsilon}}\right)\right)^{1/q_D}\right]^{1/PD}$$

Equation 2.4

Where, $\mu$ is the shear modulus $\sigma_a$ is the athermal stress, $\widehat{\sigma_I}$ is the mechanical threshold stress at 0 K that is required to force a dislocation past the obstacles, $\widehat{\sigma_S}$ is the ratio between the yield stress at any strain rate $\dot{\gamma}$ and temperature *T*, $\widehat{\sigma_D}$ is the mechanical threshold stress at saturation (i.e. when strain hardening vanishes). Whereas $S_I$, $S_S$, and $S_D$ are the friction stress required to move dislocations through the lattice and to pass short-range obstacles. *B* is the Boltzmann's constant, *b* is the Burgers vector, $g_o$ is the normalized total activation thermal enthalpy and *q* and *p* are fitting parameters for a given material.

Similarly Kotkunde et al. [28] and Babu et al [29] proposed another Kocks-Mecking set of parameters for higher temperature deformations conditions showing similar results. Nemat-Nasser et al. [30] studied higher strain rates (up to 7000 $s^{-1}$) and temperatures ranging from 77-1000 K, results shown within 15% of error on their predictions and their experiments. Despite several authors have used the phenomenological form of Kocks-Mecking equation, it has shown that fitting all the required variables is not an easy task, making it the biggest inconvenient during implementating into FE techniques, therefore Ding & and Guo [20] developed a model based on Kocks-Mecking formulation, using combined cellular automaton (CA) with classical nucleation theories derived by Roberts & Ahlblom [31] and Read & Shockley [32]. Authors simulated both quantitatively and topographically the microstructure evolution and flow stress during hot deformation when DRX occurs, good agreement with experimental shown that the model could be used to predict microstructural progression. However CA has shown that requires large computing time and high-performance computers making this approach costly. Therefore, intermediate cost options such as Artificial intelligent techniques (AI) for example artificial neural networks (ANN) [33, 34], fuzzy neural networks (FNN) [35], combined ANN and Finite Element techniques [15, 21, 36] have been used as option to reduce computational costs in order to determine this parameters using.

Another common constitutive equation is the Arrhenius-type. For instance, Xiao et al. [18] studied an equiaxed structure over temperatures of 923 to 1023 K within strain rates $5x10^{-4}$ up to $5x10^{-2}$. Using the Zener & Hollomon relation [37], the thermal activation to plastic hot deformation is controlled by the strain rate $\dot{\varepsilon}$ and temperature $T$ and can be expressed with the parameter $Z$ [38];

$$Z = \dot{\varepsilon}\exp\left(Q/RT\right)$$

Equation 2.5

Where $Z$, is the Zener-Hollomon parameter, $Q$ is the hot deformation activation energy, $R$ is the mol gas constant. The relation between Z parameter and flow stress can be expressed as;

$$Z = F(\sigma) = A_1\sigma^{n_1} \qquad \text{for } \alpha\sigma < 0.8$$

Equation 2.6

$$Z = F(\sigma) = A_2\exp\left(\beta\sigma\right) \qquad \text{for } \alpha\sigma < 1.2$$

Equation 2.7

$$Z = F(\sigma) = A_3(\sinh\left(\alpha\sigma\right))^{n_2} \qquad \text{for all } \sigma$$

Equation 2.8

Where $A_1$, $A_2$, $A_3$, $\alpha$, $n_1$, $n_2$ and $\beta$ are material constants and are independent of temperature, $\sigma$ is flow stress, $\alpha$ is the parameter of stress level and $n_1$, $n_2$ are the stress exponent. Authors combined Equations 2.5 and 2.8 stating that the hyperbolic sinusoidal Arrhenius-type equation adapts and calculates at all level of stress quite well in previous studies [39, 40].

The prediction precision of the constitutive equations shown overall averaged mean error of 5.9%. Similarly, using an Arrhenius-type equation Abbasi & Momeni [41, 42] proposed another set of material constants for Ti-64 during higher hot deformation temperatures (1073 – 1350 K) and 0.0001 $s^{-1}$. Chao et al [43] also presented another set of constants for temperatures ranging from 923 to1023 K and 0.005 up to 0.5 $s^{-1}$.

Despite reasonably good results, the model does not delivers better understanding of the physical phenomena occurring during these conditions, moreover the model is tuned for specific material, hence a large amount of set of parameters can be found within the literature. Therefore, Shafaat et al. [44] proposed the combination of hyperbolic sinusoidal equation with a physically-based model; the so-called Johnson Mehl Arami Kolmogorov (JMAK) constitutive model. The JMAK model is a classical theory that describes the nucleation and growth and was developed independently by Johnson & Mehl [45], Avrami [46-48] and Kolmogorov[49]. The JMAK equation is widely used within materials science and engineering literature, because its relative simplicity and reasonably good agreement with the experimental work.

The aim of this model is to predict the recrystallised volume fraction as a function of time. It assumes that the nucleation and grain growth rates are dependent on the initial mean grain size, strain rate, temperature and strain. The derivation by Ruitenberg et al. [50] for the isothermal JMAK equations, describing the volume fraction of the phase transformation as function of temperature and time are given by:

$$x(t) = 1 - e^{-kt^n}$$

Equation 2.9

$$k(T) = k_0 e^{-\Delta H / T k_B}$$

Equation 2.10

Where $x$ is the transformed volume fraction, $n$, $\Delta H$, $k_0$ are isothermal parameters, $t$ and $T$ are time and temperature respectively, $k_B$ is the Boltzmann constant. The exponential $n$ is defined as follows;

$$n = a + bc$$

Equation 2.11

Where $a$ is the number of nuclei per unit volume of recrystallised phase, $b$ is the growth dimensionality, $c$ is the growth index. Whereas the activation energy, is defined as;

$$\Delta H = E_n + bcE_g$$

Equation 2.12

Where $E_n$ and $E_g$ are the activation energies to nucleate and growth respectively. And, the average grain size is defined as;

$$\rho(T) = \rho_0 e^{-\Delta H'/Tk_B}$$

Equation 2.13

$$\Delta H' = \frac{ac}{a + bc}\left[E_g - \left(\frac{E_n}{a}\right)\right]$$

Equation 2.14

Where, $\rho_0$ is the initial grain size. All these constants are fitted to experimental results and calculations can be made for specific material. However, as this is not a simple task, therefore several authors [50, 51] have proposed the equations as function of strain rate, temperature using Arrhenius-type equation. Using the Avrami equation, DRX is given by;

$$X_{drex} = 1 - e^{-\left[0.693(\varepsilon - 0.8\varepsilon_p/\varepsilon_{0.5})^2\right]}$$

Equation 2.15

Where ε is the strain, $X_{drex}$ is the fraction recrystallised, $\varepsilon_p$ is peak strain and $\varepsilon_{0.5}$ is the strain when $X_{drex} = 0.5$ and can be calculated as follows;

$$\varepsilon_{0.5} = 1.214x10^{-5} d_0^{0.13} \dot{\varepsilon}^{0.04} e^{5.335x10^4/RT}$$

Equation 2.16

Where $R$ is the gas constant. Previous constants are determined by means of regression analysis from experimental data. And $\varepsilon_p$ is defined as;

$$\varepsilon_p = 4.107x10^{-3}\dot{\varepsilon}^{0.06}e^{1.318x10^4}/_{RT}$$

Equation 2.17

The recrystallised grain size is given by;

$$d_{rex} = 78.6022\dot{\varepsilon}^{0.03722}e^{-1902.72}/_{RT}$$

Equation 2.18

And the final average grain size is calculated as;

$$d = d_0(1 - X_{drex}) + d_{rex}X_{drex}$$

Equation 2.19

Implementing JMAK model into FE techniques is not an easy task due to the high number of governing equations (a total of ten equations) and fitting parameters that impede the transition between one microstructure to another even of the same alloy. An early attempt considering different initial commercial microstructures within Ti-64 by Semiatin and co-workers [22, 24, 52] and later modified by Park et al. [17] proposed a constitutive equation considering dynamic globularisation, particle coarsening and alpha phase rotation (texture effects). The flow softening produced by dynamic globularisation can be related to the fraction globularised and the flow stress as;

$$f_s = \frac{\Delta\sigma}{\sigma_p - \sigma_{ss}} = \frac{\sigma_p - \sigma}{\sigma_p - \sigma_{ss}}$$

Equation 2.20

Where $\Delta\sigma$ is the magnitude of flow softening, $\sigma_p$ is the peak stress, $\sigma_{ss}$ is the steady state stress and $\sigma$ is the actual stress. Using the empirical Equation 2.21 and substituting into Equation 2.20 the plastic behaviour considering flow stress as a function of dynamic globularisation can be written as:

$$f_s = 1 - exp[-k_s(\varepsilon - \varepsilon_c)^m]$$

Equation 2.21

$$\sigma = \left(\sigma_p - \sigma_{ss}\right) exp[-k_s(\varepsilon - \varepsilon_c)^m] + \sigma_{ss}$$

Equation 2.22

Where, $\varepsilon_c$ is the critical strain for starting dynamic globularisation, $k_s$ and m are parameters fitted from experimental data. The effects due to rotation of alpha phase and particle coarsening can be calculated as a Hall-Petch-like relation as follows:

$$\sigma = \bar{M}(\tau_0 + k_H {l_\alpha}^{-1/2})$$

Equation 2.23

Where, $\tau_0$ is the friction stress and $k_H$ is the Hall-Petch constant, $\bar{M}$ is the Taylor factor for a single alpha lattice $l_\alpha$. Then the coarsening rate can be expressed as:

$$r^3 - r_o^3 = Kt + K\varepsilon/\dot{\varepsilon}$$

Equation 2.24

Where $r$ is half of the thickness for $l_\alpha$, before globularisation, $t$ is time, $r_0$ is $r$ at $t$ = 0, and $K$ is rate constant dependent on thermodynamic variables and Taylor factor. Finally combining Equations 2.23 and 2.24 provides a general expression for flow stress:

$$\sigma = \bar{M}\left[\tau_0 + k_H 2^{-1/2}(r_o^3 + K\varepsilon/\dot{\varepsilon})^{-1/6}\right]$$

Equation 2.25

It has been presented the most common used models within the literature for hot deformation of Ti-64. Three main approaches can be found; phenomenological, physics-based and AI techniques. Within the most commonly used are the empirical due to its simple implementation into FE techniques, however the biggest inconvenient is the lack of clarity of the different phenomena occurring during plastic deformation. Whereas current physics-based models possess large number of fitting parameters making it not a simple task to calibrate the model for each alloy for specific deformation conditions (strain rate and temperature effects). AI techniques is the most recent approach due to development of faster computer, however it is required good understanding of physical phenomena in order to validate and train AI models for further analysis, without mention the computational costs involved during the development of such models

### 2.3.4 Additive Manufacturing of titanium alloys

The concept of Additive Manufacturing (AM) was first introduced in 1987, as “Rapid Prototyping (RP)” [53]. AM is a manufacturing technology that generates 3-dimensional objects from Computer-Aided Design (CAD) file, based in layer by layer manufacturing process. The American Society of Mechanical Engineers (ASME) with the collaboration of the American Society for Testing and Materials (ASTM) developed their first standardization (the F2792-09e1/F2792) in autumn of 2009 and with it, the term “Additive Manufacturing” was born [53].

As result of the high costs involved during fabrication of various titanium precursors and mill products, a large and growing amount of investigations have studied various potentially lower cost processes, including near-net shape techniques and powder metallurgy (AM) [54-58]. The last one, have shown that could be promising manufacturing route to reduce these costs [59-62]. For instance, to reach a final component, the mill products must be machined often assumed to be twice the cost of the actual component [63-65]. Therefore, special efforts are required to produce titanium components that are closer to the final shape, hence the desirability of Additive Manufacturing. Also, AM can be used to manufacture fully dense components with complex geometries that previously were impossible to manufacture or could only be produced by long lead time and expensive tooling (i.e. fixtures, machine’s time and cutting tools)[66]. Despite all these benefits, the produced parts by AM technologies are affected by poor surface integrity and geometrical accuracy that makes subtractive post processing operations essential for safety critical components [67].

#### 2.3.4.1 AM classification

According to ASTM, there are seven categories of AM technologies. Figure 2.11 shows these classifications including, the type of raw material used, the power source and some strengths and drawbacks. Since this project is focused in Powder Bed Fusion (PBF) technologies, it will be covered in more detail in the following sections.

Within AM technologies, PBF technologies have shown the best results to melt titanium alloys [61, 68-70]. Examples of PBF technologies are Selective Laser Melting (SLM), Electron Beam Melting (EBM) and Direct Metal Laser Sintering (DMLS). The three of them are the most widely used for processing Ti-64 alloy because they have the ability to produce fully dense parts (99%), despite Ti-64’s high melting temperature (1668 ºC).

| CATEGORIES | TECHNOLOGIES | PRINTED "INK" | POWER SOURCE | STRENGTHS / DOWNSIDES |
|---|---|---|---|---|
| Material Extrusion | Fused Deposition Modeling (FDM)<br>Contour Crafting | Thermoplastics, Ceramic slurries, Metal pastes | Thermal Energy | • Inexpensive extrusion machine<br>• Multi-material printing<br>• Limited part resolution<br>• Poor surface finish |
| Powder Bed Fusion | Selective Laser Sintering (SLS) | Polyamides /Polymer | High-powered Laser Beam | • High Accuracy and Details<br>• Fully dense parts<br>• High specific strength & stiffness<br>• Powder handling & recycling<br>• Support and anchor structure<br>• Fully dense parts<br>• High specific strength and stiffness |
| | Direct Metal Laser Sintering (DMLS)<br>Selective Laser Melting (SLM) | Atomized metal powder (17-4 PH stainless steel, cobalt chromium, titanium Ti6Al-4V), ceramic powder | High-powered Laser Beam | |
| | Electron Beam Melting (EBM) | | Electron Beam | |
| Vat Photopolymerization | Stereolithography (SLA) | Photopolymer, Ceramics (alumina, zirconia, PZT) | Ultraviolet Laser | • High building speed<br>• Good part resolution<br>• Overcuring, scanned line shape<br>• High cost for supplies and materials |
| Material Jetting | Polyjet / Inkjet Printing | Photopolymer, Wax | Thermal Energy / Photocuring | • Multi-material printing<br>• High surface finish<br>• Low-strength material |
| Binder Jetting | Indirect Inkjet Printing (Binder 3DP) | Polymer Powder (Plaster, Resin ), Ceramic powder, Metal powder | Thermal Energy | • Full-color objects printing<br>• Require infiltration during post-processing<br>• Wide material selection<br>• High porosites on finished parts |
| Sheet Lamination | Laminated Object Manufacturing (LOM) | Plastic Film, Metallic Sheet, Ceramic Tape | Laser Beam | • High surface finish<br>• Low material, machine, process cost<br>• Decubing issues |
| Directed Energy Deposition | Laser Engineered Net Shaping (LENS)<br>Electronic Beam Welding (EBW) | Molten metal powder | Laser Beam | • Repair of damaged / worn parts<br>• Functionally graded material printing<br>• Require post-processing machine |

Figure 2.11 AM classification according to ASTM [71].

As PBF's name suggests, these techniques use pre-alloyed powders as raw material to produce parts. Moreover, C&W processes are always involved to AM, since the powders are produced by conventional processes. Two type of powders are used; irregular shaped powders and spherical powders. An example of both shapes is presented in Figure 2.12.

It has been shown that spherical powders possess easier flow during spread of powders; whereas, irregular shaped powders have shown less favourable results [72]. Spherical powder production costs are higher compared to irregular shaped due to high quality standards, therefore it has become an issue for AM commercialization. Nonetheless, the recent interest in production of low-cost irregular shaped powders that could be used directly to AM is closing this gap [72].

a) b)

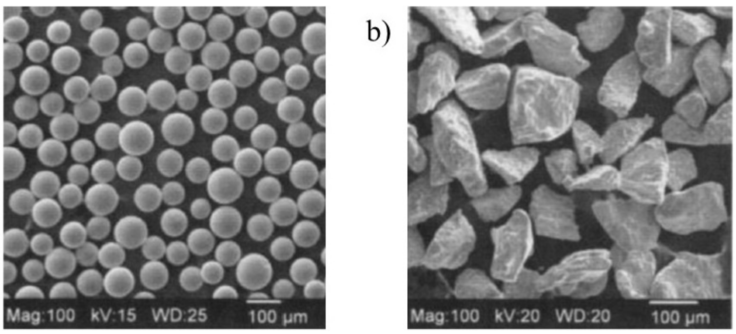


Figure 2.12 Powders for PBF technologies; a) spherical and b) irregular shape types [72].

EBM and SLM processes share the same powder deposition process, however the heat source is different. A typical configuration of the printing process is shown in Figure 2.13. The process consists of a substrate that is levelled into the machine's building platform. Both EBM and SLM procedures takes place in an inert gas chamber to reduce the interior oxygen content. Subsequently, the build chamber is filled with loose powder onto the substrate; then, a laser/electron beam scans the powder bed surface that generates the profile contour. Once the laser scans a layer, the mechanism adjusts the height, for the next layer. This process is repeated until the part is completed.

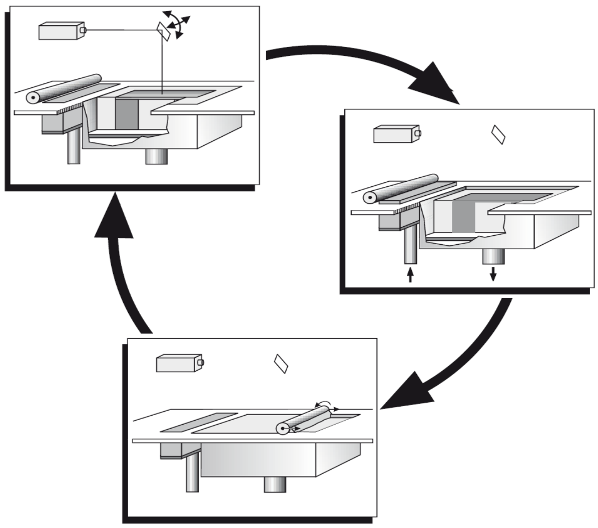

Figure 2.13 Electron beam and laser melting, scheme, adapted from [61].

PLD is a slightly different process which consist in repairing or starting a new part by using either a fresh substrate or an existing part. Figure 2.14 shows the schematic of the process wherein it could use either inert gas in the chamber or local shielding which aids avoiding the use of inert gas for less reactive metals (not the case of titanium alloys) [73].

After removing the oxygen in the chamber, a concentric laser or electron beam heats the part surface to create a meltpool, later the powder is delivered via a lateral injection nozzle (Figure 2.14a), radial symmetric powder injection nozzles (Figure 2.14b) or coaxial powder stream (Figure 2.14c). Then, the nozzle scans the predetermined toolpath created from the CAM software. As the nozzles moves away the meltpool solidifies creating a new layer. The process is repeated until the part is completed.

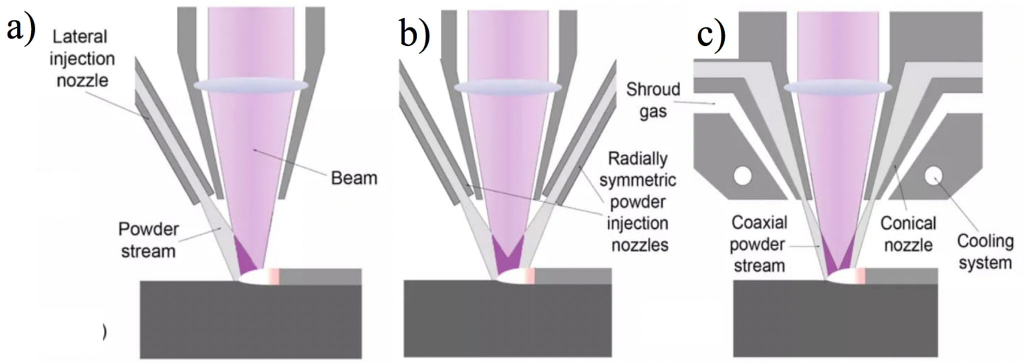


Figure 2.14 Powder layer deposition process; a) lateral injection, b) symmetric injection and c) coaxial powder stream , adapted from [74].

In this section was covered the AM classifications and PBF technologies were covered in more detail due to their exceptional capabilities to produce titanium components. However, in the following sections, it will be put more emphasis in SLM built components and their microstructures. This was decided because SLM have shown outstanding results in terms of density, good control of processing parameters and the ability to produce larger components, compared to other PBF technologies.

Regardless of the benefits mentioned previously, several problems are associated in using SLM technology to produce functional engineering components. Three major aspects strongly affect the mechanical properties of the SLM components.

Firstly, thermally induced residual stresses generated due to the high cooling rates during irregular exposure of high temperature produced by laser/beam source, which may lead to cracking of the produced parts due a phenomenon known as shrinkage [62, 64, 75].

Second one is process-induced defects such as pores within the structure, which may occur due to powder contamination or evaporation after layer deposition, eventually, these pores act as stress concentrators and lead to early failure [76-78].

Finally, acicular (α') martensite is present within SLM components. α' has hexagonal shape, generally having high dislocation density [10, 67, 79]. As a result, the SLM-fabricated components show high yield strength, but limited ductility. The formation of α' could be explained as martensitic transformation occurs by the fast heating and cooling cycles inherit during printing process, whereas during C&W technologies occurs by diffusion-controlled nucleation and growth during hot deformation [1, 67, 80]. Figure 2.15 shows a typical SLM-built Ti-64 microstructure displaying columnar β grains filled with α'.

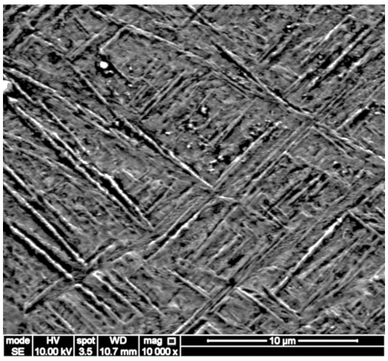


Figure 2.15 Typical Ti-64 microstructure built by SLM

Current work to overcome these problems have been done by two means; increasing the temperature in the building chamber [64], and the most common among literature is post processing heat treatments [64, 75-77, 81, 82]. Increasing the temperature close to Ti-64 melting point in the chamber results in residual stresses elimination and denser components. However, increasing the temperature could create catastrophic failure inside the SLM machine’s chamber due to overheating of the structural components [83].

On the other hand, heat treatments, have shown that can reduce or even eliminate residual stresses [75, 82, 84], as well as decomposition of α’ martensite can be achieved [77, 81, 85], however porosity is still an unsolved issue with traditional heat treatments, therefore; hot isostatic pressing (HIP) is a promising route [65, 77].

#### 2.3.4.2 Effects of processing history on mechanical properties

As discussed in section 2.2 and 2.3, the diverse mechanical properties of Ti-64 are dependent in the microstructure features. The three commercial microstructures named; lamellar, equiaxed and bimodal have been studied extensively in a wide range of deformation conditions.For instance, Park et al. [30, 86] studied the three microstructures at four different strain rates (from 0.001up to 10 $s^{-1}$) during room temperature, finding that bimodal equiaxed structures were the strongest in all conditions due to higher boundary strengthening due to constitutive phase. Similar investigation with four different structures studied by Zhang et al.[87] at higher strain rates (~2000 $s^{-1}$), finding that lamellar structures were the ones with higher strength, this was attributed due to thinner lamellar width within the components.

Also, extensive research can be found under high temperatures. Semiatin and co-workers [23, 33, 43, 88] have studied Ti-64 hot deformation ranging from 973 K up to 1273 K, within low strain rate regimes (0.0001 up to 1 $s^{-1}$) and diverse microstructures; martensitic, bimodal, equiaxed and more than four lamellar structures. Also Park et al.

[17, 89] studied the same range of temperatures (1073 up to 1273 K) and strain rates (0.01 up to 1 $s^{-1}$). Both researchers found a drastic increase of ductility of lamellar structures attributed to dynamic recrystallisation.

Within intermediate and high strain rates, Khan et al.[86, 90, 91] studied the response of three equiaxed structures, finding that grain size was the most affecting parameter into yield strength. Also, high strain rates (2000 up to 3000 $s^{-1}$) and high temperatures (973 up to 1373 K) have been studied for equiaxed structures [30, 87, 90, 92, 93]. Finding that even at such high strain rates, Ti-64 displays a drastic drop in strength when the experiments reaches the transus temperature (1263 K). From previous works, it has been reported that α grain size is the predominant parameter in Ti-64's mechanical behaviour; decreasing α grain size; yield stress, ductility, crack nucleation resistance (High Cycle Fatigue strength) are improved [30]. On the other hand, a large α grain size only enhances macrocrack propagation resistance and fracture toughness [1].

These previous works have been focused in Ti-64 conventional produced, however with the development of AM techniques, totally new microstructures are achieved, therefore it is relatively recent topic among researchers [79, 80], it was found that these new microstructure produce different mechanical properties compared to their counter wrought parts. Figure 2.16 compares the mechanical response of hot worked Ti-64 and SLM microstructures reported in the literature [67]. Where SLM built components (green area) possess higher yield and tensile strength compared to the C&W built material (red area). This, however, is achieved at the expense of reduced ductility in the former. Moreover, the ductility of the SLM build microstructure show no apparent improvement even after heat treatments, where the strength of the material reduces considerably (blue section).

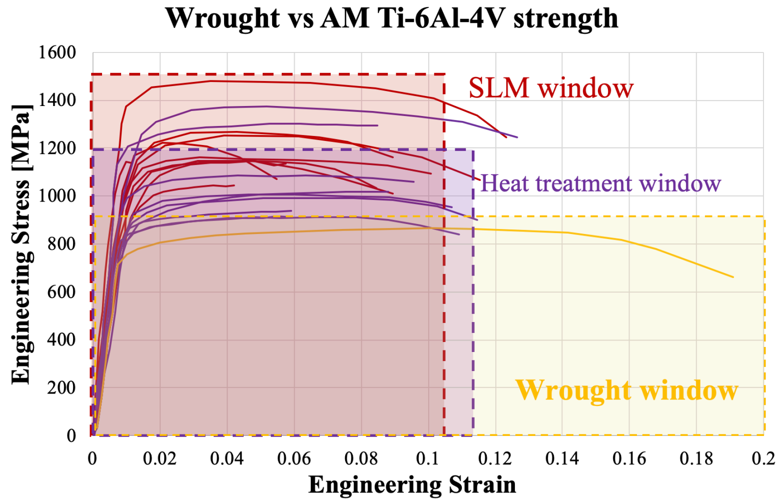


Figure 2.16 Tensile tests comparison of hot worked, SLM, heat treated SLM produced components of Ti-6Al-4V [67].

## 2.4 Machining

I has been found that 15% of mechanical components all around the world are either finished or processed by machining operations, moreover, machine tools, cutting tools and tooling represents a market of several billions of euros in industrially developed countries [94, 95]. Machining is a manufacturing process that creates shaped parts by removing unnecessary materials in the form of chips. Machining is one of the least understood manufacturing processes due to its high complexity and very high stresses and strains appearing in a small volume during very high speeds [96]. Additionally, temperature rises as high as 973K are reported during machining of Ti-64 as a result of excessive plastic deformation and frictional contact between the cutting tool and the workpiece [96, 97].

### 2.4.1 Mechanics of metal cutting

Most of the common machining operations including; turning, milling and drilling, boring, broaching, shaping and lapping involve complex three-dimensional deformation mechanics, however they share the same mechanics principles, despite their geometrical and kinematics differences [98].

To study the general mechanics of metal removal, it can be used the so-called orthogonal cutting (Figure 2.17), which is the most simplified case of cutting operations. During orthogonal cutting, it is neglected the side spreading of the material, therefore only two cutting forces are expected; one in the direction of velocity and the second in the direction of the uncut chip thickness (both in blue colour), which are commonly called tangential ($F_t$) and feed force ($F_f$) respectively.

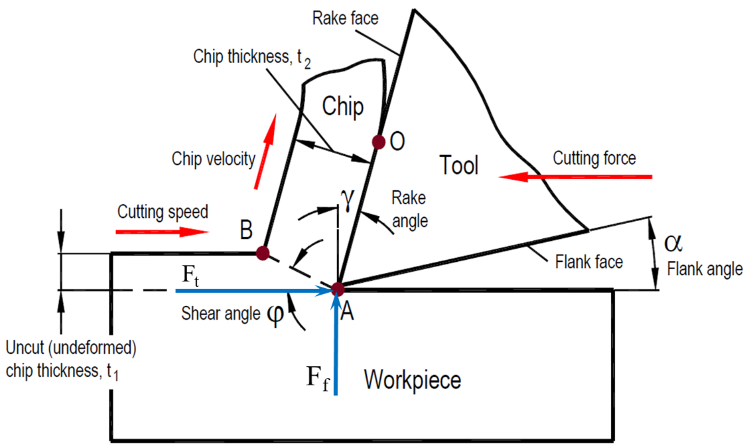


Figure 2.17 Diagram orthogonal machining, adapted from [94].

The cutting tool moves towards the workpiece so that it removes the uncut chip thickness ($t_1$) by shearing. AB is the shear plane which is defined by the shear angle φ. The actual produced chip thickness is denoted $t_2$ and the angle of contact between the tool and the chip is called rake angle, denoted as γ. Worth noting that γ determines the contact length between these two entities.

Within orthogonal formulation, three deformation zones are identified as shown in Figure 2.18a. Moreover, it is generally accepted that within these shear zones the heat dissipates through the chip, the workpiece and the cutting tool, therefore thermal properties of the workpiece are critical for good machinability [99].

The majority of shearing action and deformation happens in the primary deformation zone that is a fan shaped area starting from the tool tip and ending at the chip/workpiece interface. This zone is formed at an angel φ with respect to the cutting direction that is called shear angle. When the material is sheared away in the primary zone it flows into the secondary deformation zone ahead of the tool's rake face.

The tertiary zone also called friction area, is where the flank of the tool rubs the fresh machined surfaced. The freshly formed chip first sticks into the tool's rake face producing the sticking zone (Figure 2.18b), then the chips suffers a transition between sticking and starts sliding over the rake face with a constant sliding friction coefficient.

Finally, the new chip continues its path, losing contact with the tool [100]. Friction at the chip/tool interface plays a key role during the cutting process, due to this fact, numerous studies have proposed different models explaining the interfacial interaction of the chip and the tool [101-104]. Moreover, more recent models have been developed for titanium and nickel alloys [101, 105, 106].

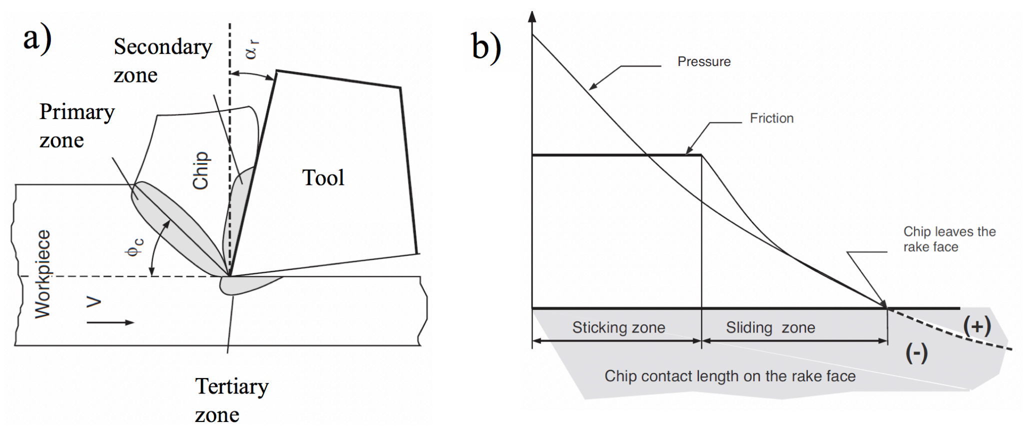


Figure 2.18 a) heat generation and b) contact zone during orthogonal machining, adapted from [98].

### 2.4.2 Chip morphologies

The factors that affect the chip form are the workpiece material, cutting fluid, tool geometry and the cutting conditions. Depending on the combination of these parameters, there are different types of chips produced during machining process. Figure 2.19 shows a classification proposed by Altintas [98].

It can be distinguished ten types, where ribbon, tangled and corkscrew type are unfavourable chips because they can scratch/ rub the freshly machined surface or could entangle around the tool, whereas short tubular chips, spiral chips and spiral chips are the highly desired during the process because they display benefits such as easy removal from the machine, they are safer for the operator due to easy disposal into the chip conveyor of the machine tool and quickly moves away from the fresh machine surface. Helical chips, long tubular chips, long and short comma chips display relatively acceptable results.

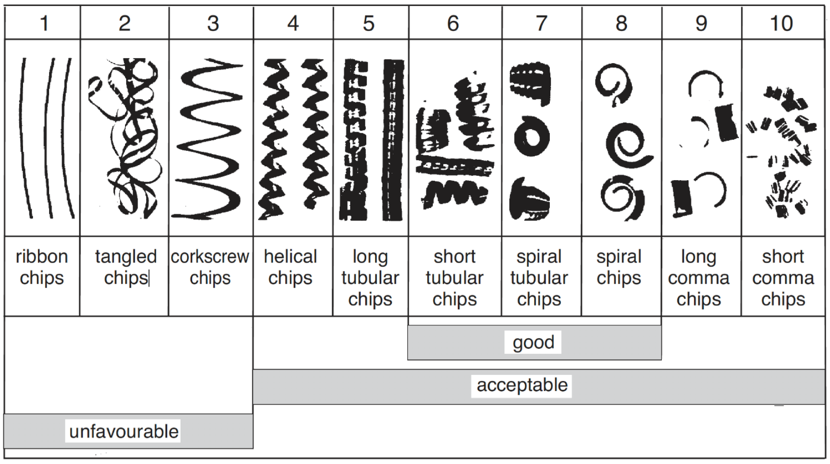


Figure 2.19 Classification of chips, adapted from [98].

### 2.4.3 Machining of titanium alloys

The ever-increasing demand for reliable and maximum safety components has boosted the production of titanium alloys for challenging applications such as aerospace and energy generation. Despite the processing route employed for production of titanium alloys it requires post machining techniques in order to achieve final shape [63, 107, 108].

Titanium alloys are part of a variety of difficult-to-cut materials that possess poor machinability (rapid tool wear), where generally speaking involves materials with a hardness of above 45 HRC [109, 110]. Examples of this classification are hardened steels alloys, martensitic steels, superalloys; Inconel, Rasp alloy, Waspaloy and titanium alloys; Commercial Pure (CP) Titanium, Ti-6Al-4V, Ti-6246 and Ti-5553 [110-112].

As discussed in section 2.2, titanium alloys possess outstanding properties, nevertheless these unique properties yield countless challenging problems during machining them. For instance, titanium alloys own low thermal conductivity which affects the possibility to extract heat from workpiece, as result; temperature is increased at the little area of the tool-workpiece contact point, therefore tool life decreases drastically [95].

Furthermore, titanium alloys have the ability of strain hardening, producing insatiability during plastic deformation [95, 113, 114]. The instability occurs due to local temperature rise within the shear plane (zone AB in Figure 2.17), drastically reducing the flow of strength, therefore deformation occurs on a thin section, giving place to the so-called periodic serrated chip (Figure 2.20), which yields in fluctuating cutting forces resulting in chatter phenomenon [112, 115-117], therefore these materials are not good candidates for High Speed Machining (HSM) [112, 118].

Additionally, titanium alloys have low Young’s modulus and high tendency of decreasing it by increasing the temperature which causes tool deflection during thin wall machining [117]. Titanium is highly reactive to most of known tool grades and tends to weld between the chip and the tool leading to early tool failure, hence coating of carbide tools such as TiN, TiCN, and TiAlN are commonly used [114, 116, 119].

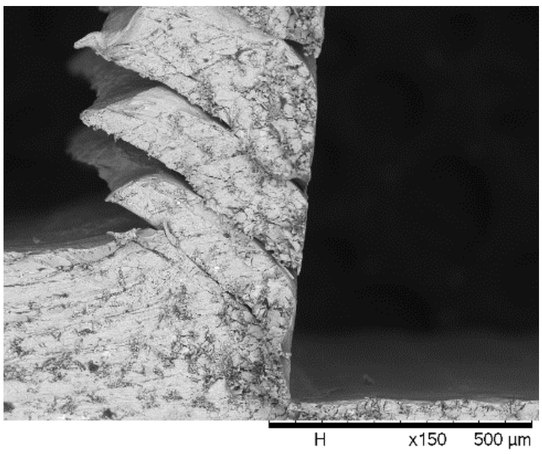


Figure 2.20 Typical saw-toothed chip of Ti-6Al-4V alloy.

Figure 2.21, shows the evolution of machining titanium alloys in the last eight decades. The grey region represents the progress in rough machining and the red region shows how the final (much more precise and therefore costly) machining has evolved. From this figure it can be seen that roughing operations had much more improvement compared to final operations. Therefore, special efforts are required to produce titanium components that are closer to the final shape.

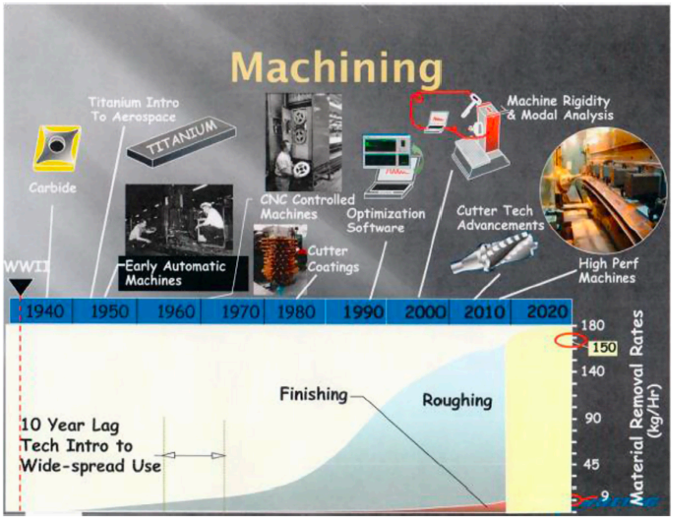


Figure 2.21 Historical perspective of the machining of titanium showing how various advancements have reduced the cost of machining [63].

There are extensive number of publications on experimental work of Ti6Al-4V alloy investigating the mechanics of deformation and the characteristics in machining using techniques ranging from metallurgical techniques [120, 121]. For instance, Puerta Velazquez et al. found no evidence of melting and/or phase transformation during machining of Ti-64 contrary to the generally believed that phase transformation occurred during machining Ti-alloys. Bayoumi et al. [122] have studied the behaviour of chip formation using various metallurgical analysis techniques, finding evidence of ductile failure within the chips.

Acoustic emissions also have been used on observations of chip formation by Barry et al. [123]. They found that increasing the cutting speed the degree of welding between the chip and the tool increases.

Other studies have investigated the performance of different tool grades in finish turning at high cutting conditions. For instance, Ezugwu [108] et al. have investigated the performance of CBN tools using high pressure coolant jet, authors found that the use of high pressure coolant during machining Ti-64 maintained constant cutting forces and reduced the contact between the chip and the tool.

Calamaz et al. [124] have reported a study on the performance of the uncoated and the multi-layer CVD-coated alloyed carbide tools. The study was focused on tool life and surface finish. It was found that new developed CVD-coated tools had longer tool life compared to uncoated carbide tools during dry machining. Bhaumik et al. [125], developed a wurtzite boron nitride–cubic boron nitride (WBN-CBN), in their investigation they indicated that the new developed tool can be used economically to machine titanium alloys.

Another approach has been the development of new lubrication systems such as cryogenic cooling [112, 126]. For example, Venugopal et al. [126] developed a new cryogenic lubrication system to improve the tool life while machining titanium alloys. They found that the new lubrication system enhanced the tool's life even for the uncoated inserts.

To date, most of the available literature on machining titanium alloys has focused in the mechanics and dynamics of the process, development of new tool grades and their effect on tool's life and surface finish and new lubrication systems. However, few studies have treated the microstructural state and evolution during machining process. In fact, the interest of researchers in microstructure and its behaviour during machining just has a decade [115, 116, 127]. The modelling community has emphasised this issue due to the lack of relievable models that can predict the microstructural effect on chip's morphology and predicted cutting forces [95, 128].

In order to predict cutting forces and chip's morphology, it is required deep understanding of microstructural evolution during machining [95]. The first step is to understand the roll that plays the strengthening mechanisms on the high-level mechanical properties of Ti-based alloys [67].

A number of studies have been begun to examine microstructure features. For instance, Wu et al. [129] developed a model capable of predict cutting forces due periodic serration within the produced chip in Ti-64, it was observed that the β grains are dragged inside the Adiabatic Shear Bands (ASB) commonly seen during machining titanium alloys and it was concluded that alpha phase is a key aspect for plastic deformation during machining titanium. Similar approach undertaken by Yu et al [130] evaluated the serration degree against cutting speed, interestingly they found that in all cutting conditions (20 up to 120 m/min), the chips were serrated, however by increasing the cutting speed the level of serration was higher and more frequent.

A more recent work by Joshi et al. [127] studied the influence of β phase fraction on deformation around shear bands produced by machining. A near-α alloy (Ti-5.5Al-2.5Sn), Ti-64 and a near-β alloy (Ti-4.1Al-3.9Mo-3.2V). It was concluded that increasing the beta phase fraction limits the spread of material deformation in the shear band and reduces the spacing between them. Similar study by Arrazola et al. [115] reported that Ti-64 machinability was approximately 56% higher than the near-beta Ti-555.3 alloy. Despite the higher specific cutting forces observed for Ti-555.3 (2900 and 2300 $N/mm^2$

for Ti-5553 and Ti-64 respectively), serrated chip was formed for both alloys in all cutting conditions. Figure 2.22 shows the serrated chips for (a) Ti-64 and (b) Ti-555.3. It can be seen ASBs for both alloys, where Ti-64 displays higher grain deformation (alpha phase), in turn less periodic serration. Whereas Ti-555.3 displays higher repetitive pattern, causing intermittent forces hence, premature tool failure at high cutting speeds (above 60 m/min). Authors attributed the machinability of both alloys was dependant of their mechanical properties, in turn; microstructural state.

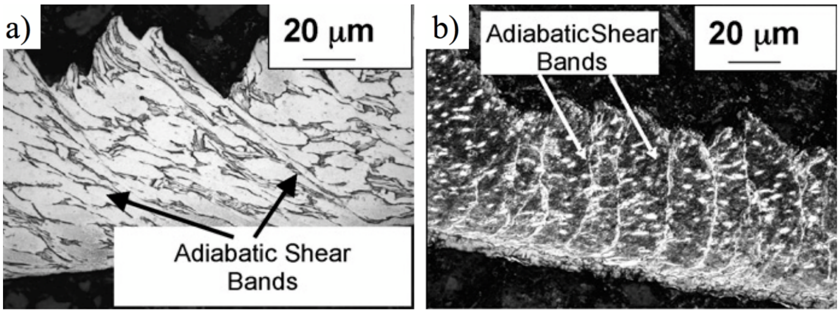


Figure 2.22 Produced chips during 60 m/min and 0.175 depth of cut of a) Ti-64 and b) Ti-5553, adapted from [115] .

Another study conducted by Armendia et al. [116] compared the machinability of two α+β alloys; Ti-64 annealed and Ti54M which is a new alloy recently developed by TIMET®. Authors found that despite differences on mechanical properties between both alloys, cutting forces were similar (around 2200 $N/mm^2$). Consequently, in order to modify Ti54M strength, they tested the cutting forces of this alloy by performing two different heat treatments; however, no clear difference was found between the other tested alloys.

These studies have shown the importance of understanding the microstructural state of Ti-64 and other titanium alloys. Figure 2.23 summarises the specific cutting forces during orthogonal machining tests for several titanium alloys within the literature. Where near-α alloys (green region) presented the lowest and near-β alloys (red region) displayed the highest specific cutting forces. Worth to mention that for the near-β alloy, it was reported that the cutting tool failed prematurely in all conditions above 60 m/min. The α+β alloys (blue region), displayed intermediate specific cutting forces, despite difference in chemical composition and microstructure. Additionally, they are shown the initial microstructures before deformation; displaying totally different type of microstructures between each other, hence they produce different cutting forces.

It can be seen that increasing the β volume fraction (Ti-555.3) will increase the cutting forces drastically (roughly 500 $N/mm^2$). These findings have not only encouraged experimental research but also modelling community to understand the microstructure evolution during machining in order to predict more accurate chip morphology, cutting forces and tool wear, just to mention some. Therefore, the following sections will treat the modelling aspects of modelling chip formation of Ti-64.

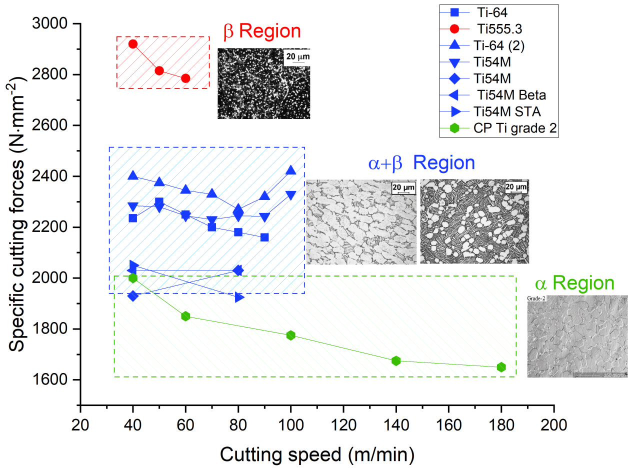


Figure 2.23 Comparison of specific cutting forces ($K_c$) generated during machining titanium alloys.

### 2.4.4 Constitutive equations for machining of Ti-64

As mentioned in section 2.4, workpiece is subjected to high levels of strain and strain rate and heat which will greatly affect the flow stress. The biggest inconvenient is the lack of available data for high speed and high stresses.

The constitutive data is commonly acquired from dynamic experimental materials tests such as Split-Hopkinson Pressure Bar (SHPB) tests. Samples are deformed under high speed (up to $10^5$ $s^{-1}$) and from room temperature up to 1373 K. However, there is currently a debate about the effectiveness of using SHPB as some researchers suggest that these tests are not sufficient for describing machining processes, especially High-Speed Machining (HSM). Therefore, values beyond the experimental data are calculated by interpolation [96]. For instance, Astakhov and Outiero suggested that SHPB tests are not specialized techniques for machining conditions, specifically for hot temperature testing, claiming that metal cutting is cold working process [94, 131].In addition, is not clear how to correlate uniaxial impact tests with material triaxially deformed [132].

As discussed in section 2.5.1, orthogonal cutting is the simplest case of metal cutting, making it the most predominate model within the FE modelling community which they refer as chip formation modelling [133].

Early attempts by Oxley [134, 135], to describe flow stress as a work-hardening behaviour, suggested a relation for carbon steel as;

$$\sigma = \sigma_1 \varepsilon^n$$

Equation 2.26

With $\sigma_1$ the material flow stress for $\varepsilon = 1$ and $n$ is the strain hardening exponent. And, for the combined effect of temperature and strain rate:

$$T_{mod} = T[1 - 0.009\log(\dot{\varepsilon})]$$

Equation 2.27

Another early constitutive model is the Usui, Maekawa and Shirakashi model [136, 137], also known as strain-path dependant model;

$$\sigma = B\left[\frac{\dot{\varepsilon}}{1000}\right]^{M} \varepsilon^{-kT}\left[\frac{\dot{\varepsilon}}{1000}\right]^{m}\left\{\int_{path} e^{KT/N}\left[\frac{\dot{\varepsilon}}{1000}\right]^{-m/N} d\varepsilon\right\}^{N}$$

Equation 2.28

Where, $B$ is the strengthening factor, $M$ is strain rate sensitivity and n the strain hardening index, all functions of temperature ($T$), and $k$ and $m$ are material constants. This unique model captures the effect of loading history and captures the blue brittleness behaviour of low carbon steels. As an empirical model, the major drawback using this model is the lack of insight of the physics behind plastic deformation. Moreover, obtaining the set parameters is difficult and requires large number of experiments, therefore, is not commonly implemented into FE techniques.

Zerilli and Armstrong (ZA) developed a physically based constitutive model centred on dislocation interaction theory [138]. Depending on the crystal structure, they suggested two different equations for body cubic centred (BCC) and face centred cubic (FCC) structures, respectively; where $C_0$ – $C_5$ and n are material constants determined experimentally:

$$\sigma = C_0 + C_1 exp[-C_3 T + C_4 T ln(\dot{\varepsilon})] + C_5 \varepsilon^n$$

Equation 2.29

$$\sigma = C_0 + C_2 \varepsilon^n exp[-C_3 T + C_4 T ln(\dot{\varepsilon})]$$

Equation 2.30

ZA model is very popular for its easy implementation within flow stress models literature, however its accuracy for predicting cutting forces using FE modelling shown large discrepancy [133].

Among the most used models for chip formation is the so-called Johnson-Cook (JC) model [139]. The model consists in three terms including, strain hardening, strain rate sensitivity and temperature softening terms:

$$\sigma = [A + B\varepsilon^n]\left[1 + C\,ln\left(\frac{\dot{\varepsilon}}{\dot{\varepsilon_0}}\right)\right]\left[1 - \left(\frac{T - T_r}{T_m - T_r}\right)^m\right]$$

Equation 2.31

Where, $\dot{\varepsilon_0}$ is the reference plastic strain rate, $T_r$ the room temperature, $T_m$ the melting temperature and $A$, $B$, $C$, $n$ and $m$ are constants that depend on the material and determined by material tests such as SHPB.

The existing research using the JC model is extensive and have contributed to the evolution of chip formation models into two main phases; first phase; accurate prediction of fundamental variables such as tool-chip contact length, cutting forces, chip thickness, etc. and second phase; accurate prediction of industrial relevant outcomes such as tool-life, surface integrity, etc [140, 141].

In the first stage, the JC model was extensively used and was found by several authors that JC parameters highly affect the accuracy of chip morphology and cutting forces prediction [142]. Even finding that constitutive laws are the most relevant in order to accurate predict cutting forces [133].

For instance, Schulze et al. [143] investigated the effect of four different set of parameters for Ti-64 on chip morphology and cutting forces. The investigation revealed that the four set of parameters underpredicted the experimental cutting forces (100 to 150 N). Also, level of serration on the chips was inferior compared to the actual experimental chips. Authors concluded that despite using different JC parameters, JC model was not capable to predict accurate both phenomena and suggested that it is required the development of constitutive models based on machining tests, rather mechanical testing.

Similar research conducted by Zhang et al. [144] found that JC model was unable to predict accurate chip morphology and cutting forces, despite using three different JC set parameters and three type of numerical of formulations. Authors suggested that it was required the formulation of new constitutive models based on crystal plasticity.

Other study by Short & Bäker [145] calibrated JC parameters using machining experiments. Authors used regression algorithms in order to fit the cutting forces with flow stress curves. The results suggested that new methodology was capable to capture successfully JC set of parameters, however no improvement on the chip morphology was achieved. Özel & Karpat [142] used evolutionary computational algorithms to identify JC parameters, authors successfully predicted cutting forces under orthogonal conditions, however they do not studied chip morphology.

Previous research has shown that using the JC model present two major drawbacks including, the set of parameters is unique for a given material with a specific processing history that is evident due to the extensive list of JC material's constants reported for Ti-64 [105, 142, 146]. Also, it was found that JC model under predicts cutting forces and level of serration within the chips. These findings encourage several authors to develop new models for difficult-to-cut materials, opening the way for the second stage (current) of chip formation models.

In second phase (current), initial efforts to improve the JC model for Ti-64 simulations have been done by adding an extra term for softening behaviour. First attempt to modify the JC model was made by Calamaz et al. [140], authors attributed the softening of the material due to a microstructural effect called "strain softening". The proposed model consisted in adding a tangent hyperbolic term to the JC model as follows:

$$\sigma = \left[A + B\varepsilon^n \left(\frac{1}{\exp\left(\varepsilon^a\right)}\right)\right]\left[1 + C\,ln\left(\frac{\dot{\varepsilon}}{\dot{\varepsilon}_0}\right)\right]\left[1 - \left(\frac{T - T_r}{T_m - T_r}\right)^m\right]\left[D + (1 - D)tanh\left(\frac{1}{(\varepsilon + S)^c}\right)\right]$$

Equation 2.32

$$D = 1 - \left(\frac{T}{T_m}\right)^d$$

Equation 2.33

$$S = \left(\frac{T}{T_m}\right)^b$$

Equation 2.34

Where $a$, $b$, $c$ and $d$ are material constants. The hyperbolic tangent model decreases the strength of the material beyond a given strain, where the flow stress decreases until a critical strain value of 1.5, when it becomes constant. At low strains, the model predicts exactly the same as the JC model.

Additionally, it is considered the thermal effects by Equations 2.8 and 2.9, where the peak stress value decreases when the temperature is increased. Authors successfully produced segmented chips during their simulations, also predicted more accurate cutting forces from experiments, however they recognised that the model required improvement for wider range of cutting speeds (strain rate effects).

Sima & Özel [105] continued Calamaz et al. work by adding strain rate effects by adding a parameter $s$ in order to further control the hyperbolic tangent function for thermal softening as follows;

$$\sigma = \left[A + B\varepsilon^n \left(\frac{1}{\exp\,(\varepsilon^a)}\right)\right]\left[1 + C\,ln\left(\frac{\dot{\varepsilon}}{\dot{\varepsilon_0}}\right)\right]\left[1 - \left(\frac{T - T_r}{T_m - T_r}\right)^m\right]\left[D + (1 - D)tanh\left(\frac{1}{(\varepsilon + S)^c}\right)^s\right]$$

Equation 2.35

$$D = 1 - \left(\frac{T}{T_m}\right)^d$$

Equation 2.36

$$S = \left(\frac{T}{T_m}\right)^b$$

Equation 2.37

Authors reported a large range cutting conditions; cutting speeds from 121 up to 240 m/min, coated and coated tools and two rake angles. They found better agreement with both cutting forces and chip serration frequency. It was suggested that chip formation process was produced by adiabatic shearing within Ti64 alloys since they used a FE commercial software that does not consider failure in the elements.

This statement also was distinguished by other authors, claiming that within the ASBs the material was affected by DRX and was the precursor of this softening, creating a high frequency intermittent cutting forces and then drastic drop in cutting force [105, 140, 147]. However, there is still a debate about the nature of this drop in forces, some authors claim that could be attributed to phase transformation [128]. From this outcome, researchers started to focus more in microstructural features not only of Ti-64 but also of other difficult-to-cut materials [111, 148-150].

Arisoy & Özel [141] continued their research using Equations 2.10-2.11 in order to predict cutting forces, however they used the Johnson-Mehl-Avrami-Kolmogorov model (JMAK) [128, 141] to predict the recrystallised material during several machining passes. Worth to mention both models were not coupled, therefore the results were presented separately. Authors compared the JMAK predictions of grain size recrystallised against experimental data. Grain diameters were determined by Selective Electron Microscopy (SEM) images and image processing.

The results showed relatively good agreement (within the 10% of error) for most of the cutting conditions presented. Later, Yameogo et al. [128], coupled the JC model and the hyperbolic tangent model through the JMAK model as a triggering function as follows;

$$\sigma = (1 - X_{DRX})\sigma_{JC} + X_{DRX}\sigma_{tanh}$$

Equation 2.38

Where $X_{DRX}$ is the volume recrystallised and is determined by the JMAK model, $\sigma_{JC}$ is the JC flow stress equation and $\sigma_{tanh}$ is the hyperbolic tangent equation. Authors presented similar results as Arisoy & Özel, however they claimed that the serration was produced by thermoplastic instability within the shear zone produced by excessive damage within the ASBs.

The last two reviewed investigations have turned the research direction of chip formation models for the future. The use of constitutive physically based in the last five years has become more common within the modelling community. As result, similar chip formation models for CP titanium [147] cooper [151] and nickel alloys [111, 148, 150] have been proposed.

Thanks to constitutive laws that describe the physical phenomenon of plastic deformation in metals not only predict accurate cutting forces and chip morphologies but also can provide better understanding of the physical phenomena occurring during chip formation, such as volume fraction recrystallised, grain evolution, dislocation density, heat affected zone, etc [133, 152]. Nevertheless, there is still a gap in knowledge related to initial microstructure within Ti-64 and even more complex alloys such as nickel alloys or high strength steels.

## 2.5 Finite Element modelling of processing titanium alloys

As this research is focused in the development of a Ti-64 constitutive model for plastic deformation for a wide range of manufacturing processes and their implementation into FE techniques, this section will cover the the most relevant Finite Element strategies used for hot forming and machining processes.

Prediction of Ti-64's mechanical properties has been a relevant topic for materials scientists and engineers. In this context, constitutive equations are used to describe flow stress of materials during plastic deformation. In order to replicate the deformation conditions during manufacturing processes, it us commonly used controlled mechanical testing. Therefore, special care has to be done during the selection of the testing method since the flow stress of the material determines the material strength and reaction to the applied deformation.

The constitutive equations are usually implemented into Finite Element (FE) techniques in order to predict relevant outputs such as reaction forces, heat affected zones, stresses, etc [29, 128]. These techniques can aid to control variables during manufacturing process also optimize them, especially those processes where it is difficult to monitor the microstructure evolution through the whole process such as forging or machining[21].

Figure 2.24 shows the most common metal working operations with associated deformation rate and possible mechanical testing method to replicate the strain rate observed in the manufacturing operations. Varying from low strain rates $10^{-6}$ s-1 followed by intermediate ($10^{-1}$ up to $10^{2}$ $s^{-1}$) up to high rate-impact testing (high strain rate $10^{2}$ $s^{-1}$ up to $10^{5}$ $s^{-1}$). Forming processes (forging, hot rolling, punching) are associated to low strain rates compared to machining process.

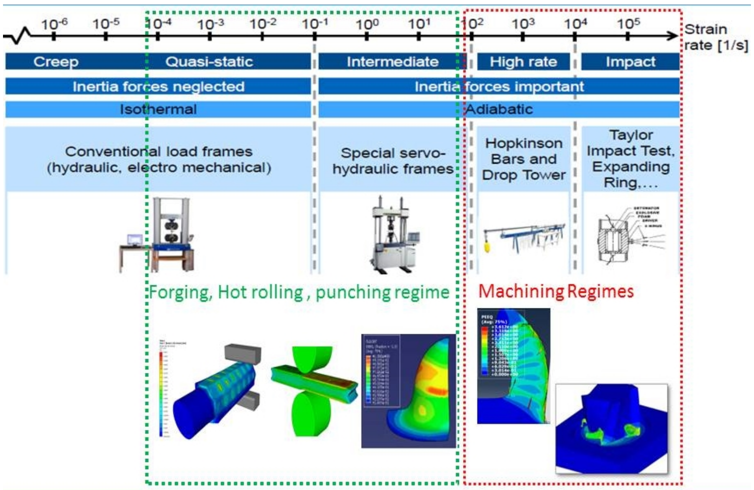


Figure 2.24 Strain rate regimes, associated testing methods and associated FE modelling manufacturing processes.

Despite that constitutive equations are developed for a specific manufacturing process, including; forging [52] and machining[133] of Ti-64. Both type of equations can be categorised into three groups including; empirical [90, 91, 139, 153], physically based [17, 27, 154-156] and the most recent, Artificial Intelligence Techniques (AIT) modelling [18, 33, 157].

Empirical models are a mathematical representation of experimental data and usually describe flow stress as a function of strain, strain rate and temperature, while the physically based models link physical phenomena with macroscopic mechanical behaviour. Finally, AIT use machine learning algorithms to predict mechanical properties during different processing histories.

Within the three approaches, empirical models are the most common implemented models into FE techniques due to small number of parameters required to calibrate the models for a given material. Despite this advantage, these models own the lack of understanding on the different mechanisms occurring during plastic deformation. In addition, model’s parameters are determined from a given material with a specific processing history, therefore large variations in the mechanical behaviour is expected. This is evident due to the extensive list for material's constants reported for Ti-64 [92, 93, 105, 133, 142, 153] for only one empirical model [67].

Whereas, early physically based models are capable to describe complex mechanisms such as dislocation evolution [27, 154], partitioning dislocation density into mobile and immobile dislocations [158] and models based in activation energy required to generate plastic deformation [30, 157]. The major drawback of these models is the high number of material constants to be validated, limiting their implementation into FE techniques [29].

The AIT based models can accurately predict the mechanical properties of any material when the processing parameters (e.g. deformation temperature, strain and strain rate) are well defined [33, 35] . However, these are computationally and experimentally expensive requiring many experimental results to train the models and, in most cases, they cannot quantify different phenomena occurring during plastic deformation.

Since AM is a relative new technology, only a few equations have been developed for describing plastic deformation of AM Ti-64 [67, 79, 159]. Therefore, it is required a new constitutive equation capable to predict AM and C&W Ti-64 for different manufacturing processes. The following sections will cover firstly FE modelling of hot forming later for machining operations.

### 2.5.1 Finite Element modelling of hot forming operations

The development of a hot deformation FE model is relatively simple compared to FE machining operations. Simulation of specific processes has been done, including hot rolling [160], hot tube extrusion [161], sheet metal hot forming[162], hot forging of impellers [163], just to mention a few. Despite their differences, all of them compromise one or two rigid bodies and the workpiece is deformable. However, the simplest case to model is axisymmetric compressions tests for simulating hot forming processes. Commonly performed in a thermo-mechanical simulator at controlled temperature and deformation speeds [15, 20].

Most of the models within the literature use a two-dimensional and half symmetric thermo-mechanical coupled model. Two anvils are used to compress the material and are usually model as rigid bodies. The anvils could be modelled either thermally coupled to the billet or could be assumed no heat transfer between the deformable and the rigid elements.

The FE model has to be capable to represent the controlled conditions performed during the experiments. A two-dimensional axisymmetric FE model the velocity is applied to anvil, whereas anvil two is fixed in both axes. The specimen is modelled as a deformable material.

In order to provide realistic and accurate FE axisymmetric compression models, it is required to consider four aspects during FE simulations, including; mathematical formulation, friction behaviour, geometrical formulation and material constitutive model.

Within the literature, two types of mathematical formulations are proposed; Eulerian, Lagrangian.

In the Eulerian formulation, the elements of the mesh are spatially fixed (control volume) and material flows through elements that do not deform. Furthermore, Eulerian elements may not always be full of a single material, many may be partially of even completely void. Whereas, in Lagrangian approach, the elements of the mesh are attached to the material; thus, the elements deformed as the material deforms. Moreover, Lagrangian elements are always defined as full of a single material, so the material boundary coincides with an element boundary. Lagrangian approach is most commonly used for large-scale plastic deformation processes such as forming and machining [21].

Within the FE forming literature, the most common friction model used is the Coulomb's law, this is due to the fact that majority of studies focused in plasticity, also is the simplest model available and most of commercial software have it embedded in their codes. Coulomb's law considers frictional stresses ($\tau$) on the flat face are proportional to the normal load ($\sigma$). The ratio of these two is the coefficient of friction $\mu$, which is constant through all the contact length between the sample and the anvils [164]:

$$\tau = \mu\sigma$$

Equation 2.39

Four geometric parameters are needed to model forming processes, named; size of mesh, type of elements, boundary conditions and type of contact. For instance, the size of the elements will affect in the results, furthermore, there is a threshold beyond further decrease of elements with marginal gain in terms of computational time. Increasing the aspect ratio of the elements drops accuracy in the model; therefore, it is recommended compact, regular shapes, i.e. quadrilateral elements.

The boundary conditions are commonly applied as follows; one anvil is fixed and the second one has the relative movement towards the deformable sample. The most common approaches for contact and contact detection between the deformable sample and the anvils are; penalty method, and Lagrangian.

The last element required to model hot axisymmetric compression tests is the constitutive equation to describe the flow stress of the material. This has been covered in section 2.4.4, however it will be presented the most predominant implemented models into FE techniques within the literature.

For instance, Matsumoto & Velay [165] proposed a revolutionary work focused in DRX, change in grain size and dislocation density during Ti-64 hot forming. The FE simulations revealed that increasing the strain rate and decreasing temperature, DRX occurs continuous. These results were validated with experimental data which consisted in an initial equiaxed structure tested at three temperatures (973, 1073 and 1173 K) and four strain rates ($10^{-3}$ up to 10 $s^{-1}$).

Authors used an Arrhenius type of equation to determine the apparent activation energy, whereas for determine the grain size evolution they used the Zener-Hollomon formulation. Together with the JMAK model, authors were capable to predict the distribution of the grains recrystallised, grain size and the distribution of the dislocation density within the deformed samples. Authors predicted volume fraction recrystallised, mean grain size, evolution of dislocation density due to plastic deformation. It was reported good agreement with experimental results (within an overall error of 10% in most conditions). Nonetheless, the complexity of the developed model hinders the use of it for other initial microstructures, since the model was developed for only one microstructure. Additionally, the JMAK does not consider the transition of alpha phase to beta phase during transus temperature (around 1073 K).

Analogously, Quan et al. [15] used the JMAK model to predict recrystallised volume fraction, grain size evolution and distribution in deformed samples by hot axisymmetric compressions tests. However, the distribution of the dislocation density was not included in their model. Authors studied an initial equiaxed microstructure in a large deformation conditions (seven temperatures ranging from 1023 up to 1323 K and four strain rates from $10^{-3}$ up to 10 $s^{-1}$). Authors successfully predicted the DRX grains within an overall 15% of error in most of conditions.

The previous research has shown the good capabilities of FE modelling for hot deformation processes. However, three needs can be highlighted form previous work; first the necessity of a constitutive equation that can predict the flow stress considering initial microstructure features such as, grain size and shape, volume fraction. Second, it is required a model capable to predict the distribution of alpha phase during and after deformation, specially at the transus temperature. Finally, a model that can be used in a wide range of metal processing.

### 2.5.2 Finite Element modelling of machining operations

Modelling of machining processes have a long trajectory. From 1950's to 1990's decades, analytical models such as mechanistic and based in slip line fields were the most predominant techniques. The most notable among these models include; Merchant's shear plane model [166], Hill's mathematical slip line foundation [167] for latter models such as Palmer & Oxley model [168], Usui & Hoshi model [136], Roth and Oxley model [169] and more recently the Fang et al. models [170, 171]. Mechanistic and slip line theories settled the foundations of prediction of cutting forces, chip geometry, average strains, temperatures and stresses of current machining models. However, their reliability was limited to a unique machining problem in a basis of 2-D analysis with single cutting edge.

In the early 1990's, with the development of faster computers, numerical modelling started to attract research community due to lesser computational times and their better accuracy compared to their predecessors. Since the approach of this thesis is based in these techniques, only these models will be covered in this section.

Simulation of specific machining processes has been done, including drilling [172, 173], milling [141] and turning/orthogonal cutting [174]. Despite their differences, all of them compromise a cutting tool and a deformable workpiece. However, the simplest case to model is orthogonal cutting also refer as chip formation modelling, making it the preferred by researchers [133, 174].

In order to provide realistic and accurate FE chip formation models, it is required to consider five aspects during FE simulations, including; mathematical formulation, friction behaviour, damage initiation criterion, geometrical formulation and material constitutive model. It has been proposed three types of mathematical formulations of continuum-based FEM; Eulerian, Lagrangian and more recently Arbitrary Lagrangian-Eulerian (ALE).

In the Eulerian formulation, in order to simulate chip formation, it is required to assumed shear angle, shape of the chip and contact conditions. Additionally, this technique cannot be applied for discontinuous chips due to strains are derived from integration of strain rates along stream lines [96].

In Lagrangian approach, the material's flow is not constraint in space, letting simulations of segmented chips and serrated chips, thus, making this approach very popular among machining modellers. However, a disadvantage of this formulation is the high mesh deformation occurring in simulations and the employment of chip separation [175, 176].

ALE approach combines Lagrangian and Eulerian formulations. The mesh is neither constrained nor attached to the material, instead, it moves arbitrarily relative to the material, the sum of a Lagrangian and an Eulerian displacement increment will be the total displacement of the mesh. Additionally, no failure criteria is required, as result the mesh is less deformed compared to Lagrangian mesh. The only inconvenient of this approach is that uses re-mapping of state variables which may be calculated wrong, which compromise the accuracy of the results [146, 177].

Cutting tool's life heavily depends on the frictional conditions between the chip and the tip's interface, hence it is of high importance the correct selection of formulation to determine cutting forces, tool wear and surface quality[106]. It has been found that during machining, friction occurs under extreme conditions at the tool-chip interface (1-2 GPa and 500-1000 °C) [178].

The most common friction model used during FE machining processes is the Coulomb's law, however, as normal stresses overpass a critical value, this relation is not valid. This issue has been corroborated from experimental analysis, and it has been identified two contact regions in dry machining, namely sticking and sliding region. Zorev [100] proposed a more accurate model known as the stick-slip temperature independent friction model. The model was based on normal and shear stresses distributions, where a transitional distance $l_c$ from sticking region, the flow stress is equal to plastic yield to sliding region, where a Coulomb model is used;

$$\tau = \begin{cases} k, 0 \leq l \leq l_c \\ \mu\sigma, l > l_c \end{cases}$$

Equation 2.40

Based on Zorev's work, several models have been developed. For instance, Usui and Shirakashi [136] derived an empirical equation based on experimental machining tests. The model aimed to describe the stresses in a friction model at the tool-chip interface as follows;

$$\tau = k\left[1 - \exp\left(-\frac{\mu\sigma}{k}\right)\right]$$

Equation 2.41

Where $k$ is shear flow stress and $\mu$ is the friction coefficient. This model approaches the sticking region using the Equation 2.15 for large stresses and for the sliding part which normally represents smaller values of stresses, it is used Equation 2.16. Dirikolu et al.

[179] modified previous model by multiplying *k* by a friction element $m$, where 0 < m < 1, and by introducing an exponent *n*:

$$\tau = mk\left[1 - \exp\left(-\frac{\mu\sigma}{mk}\right)^{n}\right]^{1/n}$$

Equation 2.42

As pointed out in section 2.5.4.1, Lagrangian formulation, require the employment of a damage criterion. Node-splitting and element deletion are the two main techniques employed to simulate chip formation [96]. Within the node-slipping formulation there are two types of criteria; geometrical and physical. Geometrical criterion uses certain a defined distance between the tool tip and the nearest node on the cutting direction. Whereas physical criteria use the critical value of a physical quantity (e.g. the plastic strain criterion chip separated when the calculated plastic strain at the nearest node to the tool reaches a certain value) to estimate the onset of separation [96]. The disadvantage of this criterion is that node separation may propagate faster than the cutting speed.

It is generally accepted that ductile failure occurs during chip separation and formation [180, 181]. Therefore, most of FE chip formation models within the literature use a ductile failure criterion [133] which commonly employs three failure criteria namely, critical strain, critical strain to fracture and maximum shear stress. Within these methods, critical strain method is the most easily to implement [182]. However, the most commonly used for Ti-64 chip formation model, is the Johnson-Cook damage model [183] which is based on strain-to-fracture:

$$\varepsilon_f = [D_1 + D_2 exp(D_3\sigma^*)][1 + D_4 ln\dot{\varepsilon}^*][1 + D_5 lnT^*]$$

Equation 2.43

Where, $D_1$- $D_5$ are material fracture constants and $\sigma^*$, $\dot{\varepsilon}^*$ and $T^*$ are the triaxial stress, strain rate and temperature. After the damage is reached, it could be applied a damage evolution before the total failure of the element. Damage evolution defines the post damage-initiation material behaviour; moreover it describes the rate of degradation of the material once the initiation criterion is satisfied [96]. Damage evolution can be specified either in terms of fracture energy (per unit area) or equivalent plastic displacement. However, the damage evolution will be treated in more detail in simulation procedure.

Four geometric parameters are needed to model machining processes, named; type of elements, boundary conditions and type of contact. The type of element will depend the thermo-mechanical coupling method. As the heat is conducted into the tool and the chip and transferred away from the chip into the environment by convection. This process is modelled by either heat sources at the generation regions or usually with material and tribological models. Two boundary conditions approaches can be applied; the workpiece is fixed and the tool has the relative movement towards the workpiece, or all the way around, tool is fixed and the workpiece advanced towards the tool. The most common approaches for contact and contact detection between the chip and the tool are; penalty method, and Lagrangian multipliers [96, 133].

The last element required to model chip formation is the constitutive equation to describe the flow stress of the material. This has been covered in section 2.4.4, however it will be presented the most predominant implemented models into FE techniques within the literature. Calamaz et al.[124] proposed a revolutionary work focused in adiabatic heating during high speed machining of Ti-64. Authors predicted good agreement in terms of cutting forces and chip morphology. It was found that at high speeds (100-180 m/min) was capable to predict accurate, however at low speeds (below 80 m/min) the results shown that the model started to lose accuracy.

Years later, Sima & Özel [105] modified the model TANH model by adding extra term to control the strain rate, hence the model predicted accurate in a wider range of cutting conditions (i.e. cutting speeds form 20 m/min up to 180 m/min). Authors reported that the model was capable to replicate the chip morphology more accurate than their predecessors.

A more recent work by Yameogo et al. [128] combined the enhanced TANH and the JMAK models in order to replicate the work performed by Sima & Özel [105]. Authors argued that the serration formed in Ti-64's chips was not only due to adiabatic heating but also due to DRX creating an extreme softening due to both competing factors. Additionally, authors used the Johnson-Cook initiation failure criterion combined with a power law of degradation based on energy.

Authors successfully predicted serrated chips including formed cracks produced due to insatiability during plastic deformation. Despite that the authors predicted more accurately than their predecessors, the model does not give more insight of the mechanics during chip formation, for example DRX and grain size distribution within the chip formed and the produced surface, despite that the model already predicted (JMAK), however authors did not report this.

## 2.6 Background Summary

This chapter has highlighted the areas of research explored. It was found that the titanium alloys are sensitive to microstructure. Additionally, due to titanium high costs involved during conventional processing and machining process, Ti-alloys are good candidates for AM techniques in order to reduce production time cycles, waste and time during finishing operations. Despite the reviewed AM's benefits, the produced parts by AM technologies are affected by poor surface finish, geometrical accuracy and the usage of building supports makes subtractive post processing operations essential. Therefore, this research is critically important to understand the mechanics of deformation of these components. To do so, development of material models sensitive to microstructure is required.

The cited constitutive material models have been focused on mechanical behaviour of C&W Ti-64, since modelling of the AM components is a relative new field. Additionally, to the best knowledge of the author, no constitutive model is available for Ti-64 manufactured under a wide range of processing routes (C&W and AM). Also, it was presented the most important FE models used for simulation forming and machining processes. It was found that the current modelling trend is the use of constitutive physically based laws which have shown more accurate results, but also providing more insight of the manufacturing processes aiding optimization and process control.

From this literature review it can be drawn the following conclusions;

1) There is no link between FE modelling communities (i.e. forming and machining modellers), therefore a gap of knowledge in terms of constitutive laws has been created
2) There is no available constitutive model capable to predict flow stress for conditions suitable for machining (high strain rates and temperatures) and hot forming conditions (hot temperatures and low-intermediate strain rates).
3) No constitutive model is available to link microstructural features such as; grain type and size, volume fraction and chemical composition irrespective of the processing route (i.e. C&W and AM)

This study aims to present a new physically based model capable of linking relevant microstructural features with flow stress. The new proposed model aims to describe plastic deformation irrespective of the processing route (C&W and AM Ti-64 components) in a wide range of manufacturing processes. The proposed model is implemented in a user subroutine VUMAT in commercial FE Abaqus software and validated using produced experimental data and within the literature.

# 3. Experimental methodology

## 3.1 Introduction

This chapter focuses on the methodology adopted for the experiments conducted in this project. The aim of mechanical testing was to study the mechanical properties of Ti-64 SLM built components at various deformations conditions suitable for machining and hot forming conditions. Mechanical testing is divided in high strain rates at room temperature (2000 $s^{-1}$) and high temperature (973 -1273 K) axisymmetric compressions tests at low and intermediate strain rates (1-100 $s^{-1}$).

The orthogonal machining tests aimed to compare the cutting forces and the chip morphologies of SLM and C&W Ti-64. Ti-64 SLM samples were tested in the two building directions (vertical and horizontal), whereas conventional Ti-64 was only tested in one direction (opposite to rolling direction).

Also, this chapter will cover the manufacture and preparation of samples and characterisation techniques performed in order to validate experimental results with the numerical predictions.

## 3.2 Manufacture and preparation of samples

Two set of samples were prepared for mechanical testing; Ti-64 SLM built samples for SHPB tests and thermomechanical compression testing (TMC). Whereas orthogonal cutting consisted in three set of samples were manufactured; commercial Ti-64 grade and Ti-64 SLM built parts.

### 3.2.1 Mechanical testing samples

The samples for both, SHPB and TMC tests were built in a SLM 125, Renishaw machine. All samples were built in the vertical direction. A schematic of both set of samples is presented in Figure 3.1; a) SHPB specimens consisted in cylindrical shape with 10 mm diameter by 5 mm height, whereas b) TMC specimens consisted in cylindrical shape, 10 mm diameter by 15 mm height, in addition, a hole of 1.1 mm diameter by 5 mm depth was made in the centre of the side to attach a N-type thermocouple. Due low accuracy and surface quality in the flat surfaces, all samples were grinded in both surfaces to make the surfaces parallel to each other and ensure constant compression rate.

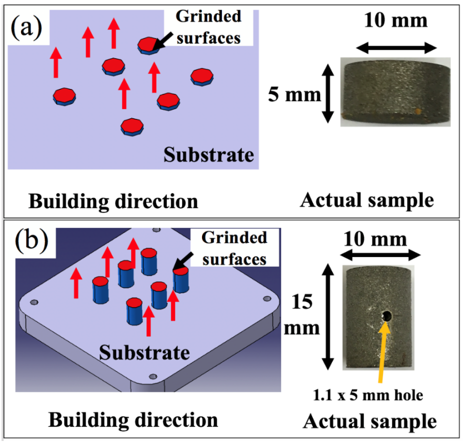


Figure 3.1 Manufactured mechanical testing samples: a) SHPB and b) TMC tests

### 3.2.2 Orthogonal machining samples

The SLM workpiece specimens consisted in square samples of 25X25 mm and 3 mm thickness. It was studied the effect of sample's building direction; hence they were built in both directions (horizontal and vertical directions) in a SLM 125, Renishaw machine. A schematic of both set of samples is presented in Figure 3.2a. Whereas the C&W specimens consisted in rectangle samples of 25X20 mm and 3 mm thickness, the actual sample is presented in Figure 3.2b. After building, all samples required post processing owing support removal. Samples were squared and grinded in all faces in order to use samples' surfaces for referencing the CNC machine's set up.

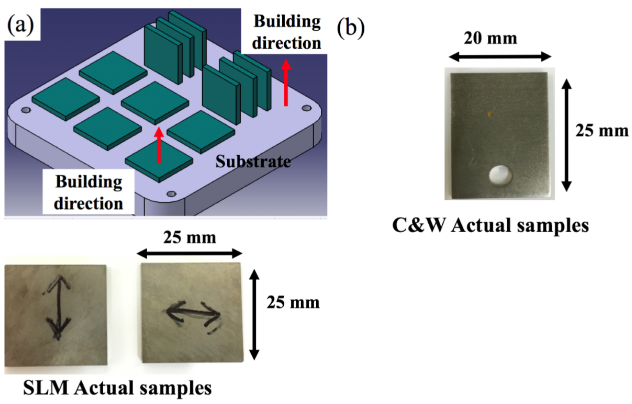


Figure 3.2 Manufactured orthogonal machining samples: a) SLM b) C&W.

### 3.2.3 Sample preparation

The SHPB and TMC deformed samples were sectioned parallel to the compression axis. Standard metallographic preparation was used; hot-mounting conductive Bakelite, following by two stages of grinding; using the MD-Mezzo #220 adding water for ten minutes and the MD-Largo #150 using a solution DiaDuo-2 (9 μm particle size) for 15 minutes. Mechanical polishing was performed using MasterMet colloidal silica of 0.5 μm for 7 minutes. Finally, Kroll's reagent was used to etch the samples to reveal the microstructure.

## 3.3 High strain rate tests

### 3.3.1 Description of the SHPB rig.

Material properties reported in handbooks and design manuals commonly obtained under quasi-static loading conditions using common load frames. However, high strain rate loading conditions are beyond the capabilities of conventional material testing machines [184]. The use of high strain-rate tests is to determine the material properties under impact conditions, which are corresponds to dynamic events encountered in engineer applications, including helmet impact on hard surfaces, armour testing for ballistic applications and bird impact on aircraft engine components and during machining processes.

To obtain dynamic response of materials under controlled conditions, Kolsky developed the first high-rate testing machine in 1949 [185]. The testing machine became famous and still remains essentially the same in the present, however today is known as Split Hopkinson pressure bar (SHPB).

Figure 3.3 shows the schematic of the set up used in the trials. SHPB rig consist in three main components; loading device, bar components and data acquisition and recording system. The bars involved; incident and transmission bar, both instrumented with strain gauges and coupled to the recording system. The bars were aligned to the action plane using levels provided in the rig in order to ensure one-dimensional wave propagation in the bars.

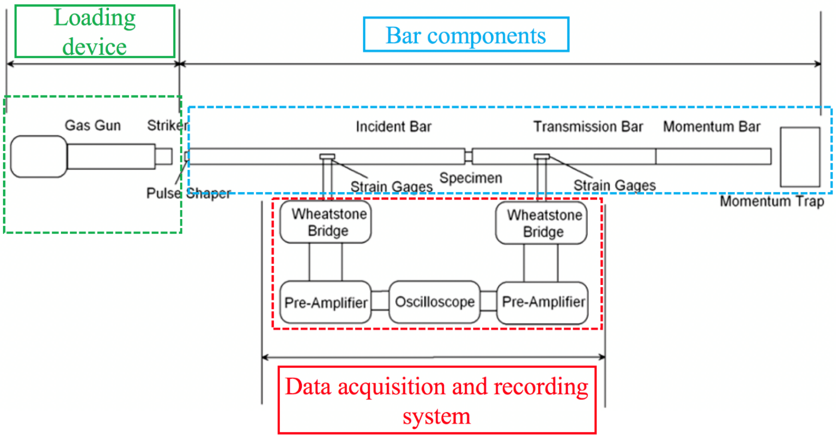


Figure 3.3 SHPB schematic set up, adapted from [186].

The loading device consisted in a gas gun provided with venting holes near the exit to ensure a constant speed, launched the striker by a sudden release of compressed air from the pressure storage vessel. The striker accelerated inside the barrel's gas gun until impacted on the end of the incident bar. The stored energy is released into the initially unstressed section of the incident bar. This produces a compression wave propagating in the incident bar on the specimen. The use of a gas gun and sticker mechanism produces a good controllable and repeatable impact on the incident bar. To tests different striking speeds, the pressure of the compressed gas in the tank can be changed.

The data acquisition system consisted two strain gauges attached symmetrically on each bar surfaces across the bars diameter. The strain gages signal was conditioned with a Wheatstone bridge. Commonly the output of the Wheatstone bridge is generally in the order of millivolts, therefore a signal amplifier was required to accurately record the low-amplitude voltage with a digital oscilloscope. Both amplifier and oscilloscope had sufficiently high frequency response to record the signal.

The experiments were conducted with the collaboration of the blast and impact engineering research group within the Civil and Structural Engineering department at the University of Sheffield. Figure 3.4 shows the actual rig used. (a) The incident bars were aligned to the action plane using levels before the load of the sample. (b) A high-speed camera was used to record the impact tests. (d) A piece of wood used as momentum trap. (e) A gas gun used to launch a Nylamid striker was used. Also, a front view of the rig is shown in Figure 3.4c.

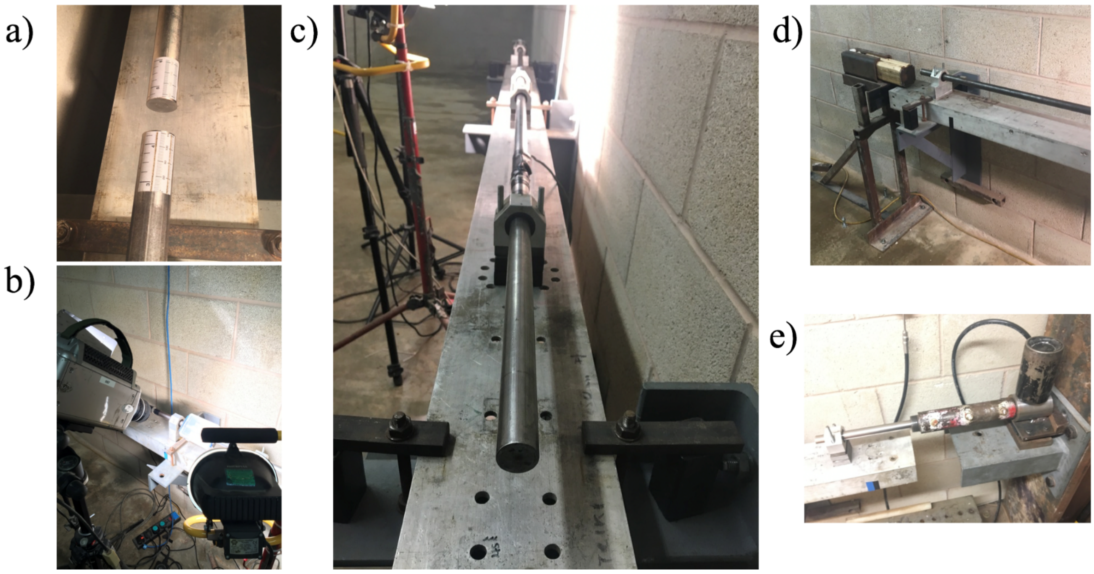


Figure 3.4 Actual SHPB rig used for high speed compression tests

### 3.3.2 General procedure for SHPB tests

The duration of each test is usually shorter than one millisecond. Therefore, the minimum frequency response of all components of the data acquisition system has to be 100 KHz [153]. To show the effect of the frequency of the data acquisition system, Figure 3.5 shows the comparison of the signal produced by a SHPB experiment with different low-pass filters (full, 100 and 3 kHz and 100 Hz). These plots show that the recorded signals are significantly distorted when using 3 kHz and 100 Hz. Therefore, it is the great importance to have a high-speed recording system.

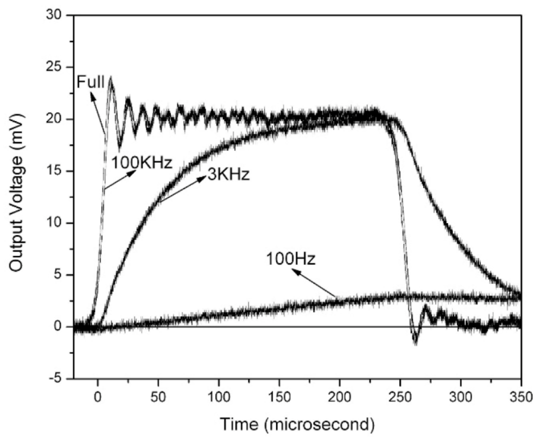


Figure 3.5 A comparison of oscilloscope records with different filters, adapted from [184].

During SHPB experiments, the wave of stress is created by the impact of the striker on the incident bar. Figure 3.6 shows a diagram of the stress wave propagation in the bars with a position-time diagram (X-t). After the compression wave propagates in the incident bar, part of the wave is reflected back into the incident bar while the rest propagates into the specimen and gets reflected back inside the sample due to impedance mismatch between bars and the sample. This process builds up the stress level in the sample gradually and finishes compressing the sample. At the same time, the sample/transmission bar builds the profile of the transmitted signal [184].

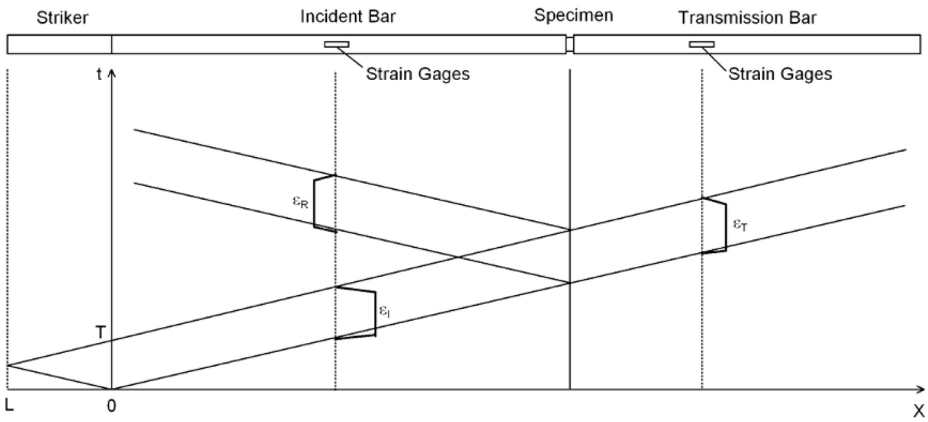


Figure 3.6 X-t stress diagram wave propagation in SHPB test machine, adapted from [184].

The impact between the striker and the incident bar also generates a compression wave in the striker, which is reflected back at the free end as tension wave (Figure 3.6). This tension wave transmits as an unloading wave. When the striker has the same material and diameter as the incident bar, the stress amplitude $\sigma_I$ of the incident pulse, generated by the striker impact depends on the velocity of the striker.

$$\sigma_1 = \frac{1}{2}\rho_B C_B v_{st}$$

Equation 3.1

or

$$\varepsilon_1 = \frac{1}{2}\frac{v_{st}}{C_B}$$

Equation 3.2

Where $\rho_B$ is the density of the bar and $C_B$ is the elastic wave speed of the bar. Figure 3.7 shows a schematic of how the reflected and incident pulses are measured by strain gages on the incident and transmission bars respectively.

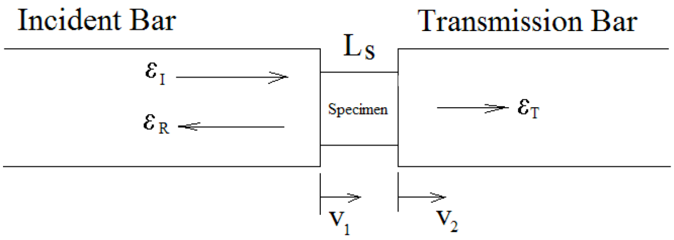


Figure 3.7 Testing section of SHPB, adapted from [185].

Assuming that there is no dispersion of the stress waves propagated in both bars. The velocity of both bars can be calculated as follows:

$$v_1 = C_B(\varepsilon_1 - \varepsilon_2)$$

Equation 3.3

$$v_2 = C_B \varepsilon_T$$

Equation 3.4

The subscripts *I*, *R* and *T*, are the incident, reflected and transmitted pulses, respectively. Therefore, the average engineering strain rate and strain in the specimen are:

$$\varepsilon = \frac{v_1 - v_2}{L_s} = \frac{C_B}{L_s}(\varepsilon_1 - \varepsilon_R - \varepsilon_T)$$

Equation 3.5

$$\varepsilon = \int_0^t \varepsilon dt = \frac{C_B}{L_s}\int_0^t (\varepsilon_1 - \varepsilon_R - \varepsilon_T)dt$$

Equation 3.6

Where $L_s$ is the initial length of the sample. Finally, the stresses at both ends of the specimen can be calculated with the following elastic relations as follows:

$$\sigma_1 = \frac{A_B}{A_s} E_B(\varepsilon_1 + \varepsilon_R)$$

Equation 3.7

$$\sigma_1 = \frac{A_B}{A_s} E_B \varepsilon_T$$

Equation 3.8

### 3.3.3 Experimental plan

Three strain rates (1000, 2000 and 2500 $s^{-1}$) were determined on the capabilities of the SHPB machine. All conditions were repeated three times each. An example of the acquired data is shown in Figure 3.8, where the transmitted and the reflected stresses in MPa are plotted against time in milliseconds at a strain rate of 500 $s^{-1}$. Worth to mention that this test was used to calibrate the machine. The data was post processed and converted to strain-stress plots by the blast and impact engineering research group within the Civil and Structural Engineering department at the University of Sheffield.

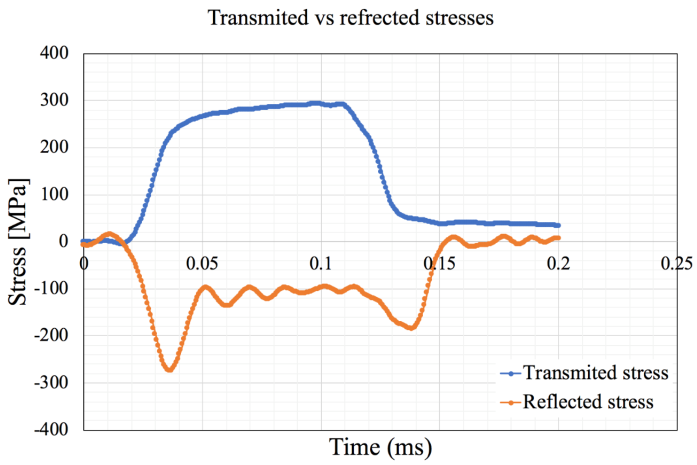


Figure 3.8 Example of acquired stresses at 500 $s^{-1}$.

## 3.4 Axisymmetric hot compression tests

The experiments were conducted at the Thermomechanical compression machine (TMC) at the University of Sheffield (Figure 3.9a). The TMC was designed to simulate metal forming processes and is equipped with a controlled heating unit via induction coil. It consists of an upper and lower M22 steel dies. The lower die remains and the upper is ram driven. The machine has a maximum capability of 500 KN and a ram velocity of 0.01 to $2.9 \times 10^{2}$ mm $s^{-1}$. Ram also possesses a plus-minus 0.1 mm accuracy for stopping. Furthermore, it has the capability to cool down the samples thru water mist and forced air.

### 3.4.1 General procedure for TMC tests

After the specimens were prepared with a boron nitride coating to reduce friction and reduce the likelihood of interstitial pick up. Figure 3.9b shows the schematic of the procedure used to perform the hot deformation experiments; first step was to heat up the samples with a 4 °C/s rate up to a specific temperature, then hold the sample's temperature for 2 minutes and then with a robotic arm position the sample in the compression machine, after deforming the sample, it was cooled down with forced air for 5 minutes.

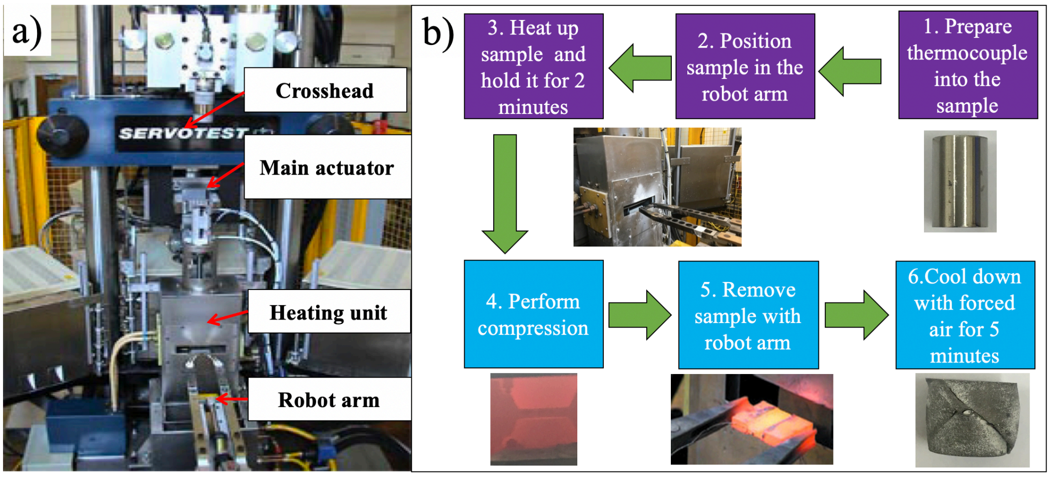


Figure 3.9 Axisymmetric compression tests; a) TMC machine and b) procedure compression tests.

Figure 3.10 a shows an example of the force-displacement curves recorded. The testing conditions were 973 K and 10 $s^{-1}$. Postprocessing data consisted in converting force-displacement to engineering strain-stress data using Equations from 3.9 & 3.10.

Where $\sigma_E$ and $\varepsilon_E$ are the engineering stress and strain respectively, $F$ is force, $A$ is area, $l_i$ is the initial length and $l_f$ is the final length:

$$\sigma_E = {}^{F}\!/_{A} \qquad \text{Equation 3.9}$$

$$\varepsilon_E = {}^{l_f - l_i}\!/_{l_i} \qquad \text{Equation 3.10}$$

The converted plot is shown in Figure 3.10b. Once it was calculated engineering strain-stress curves, they converted to true strain-stress curves using Equations 3.11 & 3.12. Where $\varepsilon_T$ is true strain and $\sigma_T$ is true stress. An example of the resulted true strain-stress plots is presented in Figure 3.10c.

$$\varepsilon_T = \ln\left(1 + \varepsilon_E\right) \qquad \text{Equation 3.11}$$

$$\sigma_T = \sigma_E\left(e^{\epsilon_T}\right) \qquad \text{Equation 3.12}$$

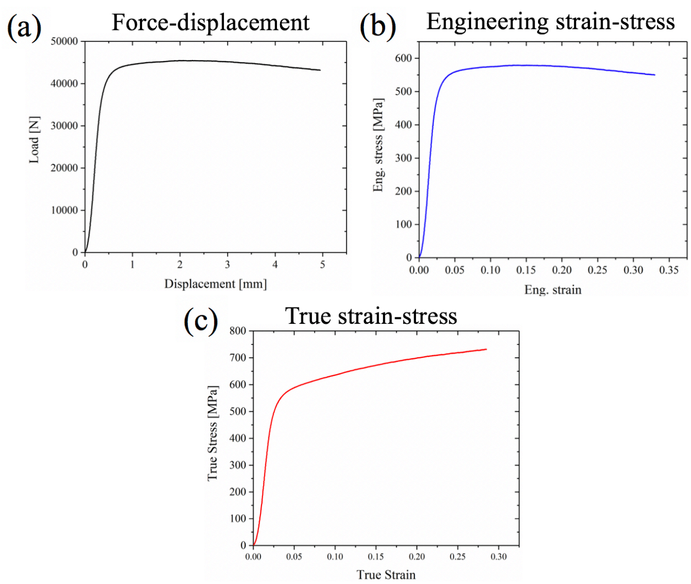


Figure 3.10 Example of post processing data for a) Force-displacement, b) Engineering strain-stress and c) True-stress plots for a testing condition at 973 K and 10 $s^{-1}$.

### 3.4.2 Experimental plan

The testing matrix with the deformation conditions is shown in Table 3.1. All conditions were repeated three times each. Three strain rates (1, 10 and 100 $s^{-1}$) were determined on the capabilities of the TMC machine and four temperatures (973, 1073, 1173 and 1273 K). The temperatures were carefully selected; it has been reported that the initial martensitic decomposition temperature starts from ~973 K and finishes at ~ 1173 K, when reaches the transus temperature from alpha to beta regimes [6, 67, 187].

Table 3.1 Experimental matrix for axisymmetric hot compression tests

| Strain rate ($s^{-1}$) | Temperature (K) | | | |
|---|---|---|---|---|
| 1 | 973 | 1073 | 1173 | 1273 |
| 10 | 973 | 1073 | 1173 | 1273 |
| 100 | 973 | 1073 | 1173 | 1273 |

Within the three strain rates selected, 100 $s^{-1}$ displayed dynamic response. An example at 973 K and 100 $s^{-1}$ is shown in Figure 3.11. An engineering strain-stress plot is presented in colour black and the fitted curve using MATLAB fitting toolbox is presented in red colour. After obtaining the fitted engineering curves, it was used Equations 3.11 & 3.12. All recorded plots at this strain rate were fitted using the same procedure with a confidence of 98%.

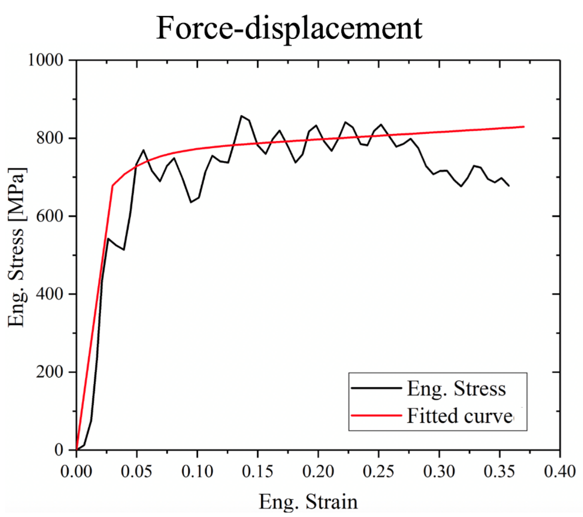


Figure 3.11 Example of dynamic response at 100 $s^{-1}$ and 973 K and its fitted curve

## 3.5 Orthogonal machining tests

Numerical modelling is a complementary and attractive tool to predict relevant outputs such as cutting forces, temperature in the tool's tip-workpiece, etc. However, it has to be validated with experimental work which compromises high costs and often difficult to implement complex set ups. One of the purposes of this research was to designed and manufactured a bespoke cutting rig capable to provide experimental data to validate with the numerical results. The novel rig was designed based on cost reduction and simple implementation but at the same time reliable.

During orthogonal machining, the plane strain assumption is adopted, this hypothesis is correct only when the workpiece's width is large compared to the depth of cut (roughly a ratio of three). The most commonly classical orthogonal cutting configurations include; face turning of the end of a tube with a large diameter and small thickness [98] and plunge turning of large diameter radial grooves [188].

Plunge turning (Figure 3.12a) is commonly used because it alloys several experiments on a single part, since it is performed one experiment per groove. The inconvenient of this method is for small depths of cut, since the radius of the sample affects the cutting due to the curvature of the surface to machine. Machining tubes or face turning (Figure 3.12b) is always the same machined surface, however two major inconvenient arise; tool erases each test the produced surface, making impossible to recover the data for further investigations, also preparing the tubes is not easy task since is not easy to find Ti-64 tubes, hence cylinders have to be prepared in turn not an economical solution[189].

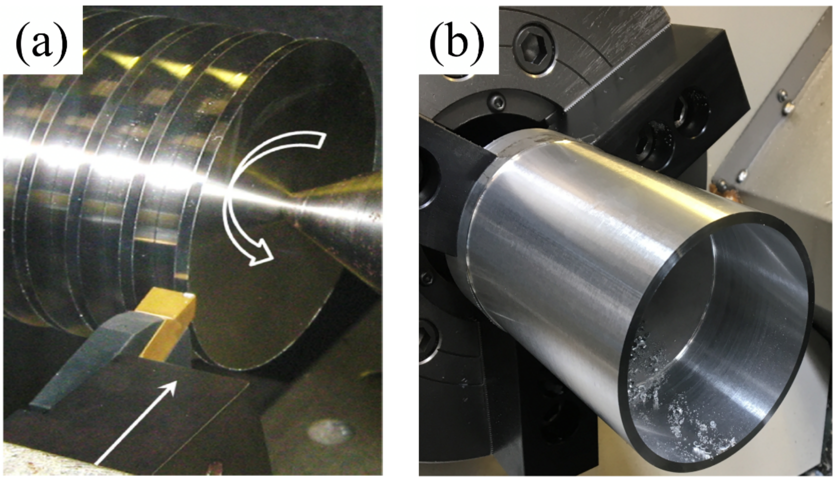


Figure 3.12 Orthogonal machining: a) Plunge turning and b) face turning tube, adapted from [189].

It must be noted that orthogonal machining resembles a shaping machining method. Hence, it was decided to replicate the process on a three-axis CNC milling machine. The benefits of this configuration are the great reduction of the workpiece, reduction of the costs involving the manufacture of the samples on the SLM 125 Renishaw either tubes or round bars not to mention the restriction of the SLM's working area to print the samples (80 mm maximum diameter).

### 3.5.1 The set up

A bespoke cutting rig was designed and manufactured to be used on a three-axis CNC milling machine (HD VMC, XYZ brand). This ensures the high positional accuracy and repeatability of the experiments due to the CNC control level from the machine. Figure 3.13 shows a schematic of the set up for the machining trials.

The set up consisted in four main components; cutting tool, fixture, dynamometer and acquiring data system. Orthogonal cutting was carried out by the mechanical components (CNC machine, tool holder, cutting tool and fixture), at the same time the measurement unit (dynamometer) recorded the data which later was treated by the signal acquisition system (amplifier and data acquisition card), after post processing with the LabView process, the cutting forces were achieved. Following sections will describe each component.

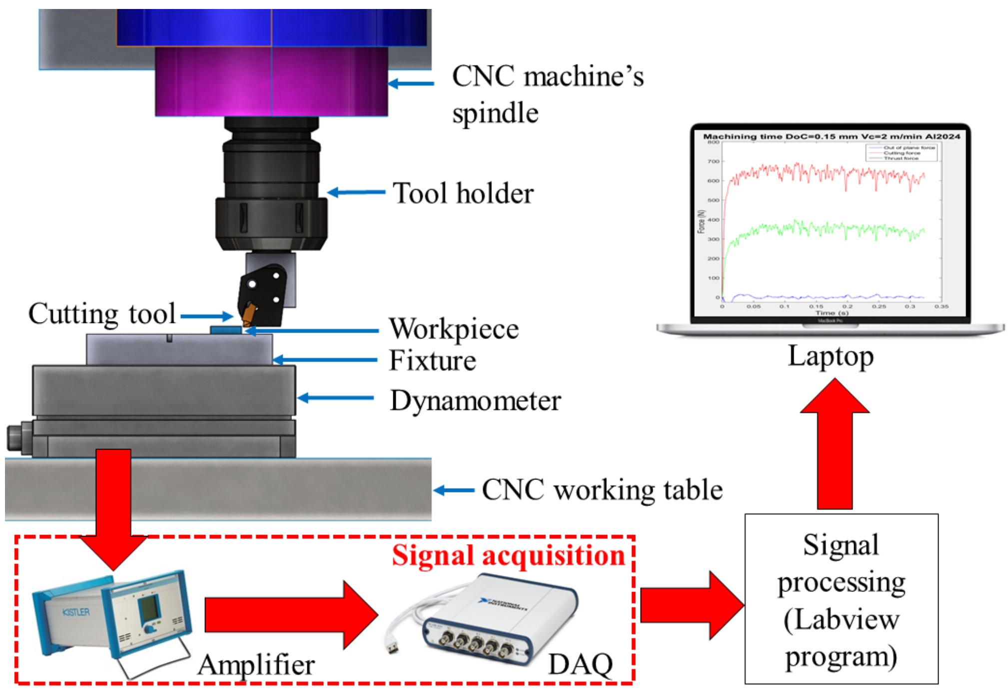


Figure 3.13 Schematic of orthogonal machining set up.

### 3.5.1.1 Cutting tool

The cutting tool was located in the main spindle of the machine using a BT40 tool holder and the cutting edge was provided by a commercial cutting insert and insert holder by SECO Tools (LCGN 160602-0600-FG, CP500 for the tool and CGHN-06 for the blade). An adaptor was designed and manufactured in EN24 steel grade to incorporate rake and relief angles to the cutting edge as it is shown in Figure 3.14. A rake angle of 7º and a relief angle of 7º were obtained. The rake angle is mostly affecting the generated cutting forces as smaller (negative) rake angles lead to higher cutting forces due to the increased deforming volume of the material. In contrast, the presence of the relief angle ensures that there is limited (almost none) friction between the newly generated surface and the flank surface of the cutting tool. The cutting nose radius was experimentally measured after the experiments from the cross section of the machined samples. The engineering drawing of the design are accessible in Appendix A.

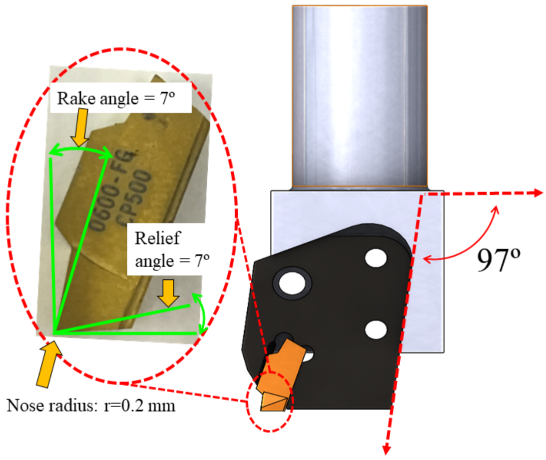


Figure 3.14 Designed adaptor for cutting tool holder.

### 3.5.1.2 Fixture

A bespoke fixture was designed and manufactured in EN24 steel grade to hold square samples as shown in Figure 3.15a. The fixture consisted in two main components; 1) a frame attached the force dynamometer's plate which was used as reference of the a) two moving jaws restricting the free movement of the sample on both axes of the CNC machine (x and y). Sample was tightened by the moving jaws using M8 screws. The fixture was attached with M8 screws into the force dynamometer's plate as shown in Figure 3.15b. The engineering drawing of the design are accessible in Appendix A.

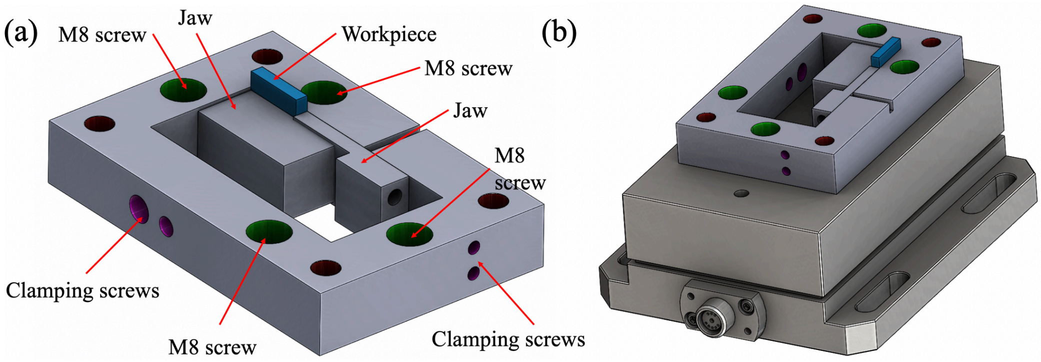


Figure 3.15 Holding system; a) bespoke fixture and b) fixture assembly to dynamometer

### 3.5.1.3 Dynamometer

The Klister dynamometer type 9257B together with multichannel charge amplifier Klister type 5070 was used. The dynamometer was fixed on the CNC's table using clamps. The multicomponent 9257B dynamometer provides dynamic and quasi-static measurement forces of the three components of a force acting onto the top plate. One of the benefits of using this brand is that the 9257B can measure the active cutting force regardless of its application point, both average value and dynamic forces.

### 3.5.1.4 data acquisition

A data acquisition card (type NI-USB 4431 national instruments) was used to record the cutting forces with a sampling rate of 10 KHz. Also, it was generated a program in commercial software LabVIEW 8.2 in order to plot the three components of the acting forces.

## 3.5.2 Set up implementation and verification

To ensure orthogonal cutting, the dynamometer (Figure 3.16a) and the designed fixture (Figure 3.16b) were aligned to the machine's axes (X & Y) using a dial gauge, whereas for the tool's height (depth of cut) it was used the tool's tip and was made zero height at the top of each sample.

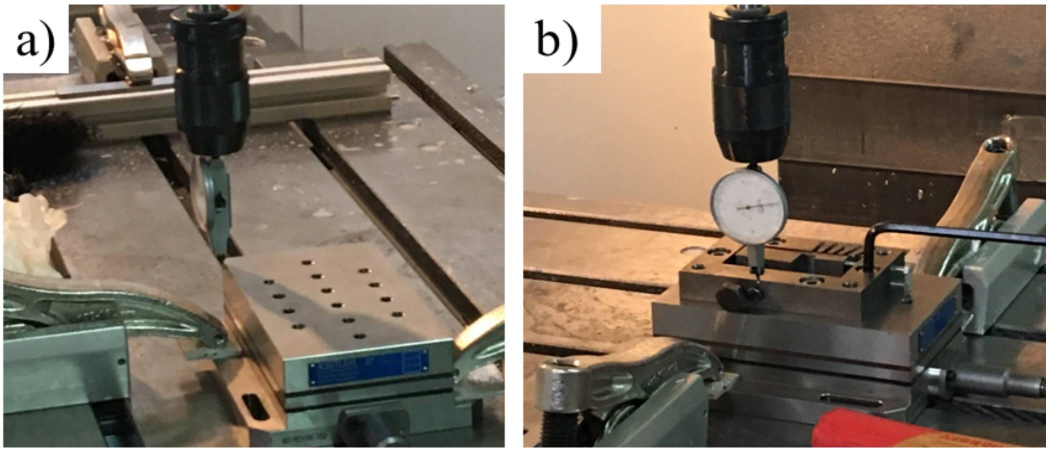


Figure 3.16 Alignment of set up components; a) dynamometer and b) fixture alignment with respect CNC machine's axes.

Figure 3.17a shows the convention used to determine the force components during experiments. This convention was determined by the dynamometer referencing system. An example of recorded forces is presented in Figure 3.17b. As expected, the cutting force was the highest (red colour), followed by the thrust force (green colour) and out of plane force (blue colour), the last one is expected to be zero. However, due to the fact that is a three-dimension phenomenon, the spread of material occurs during machining as result the dynamometer acquired forces in this component direction.

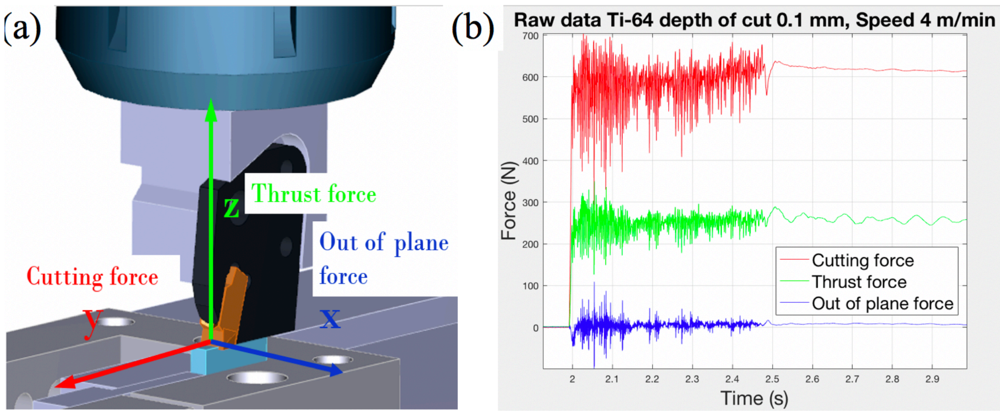


Figure 3.17 Set up verification: a) force convention and b) example of cutting forces acquired

To study the out of plane forces in more detail, Figure 18 shows the steady state section of out of plane cutting force component with the average value (8.5 N) shown by the broken line in red. This figure shows that the orthogonal condition is satisfied in the designed rig as the out of place cutting force is very small compared to the other two forces. The small measured value could be linked to the side spreading of the material during the cut that is unavoidable. Hence the orthogonal condition was satisfied.

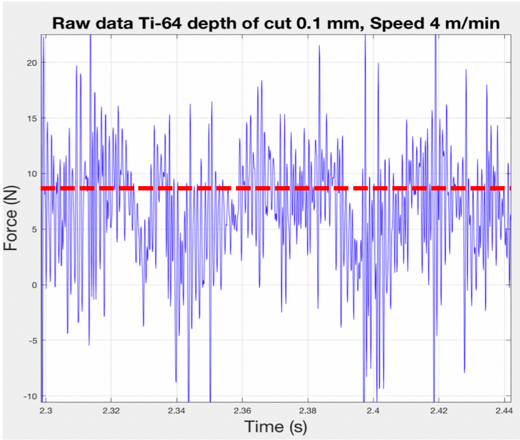


Figure 3.18 Out of plane force

Several authors suggest that the average value of the machining forces, especially during machining titanium alloys is not a representative value of the steady state of the machining forces, instead it was decided to use the average root mean square (RMS) of the measured forces as recommended within literature [189-192]. The RMS value of a quantity x is calculated as follows:

$$RMS\ of\ x = \sqrt{\frac{1}{n}\sum_{i=1}^{n} x_i^2}$$

Equation 3.13

Where, $n$ is the number of values $x_i$

### 3.5.3 Experimental plan

The testing matrix designed for orthogonal is shown in Table 3.2. Three cutting speeds (2, 4 and 6 m/min, these speeds were determined on the capabilities of CNC milling machine's linear feed rate) and two depth of cuts (0.1 and 0.2 mm, these were determined on the tool's geometry, i.e. nose radius) were selected. Smaller values of depth of cut were used in the screening study that showed at depth of cut smaller than 0.1

mm, the uncut chip size is in the order to cutting nose radius that adversely affects the mechanics of cutting shifting it from cutting to ploughing and compression.

Table 3.2 Experimental matrix for orthogonal machining tests

| | **Processing route** | | | | | | | | |
|---|---|---|---|---|---|---|---|---|---|
| | 3D printed Vertical | | | 3D printed Horizontal | | | Cast & Wrought | | |
| | **$V_c$ (m/min)** | | | | | | | | |
| **DoC (mm)** | 2 | 4 | 6 | 2 | 4 | 6 | 2 | 4 | 6 |
| 0.1 | | | | | | | | | |
| 0.2 | | | | | | | | | |

# 4. New physically-based model for plastic deformation of Ti-6Al-4V

## 4.1 Introduction

The background chapter introduced the available models for forging and machining processes. It was found that the available models are unsensitive to relevant microstructure features such as grain type and size, volume fraction of constitutive phases, etc. This section aims to describe a new physically based model that will link different initial microstructure (different processing routes such as C&W and AM) with Ti-64's mechanical behaviour under a wide range of deformation conditions suitable for forging and machining processes.

The new physically based model will describe DRV and DRX phenomena separately and later both will be incorporated into one general expression for prediction of flow stress in a wide range of deformation conditions. Later, it will be described the simulation procedure to implement the new physically-based constitutive model into commercial FE software Abaqus.

### 4.1.1 Grain boundary hardening

Ti-64 as part of the $\alpha$+$\beta$ family, is a polycrystalline material that can be found commercially with 85% and 15% of $\alpha$ and $\beta$ phases respectively [67]. During plastic deformation, slip must take place across adjacent $\alpha$ and $\beta$ grains, however; both phases normally have different orientation acting as a barrier to dislocation motion because the dislocations have to change their motion direction [156]. Therefore, a coarser grained will have less strength than a fine-grained metal owing to less total grain boundary area to hinder dislocation motion.

To comprehend the effect of grain size and the strength of a given material, the Hall-Petch relation (Equation 4.1) [193], is commonly used. Where $D_\alpha$ is the mean grain size of $\alpha$ phase, $k_{HP}$ is the Hall-Petch coefficient and $\sigma_0$ is the friction stress that is the critical resolved shear stress to initiate slip in a grain.

$$\sigma_Y = \sigma_0 + \frac{k_{HP}}{\sqrt{D_\alpha}}$$

Equation 4.1

For instance, Hyun & Kim [194] determined the Hall-Petch values as $k_{HP}$ =238.3 MPa and $\sigma_0$ =7.45 for pure titanium. Authors found that $\sigma_Y$ highly depend on grain size, which in turn depended in the processing route. To quantify the grain boundary effect, using the values reported by Hyun & Kim [195] and using Equation 1, Figure 4.1 shows the variation of average grain size in a range of 1 to 20 µm.

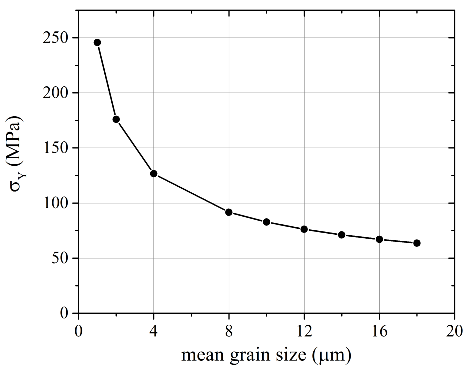


Figure 4.1 Pure titanium Hall-Petch relationship.

### 4.1.2 Forest Hardening

In polycrystalline materials such as Ti-64, plastic deformation often involves the motion of large numbers of dislocations, this process is called slip. Macroscopic plastic deformation corresponds to slip in response to an applied stress. All metals possess a number of dislocations that were introduced during hot working. For instance, if Ti-64 is cooled down considerably fast enough from the $\beta$ phase field, it will cause the reduction of the $\alpha$ grain size to a few $\alpha$ plates or even producing martensitic transformation. In both cases, a high number of dislocations is generated which in turn will contribute to the hardening of the material [1].

The number of dislocations is mostly referred as dislocation density in a material and is expressed in total dislocation that intersect a unit area of an arbitrary section. Its units are millimetres of dislocation per cubic millimetre. For materials carefully solidified, dislocation densities could be as low as $10^3$ mm$^{-2}$, whereas for deformed metals, the density may go as high as $10^9$ mm$^{-2}$. Heat treatments can turn back the dislocation density on the other of $10^5$ mm$^{-2}$[4].

### 4.1.3 Solid solution hardening

Solid solution mechanism is commonly used in almost all commercial titanium alloys by adding impurity atoms that go into either substitutional or interstitial solid solution. Increasing the concentration of the impurity in pure titanium results in increase of strength, hence pure titanium is often softer than its alloys. The reason is because impurity atoms impose lattice strains on the surrounding host atoms, the interaction of lattice strain between dislocations and impurity atoms result in restraint of dislocation movement [4].

Aluminium is the most preferred substitutional element in $\alpha$+$\beta$ family because it is the only common metal capable of raising the transition temperature and at the same time having high solubility in both $\alpha$ and $\beta$ phases [196]. There are few studies that treat solid solution effects separately (i.e. one single element) especially for substitutional elements in near beta alloys, due to the fact that in order to retain beta phase, it is required several alloying elements [197].

For instance, Figure 4.2 shows the tensile flow stress at a strain =0.02 and a strain rate of $8 \times 10^{-4}$ s$^{-1}$ as function of aluminium content and temperature [196]. From this plot it could be notice that pure titanium has three times less strength than the bi-phasic Ti-15Al alloy. Also, from these trends it could be seen that the relation is almost linear, therefore Al plays a definitive role in the strengthening of Ti-64.

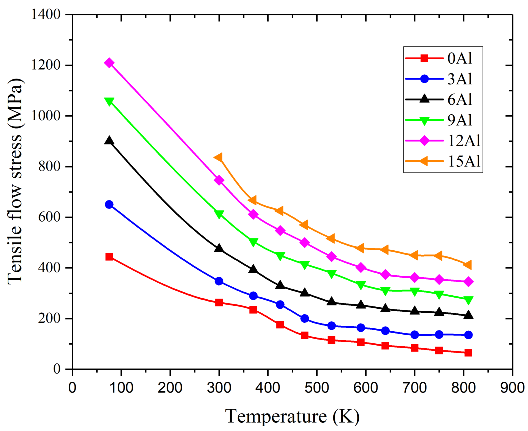


Figure 4.2 Flow stress as influenced by temperature and alloy content, adapted from [196].

### 4.1.4 Precipitation hardening

Precipitation hardening consists in the formation of second phase particles (precipitates) within the original phase matrix, this is accomplished by appropriate heat treatments. Precipitation hardening is the most complex mechanism within metallic systems which comprehends the rearrangement of atoms in certain way that the particles increase the total grain boundary, the crystallographic arrangement (second phases) and increase of number of dislocations within the metal.

Increasing the $\alpha$ phase, precipitation occurs by coherent $Ti_3Al$ or $\alpha_2$ particles, both having a hexagonal structure which by increasing their size become ellipsoidal. Whereas for $\beta$ phase occurs by metastable $\omega$ and $\beta$' phases. Both cases it is a miscibility breach into two BCC phases ($\beta_{\text{lean}}$ and $\beta_{\text{lean}}$). Worth to mention that precipitation hardening is the most effective method for increasing strength of near-$\beta$ alloys [198].

## 4.2 Modelling Procedure

Figure 4.3 shows the modelling procedure to model Ti-64 flow stress. As it is shown, the new model is built in such fashion that first it will predict yield strength in relation to strengthening mechanisms; grain type and size and solid solution (volume fraction of alpha phase). Followed by the prediction of flow stress due to dynamic recovery $\bar{\sigma}_{DRV}$ and later by $\bar{\sigma}_{DRX}$. Both flow stresses will be related to forest hardening and its evolution due to plastic deformation.

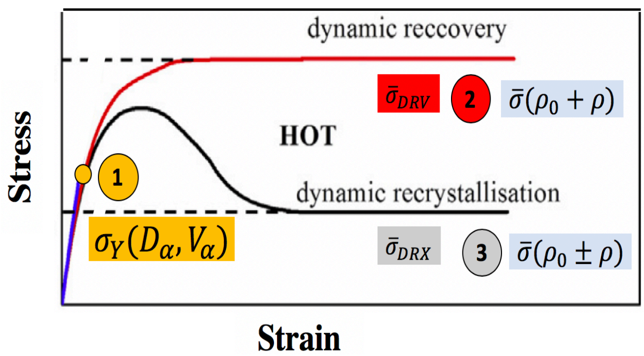


Figure 4.3 Modelling procedure

## 4.3 Dynamic Recovery

### 4.3.1 Yield Strength prediction

Assuming that there are three main strengthening mechanisms to take place including, grain boundary, solid solution relative to volume fraction of α+β, and forest hardening, the first step is to incorporate the grain size and shape effect into Ti-64's strength. In previous section, the Hall-Petch relation (Equation 4.1) was used to associate yield strength ($\sigma_Y$) with the average grain size of α phase ($D_\alpha$) in microns.

Worth to mention that Equation 4.1 does not distinguished the different shape of grains found in Ti-64. However, given the fact that most of Ti-64's commercial microstructures contain well defined α phase, only this phase was considered in the grain boundary strengthening mechanism. Therefore, Equation 4.1 is used for equiaxed structures (globular type) and for lamellar structures, it is considered the width's lath ($W_\alpha$) (the thinner side of the lath). Whereas for bimodal microstructures (constituted by two type of alpha phases; $\alpha_p$ and $\alpha_s$), Equation 4.1 will be converted to Equation 4.2. where the second term is substituted by a rule of mixture that considers primary α phase ($D_\alpha$), secondary alpha grain size ($D_{\alpha s}$) and the relative volume fraction of secondary alpha phase ($V_{\alpha s}$);

$$\sigma_Y = \sigma_0 + k_{HP}\left(\frac{V_{\alpha s}}{\sqrt{D_\alpha}} + \frac{1 - V_{\alpha s}}{\sqrt{D_{\alpha s}}}\right)$$

Equation 4.2

Although some studies have studied friction stress ($\sigma_0$), experimental results exhibit scattered information [194], this is due to different processing techniques and testing methods employed, therefore for this study, it is assumed $\sigma_0$ is influenced mainly by solid solution effects ($\sigma_{ss}$), hence $\sigma_0 \sim \sigma_{ss}$ [196, 199]. This is achieved by considering the friction stress of individual phases ($\sigma_\alpha$ in $\alpha$ and $\sigma_\beta$ in $\beta$ phases) and the volume fraction of $\alpha$ ($V_\alpha$) as shown in Equation 4.3:

$$\sigma_0 = \sigma_\alpha V_\alpha + \sigma_\beta (1 - V_\alpha)$$

Equation 4.3

To predict the friction stress ($\sigma_\alpha$) in $\alpha$, Equation 4.4 considers two terms; where $\sigma^{\alpha}_{prism}$, is the stress required to activate prismatic slip that is the main slip mode in $\alpha$-Ti, and $\sigma^{\alpha}_{ss}$ which is a solid solution strengthening term in $\alpha$, $\sigma^{\alpha}_{ss}$;

$$\sigma_{\alpha} = \sigma_{ss}^{\alpha} + \sigma_{prism}^{\alpha}$$

Equation 4.4

The $\sigma_{prism}^{\alpha}$ for prismatic slip in $\alpha$-Ti single crystals [197] was reported of 90 MPa by measuring the critical resolved shear stress. Whereas for the $\sigma_{ss}^{\alpha}$ is calculated using Equation 4.7, derived by Labusch [200]:

$$\sigma_{ss}^{\alpha} = \left(\sum_i B_i^{3/2} x_i\right)^{2/3}$$

Equation 4.5

where $x_i$ is the atomic concentration of element $i$ in $\alpha$ and $B_i$ is a strengthening constant related to the local size and modulus distortions of element $i$ in $\alpha$-Ti, given by:

$$B_i = \mathrm{K}(\eta_i{}' + 16\delta_i)^{3/2}$$

Equation 4.6

where K is a constant that depends on the base alloy and $\eta_i{}'$ and $\eta_i$ are the modulus differences (Equation 4.7 and 4.8 respectively) and $\delta_i$is the lattice strain of element $i$ in Ti Equation 4.9.

$$\eta_i{}' = \frac{|\eta_i|}{1+0.5\eta_i}$$

Equation 4.7

$$\eta_i = \frac{\mu_i - \mu_{Ti}}{\mu_{Ti}}$$

Equation 4.8

$$\delta_i = \frac{r_i - r_{Ti}}{r_{Ti}}$$

Equation 4.9

Where $\mu_i$ and $r_i$ are the shear modulus and atomic radius of element $i$, respectively. The values of $\mu_i$ and $r_i$ for Ti, Al and V were obtained from [201]. Whereas, K was determined using experimental data of binary Ti-Al and Ti-Zr alloys through fitting Equation 4.6 to the resolved stress increasing with composition [196, 202]. Table 4.1 summarises the parameters obtained for $\sigma_{ss}^{\alpha}$.

Table 4.1 Parameters used for solid solution strengthening contributions

| Parameter | Dimension | Value | Reference |
|---|---|---|---|
| K | dimensionless | 0.0082 | Fitted |
| $B_{Al}$ | MPa/at$^{2/3}$ | 1813 | calculated |
| $B_V$ | MPa/at$^{2/3}$ | 127 | calculated |
| Al concentration in α | dimensionless | 0.125 | [23] |
| V concentration in α | dimensionless | 0.018 | [23] |

Using the values presented in Table 4.1 into Equation 4.6, the solid solution strengthening contribution in $\alpha$ can be calculated as $\sigma_{ss}^{\alpha} = 454$ MPa. Substituting this value in Equation 4.4 gives the friction stress in $\alpha$ to be equal to $\sigma_{\alpha} = 544$ MPa.

Whereas, for the friction stress of $\beta$, there are very few studies reporting solid solution strengthening effects in near-β titanium alloys. In addition, it is difficult to estimate β–size strengthening effects due to the complex variations in $\beta$ distribution in Ti-64. Experimental studies of near-β alloys containing V and Al (Ti-10V-2Fe-3Al, Ti-5Al-5V-5Mo-3Cr and Ti-4.5Fe-7.2Cr-3Al) report yield stress values in the range 1000-1500 MPa [203-205]. Therefore, for this work it is assumed a friction stress of $\sigma_{\beta} = 1350$ MPa and fitted to Equation 4.3. Combining Equation 4.1 and 4.3 describes the athermal contributions to $\sigma_Y$ including; grain size and volume fraction as:

$$\sigma_Y = \left(\sigma_\alpha V_\alpha + \sigma_\beta(1 - V_\alpha) + \frac{k_{HP}}{\sqrt{D_\alpha}}\right) \mathrm{G}(T, \dot{\varepsilon})$$

Equation 4.10

The thermally-activated processes are incorporated in Equation 4.10 using a normalised activation energy $G$ for dislocation cross-slip and it depends on the temperature ($T$) and strain rate($\dot{\varepsilon}$). It can be described as follows [26, 156]:

$$G = \left(\frac{\kappa\mu b^3}{k_B T ln(10^7/\dot{\varepsilon})}\right)^n$$

Equation 4.11

with $k_B$ is the Boltzmann constant and $n$ and κ are constants adjusted to the experimental data reported in [68, 77, 86, 87, 159, 206], giving values of 0.4 and 0.23, respectively. The shear modulus (μ) was determined as μ=(54-0.03T) GPa according to [156].

### 4.3.2 Flow stress and strain hardening behaviour

The flow stress due to dynamic recovery $\bar{\sigma}_{DRV}$ is related to $\sigma_Y$ and the dislocation evolution using the Taylor´s equation [207], as follows:

$$\bar{\sigma}_{DRV} = \sigma_Y + 0.3M\mu b\sqrt{\rho}$$

Equation 4.12

Where $M$ is the Taylor factor ranging from 0.05 to 3 for different materials, $b$ is the Burgers vector and $\rho$ is the average dislocation density of the material. The dislocation evolution is related to the competition between dislocation generation and annihilation with respect to the applied strain $\varepsilon$ according to the Kocks-Mecking formulation[154], is described as follows:

$$\frac{d\rho}{d\varepsilon} = \frac{k_1}{b}\sqrt{\rho} - f\rho$$

Equation 4.13

where $k_1$ is the dislocation generation coefficient and $f_{DRV}$ is the recovery coefficient. By integrating and solving Equation 4.13 the total dislocation density is calculated as:

$$\rho = \left[\left(\frac{k_1}{bf_{DRV}}\left(\frac{k_1}{bf_{DRV}} - \sqrt{\rho_0}\right)\right)e^{-\frac{1}{2}f_{DRV}\varepsilon}\right]^2$$

Equation 4.14

where $\rho_0$ is the initial dislocation density. It is worth to mention that for Ti-64 wrought, $\rho_0$ is usually considered to be very low, in the range of $1\text{x}10^{11}$ $m^{-2}$ [208], whereas, for martensitic structures (SLM and quenched C&W alloys) its value has not been reported [6]. Therefore, this parameter was estimated using the approach developed in [209].

The formation of martensite during rapid cooling is controlled by the transformation strain ( $\varepsilon_{trans}$) of the transition from the $\beta$ to $\alpha'$ phases [209]. The transformation strain is accommodated by dislocations and fine lamellar distributions forming in the as-quenched state. As a result, grain refinement and increased dislocation density, $\rho_{\alpha'}$ [67, 209], will promote an increase in the yield and flow stress (Equation 4.15).

The dislocation density has been obtained for $\alpha'$ in steels by estimating the net strain energy accommodated by dislocations in a single martensite unit; $\rho_{\alpha'}$ was found to be proportional to $\varepsilon_{trans}$ and the mean lamellar spacing $d_{\alpha'}$ [210] as:

$$\rho_{0\alpha'} = \frac{12Ew_{\alpha'}}{(1+2\nu^2)\mu b}\frac{\varepsilon_{trans}^2}{d_{\alpha'}^2}$$

Equation 4.15

where $w_{\alpha'}$, is the $\alpha'$ lamellae thickness, $E$ is the Young's modulus of Ti-64, $\varepsilon_{trans}$ is the transformation strain for Ti. The procedure and calculations to obtain $\rho_{0\alpha'}$ is presented in Appendix B. the initial dislocation density for the martensite phase is calculated as $\rho_{0\alpha'} = 1.7 \times 10^{13}$ $m^{-2}$. Combining Equations 4.10, 4.11, 4.12 and 4.14, gives the expression of $\bar{\sigma}_{DRV}$ flow stress as follows:

$$\bar{\sigma}_{DRV} = \left(\sigma_\alpha V_\alpha + \sigma_\beta(1-V_\alpha) + \frac{k_{HP}}{\sqrt{D_\alpha}}\right)\left(\frac{\kappa\mu b^3}{k_b T ln(10^7/\dot{\varepsilon})}\right)^n + 0.3M\mu b\left[\left(\frac{k_1}{bf_{DRV}}\left(\frac{k_1}{bf_{DRV}} - \sqrt{\rho_0}\right)\right)e^{-\frac{1}{2}f_{DRV}\varepsilon}\right]$$

Equation 4.16

## 4.4 Dynamic Recrystallization effect

The Kocks-Mecking formulation (Equation 4.14) only considers the average dislocation density and the ability of a metal to recover (recovery coefficient $f_{DRV}$), however it does not distinguish recrystallised and unrecrystallised regions during plastic deformation. In order to preserve the dependence of homogenous dislocation density, Galindo-Nava & Rivera del Castillo [211] proposed an extra term in the Kocks-Mecking equation; $\rho_{DRX}$ which is the density inside the recrystallised region and was postulated to evolve at the same rate than when the material was initially deformed. Worth to mention that $\rho_{DRX}$ is proportional to the capacity of dislocation-free grains to occupy the highly deformed matrix and represents an incubation strain to form high-angle grain boundaries (HAGBs). Equation 4.17 describe the new equation adding the extra term $\rho_{DRX}$ as follows:

$$\rho_{DRX} = \left[\left(\frac{k_1}{bf_{DRV} + f_{DRX}} - \left(\frac{k_1}{bf_{DRV} + f_{DRX}} - \sqrt{\rho_0}\right)\right) e^{-(f_{DRV}+f_{DRX})\varepsilon}\right]^2$$

Equation 4.17

where $f_{DRX}$ is the dynamic recrystallization coefficient and determines the capability of the recrystallised grains to grow and reside in the deformed regions. $f_{DRX}$ is estimated by the proportion of the potential sites for grain growth and the number of growing grains as:

$$f_{DRX} = e^{\frac{Q_{DRX}}{k_B T}} - 1$$

Equation 4.18

where, $Q_{DRX}$ is the energy barrier required for grain growth and is dependant of temperature and strain rate as follows:

$$Q_{DRX} = \omega(Tk_B \ln\left(\frac{10^7}{\dot{\varepsilon}}\right) - \lambda\mu b^3)$$

Equation 4.19

Where, ω and $\lambda$ are constants adjusted to the experimental data reported in [9, 15, 17, 23, 24, 52, 88, 89], giving values of 0.24 and 0.6, respectively. Galindo-Nava & Rivera del Castillo [211] proposed Equations from 4.17 to 4.19 based on microscopic level (dislocation interaction), however in order to relate these equations into macroscopic level, in this work it is proposed a type-Taylor equation. The macroscopic stress due to dynamic recrystallisation ($\sigma_{DRX}$) can be calculated as:

$$\sigma_{DRX} = 0.3M\mu b\sqrt{\rho_{DRX}}$$

Equation 4.20

Worth to note that, $\sigma_Y$ was not considered in Equation 4.20 because it was assumed $\sigma_Y$ evolves at the same rate than when the material was initially deformed (in this case $\bar{\sigma}_{DRV}$). Additionally, $\sigma_{DRX}$ is incubated until a critical strain initiates it. The critical strain to produce recrystallisation can be related to the instantaneous $V_\alpha$ and $f_{DRX}$ :

$$V_{REX} = 1 - e^{-f_{DRX}\varepsilon V_\alpha}$$

Equation 4.21

where $V_{REX}$ is the volume of recrystallised zones. Equation 4.21 considers $\alpha$ phase ($V_\alpha$) is the only phase recrystallised during the deformation [34].The combination of $\bar{\sigma}_{DRV}$ (Equation 4.16) and $\sigma_{DRX}$ (Equation 4.20) and $V_{REX}$ (Equation 4.21) gives the general expression to determine the total flow stress considering DRV and DRX effects:

$$\bar{\sigma} = \bar{\sigma}_{DRV}(1 - V_{REX}) + \bar{\sigma}_{DRX}V_{REX}$$

Equation 4.22

## 4.5 Phase transformation effect

Equation 4.22 only considers flow stress as function of DRV and DRX, however depending on the process, phase transformation may occur during hot deformation. Worth noting that all presented equations consider the effect of $\alpha$ phase ($V_\alpha$), $\beta$ phase is only considered in the solid solution effects ($V_\beta$) on ti-64's strength. Therefore, in this work phase transformation contribution is assumed to be only by thermally-activated processes, in this context the activation energy (Equation 4.11) is decomposed into individual phases on the flow stress:

$$G_{\alpha} = \kappa_{\alpha}\left(\frac{0.5\mu b^{3}}{Tk_{B}\ln\left(10^{7}/\dot{\varepsilon}\right)}\right)^{n_{\alpha}}$$

Equation 4.23

$$G_{\beta} = \kappa_{\beta}\left(\frac{0.5\mu b^{3}}{Tk_{B}\ln\left(10^{7}/\dot{\varepsilon}\right)}\right)^{n_{\beta}}$$

Equation 4.24

With, $\kappa_{\alpha}$ and $n_{\alpha}$ are materials constants related to $\alpha$ phase contribution and were adjusted to hot deformation of Ti-64 experimental data reported in [23, 88, 212] giving values of 0.4 and 0.23, respectively. $\kappa_{\beta}$ and $n_{\beta}$ are materials constants related to $\beta$ phase contribution. These constants were adjusted using hot deformation experimental data for four near-$\beta$ alloys (Ti-5Al—5M0-5V-1Cr-1Fe, Ti-1300, Ti-40, Ti-10AV-2Fe-3Al) reported in [34, 213-215] giving $\kappa_{\beta}$ and $n_{\beta}$ values of 2.8 and 0.088, respectively. Substituting Equations 4.23. & 4.24 into Equation 4.16, gives the expression for flow stress due to DRV when phase transformation occurs:

$$\sigma_{DRV} = \left(\sigma_{0}^{\alpha} + \frac{k_{HP}}{\sqrt{D_{\alpha}}}\right)G_{\alpha}V_{\alpha} + \sigma_{0}^{\beta}G_{\beta}(1 - V_{\alpha}) + 0.3M\mu b\left[\left(\frac{k_{1}}{bf_{DRV}} - \left(\frac{k_{1}}{bf_{DRV}} - \sqrt{\rho_{0}}\right)\right)e^{-\frac{1}{2}f_{DRV}\varepsilon}\right]$$

Equation 4.25

Worth to notice that both solid solution effects ($\sigma_{0}^{\alpha}$and$\sigma_{0}^{\beta}$) are related to each constitutive phase ($V_{\alpha}$ and $V_{\beta}$), however grain boundary strengthening is only related to alpha phase. Indirectly $V_{\beta}$ is restricted by the function $(1 - V_{\alpha})$, where it is assumed that only two stable phases coexist, i.e. the volume fraction of beta phase is equal to the result of the subtraction of $V_{\alpha}$.

Phase transformation temperature of Ti-64 has been reported to be around 1263 K [8]. Semiatin et al. [23] corroborated this temperature by measuring retained volume fraction of $\beta$ using quantitative metallography within temperatures from 1000 K up to 1273 K. Their results are shown in Figure 4.4, as can be seen from this plot, retained beta phase starts at 20% when temperature is around 1000 K and increases exponentially until temperature reaches around 1273 K when Ti-64 has fully retained beta phase (100%). To implement this transition into the model, a function was developed and calibrated as shown in Figure 4.4 (exponential fitted curve).

The phase transformation can be to determine using Equation 4.25, where the volume fraction of alpha phase ($V_\alpha$) decreases exponentially as temperature ($T$) reaches the transus temperature ($T_\beta = 1273\ K$):

$$V_\alpha = 1 - e^{-0.0058(T_\beta - T)}$$

Equation 4.26

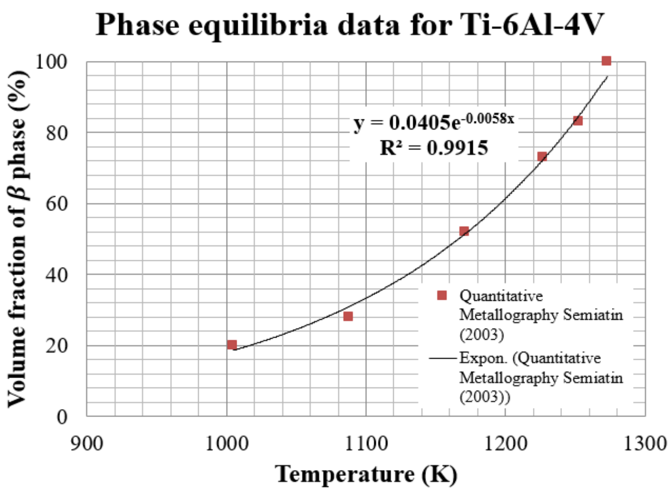


Figure 4.4 Beta volume fraction curve during different temperatures.

## 4.6 Adiabatic heating effect

During adiabatic analysis, the heat conduction is neglected as the event happens so fast that the heat has no time to diffuse. This is generally accepted to be true for high speed phenomena such as machining and some forming processes. This type of analysis is especially important considering the low thermal conductivity of Ti64, a local temperature rise leads to the adiabatic thermal softening. To implement the temperature effect, it is solved as part of the constitutive equations in the user material subroutine (VUMAT) implemented.

The temperature rise due to adiabatic heating ($\Delta T$) is calculated using Equation 4.27 where $\theta$ is the fraction of the heat generated due to plastic work and it was assumed to be

0.9, $\sigma$ is the current stress state, $\Delta\varepsilon^{pl}$ is the increment of equivalent plastic deformation, $\rho$ is the material density that was assumed to be 4430 kg/m$^3$ and $Cp$ is the specific heat (which is assumed 560 J/Kg K and constant) for a Ti64 alloy.

$$\Delta T = \frac{\theta\sigma\Delta\varepsilon^{pl}}{2\rho C_p}$$

Equation 4.27

## 4.7 Model implementation

Implementing constitutive material models in Abaqus requires evaluating the of the material at an integration point over time increment during a nonlinear analysis. VUMAT subroutine in Abaqus is formulated in terms of the updated Lagrangian or material description. As mentioned in section 2.5.1, in this formulation the elements deform with the material. Previous state of the elements is treated as reference state of the beginning of each time step, therefore small strain assumptions are valid throughout the analysis due to small time steps. The total strain increment components for each time step are passed to the VUMAT for each integration point and these are then used to update the stresses.

For the implementation of the constitutive equation into VUMAT code, it was used the approach used by Bonorchis [216] (Figure 4.5). The total strain rate can be decomposed into elastic and plastic rate components as follows:

$$\underline{\dot{\varepsilon}} = \dot{\varepsilon}^{el} + \dot{\varepsilon}^{pl}$$

Equation 4.28

The isotropic linear elasticity can be written in terms of the bulk modulus K, and the shear modulus G, defined as follows:

$$K = \frac{E}{3(1-2\upsilon)}$$

Equation 4.29

$$G = \frac{E}{2(1+\upsilon)}$$

Equation 4.30

Where E is the Young's modulus and v is the Poisson's ratio which are assigned by the user. The constitutive material model was developed in terms of strain increments. The volumetric strain increment is defined as $\Delta_{\varepsilon_{vol}} = trace(\Delta_{\underline{\dot{\varepsilon}}})$, which is an elastic volumetric strain because the plastic volumetric strain increment is zero. The deviatoric strain increment is therefore:

$$\Delta_{\underline{e}} = \Delta_{\underline{\varepsilon}} - \frac{1}{3}\Delta_{\varepsilon_{vol}}\underline{I}$$

Equation 4.31

The elastic component is defined in volumetric and deviatoric form. The trial deviatoric stress increment is; $\Delta S^{trial} = 2G\Delta_{\underline{\varepsilon}}$, the volumetric part could be dined as hydrostatic or equivalent pressure stress increment $\Delta p^{trial} = -K\Delta\varepsilon_{vol}$, hence it is possible to find the total elastic trial stress, if it is later that the yield criterion has not been exceeded:

$$\sigma_{old}^{trial} = \underline{\sigma}_{old} + \Delta S^{trial} - \Delta p^{trial}$$

Equation 4.32

The total hydrostatic stress can be found from the new trial stress (note the negative sign): $p = -\frac{1}{3}trace(\underline{\sigma}_{new}^{trial})$, therefore the total deviatoric stress can be found:

$$S^{trial} = \underline{\sigma}_{new}^{trial} + pI$$

Equation 4.33

Using the total deviatoric stress, the equivalent Mises stress for an assumed purely elastic response takes the form:

$$q^{trial} = \sqrt{\frac{3}{2} S^{trial} : S^{trial}}$$

Equation 4.34

When material has yielded, $q^{trial}$ exceeds the equivalent uniaxial yield stress, therefore it is required to solve for the plasticity state. To start iterating, the olf devistoric stresses are needed. These are easily found by calculating the old total hydrostatic stress: $\underline{p_{old}} = -\frac{1}{3} trace(\underline{\sigma}_{old})$ and then the old deviatoric stress is $\underline{S}_{old} = \underline{\sigma}_{old} + p_{old}\underline{I}$, then the total deviatoric strain is calculated as:

$$\underline{\hat{e}} = \underline{e}_{old}^{el} + \Delta\underline{e} = \frac{\underline{S}_{old}}{2G} + \Delta\underline{e}$$

Equation 4.35

Therefore, the total equivalent deviatoric strain can be found:

$$\underline{\hat{e}} = \sqrt{\frac{2}{3} \underline{e} : \underline{e}}$$

Equation 4.36

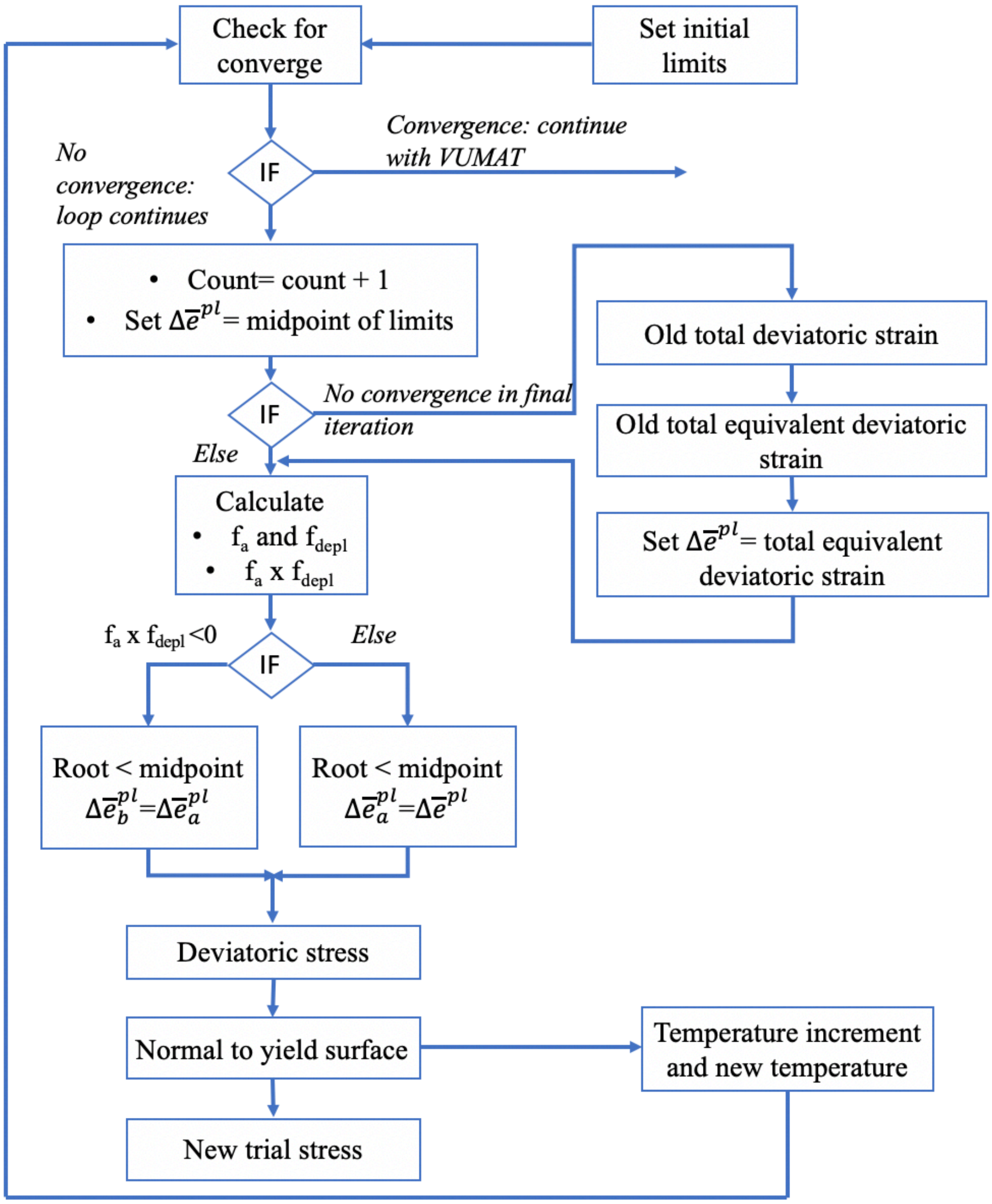


Figure 4.5 Implemented algorithm to solve for equivalent deviatoric plastic strain increment

## 4.8 Model verification

To validate the correct implementation of the new plasticity law in Abaqus through a VUMAT, Figure 4.6 shows the procedure performed; Stage 1, since the JC model is embedded in Abaqus, it was decided as first step to write a VUMAT with the JC model and compared it against the JC Abaqus. This test was useful since there is no other way to verify the correct implementation of the new model in more complex conditions.

Single element tests at room temperature and four strain rates (1, 10, 100 and 2000 $s^{-1}$) were carried out during tensile, compression and shear deformation conditions. Then, the effect of mesh size was tested through 125 and 512 elements same deformation conditions. Stage 2; consisted in comparing JC Abaqus against the DRV-VUMAT (Equation 4.16) through single element tests at different temperatures (973-1373K) at a strain rate of 2000 $s^{-1}$.

Finally, DRV VUMAT was compared with the general equation for flow stress (Equation 4.25, from now on it will be referred as DRX-VUMAT) through single element tests at different temperatures (973-1373K) at a strain rate of 1 $s^{-1}$. For the single element tests, the Von-Mises stresses and temperatures are only reported two strain rates (1 and 2000 $s^{-1}$) in this chapter, while 10 and 100 $s^{-1}$ single element and multiple element tests are reported in Appendix C.

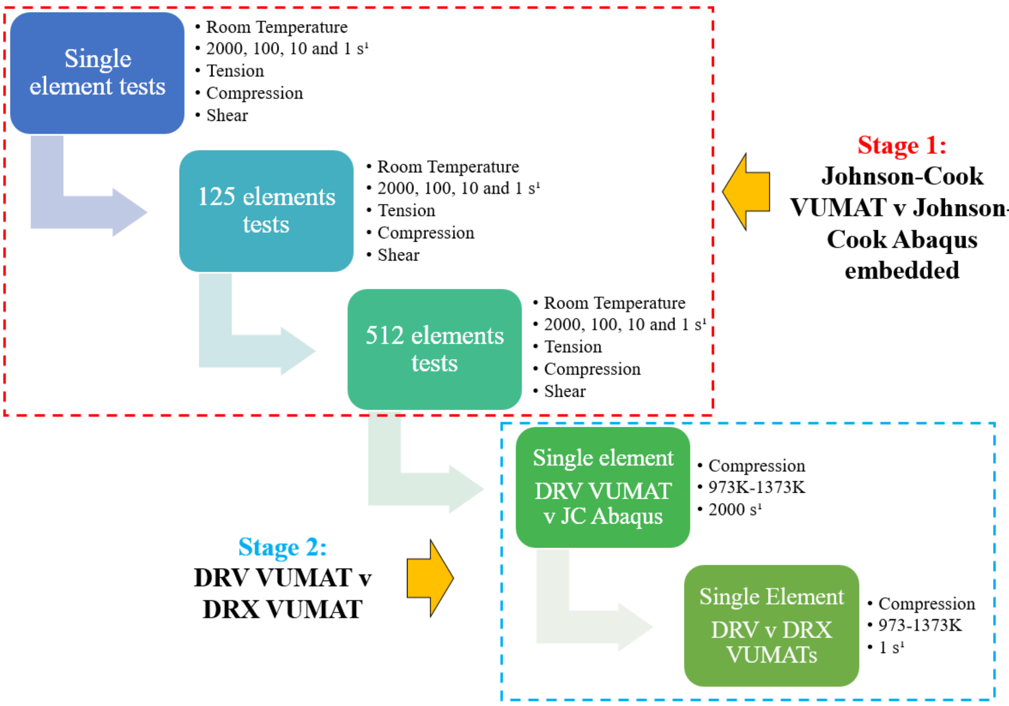


Figure 4.6 VUMAT Validation procedure

### 4.8.1 Single Element tests

The test consisted on a single element 5X5X5 $mm^3$. Four sets of velocities were tested, 10 m/s, 0.5 m/s, 0.05 m/s and 0.005 m/s with expected strain rates of 2000, 100 and 1 $s^{-1}$ respectively. Additionally, Figure 4.7 shows the loading conditions tested under (a) tension, (b) compression and (c) shear modes. Both, JC Abaqus and JC-VUMAT results were compared in terms of Von-Mises stresses and the increment on temperature.

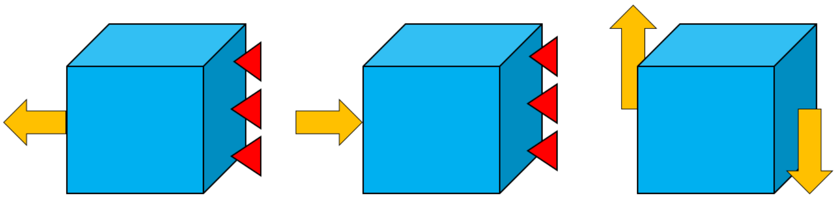


Figure 4.7 Loading modes for single element tests.

#### 4.8.1.1 Compression

The velocity is applied to the entire geometric face, therefore is independent of the number of elements. In the case of increasing the elements (i.e. 125 and 512), the velocity will be assigned to the nodes that are on the geometric face. The values of the Mises stresses and the increment on temperature for a strain rate of 2000 $s^{-1}$ are presented in Figure 4.8a and b respectively. Whereas Figure 4.8c and d show the results for a strain rate of 1 $s^{-1}$. The JC-VUMAT predictions show exactly same results as the JC- Abaqus, therefore both plots are superimposed. JC-VUMAT behave correctly for this loading condition despite the velocities applied (10 and 0.5 m/s).

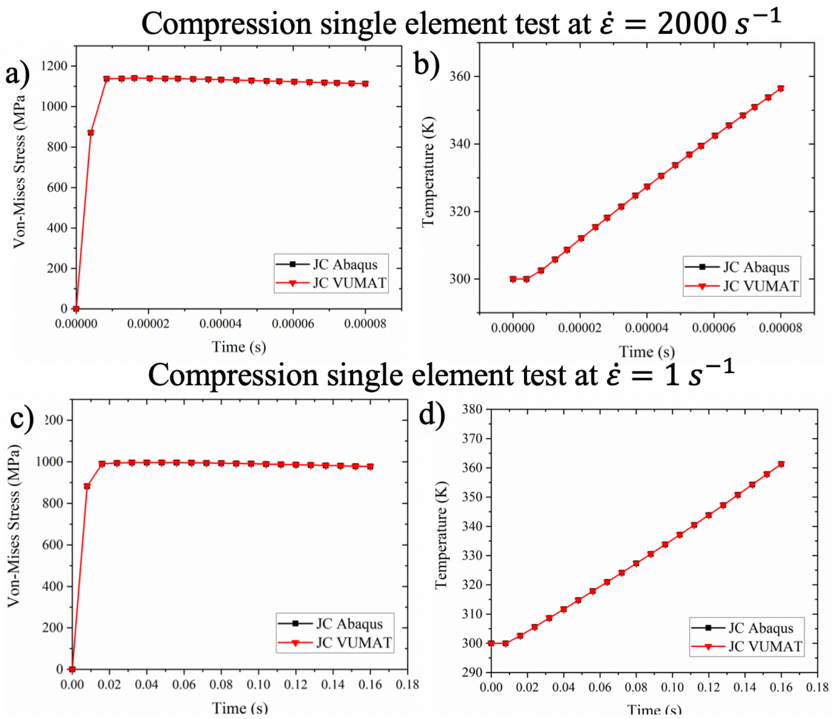


Figure 4.8 Compression tests: Von Mises stresses (a and c), increase of temperature (b and d) at 2000 $s^{-1}$ and 1 $s^{-1}$ respectively.

### 4.8.1.2 Tension

The values of the Mises stresses and the increment on temperature for a strain rate of 2000 $s^{-1}$ are presented in Figure 4.9 a and b respectively. Whereas Figure 4.9c and d show the results for a strain rate of 1 $s^{-1}$. Again, JC-VUMAT predictions show exactly same results as the JC- Abaqus, therefore both plots are superimposed. JC-VUMAT behave correctly for this loading condition despite the velocities applied (10 and 0.5 m/s).

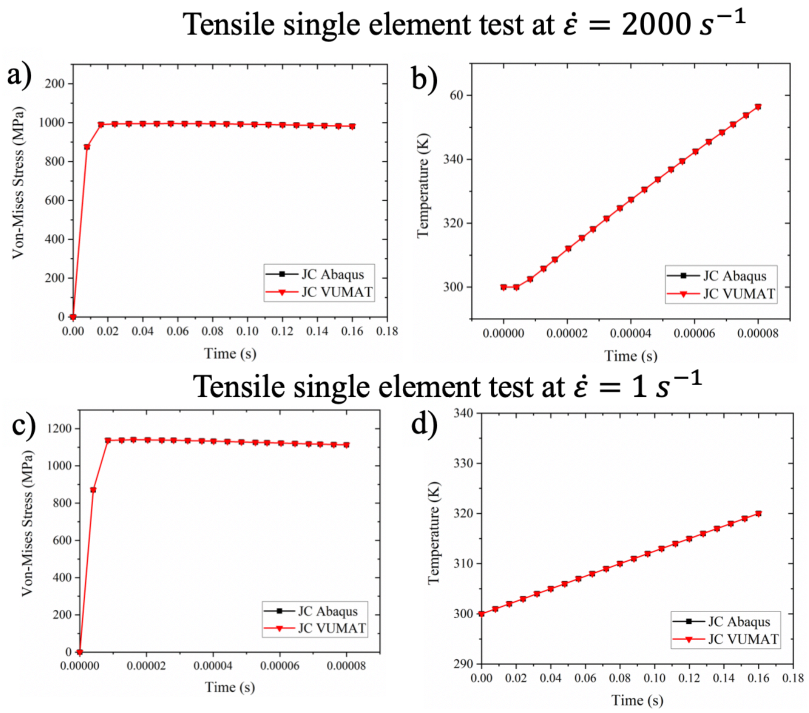


Figure 4.9 Tensile tests: Von Mises stresses (a and c), increase of temperature (b and d) at 2000 $s^{-1}$ and 1 $s^{-1}$ respectively.

### 4.8.1.3 Shear

The velocity loading is applied to the entire geometric face. The faces to which the velocities are applied are restrained from moving towards each other (i.e. the displacement in the third direction is zero causing the faces to remain parallel to each other). The values of the Mises stresses and the increment on temperature for a strain rate of 2000 $s^{-1}$ are presented in Figure 4.10a and b respectively. Whereas Figure 4.10c and d show the results for a strain rate of 1 $s^{-1}$. Again, JC-VUMAT predictions show exactly same results as the JC- Abaqus, therefore both plots are superimposed. JC-VUMAT behave correctly for this loading condition despite the velocities applied (10 and 0.5 m/s).

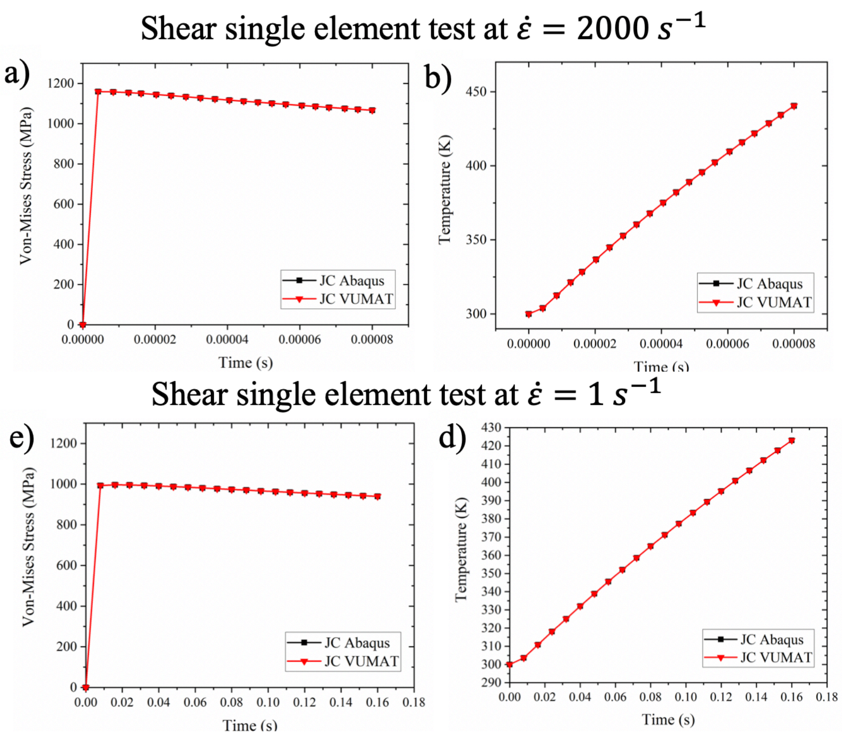


Figure 4.10 Shear test: Von Mises stresses (a and c), increase of temperature (b and d) at 2000 $s^{-1}$ and 1 $s^{-1}$ respectively.

### 4.8.1.4 Single element DRV-VUMAT and JC-Abaqus results

After verifying the correct implementation of the JC-VUMAT, the next step consisted in comparing the DRV-VUMAT against JC-Abaqus in a qualitative sense since both models predict different Von-Mises values. Single element compression tests at a strain rate of 2000 $s^{-1}$ and temperatures ranging from room temperature to 1373K were tested. Figure 4.11a shows the Von-Mises results for both models. Where dotted lines indicate JC-Abaqus model and solid lines indicate DRV-VUMAT predictions.

The results shown that DRV model is more sensitive to adiabatic heating during room temperature compared to JC model, while at higher temperatures (973 K and above) DRV-VUMAT predicts higher stresses (around 100 MPa in all hot deformation conditions). This can be explained easily as JC model comprehends a three-element multiplying each other, whereas the proposed model is a summation. Additionally DRV model, predicts closer to experimental results presented by Lee & Li [206] specially above1073K temperature. Whereas, Figure 4.11b indicate the results of both models in terms of increase of temperature due to plastic work. Interestingly, despite both models predict different level of Mises stresses, the results in increase of temperature is exactly the same for both subroutines.

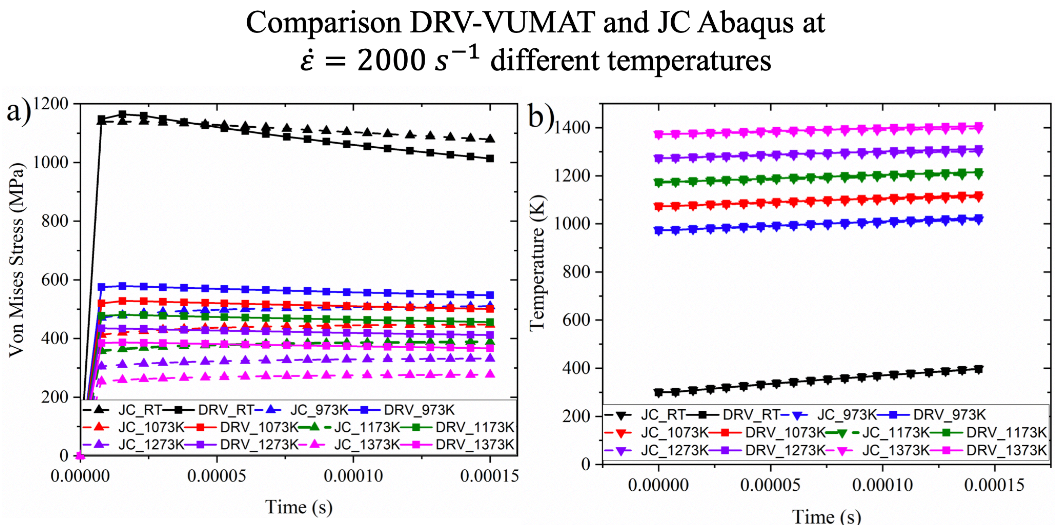


Figure 4.11 Single element test DRV-VUMAT and JC-Abaqus comparison, a) Von-Mises and b) increase of temperature predictions.

4.8.1.5 Single element DRV-VUMAT and DRX-VUMAT

The final verification consisted in comparing DRV-VUMAT against DRX-VUMAT. Single element compression tests at a strain rate of 1 $s^{-1}$ and temperatures ranging from room temperature to 1373K were tested. Figure 4.12a shows the Von-Mises results for both models. Where dotted lines indicate DRV-VUMAT model and solid lines indicate DRX-VUMAT predictions.

The results shown again that DRV-VUMAT is more sensitive to adiabatic heating compared to DRX-VUMAT during room temperature (black lines). Moreover, at the same condition, DRX-VUMAT predicts very low yield strength (around 400 MPa) compared to DRV-VUMAT (around 980 MPa). While at higher temperatures (973 K and above) DRV-VUMAT predicts higher yield strength (around 250 MPa in all hot deformation conditions).

Worth to notice that during hot temperatures, DRX-VUMAT predicted a sharper decrease on strength, especially at 1273 and 1373 K (purple and magenta respectively). The results show that DRV-VUMAT predicts higher increase of temperatures during 300 K condition (black lines), while at 973 K and above DRX-VUMAT (solid lines) does not reported any increase of temperature. From these results it can be seen that DRX predicts very low strength of the material, this is due to the fact that the model considers instant phase transformation, without considering time, moreover it has been reported that Ti-64, depending on the processing parameters (strain rate and temperature) undergoes through DRV+DRX and phase transformation simultaneously. In addition, comparing both models it could be assumed that at high strain rates (2000 $s^{-1}$) it is not probable DRX effect, instead; phase transformation, therefore DRV model possess closer predictions to experimental work by Lee & Li [206]. Figure 4.12b indicate the results of both models in terms of increase of temperature due to plastic work.

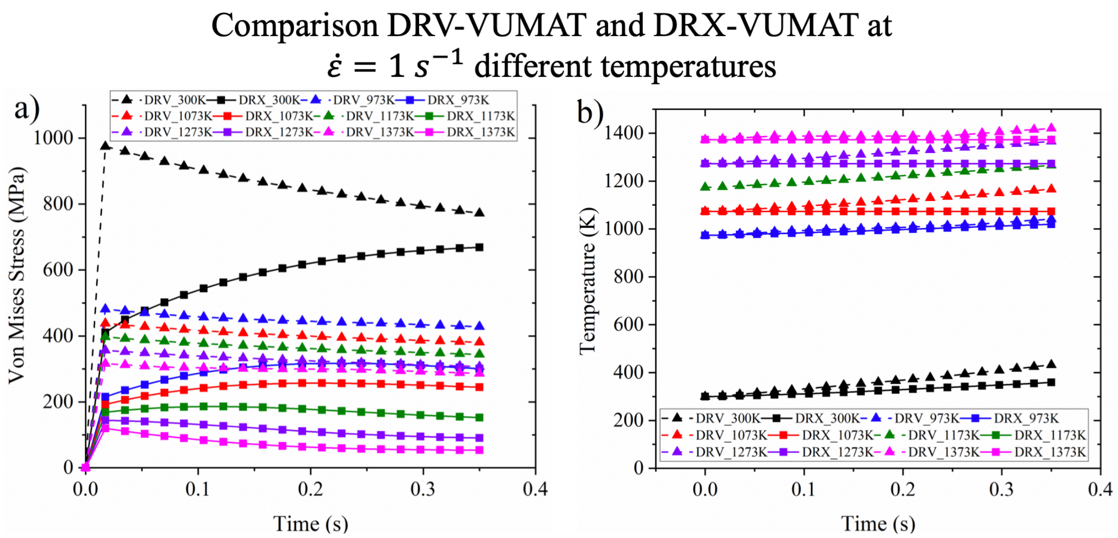


Figure 4.12 Single element test DRV-VUMAT and JC-Abaqus comparison, a) Von-Mises and b) increase of temperature predictions.

After verifying the correct implementation in Abaqus of both subroutines (DRV and DRX VUMATs) the next step is the assessment of the subroutines at the same deformation conditions as the mechanical testing and orthogonal machining tests presented in chapter 3. The following sections will explain the three FE models developed for the numerical simulations

## 4.9 High strain rate modelling

The numerical SHPB simulations were carried out using Abaqus/explicit. DRV and DRX VUMATs subroutines were used as material constitutive models. A two-dimensional and half-symmetry model was built as shown in Figure 4.13a. The simulations were conducted under the Lagrangian configuration where the specimen was modelled as a deformable body while the two anvils were modelled as rigid bodies.

Three boundary conditions were applied: one anvil was fixed in all directions, whereas a velocity boundary condition was applied to the second anvil (Figure 4.13a). While a symmetry boundary condition was applied on the vertical direction (x axis of the specimen in Figure 4.13a). The specimen was given an initial temperature of 300 K. A finite element mesh was generated for the specimen with eight node, quadrilateral elements (code C3D8R).

The specimen was given an initial temperature of 300 K. A mesh convergence analysis was carried out to determine the optimum mesh size, giving one thousand elements the optimum size. The friction between the two anvils and the specimen was modelled with Coulomb's friction law with a friction coefficient of 0.05 as suggested in [21].

The half-symmetry sample dimensions were modelled same as the actual samples in the experiments (5 and 10 mm length and diameter respectively). The samples were pressed to a height reduction of 50% under a constant velocity (Figure 4.13b). For the three testing speeds, the acquired Von-Mises stresses were acquired from the centre of the deformed specimen as shown in Figure 4.13c.

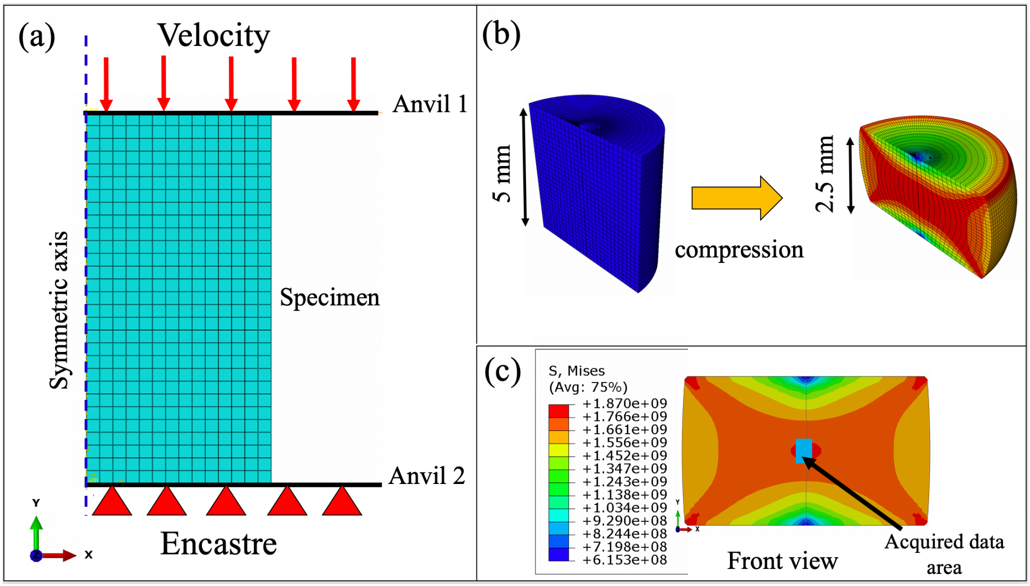


Figure 4.13 SHPB FE model: a) boundary conditions setup b) schematic illustration of SHPB compression test and, c) Von Mises acquired point in the model.

## 4.10 Axisymmetric hot compression modelling

The numerical axisymmetric hot compression simulations were carried out using Abaqus/explicit. DRV and DRX VUMATs subroutines were used as material constitutive models. A two-dimensional and half-symmetry model was built as it is shown in Figure 4.14a.

The simulations were conducted under the Lagrangian configuration where the specimen was modelled as a deformable body while the two anvils were modelled as rigid bodies. Three boundary conditions were applied: one anvil was fixed in all directions, whereas a velocity boundary condition was applied to the second anvil (Figure 4.14a). While a symmetry boundary condition was applied on the vertical direction (x axis of the specimen in Figure 4.14a). The specimen was given four initial temperature of 973, 1073, 1173 and 1273 K. A finite element mesh was generated for the specimen with eight node, quadrilateral elements (code C3D8R). A mesh convergence analysis was carried out to determine the optimum mesh size, giving one two thousand elements the optimum size. The friction between the two anvils and the specimen was modelled with Coulomb's friction law with a friction coefficient of 0.05 as suggested in [21].

The half-symmetry sample dimensions were modelled same as the actual samples in the experiments (15 and 10 mm length and diameter respectively). The samples were pressed to a height reduction of 35% under a constant velocity (Figure 4.14b). For the three testing speeds and four temperatures, the acquired Von-Mises stresses were acquired from the centre of the deformed specimen as shown in Figure 4.14c.

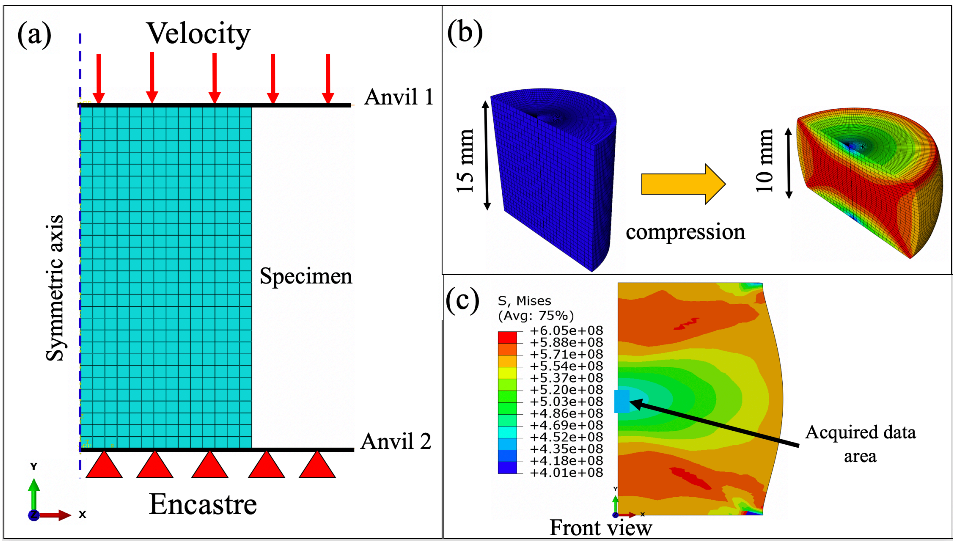


Figure 4.14 Hot compression FE model: a) boundary conditions setup b) schematic illustration of hot compression test and, c) Von Mises acquired point in the model.

## 4.11 Orthogonal machining modelling

The numerical orthogonal machining simulations were carried out using Abaqus/explicit. The Johnson-Cook plasticity and damage initiation criterion models were used as material constitutive models. For the JC damage initiation criterion, it was modelled an exponential degradation behaviour of each element after reaching the critical strain $\varepsilon_f$. The damage variable $d$ is given as:

$$d = \frac{1 - e^{-\alpha\left({}^{\varepsilon_p}/_{\varepsilon_f}\right)}}{1 - e^{-\alpha}}$$

Equation 4.37

Where, $\varepsilon_p$ is the effective plastic displacement and $\alpha$ is a material constant. The deterioration is measured by the $d$, which varies from 0 to 1, where 0 is when the degradation begins and evolves exponentially (Equation 4.28) until reaches 1 which is when the element is deleted.

Chip formation simulations were conducted under the Lagrangian configuration. The FE two-dimensional model consisted in a rigid body cutting tool and a workpiece the specimen modelled as a deformable as shown in Figure 4.15. Two boundary conditions were applied: the workpiece was fixed at the bottom and at one the end, whereas a velocity boundary condition was applied to the cutting tool as shown in Figure 4.15. The specimen was given a temperature of 300 K. The workpiece dimensions consisted in 1 mm and 3 mm height and length respectively.

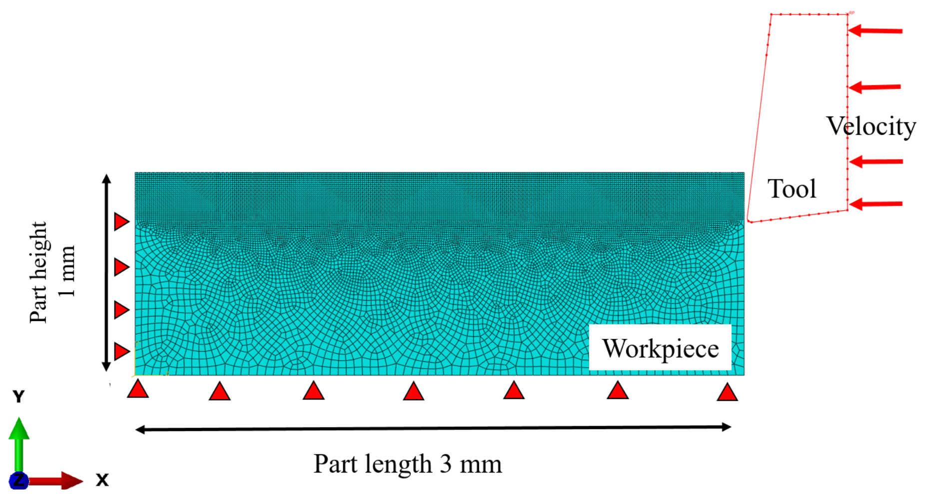


Figure 4.15 FE orthogonal cutting model

The workpiece was divided in three parts including: chip layer, separation layer and main part of the workpiece as shown in Figure 4.16a. This method is commonly used within literature in order to achieve continuous chips rather broken unsegmented chips [128, 146]. A finite element mesh was generated for three zones of the workpiece with eight node, quadrilateral elements (code C3D8R).

A total of twenty thousand elements were used to mesh all workpiece. The cutting tool as modelled with a nose radius of 200 µm, and seven degrees rake and relief angles as shown in Figure 4.16b. The friction between the tool and the workpiece was modelled with Coulomb's friction law with a friction coefficient of 0.05 as suggested in [128]. Three cutting speeds (2,4 and 6 m/min) and two depth of cuts were modelled, exact same experimental conditions described in section 3.5.

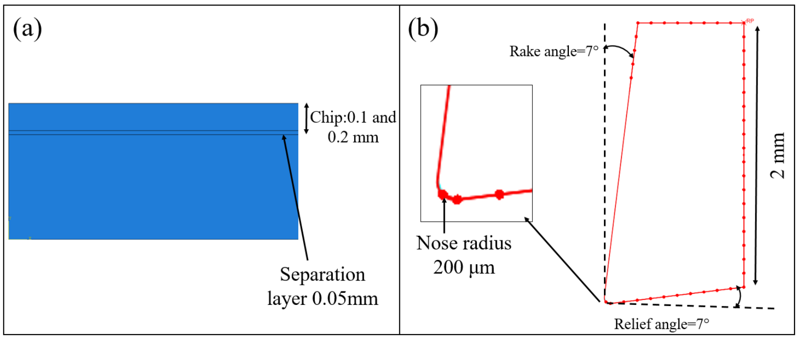


Figure 4.16 Orthogonal FE modelling: a) workpiece areas and b) cutting tool features

## 4.12 Summary

In this chapter, it was presented the new physically based model. Firstly, it was described the DRV and DRX phenomena separately and later incorporated into one general expression for prediction of flow stress. The proposed model considers four hardening mechanisms, including: grain boundary hardening, forest hardening (dislocation density), solid solution and precipitation hardening.

Later, it was presented the verification steps of the correct implementation of the user subroutines DRV and DRX. Results shown that DRV-VUMAT was more sensible to adiabatic heating effects compared to JCmodel. The last verification consisted comparing DRV-VUMAT against DRX-VUMAT. Results shown that DRX-VUMAT predicted less yield strength (around 250 MPa) in all hot deformation conditions. In the last section, it was explained the three FE models developed in order to simulate SHPB, hot axisymmetric compression and orthogonal machining tests.

Next chapter will present the results obtained for the experimental work carried out, the validation and verification of the predictions of new constitutive equation. It is presented the FE simulations results and are compared with the experimental ones.

# 5. Results

## 5.1 Introduction

This chapter covers all the results of this project. Experimental results comprehend the response of SLM samples at high strain rate, followed by the response during axisymmetric hot compression tests and the orthogonal machining results in terms of machining forces and chip morphology. On the modelling side, it is presented the predictions of the new physically-based model for yield strength and flow stress with experimental data reported within the literature.

Subsequently it is presented the results for numerical simulations. The DRV-VUMAT predictions is compared with SHPB experimental results, whereas the DRX-VUMAT predictions is compared against the hot compression experimental results. The final section covers the chip formation numerical simulations. As discussed in chapter four, this model was fully developed using embedded tools in Abaqus instead of testing the developed VUMATs, because the approach of this project was focused in plasticity instead of damage modelling and in order to produce chips it is required element deletion routine inside the VUMAT formulation. However, the results are assessed with the experimental data for completeness.

## 5.2 Experimental results

### 5.2.1 High strain rate experimental results

Three strain rates were tested at SHPB machine. Figures 5.1 to Figures 5.3 shows the footage recorded for 1000, 1500 and 2000 $s^{-1}$ respectively. As can be seen in these figures, all conditions show sparks produced by the fast mechanical work applied. Additionally, the presence of sparks at the beginning of deformations suggests poor ductility of the AM produced material compared to C&W counterparts [ref].

Increasing the strain rate the material produces high amount of sparks during deformation, especially at the 2000 s$^{-1}$ condition. During dynamic testing it is commonly reported adiabatic shear bands due to the event happens so fast that the heat has no time to diffuse. For instance, step 2 in Figures 5.2, captures the initial mode of failure forming a “V” shape, where glowing material inside the “V” can be seen, followed by high sparking. This figure also shows that the material does not exhibit high deformation in surrounding areas, instead all the stresses are localized in the same area. Figure 5.1 shows the lowest strain rate tested, where the material produced less sparks, however the footage does not reveal clearly the main mode of failure, whereas in Figure 5.3, the event occurs so fast that the high-speed camera did not captured this phenomenon, instead it can only be seen higher amount of sparks in step 2.

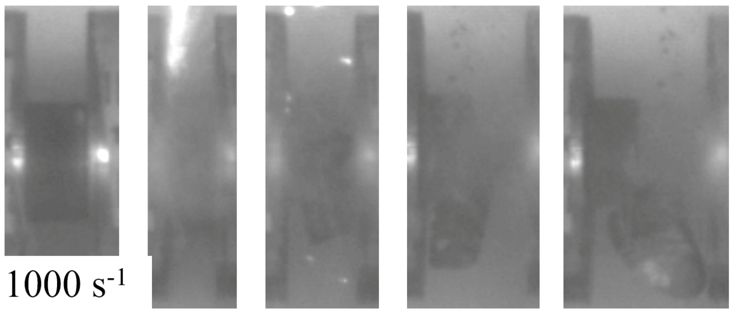


Figure 5.1 Deformation evolution at 1000 s$^{-1}$.

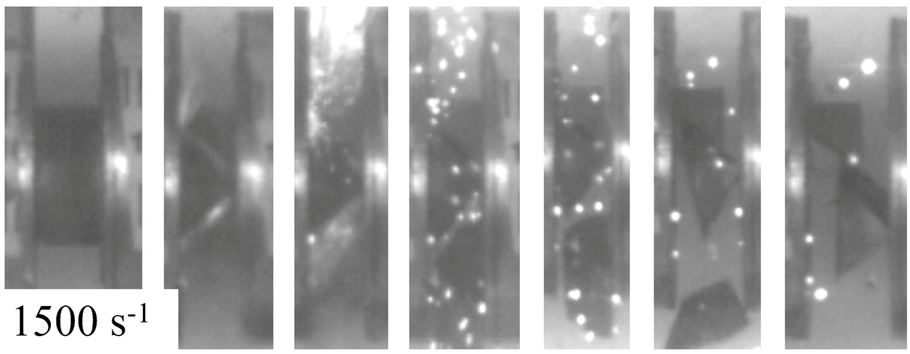


Figure 5.2 Deformation evolution at 1500 s$^{-1}$.

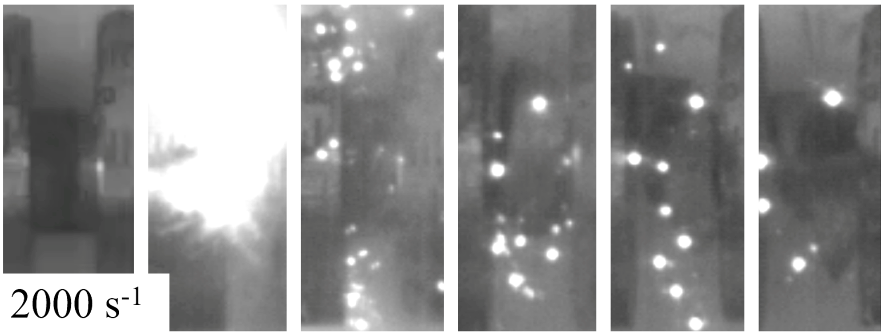


Figure 5.3 Deformation evolution at 2000 $s^{-1}$.

Despite the material was tested at three strain rate conditions, all samples failed in similar manner. Figure 5.4 shows examples of deformed samples at (a) 1000, (b) 1500 and (c) 2000 $s^{-1}$. Moreover, it can be seen that the material was subjected to high temperatures as the fracture areas display certain level of melting, specially at the highest strain rate (2000 $s^{-1}$). Comparing Figure 5.3 and Figure 5.4, it can be established that adiabatic heating effects are crucial considering the low thermal conductivity of Ti-64, as the local temperature rise leads to catastrophic failure.

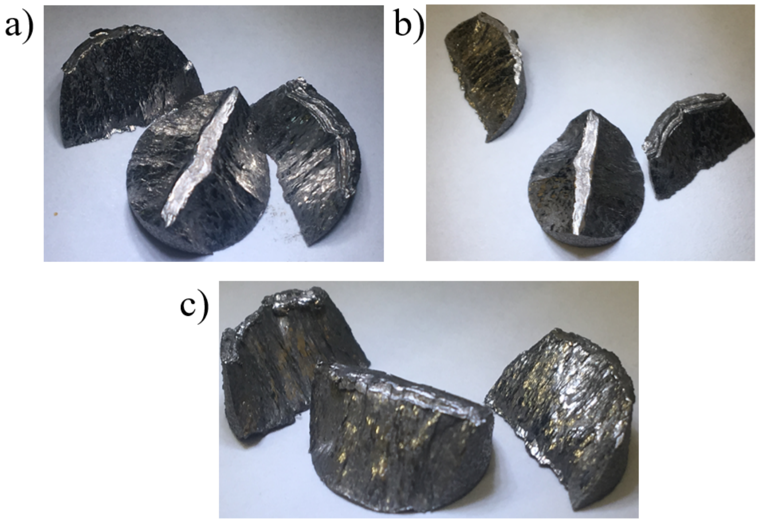


Figure 5.4 SHPB deformed samples at a) 1000, b) 1500 and c) 2000 $s^{-1}$.

5.2.1.1 Strain-stress flow curves

As mentioned previously, these tests were performed with the collaboration of the blast and impact research group within the civil and structural engineering department at the University of Sheffield. The engineering stress-strain curves were delivered to the author, which converted to true strain-stress curves using Equations 3.11 & 3.12. The resulted curves are presented in Figure 5.5. Within the three conditions, SLM Ti-64 displayed an elevated strain hardening.

The strain rate 1000 $s^{-1}$, displayed the lowest strength, whereas 1500 and 2000 $s^{-1}$ do not displayed a clear difference, however before failure, the highest strain rate displayed higher strength (around a strain of 0.13). As expected, the mechanical response also displayed low ductility, as plasticity only reaches up to 13% elongation. These results correlate as discussed in chapter 2, SLM components display roughly half of the elongation that its C&W counterparts. For instance, Lee & Li [93] reported at a strain rate of 2000 $s^{-1}$ of C&W Ti-64 maximum elongation of 20% during room temperature.

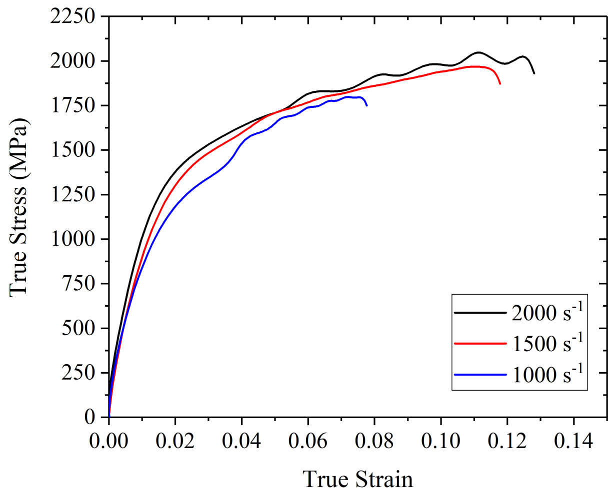


Figure 5.5 Flow stress curves of SLM Ti-64 samples at room temperature and strain rates of 1000, 1500 and 2000 $s^{-1}$.

### 5.2.2 Axisymmetric hot deformation experimental results

The hot deformation experiments consisted in three strain rates (1, 10 and 100 $s^{-1}$) and four temperatures (973- 1273K), the details are discussed in section 3.4. SEM micrographs with the initial microstructure before deformation is presented in Figure 5.6. A typical fully martensitic microstructure can be seen from this figure, where two magnifications are presented ((a) 10,000 and (b) 30,000).

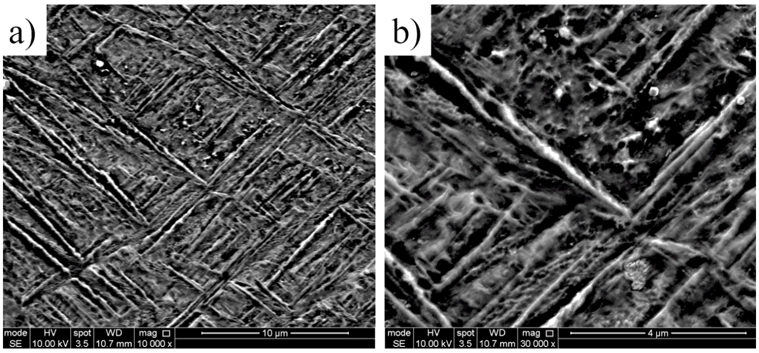


Figure 5.6 SEM micrographs showing Before deformation Ti-64 SLM samples microstructures.

5.2.2.1 Strain-stress flow curves

After post processing the acquired force-displacement curves, the resulted true strain-stress curves are presented in Figure 5.7. As expected, the deformation conditions at lowest temperature (973 K) displayed the highest strength of the material within the three strain rates, whereas the highest temperature displayed the lowest values in strength. In addition, by increasing the strain rate, the material displayed higher strength. Interestingly, the highest strength was achieved at intermediate strain rate (10 $s^{-1}$) at 973K, contrary of what was expected to be at 100 $s^{-1}$.

Despite the deformation rate, the three strain-stress curves presented an abrupt drop in strength between 1073 and 1173 K. In addition, within the twelve conditions, the results shown no apparent softening due to DRX or dynamic globularisation in all conditions, instead an increase on strength can be appreciated. This could be explained because two reasons; as the tested strain rates are relatively high (compared to other studies at forging conditions around $1 \times 10^{-4}$ up to 1 $s^{-1}$ [15, 21, 165]), it is apparent that DRV effect is stronger than DRX as the last requires time and temperature as result work hardening takes place. Adding to this, the initial microstructure is fully martensitic, whereas other studies have reported conventional C&W samples [9, 11, 88, 217]. Therefore, it is expected a different evolution of the structure during hot deformation, in order to explore this possibility, it will be presented the after-deformation SEM micrographs in the section.

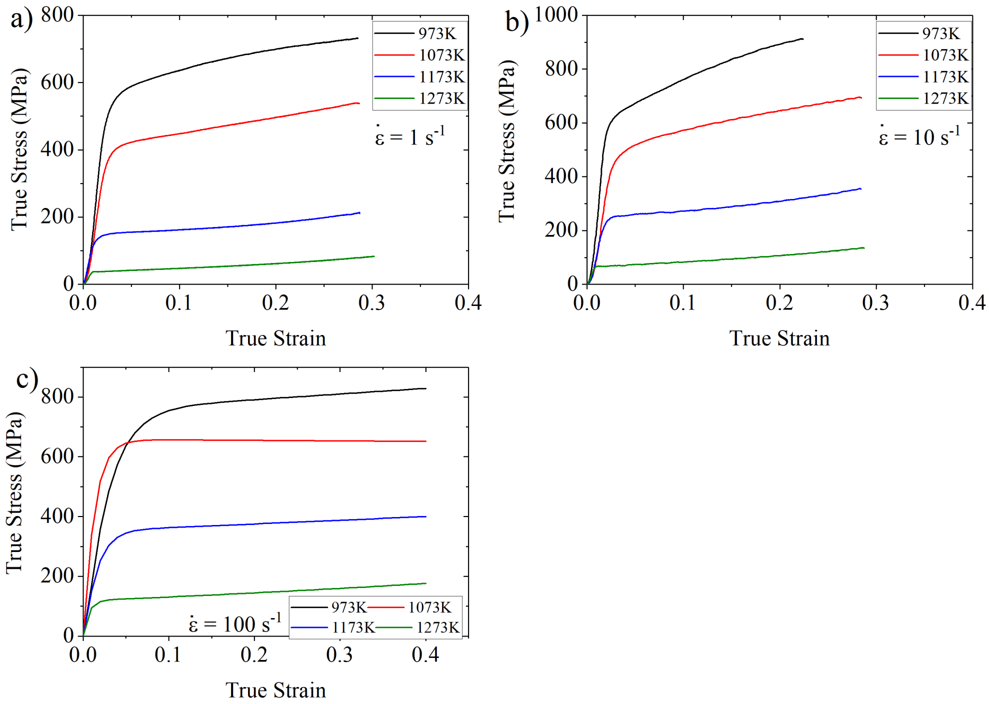


Figure 5.7 Strain-stress curves for: a) 1, b) 10 and c) 100 $s^{-1}$ at 973 up to 1273K.

5.2.2.2 Selective electron micrographs of deformed samples

Figure 5.8 shows the acquired SEM images for the 100 $s^{-1}$ strain rate of after deformed samples. Figure 5.8a and b show the condition of temperature of 973 K within two magnifications (5,000 and 10,000). As can be seen in these images, the material prevails in martensitic regime, as reported in [6, 67, 187], the initial α' decomposition temperature starts from ~973 K and finishes at ~1173 K, when reaches the transus temperature from alpha to beta regimes. However, it can be appreciated the lath's thickness growth. Worth noting that after deformation there are white dimples all over the martensite laths (Figure 5.8b) that were not present in initial microstructure (Figure 5.8b).

Figure 5.8c and d show the temperature of 1073K. These figures show a considerable increase of the *α'* lath thickness, the progression of *α'* in this state can be seen as almost decomposed. From the crystallographic point of view, the hexagonal structure *α'* becomes distorted by the solute content, strain and temperature, as result *α'* loses its hexagonal shape forming the so-called orthorhombic martensite (*α''*) [6]. Figure 5.8d shows 20,000 magnification, where the white dots inside the *α''* laths became coarser.

Figure 5.8e and f show the temperature of 1173K. These figures show the total decomposition of *α''* martensite. A drastic increase of the lath's thickness is achieved, in addition no apparent presence of white dots within the laths is seen (Figure 5.8e). This can be explained as the orthorhombic martensite (*α''*) decomposed into solute lean and solute reach regions just before the beta phase is precipitated [6]. This sequence can be summarised as follows: $\alpha''_{lean} + \alpha''_{rich} \Rightarrow \alpha + \beta$. As result, a totally new microstructure in terms of constitutive phases and grain size is achieved.

Figure 5.8g and h show the temperature of 1173K. As can be seen, in the last condition the microstructure have evolved until a point that $\alpha'$ or the small particles are not visible. Displaying $\alpha + \beta$ structure with the highest lath thickness within all tested temperatures.

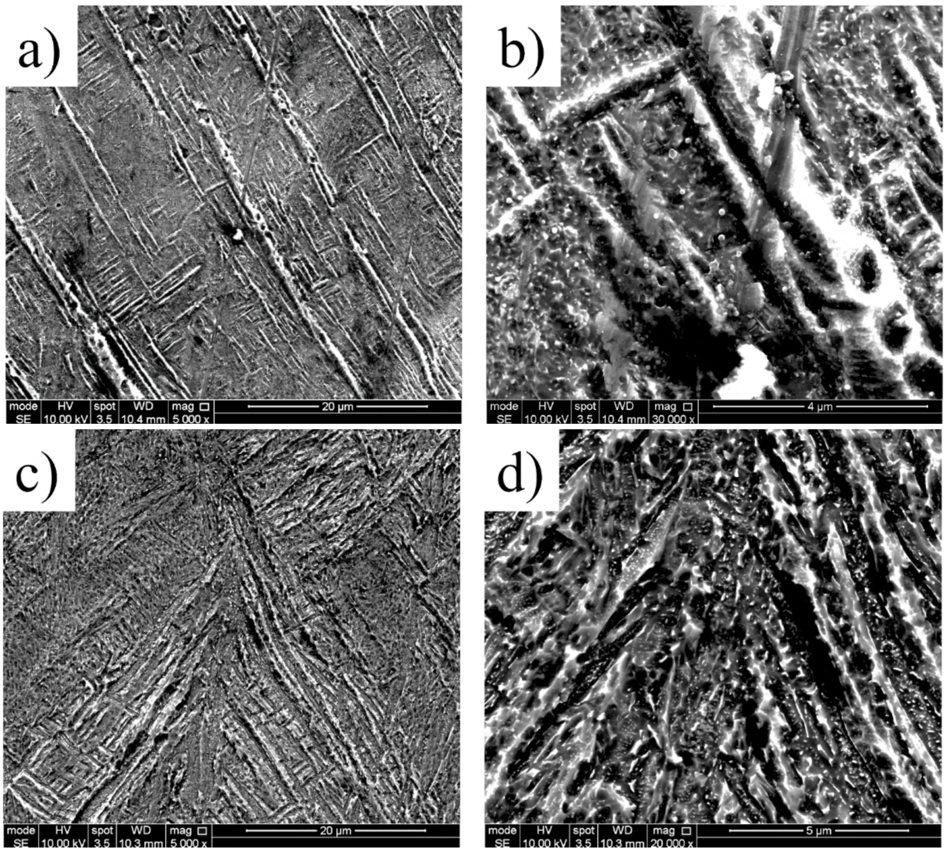

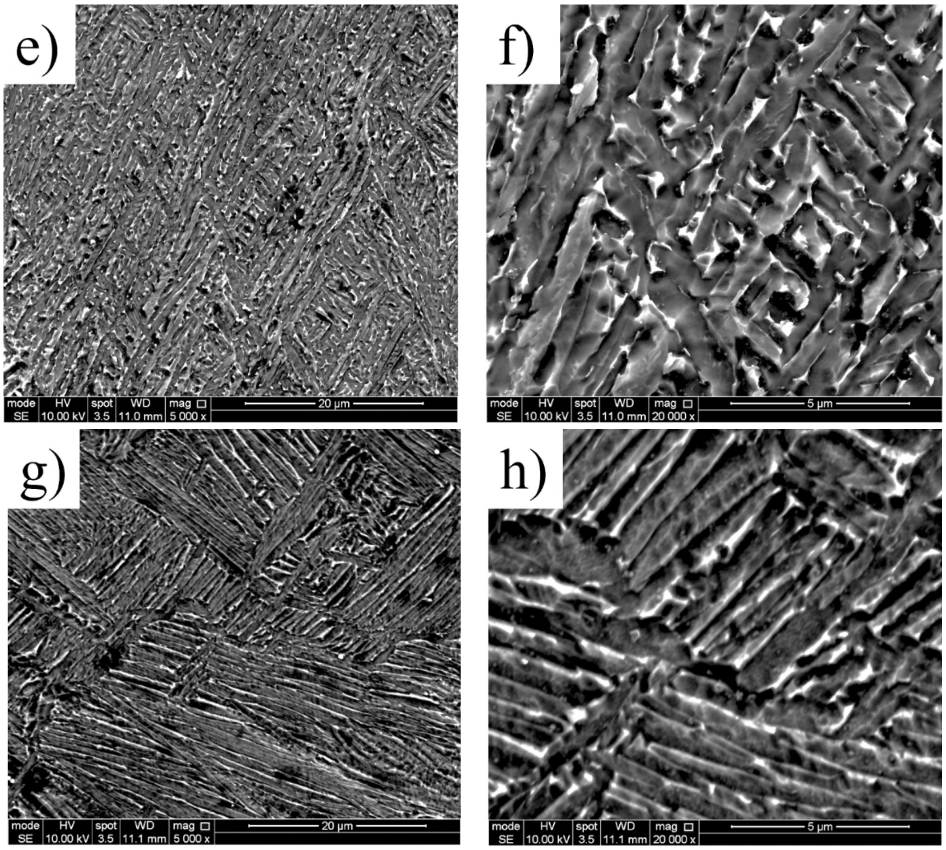


Figure 5.8 SEM micrographs during hot deformation at 100 $s^{-1}$ at: a, b) 973K, c, d)1073K, e, f)1173K and g, h)1273K.

To correlate the mechanical response with the microstructure evolution during hot deformation of SLM samples, Figure 5.9 shows the $\alpha' = \alpha + \beta$ sequence. Also, it is shown the mechanical response, as can be seen the transition of the microstructure between 1073 to 1173 K temperatures highly affect the flow stress.

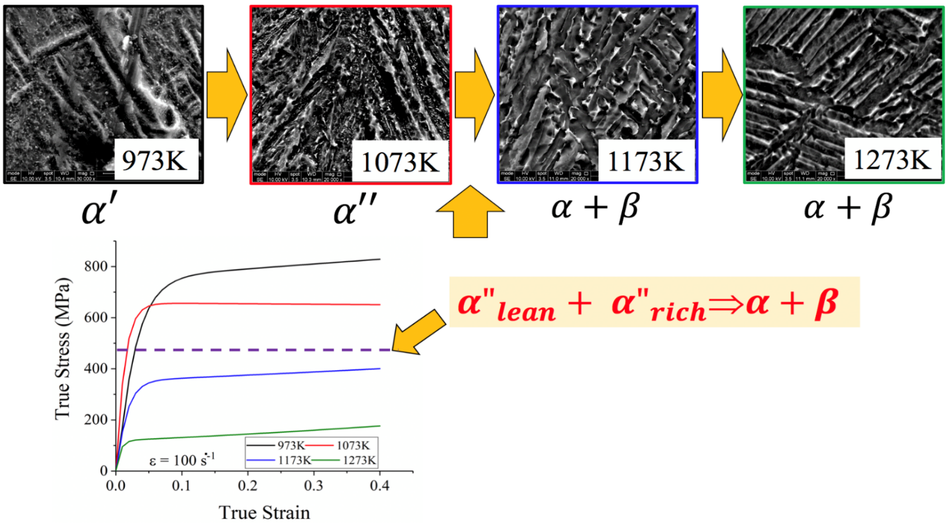


Figure 5.9 Martensite decomposition sequence

### 5.2.3 Orthogonal cutting experimental results

#### 5.2.3.1 Chip morphology results

Using the Dyno-lite optical microscope, Figure 5.10 shows an example of the procedure used to measure the distance between serrations (DL3 to DL5 measures in Figure 5.10), whereas the chip's thickness was measure by the distance between the chip's root and the peak of the chip (DL0 to DL2 measures in Figure 5.10). For both measurements, three measures were recorded and averaged. It was measured three types of Ti-64 alloys; two SLM with horizontal and vertical building direction and C&W.

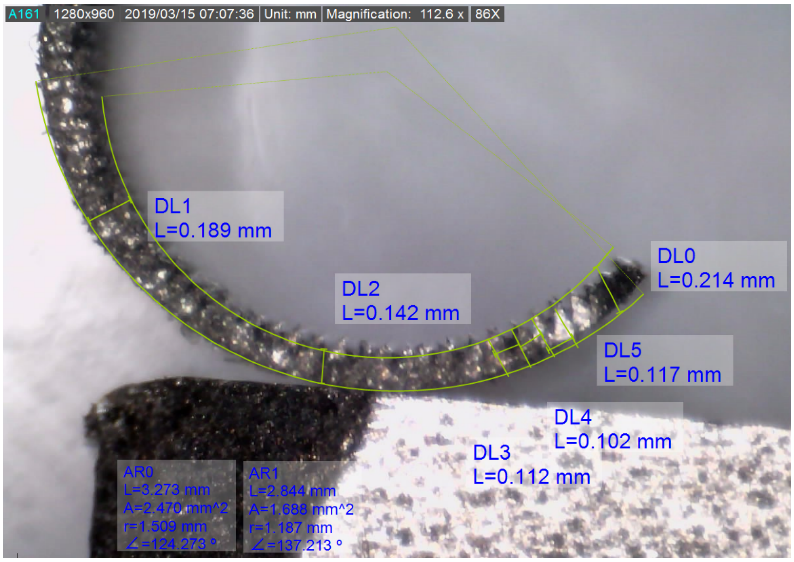


Figure 5.10 Example of the methodology used for measuring the chips

Table 5.1 summarises the recorded values for the three alloys, where D1 is the distance between serrations and D2 is the distance between the root to the peak of the chips both values in millimetres. The results shown that by increasing the cutting speed the distance between serrations is reduced, whereas chip thickness also was reduced by the cutting speed within the three tested materials.

Additionally, Ti-64 C&W produces thicker chips compared to its AM counterparts when machining 0.1 mm depth of cut for around 5% and 0.2 mm was roughly 4%. The thinner chips were produced by the SLM-horizontal material (0.112 and 0.213 for 0.1 and 0.2 mm respectively), which displayed in most cases poor ductility making more difficult to measure the chips. In terms of distance between serrations, again SLM-horizontal produced the shortest distances and the sharpest tooth-chips from the three of them. The smallest value between serrations was achieved during 0.1 mm depth of cut and 6 m/min cutting speed for SLM-horizontal.

The actual chips formed during the three cutting speeds and the two depth of cut tested are presented in Figure 5.11 for C&W, Figure 5.12 for SLM-built vertically and Figure 5.13 for SLM-built horizontally.

Table 5.1 Experimental chip morphology measurements

| 0.1 depth of cut | | | | | | |
|---|---|---|---|---|---|---|
| | C&W | | SLM-vertical | | SLM-horizontal | |
| **Cutting speed (m/min)** | **D1 (mm)** | **D2 (mm)** | **D1 (mm)** | **D2 (mm)** | **D1 (mm)** | **D2 (mm)** |
| 2 | 0.052 | 0.155 | 0.050 | 0.142 | 0.048 | 0.137 |
| 4 | 0.041 | 0.132 | 0.036 | 0.128 | 0.032 | 0.122 |
| 6 | 0.037 | 0.124 | 0.032 | 0.118 | 0.025 | 0.112 |
| **0.2 depth of cut** | | | | | | |
| | C&W | | SLM-vertical | | SLM-horizontal | |
| **Cutting speed (m/min)** | **D1 (mm)** | **D2 (mm)** | **D1 (mm)** | **D2 (mm)** | **D1 (mm)** | **D2 (mm)** |
| 2 | 0.122 | 0.241 | 0.097 | 0.238 | 0.092 | 0.229 |
| 4 | 0.111 | 0.235 | 0.078 | 0.229 | 0.088 | 0.225 |
| 6 | 0.092 | 0.228 | 0.068 | 0.219 | 0.079 | 0.213 |

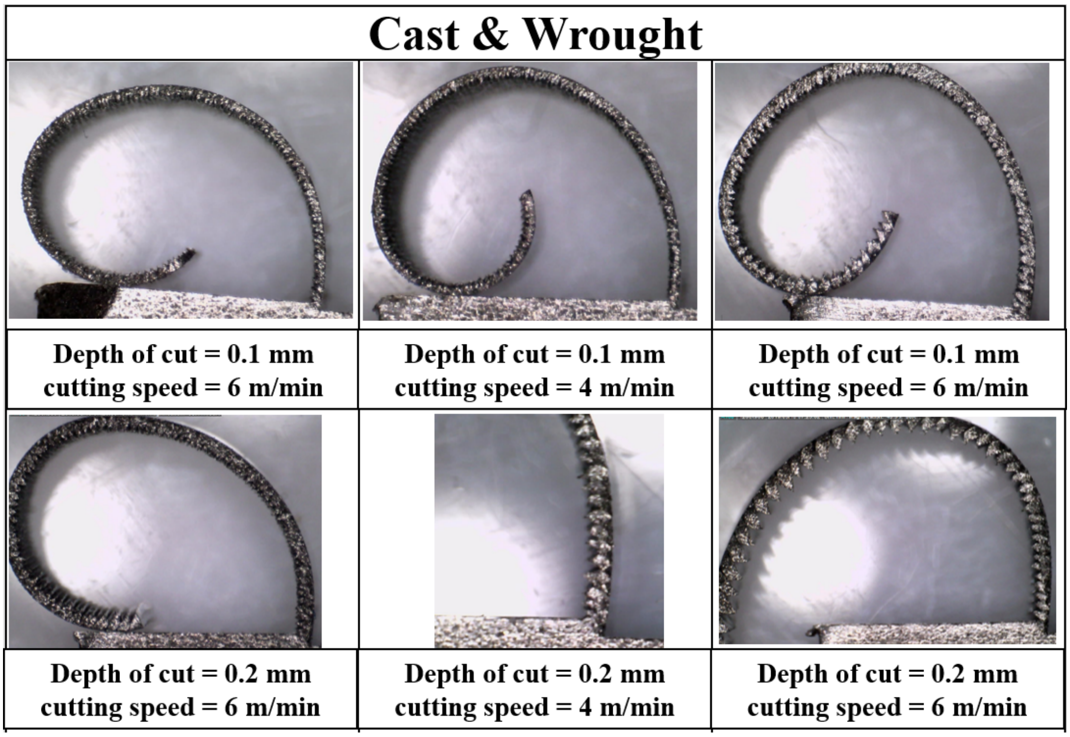


Figure 5.11 Resulted chips for Ti-64 C&W alloy

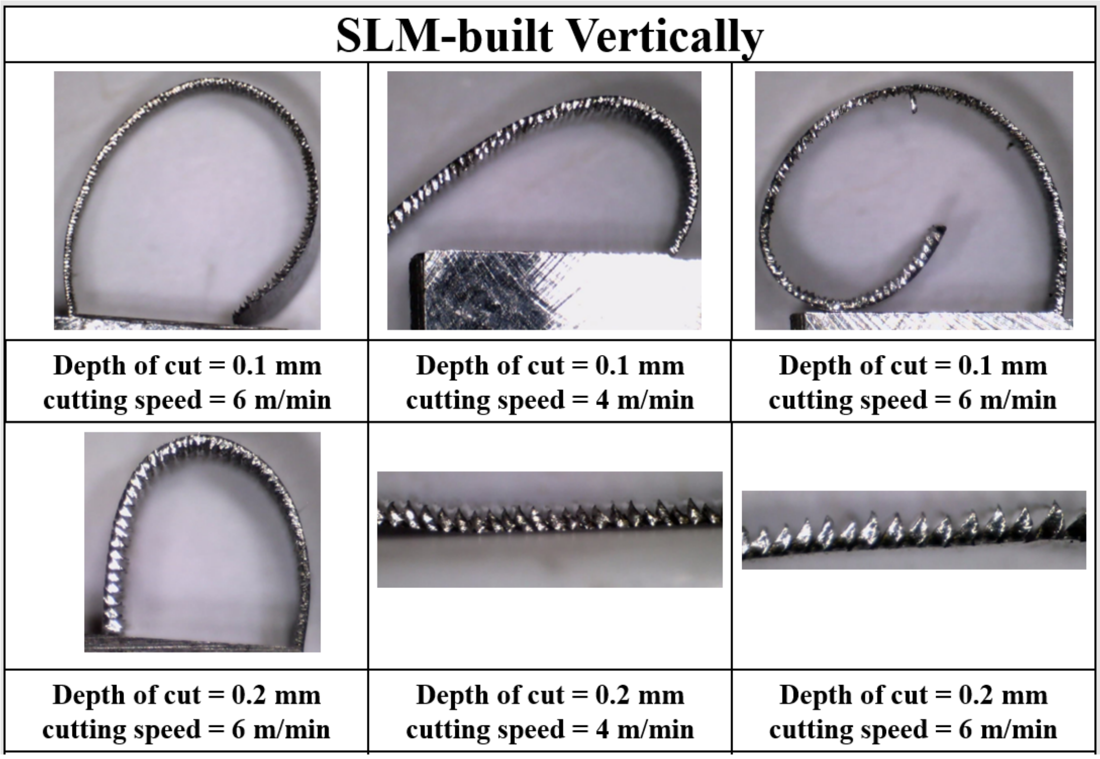


Figure 5.12 Resulted chips for Ti-64 SLM-vertical built alloy

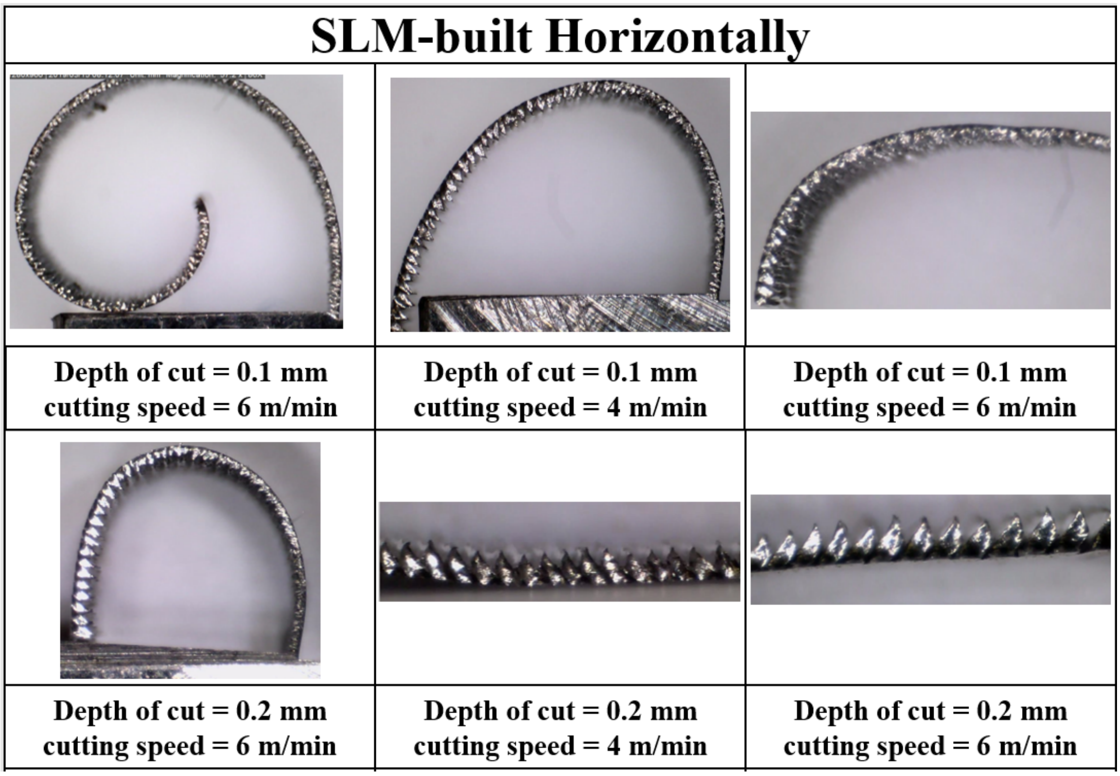


Figure 5.13 Resulted chips for ti-64. SLM-horizontal built alloy

### 5.2.3.2 Cutting forces results

The orthogonal machining forces results are presented from Figures 5.14 to 5.16 for C&W, SLM-built vertically and horizontally respectively. Three repeats were performed for each condition and averaged. In addition, together with all values reported are the error bars representing plus/minus 10 error. The three materials presented an increase of forces due to cutting speed. The highest cutting force ($F_y$) for all materials was found at 0.2 and 6 m/min machining conditions, where SLM-built horizontally presented the highest forces (3182 N), followed by SLM-built vertically (2732 N) and C&W sample presented the lowest value (2285 N). Similarly, the highest thrust force ($F_z$) was generated by SLM-built horizontally with 2437 N, followed by SLM-built vertically and C&W materials with 1899 N and 1675 N respectively.

Due to high cutting and thrust forces recorded, the out of plane forces ($F_x$) were also high in all tested materials. For instance, SLM-built horizontally during 0.2 mm depth of cut and 6 m/min cutting speed, the material displayed 122 N (the highest out of plane force recorded in all trials). Considering that 3182 N were recorded for cutting force at the same cutting conditions, the out of plane force only represented 3.8% of the total cutting force, therefore the assumption of orthogonal cutting is satisfied. The rise of out of plane forces is commonly accepted that is because of the spread of material occurring, as the phenomenon occurs in a three-dimensional environment, this peculiarity is almost unavoidable.

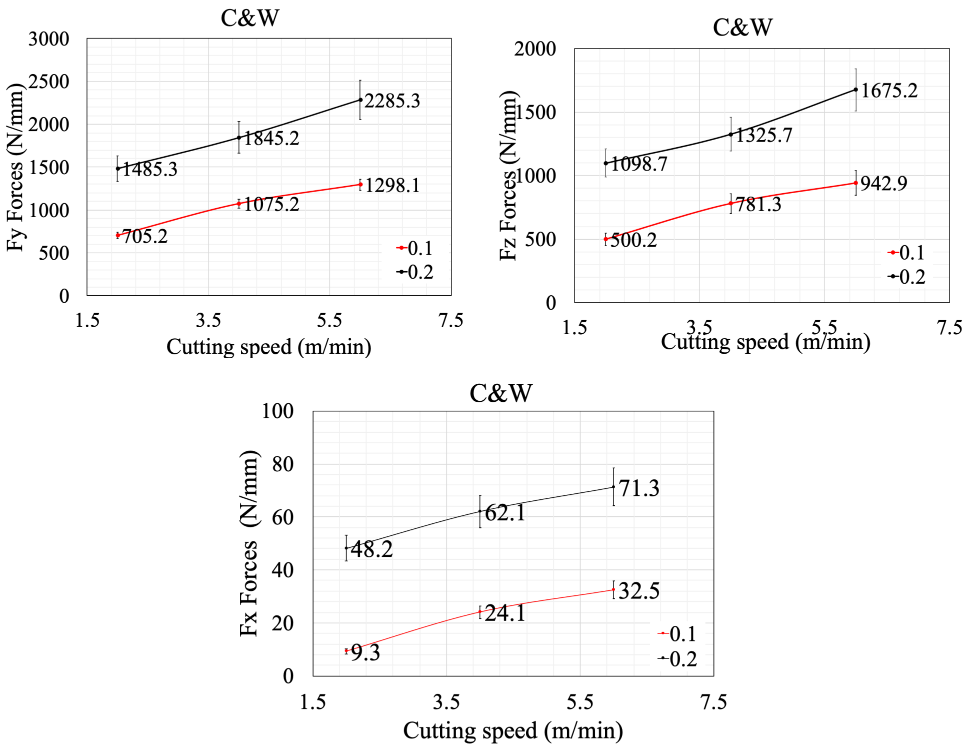


Figure 5.14 Orthogonal machining forces results for C&W.

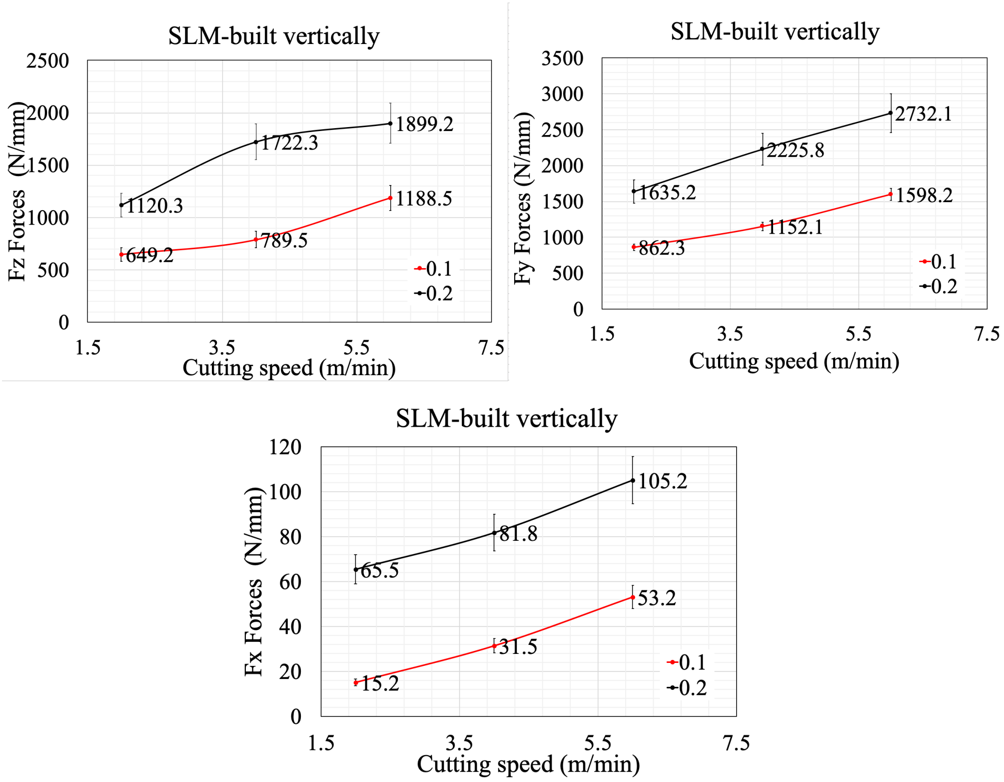


Figure 5.15 Orthogonal machining forces results for SLM-built vertically

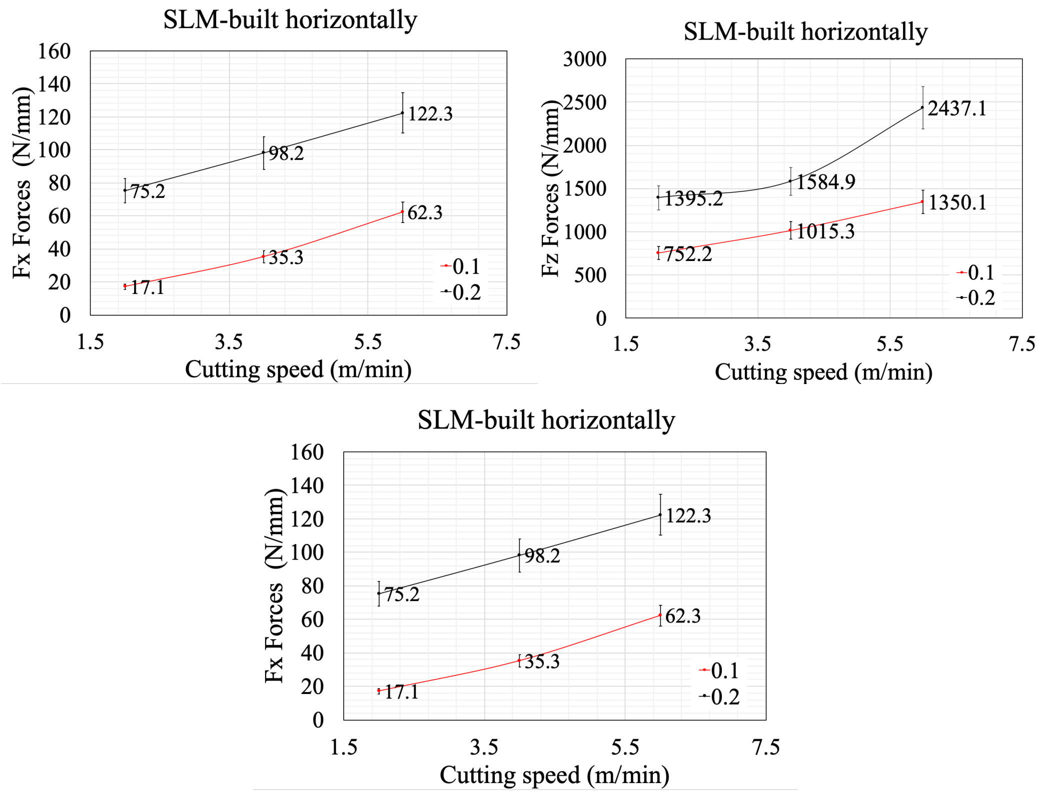


Figure 5.16 Orthogonal machining forces results for SLM-built horizontally

## 5.3 New physically-based model results

### 5.3.1 Yield Strength predictions

This section presents the model predictions and its comparison with reported experimental data. Table 5.2 presents the physical constants used to calibrate the model whereas the tested microstructural features within the literature is reported in Appendix B.

Table 5.2 Parameters used to calibrate model

| No. | Constant | Value | Units | Reference |
|---|---|---|---|---|
| 1 | $k_{HP}$ | 300 | MPa | [194] |
| 2 | $\sigma_\alpha$ | 550 | MPa | Calculated |
| 3 | $\sigma_\beta$ | 1350 | MPa | Calculated |
| 4 | $M$ | 3 | - | Fitted |
| 5 | $b$ | $2.9\text{x}10^{-10}$ | m | [218] |
| 6 | $k_B$ | $1.38\text{x}10^{-23}$ | J/K | [218] |
| 7 | $\eta$ | 0.4 | - | Fitted |
| 8 | $\kappa$ | 0.23 | - | Fitted |
| 9 | $f_{DRV}$ | 8 | - | Fitted |
| 10 | $k_1$ | 0.07 | - | Fitted |
| 11 | $\rho_0$ | $1\text{x}10^{11}$ | $m^{-2}$ | [208] |
| 12 | $\rho_{0\alpha'}$ | $1.7\text{x}10^{13}$ | $m^{-2}$ | Calculated |
| 13 | $\omega$ | 0.24 | - | Fitted |
| 14 | $\lambda$ | 0.6 | - | Fitted |

Figure 5.17 shows the results compared with the experimentally measured values for AM processing routes (Fig. 17a) and three microstructures (Fig. 17b) including bimodal, lamellar and equiaxed structures. The dashed lines in Fig. 5.17 present the 5% error margin showing that the majority of the predicted results are within the ±5% error compared with the experimentally observed values reported in the literature.

Worth noting that the predictions outside the ±5% error region (dotted lines) are the ones heat treated, thus the discrepancies could be attributed to the resulted uniformity of the samples and some defects could be introduced during the heat treatment process.

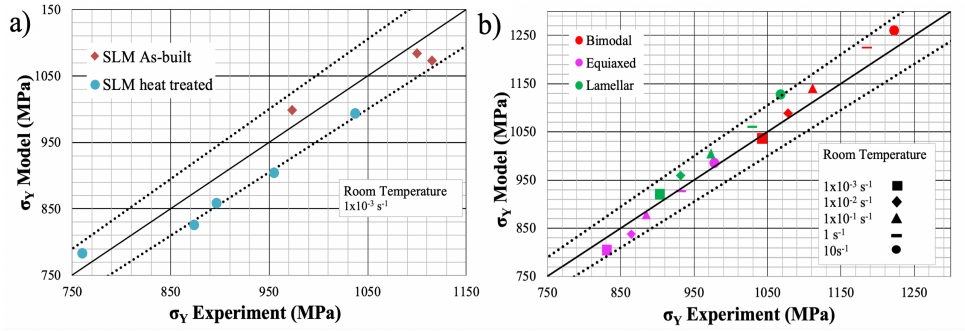


Figure 5.17 Predicted of $\sigma_Y$ for (a) SLM as-built and SLM heat treated [77] (b) hot worked structures at different strain rates [86].

The model was validated against experimentally measured yield strengths under different deformation/microstructure conditions. Figure 5.18a shows the predicted yield strength for a martensitic structure produced by Powder Layer Deposition (PLD) technique at low and high strain rates (0.1 s$^{-1}$ and 5000 s$^{-1}$) and temperatures ranging from 298 -1273 K compared with the experimental results obtained from literature. Figure 5.18b presents the results of model validation for an equiaxed structure tested under different deformation conditions (5 strain rates and four temperatures). The dashed lines in Figure 5.18 represent that the majority of the predicted results are within the ±5% error compared with the experimentally observed values reported in the literature.

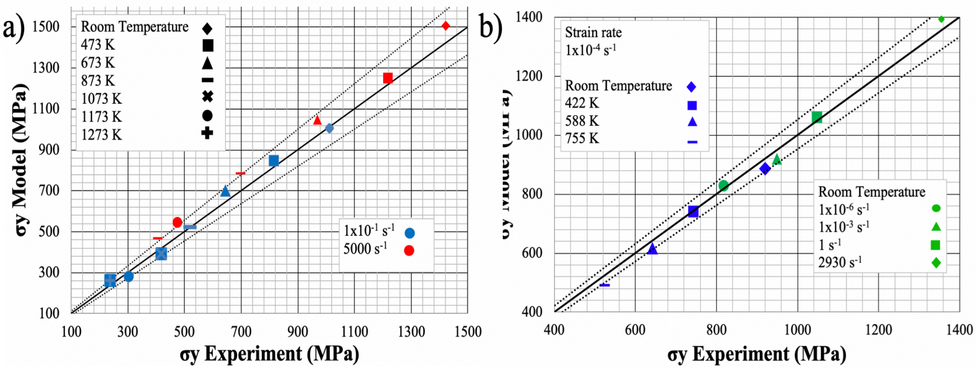


Figure 5.18 Prediction of $\sigma_Y$ for (a) SLM structures tested at various temperatures and under high and low speed testing condition[159], (b) equiaxed structure tested at various temperature and strain rates [90].

### 5.3.2 Flow stress predictions

In order to validate the flow stress ($\bar{\sigma}_{DRV}$) predictions, the effect of grain's shape and size on the flow stress of C&W structures (equiaxed, lamellar and bimodal) at low and high strain rates (1x10$^{-2}$ up to 2600 s$^{-1}$) during room temperature was assessed. The model was then implemented for equiaxed and PLD ($\alpha'$) structures at an extensive range of deformation conditions. This is followed by final validation tests to compare the predicted flow stress for as-built SLM, SLM heat-treated and an equiaxed structures with the experimentally measured values reported in the literature.

#### 5.3.2.1 C&W microstructures

Figure 5.19 shows the predicted plastic behaviour (solid lines) of hot worked structures (equiaxed, lamellar and bimodal) using low and high strain rates (1x10-2 up to 2600 s-1) at the room temperature compared with the experimentally measured compression test results. The error bands show an error margin of 5% in the predicted results. The predicted results show the least error (Figure 5.19a) for the lowest strain rate (1x10-2 s-1) and the highest error (Figure 5.19.c) for 10 s-1 strain rate. This phenomenon was explained by the authors of the produced experimental data as could be caused by adiabatic shear bands generation, possibly, due to the presence of microstructural defects and inhomogeneities, rather than morphological effect during plastic deformation [86]. Whereas, strain rates within 1 s-1 and 2600 s-1 show intermediate results (Fig. 5.19b and d).

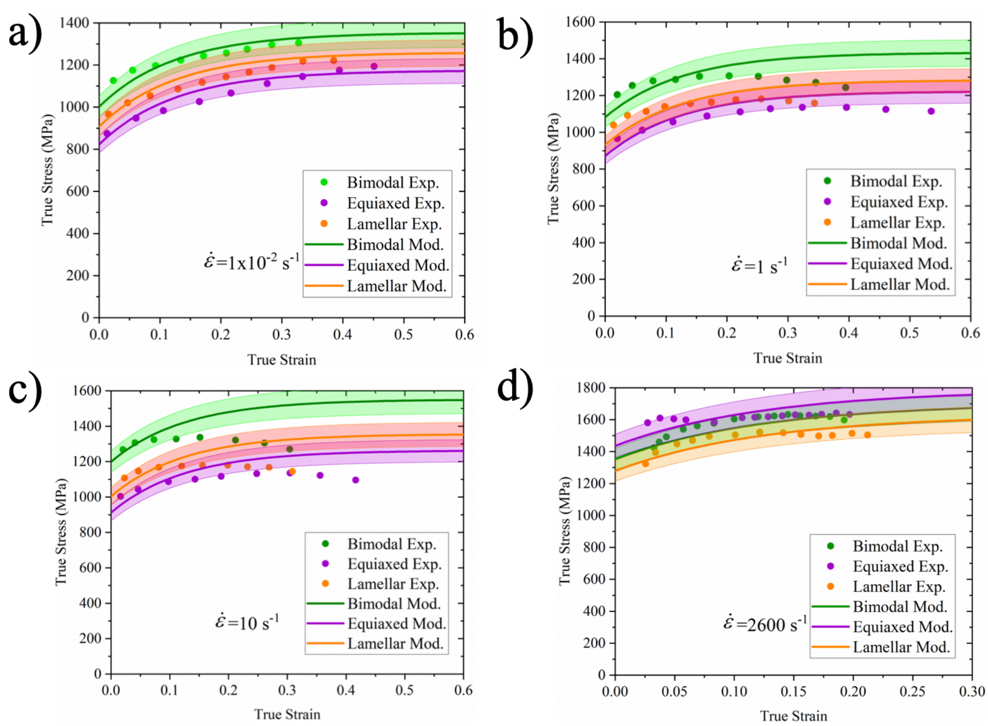


Figure 5.19 Flow stress of hot worked Ti-64 structures [86, 87], (a) 1x10-2 s-1, (b) 1 s-1 (c) 10 s-1, (d) 2600 s-1.

5.3.2.2 C&W v AM microstructures at different deformation conditions

The predicted flow stresses for an equiaxed microstructure under low ($1x10^{-4}$ $s^{-1}$) and a high (2000 $s^{-1}$) deformation conditions are shown in Figure 5.20 a and b, respectively. The deformation temperature varied from 233K up to 1373 K in both cases.

According to the graphs of Figures 5.20a and b, the model predictions are closer to the experimental data at low strain rates. However, the model behaviour shows a deviation with the experimental data at the highest temperature tested (755 K) that can be related to the fact that the thermal softening prevails the strain rate hardening effect. In the deformation regime where the strain rate is much larger, this effect is less obvious therefore; the predicted results are closer to experiments even until a deformation temperature of 1173 K.

Martensitic structures were verified from room temperature up to 1273 K and strain rates of 0.1 s-1 (Figure 5.20c) and 5000 s-1 (Figure 5.20d). Experimental data suggests that martensitic structures experience high strain hardening effect at low strain rates even at very high temperatures (1073 - 1273 K), whereas during a high strain rate deformation a thermal softening effect starts around 873 K.

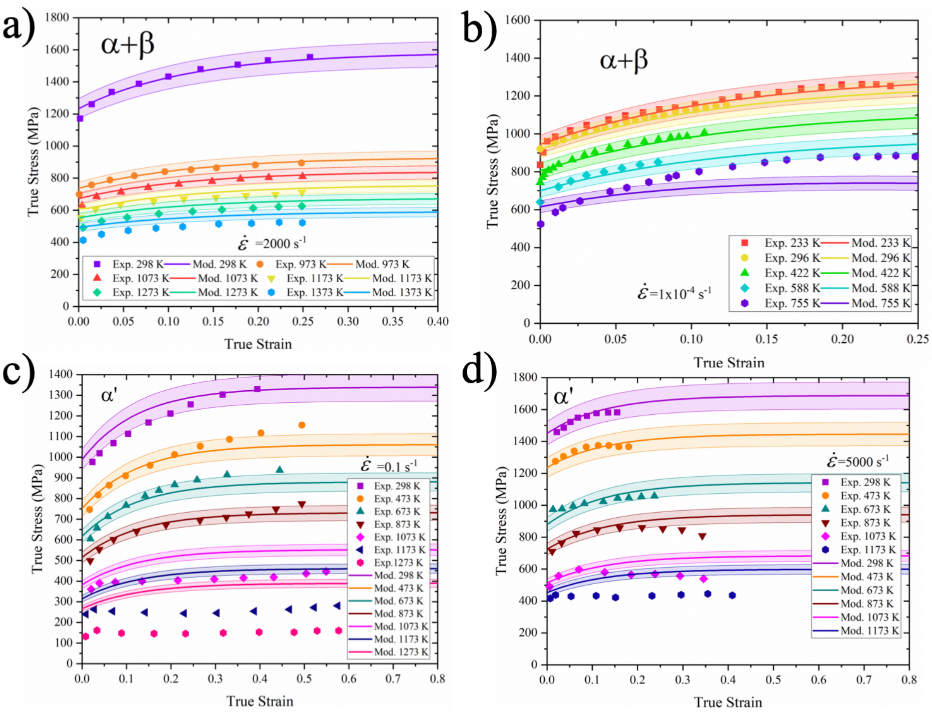


Figure 5.20 Flow stress of equiaxed structures [90, 93], (a) different temperatures and at 1x10-4 s-1 strain rate, (b) different temperatures and 2000 s-1. Flow stress of martensitic structures [159] (c) 0.1 s-1 and (d) 5000 s-1 from room temperature up to 1273 K.

Figure 5.20 showed predicted results of two distinct processing routes (C&W and AM). However, it is common practice to post heat treat [77, 83, 84, 219] and hot isostatic press (HIP) the AM components [77, 83] in order to reduce the porosities and internal stresses within the produced parts[68]. Therefore, the model was validated during progression of AM microstructures (heat treated).

### 5.3.2.3 SLM microstructures and SLM-heat treated

Figure 5.21 shows stress-strain curves of SLM as-built (orange curve), SLM heat treated at 700 ºC (red curve), 900 ºC (grey curve) and HIP-ing at 900 ºC (purple curve) and their corresponding microstructures [77]. The studied microstructural features are shown in Table 1 in Appendix B. An equiaxed structure (green curve) with its mechanical response was added to compare C&W with SLM conditions. The schematics of the microstructures are presented to show their progress during post heat treatments and their mechanical response during tensile deformation.

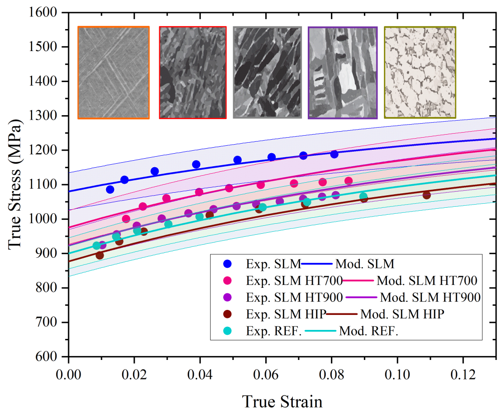


Figure 5.21 Flow stress of Ti-64 structures; SLM as-built (orange) SLM heat treated at 700 C (red), 900 C (grey) and HIP-ing at 900 C (purple) equiaxed structure (green). Micrographs adapted from[77] together with error margin of 5 % indicated by the error bands.

The as-built SLM structure displays the highest strength compared to the post heat-treated (red, grey and purple curves) and equiaxed structures. The drop in strength is due to the coarsening of laths (transition between orange to purple microstructures) as well as the decomposition of $\alpha'$ to $\alpha_s$+ $\beta$ phases [77, 80]. Together, the results show that the developed model was capable of predicting yield strength and hardening effect within the ±5% error compared with the experimental data of seven different Ti-64 microstructures (three C&W and four AM) in a wide range of deformation conditions.

## 5.4 Numerical simulation results

### 5.4.1 High strain rate simulations results

The numerical simulation for the SHPB tests were developed using the material properties in Table 5.3, whereas for the DRV-VUMAT, it was used the calibrated parameters in Table 5.2. Three set of velocities were tested, 10 m/s, 7.5 m/s and 5 m/s with expected strain rates of 2000, 1500 and 1000 $s^{-1}$ respectively.

Table 5.3 Ti-64 material properties used for SHPB simulations

| Constant | Symbol | Value | Units | Reference |
|---|---|---|---|---|
| Material density | $\rho$ | 4430 | $Kg/m^3$ | [105] |
| Young Modulus | E | 113 | GPa | [75] |
| Poisson ratio | $\nu$ | 0.33 | - | [75] |
| Specific heat | $C_p$ | 560 | J/Kg K | [105] |
| Inelastic heat fraction | I | 0.9 | - | [128] |
| Thermal conductivity | $\lambda$ | 7.3 | W/mK | [128] |
| Martensite's lath | $D_{\alpha'}$ | 0.75 | μm | Measured (Appendix B) |
| Volume fraction of martensite | $V_{\alpha'}$ | 100 | % | Measured (Appendix B) |

The simulation results for a strain rate of 2000 $s^{-1}$ are presented in Figure 5.22, where a) shows the true strain-stress simulation results (black line) against the experimental results (red line) presented in section 5.2.1.

The model's prediction is very close to the experimental data, in terms of yield strength and hardening behaviour, worth noting that the model predicts higher stresses (when strains are above 0.14) because the model does not consider failure of the material, however in reality the material already has failed after 0.14 strain.

Also, the distribution of Von-Mises stresses is presented in Figure 5. 22b, displaying the maximum values of stresses in the four corners of the cross-sectional area of the sample. The equivalent plastic strain (PEEQ) is shown in Figure 5. 22c, the centre of the sample is expected maximum value around 1.95, where the temperature is expected to increase from 300K up to 422 K as shown in Figure 5.22d and the distribution of temperature around the sample.

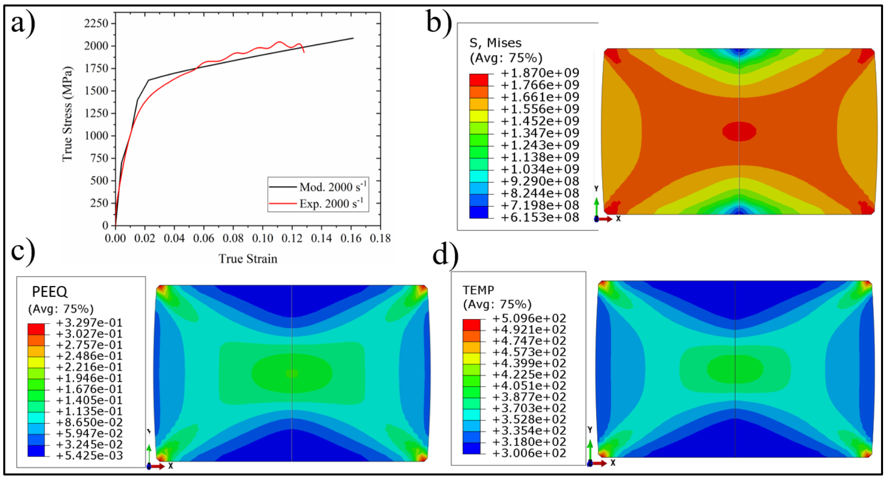


Figure 5.22 FE SHPB tests simulation at a strain of 2000 $s^{-1}$: a) flow stress-curve; line in red the experiment and black the simulation, b) Von-Mises stresses distribution, c) PEEQ distribution and d) temperature distribution.

The simulation results for a strain rate of 1500 $s^{-1}$ are presented in Figure 5.23, where a) shows the true strain-stress simulation results (black line) against the experimental results (red line) presented in section 5.2.1.

The model's prediction is very close to the experimental data, in terms of yield strength and hardening behaviour. Also, the distribution of Von-Mises stresses is presented in Figure 5. 23b, displaying the maximum values of stresses in the four corners of the cross-sectional area of the sample.

The equivalent plastic strain (PEEQ) is shown in Figure 5. 23c, the centre of the sample is expected maximum value around 1.35, where the temperature is expected to increase from 300K up to 413 K as shown in Figure 5. 23d and the distribution of temperature around the sample. The last simulation results for a strain rate of 1000 $s^{-1}$ are presented in Figure 5.24a, where a) shows the true strain-stress simulation results (black line) against the experimental results (red line) presented in section 5.2.1.

The model's prediction is very close to the experimental data, in terms of yield strength and hardening behaviour. Also, the distribution of Von-Mises stresses is presented in Figure 5. 24 b. The equivalent plastic strain (PEEQ) is shown in Figure 5. 24 c, the centre of the sample is expected maximum value around 0.9, where the temperature is expected to increase from 300K up to 363 K as shown in Figure 5. 24 d and the distribution of temperature around the sample.

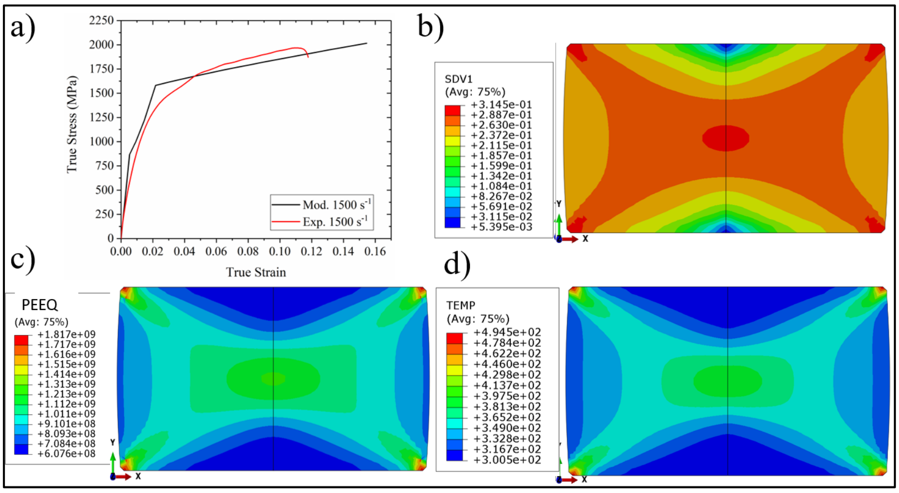


Figure 5.23 FE SHPB tests simulations at a strain rate of 1500 $s^{-1}$: a) flow stress-curve; line in red the experiment and black the simulation, b) Von-Mises stresses distribution, c) PEEQ distribution and d) temperature distribution.

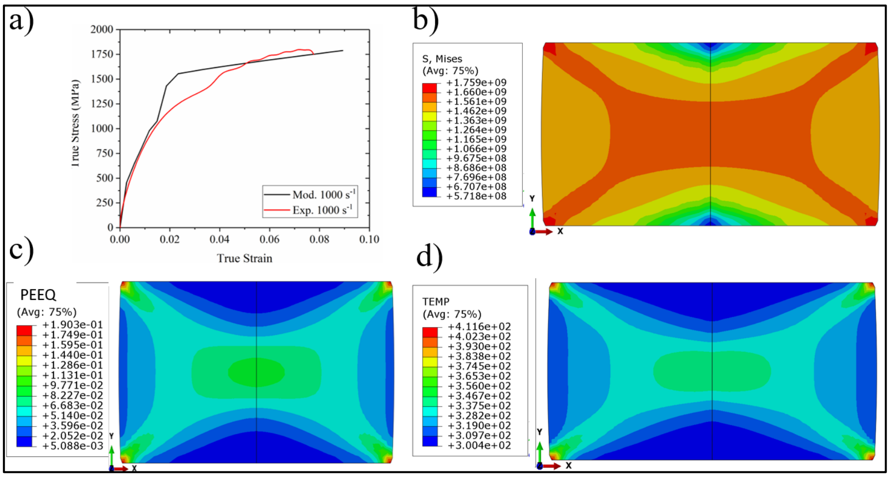


Figure 5.24 FE SHPB tests simulation at a strain rate of 1000 $s^{-1}$: a) flow stress-curve; line in red the experiment and black the simulation, b) Von-Mises stresses distribution, c) PEEQ distribution and d) temperature distribution.

The overall results shown that the DRV-VUMAT successfully predicts the SLM components plasticity behaviour at the three actual experimental conditions (three strain rates). In order to assess the DRV-VUMAT at hot deformation conditions, the next section will compare both user subroutines (DRV and DRX) with force-displacement curves acquired from the axisymmetric hot compression tests discussed in section 3.4.

### 5.4.2 Axisymmetric hot deformation simulation results

The numerical simulation for the axisymmetric hot compression tests were developed using the material properties in Table 5.3. Whereas, for the DRV and DRX VUMATs, it was used the calibrated parameters in Table 5.2. Three set of velocities were tested, 1.5 m/s, 0.15 m/s and 0.015 m/s with expected strain rates of 100, 10 and 1 $s^{-1}$ respectively.The numerical simulations were tested against force-displacement curves acquired from experimental results before converting them to flow strain-stress curves.

Figure 5.25 shows the DRV-VUMAT simulations results at a)1, b)10 and c)100 $s^{-1}$. As can be seen the subroutine does not predict accurately for the three strain rates, as the experiments displayed lower strength compared to the simulations at the four temperatures. This can be explained as for the prediction of yield strength, DRV-VUMAT only considers strengthening mechanisms such as DRV (dislocation strengthening produced by plastic deformation) and instant phase transformation from alpha to beta phase (beta phase represents higher strength compared to alpha phase), especially within1 073-1273K temperatures, whereas the followed softening is produced due to adiabatic heating. In addition, DRV-VUMAT does not consider softening due to DRX occurring during hot deformation, as result the predictions are always higher than the experiments. However, this test was used to understand the mechanisms occurring during hot deformation. Therefore, the next step was to assess the DRX-VUMAT performance.

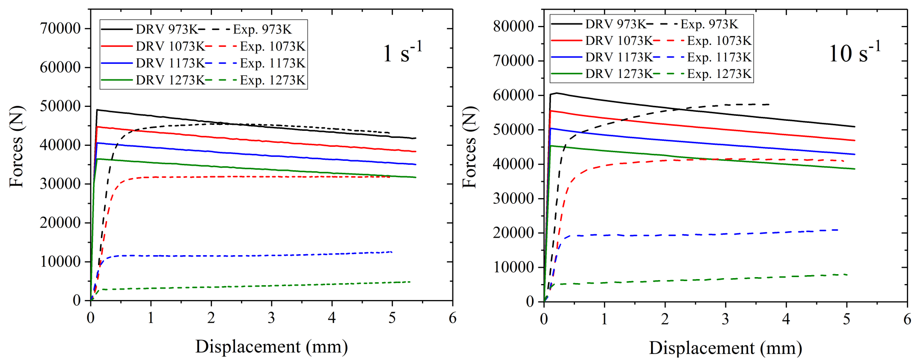

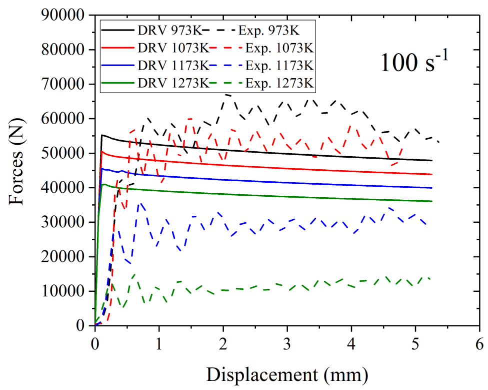


Figure 5.25 DRV-VUMAT predictions compared with experiments at: a)1, b)10 and c)100 $s^{-1}$.

Figure 5.26 shows the DRX-VUMAT predictions for same deformations as previous examination. The results shown that DRX subroutine predicts a prevailing hardening effect rather a softening due to DRX effect. This could be explained as for prediction of yield strength is mostly affected by DRX, hence lower strength is predicted. Whereas, flow stress evolves with displacement (applied strain), DRV is therefore more predominant in the force-displacement plots.

Another outcome during 1173 K, the DRX-VUMAT predicts higher strength at the lowest strain rate (1 $s^{-1}$), whereas at 100 $s^{-1}$ under predicts strength and at 10 $s^{-1}$ the prediction is reasonably the closest. A possible explanation for this is that DRV effect prevails at higher strain rates (100 $s^{-1}$), whereas at lower strain rates (1 $s^{-1}$) DRX is more predominant. As result, during 10 $s^{-1}$ condition DRV and DRX effects almost contribute on the same manner since both effects occur simultaneously.

Additionally, during 973 and 1073 K, the results shown that the DRX-VUMAT under predicts for the three strain rates. This could be explained as the current state of the DRX subroutine does not consider Ti-64 phase transformation effect. Nevertheless, in more detail will be covered the implementation of this effect in discussion section in chapter 6.

Two main outcomes from these simulations can be drawn; SLM-Ti64 does not display a softening behaviour during hot deformation, therefore both subroutines are not capable of predict accurately and there is drastic change of microstructure between temperatures 1073K and 1173K that could be attributed to martensite decomposition, however the rate it evolves is totally affected by the initial microstructure and deformation rate, therefore it will be studied in more detail this phenomenon in chapter 6.

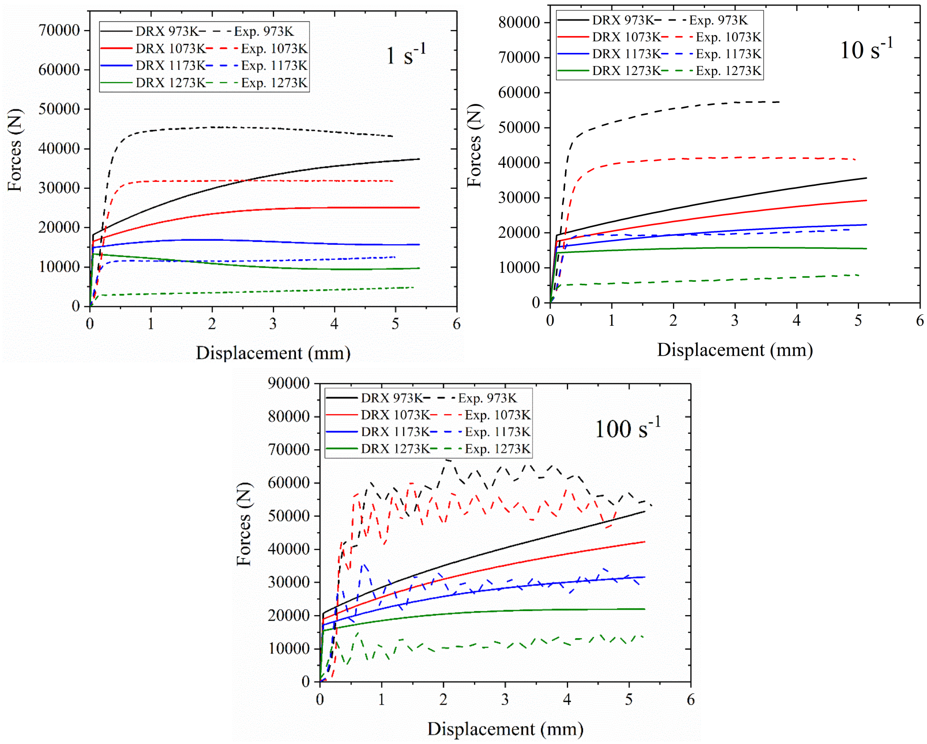


Figure 5.26 DRX-VUMAT predictions compared with experiments data at: a)1, b)10 and c)100 $s^{-1}$.

### 5.4.3 Orthogonal cutting simulation results

The chip formation simulations were developed using the material properties in Table 5.4, whereas for JC plasticity and damage initiation criterion parameters are presented in Table 5.4 and 5.5 respectively. Three set of cutting speeds were tested, 2 m/min, 4 m/min and 6 m/min and 0.1 and 0.2 depths of cut. Because the reported JC parameters for plasticity and damage reported within the literature are for C&W Ti-64, it will only be compared with the experimental C&W Ti-64 machining forces and chip morphologies shown in section 5.2.3

Table 5.4 Ti-6Al-4V material properties

| Constant | Symbol | Value | Units | Reference |
|---|---|---|---|---|
| Material density | ρ | 4430 | $Kg/m^3$ | [105] |
| Young Modulus | E | 113 | GPa | [75] |
| Poisson ratio | ν | 0.33 | - | [75] |
| Specific heat | $C_p$ | 560 | J/Kg K | [105] |

| | | | | |
|---|---|---|---|---|
| Inelastic heat fraction | I | 0.9 | - | [128] |
| Thermal conductivity | λ | 7.3 | W/mK | [128] |

Table 5.5 Johnson-Cook plasticity model for Ti-6Al-4V

| Material | A (MPa) | B (MPa) | C | n | m | $\dot{\varepsilon}_0$ ($s^{-1}$) | Reference |
|---|---|---|---|---|---|---|---|
| Ti-6Al-4V | 968 | 380 | 0.0197 | 0.421 | 0.577 | 1 | [105] |

Table 5.6 Johnson-Cook damage initiation criterion for Ti-6Al-4V

| Material | $d_1$ | $d_2$ | $d_3$ | $d_4$ | $d_5$ | Exponential law parameter | Reference |
|---|---|---|---|---|---|---|---|
| Ti-6Al-4V | -0.09 | 0.25 | -0.05 | 0.014 | 3.87 | 0.5 | [105] |

Figure 2.27 shows the distribution of the Von-Mises stresses, equivalent plastic strains (PEEQ) and temperatures for the simulation results with a 0.1 mm depth of cut. Typical serrated chips were achieved for 4 and 6 m/min cutting speeds, whereas 2 m/min condition shown an irregular shape chip. The temperature increase within adiabatic shear zones for the three conditions was around 873K (600K increase), whereas the PEEQ was around 18.5 and the maximum stresses were in the shear zone with around 1.4 GPa. Sever deformation is present during 2 and 4 m/min creating the material fail prematurely, even much before the chip is generated.

Whereas, Figure 2.28 shows the simulation results with a 0.2 mm depth of cut. The results shown fragmented chips for all conditions. This could be explained as the exponential law parameter within the JC damage initiation criterion triggers faster the deletion elements due to the high amount of stresses found in the shear zone, as result, the stresses level maintains in somehow same than the ones reported at 0.1 mm depth of cut. PEEQ levels were reduced considerably up to half of the ones reported at 0.1 mm depth of cut (roughly 9.5), whereas temperature increase due to adiabatic heating effects was also reduced up to 504 K (230 K increase). From these results can be stated that the damage initiation criterion is very important to predict chip's morphology specially at higher depths of cut. Moreover, the exponential law parameter plays a key role during simulations as this value will determine the stress levels at specific time when the chip starts forming, however in more detail this parameter will be explored in more detail in next chapter.

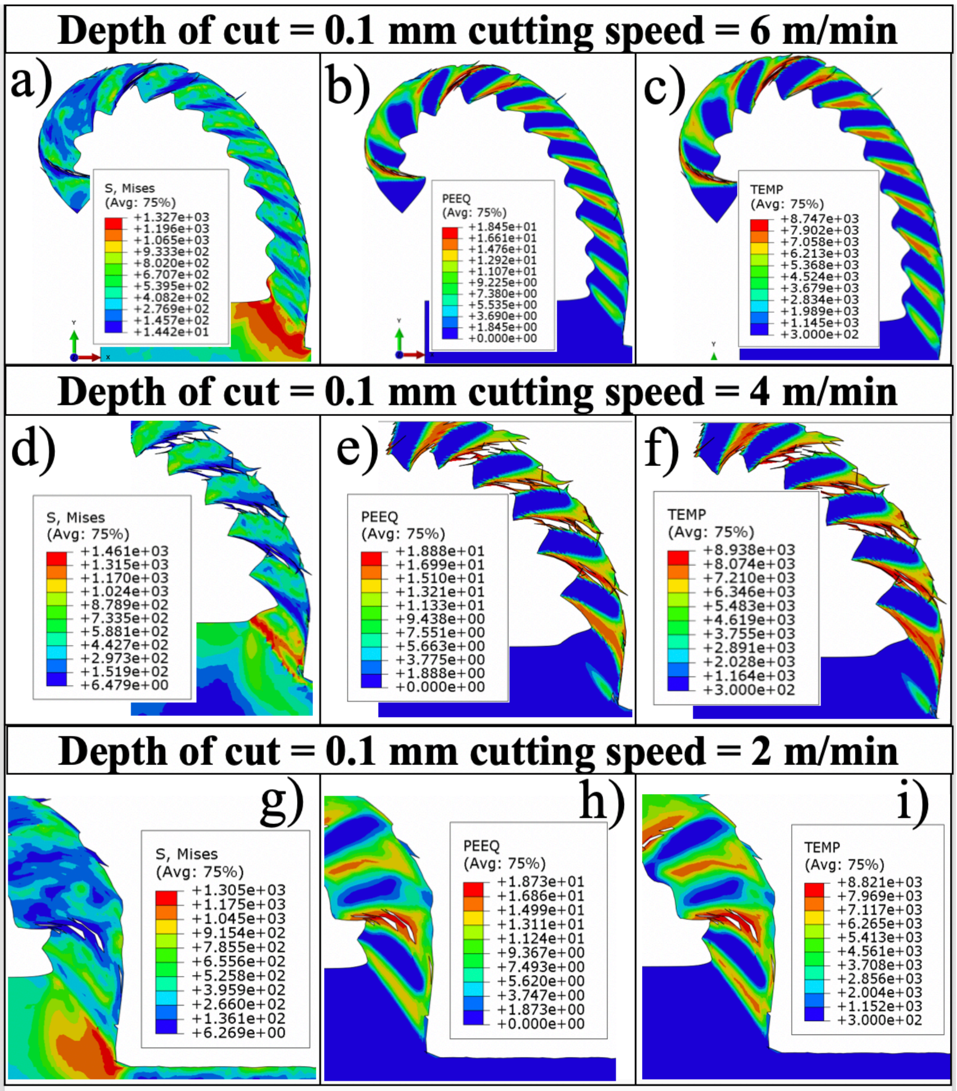


Figure 5.27 Chip formation Von-Mises stresses, PEEQs and temperature distribution during 0.1 mm depth of cut

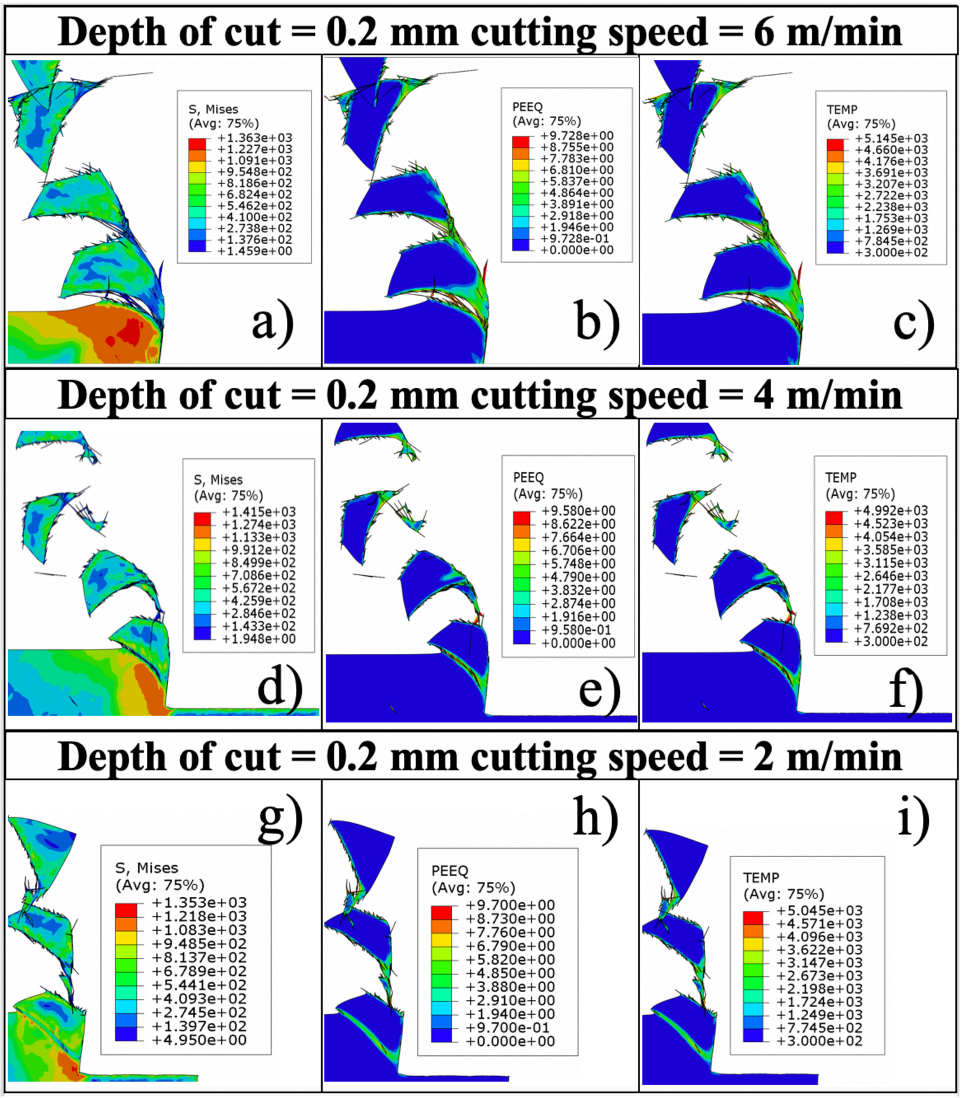


Figure 5.28 Chip formation Von-Mises stresses, PEEQs and temperature distribution during 0.2 mm depth of cut

### 5.4.3.1 Cutting forces prediction

An example of the predicted cutting and thrust forces during 6 m/min and 0.1 mm is presented in Figure 5.29. In order to post-process the simulated machining forces, it was used the RMS value of the predicted forces, exactly the same strategy as the experimental forces.

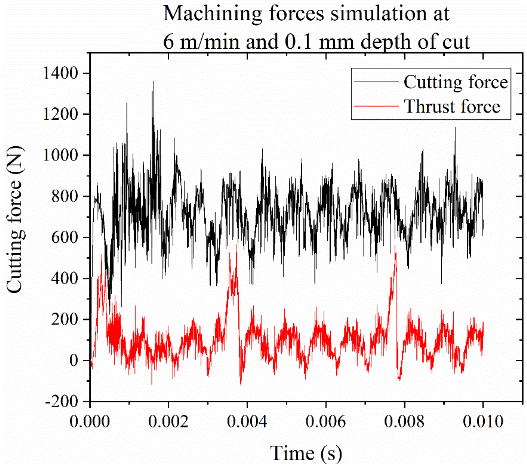


Figure 5.29 Example of machining forces

Figure 5.30 shows the predicted a) cutting and b) thrust forces in solid lines together with error bars displaying the plus-minus ten percent error, whereas the experimental measured forces are also presented in dotted lines next to each simulation. Results of simulation of cutting forces (Figure 5.30 a) shown lower values in the six cutting conditions studied. The biggest difference with the experimental data was displayed during 0.2 mm depth of cut and 6 m/min giving a value of 1732.3 N, whereas the experiment value was 2285.3 N (around 35% less than forces than the experiment). The closest predicted cutting forces recorded were during the lowest speed and smaller depth of cut (2 m/min and 0.1 mm depth of cut) giving a value of 521.1 N (25% less than experimental values).

Predicted thrust forces shown in Figure 5.30b, displayed significant amount of discrepancy with the experimental results during all cutting conditions. Similarly, to smaller depth of cut, the biggest discrepancy with the experimental data was displayed during 0.2 mm depth of cut and 6 m/min with 1675 N experimental data and 1103.5 N predicted force (35% less). Whereas, the closest predicted cutting forces recorded were during the lowest speed and smaller depth of cut (2 m/min and 0.1 mm depth of cut) giving a value of 202.1 N (55% less than experimental values).

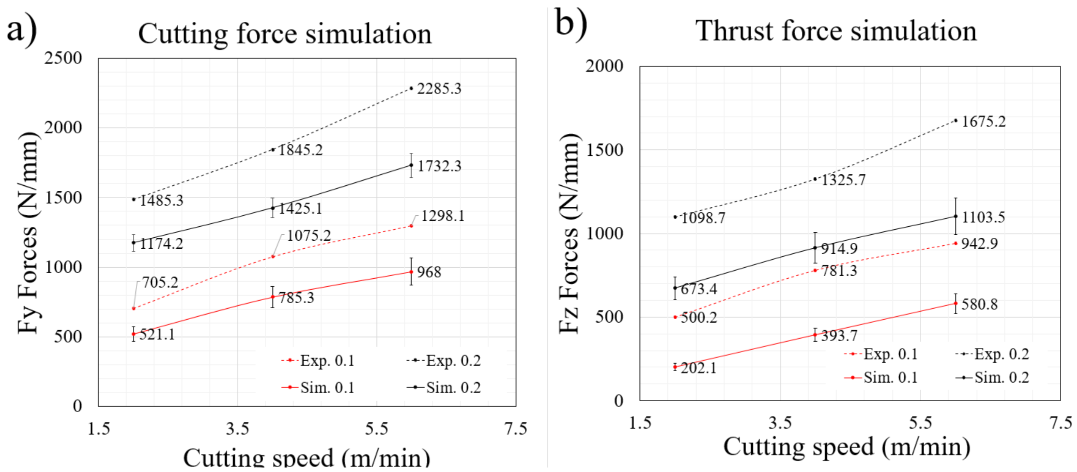


Figure 5.30 FE simulated machining: a) cutting and b) thrust forces

### 5.4.3.2 Chip morphology prediction

To assess the chip morphology, it was used the measuring tool in Abaqus to measure between nodes. Figure 5.31 shows an example of a resulted chip during 0.1 mm depth of cut and 6 m/min cutting speed. Two distances were measured; d1 which is the distance between serrations and d2 that is the chip's thickness and was measured from the root up to the peak of the chip.

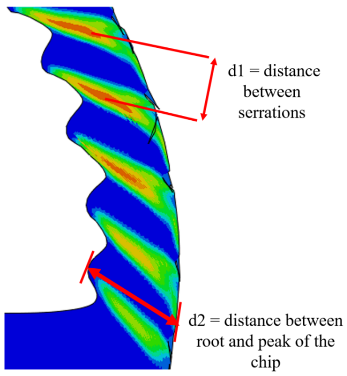


Figure 5.31 Measurement procedure for the simulated chips

Tables 5.7 and 5.8 show the measurement recorded for 0.1 and 0.2 depth of cut respectively. Also, it is presented the C&W measured chips presented in section 5.2.3. The overall results shown that are within less than the 20% error. It was found that predictions at 0.2 mm depth of cut are closer to the experimental data. The smallest error is reported in Table 5.7 for 0.1 mm depth of cut and 6 m/min with an error of 4.84%.

Table 5.7 Predicted chip morphology at 0.1 mm depth of cut

| Cutting speed (m/min) | Exp. D1 (mm) | Predicted D1 (mm) | D1 Error (%) | Exp. D2 (mm) | Predicted D2 (mm) | D2 Error (%) |
|---|---|---|---|---|---|---|
| 2 | 0.052 | 0.0832 | **19.23** | 0.155 | 0.148 | **21.94** |
| 4 | 0.041 | 0.0701 | **19.51** | 0.132 | 0.138 | **15.91** |
| 6 | 0.037 | 0.0657 | **18.92** | 0.124 | 0.125 | **4.84** |

Table 5.8 Predicted chip morphology at 0.2 mm depth of cut

| Cutting speed (m/min) | Exp. D1 (mm) | Predicted D1 (mm) | D1 Error (%) | Exp. D2 (mm) | Predicted D2 (mm) | D2 Error (%) |
|---|---|---|---|---|---|---|
| 2 | 0.122 | 0.150 | **21.31** | 0.241 | 0.358 | **17.01** |
| 4 | 0.111 | 0.126 | **13.51** | 0.235 | 0.276 | **20.70** |
| 6 | 0.092 | 0.105 | **14.13** | 0.228 | 0.196 | **14.04** |

## 5.5 Summary

This section aimed to present the experimental and modelling results of this research. The experimental results were divided in two main areas; mechanical testing and machining trials.

The SHPB tests shown that Ti-64 SLM components possess low ductility. This was confirmed through fast camera footage, true strain-stress curves displaying less of 13.5% elongation. The axisymmetric hot compression results shown that Ti-64 SLM components possess a characteristic flow stress behaviour during high temperatures, this was found due to microstructure evolution as the fully martensitic microstructures decompose in a complex process as follows: $\alpha' \Rightarrow \alpha"_{lean} + \alpha"_{rich} \Rightarrow \alpha + \beta$. Therefore, SLM components did not display any flow softening behaviour characteristic of metals during hot deformation due to dynamic recrystallisation.

Machining trials revealed that SLM components produced higher machining forces compared to C&W Ti-64 samples in all cutting conditions (around 15% force). Two SLM types of samples were tested; vertically and horizontally built. The last one exhibited the highest machining forces (in the three force components), followed by vertically built and C&W samples.

On the modelling side, the new physically-based model was assessed and calibrated with experimental data reported within the literature, first the yield strength predictions were presented followed by the flow stress predictions. Results shown that the model is capable to predict within less than 5% error for yield strength whereas the flow stress predictions shown within less than 10%.

Three FE models where developed for validation of the new proposed model. First it was shown the results of the user subroutine DRV-VUMAT for SHPB tests, showing high accuracy to predict the hardening effect due to high impact tests. Following by the FE axisymmetric model, DRV-VUMAT and DRX-VUMAT shown high discrepancy with the experimental force-displacement curves, this was found due to neither DRV nor DRX effects commonly displayed by C&W Ti-64 alloys, instead an increase of strength was found due to progression of the microstructure (i.e. constitutive phases).

The last FE model consisted in 2D orthogonal cutting using embedded JC plasticity and damage initiation criterion, results shown that the model under predicts cutting and thrust forces reported for C&W alloy for all conditions. Subtracting the model's chip morphologies prediction from the experimental value and divided by the experimental value and finally multiplying by one hundred, the values suggest that the model predicts under 20% error for all conditions. These results suggest that the model predicts accurately chip morphologies at the expense of low machining forces.

Next chapter will treat the discussion for both, experimental and modelling results. Several sensitivity analyses will be presented for the three FE models in order to assess in more detail their capabilities. First it will be presented for SHPB followed by hot deformation axisymmetric tests. Special efforts will be put on the last one since the implemented subroutines were not able to describe the actual phenomenon occurring. This will be achieved by microscopy analysis and reported data for C&W alloys in order to understand the discrepancy of the model and tune it in order to predict more accurately.

# 6. Discussion

## 6.1 Introduction

This chapter covers the discussion for the experimental and modelling results presented in chapter 5. First, it will be discussed the SHPB experimental followed by the modelling results, showing an analysis of the modelled samples and the distribution of the physical mechanisms occurring during plastic deformation at these high speeds. Afterwards, the hot deformation discussion consists in characterisation analysis of deformed samples followed by a sensitive analysis of the model's prediction and modification of the proposed model for high temperatures for both C&W and SLM Ti-64.

## 6.2 Analysis of SHPB modelling results

To study in more detail the performance of the model, it was used an extra simulation to study the evolution of initial dislocation density and its contribution to the Ti-64 strength during 2000 $s^{-1}$ condition. Figure 6.1 shows the distribution of a) Von-Mises stresses and b) the stresses due to dislocation evolution ($\sigma_{dis}$) both in Pa.

As can be seen in Figure 6.1b the strength to dislocation evolution is mostly distributed in the centre of the sample (red area and about 275-293 MPa) creating an "X" shape through the sample. Whereas, the lowest values were distributed in top and bottom of the centre of the sample (blue are and about 76-94 MPa). If it is subtracted $\sigma_{dis}$ to the current Von-Mises stresses within the centre of sample (red area and around 1550 MPa) it can be found that the contribution due to dislocation evolution (293 MPa) is around 18.9% of the total strength of the material. As result, forest hardening is very important to be consider specially during high speed processes such as machining.

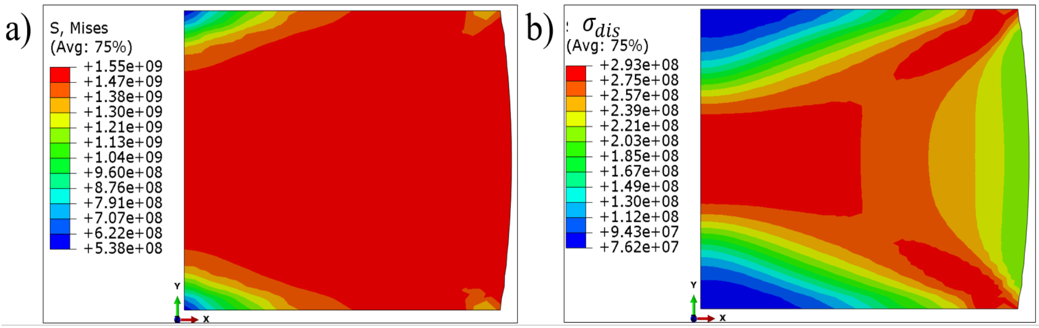


Figure 6.1 Forest hardening distribution: a) Von Mises stresses b) stresses due to dislocation evolution at 2000 $s^{-1}$.

The $\sigma_{dis}$ are highly affected to dislocation evolution due to DRV ($\rho_{DRV}$). However, this evolution is not homogenous through the entire sample as shown in Figure 6.1. Therefore, Figure 6.2a shows the distribution of $\rho_{DRV}$ together with four localised points for further analysis. As can be seen in this plot, two main areas are subjected to sever deformation (P1 & P4), whereas P2 & P3 are within intermediate values. Figure 6.2b shows the plot of $\rho_{DRV}$ against time for the four points selected. Additionally, it is presented the Kocks-Mecking equation, which is the rate of $\rho_{DRV}$ evolves. At the beginning of the simulation the material was considered with homogenous dislocation distribution ($1.7 \times 10^{13}$ $m^{-2}$), however during plastic deformation, P4 displayed a faster and higher evolution ($9.04 \times 10^{14}$ $m^{-2}$) due to boundary conditions, followed by P1 which displayed the second most affected zone ($8.11 \times 10^{14}$ $m^{-2}$).

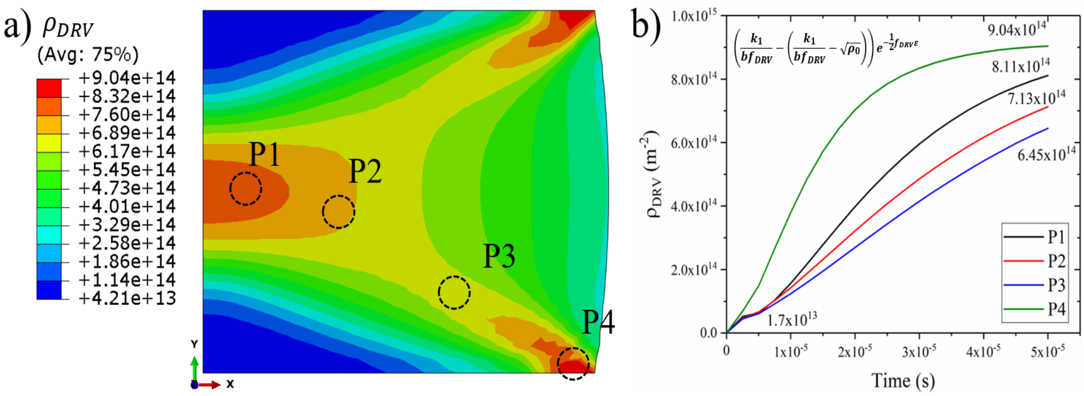


Figure 6.2 Dislocation evolution: a) distribution and b) evolution through time of simulation.

To better understand the distribution of $\rho_{DRV}$ through the samples, Figure 6.3 shows; a) $\sigma_{dis}$ distribution and b) $\sigma_{dis}$ distribution with elements removed with less of 206 MPa contribution. From the cross-sectional area, it can be seen that most of the interaction of dislocations occurs in the zone in form of “X”, whereas a minimum interaction occurs on both, top and bottom surfaces and external cylindrical faces.

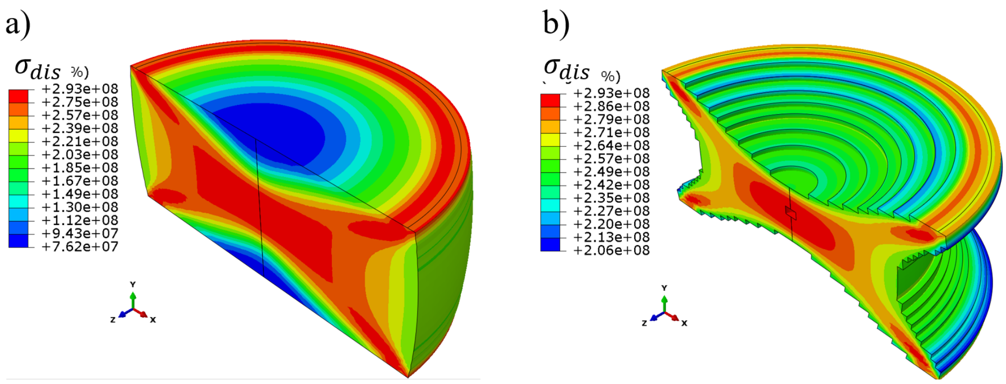


Figure 6.3 $\sigma_{dis}$ distribution: a) contribution through full sample and b) contribution of the elements with higher stresses above 205 MPa.

## 6.3 Axisymmetric hot deformation modelling analysis

### 6.3.1 Experimental results analysis

The results of the DRX-VUMAT discussed in section 5.4.2 shown that current state of the model does not reflect the actual physical phenomenon occurring during hot deformation of SLM Ti-64. The experimental results revealed a hardening effect during the three strain rate studied, moreover it was presented the micrographs for the deformed samples at four different temperatures and at a strain rate of 100 $s^{-1}$. Results shown that SLM Ti-64 martensitic structures undergo through a phase transformation; however, it was required more extensive analysis to validate previous results. Therefore, it was examined in more detail through selective electron microscopy the deformed samples for the remaining strain rates.

Figure 6.4 shows the deformed microstructures at a strain rate of 1 $s^{-1}$ and temperatures of a) 973K, b)1073K, c)1173K and d)1273K. Where, 973K temperature shows fine particles inside the thin alpha laths, however in the next temperature (1073K) apparently, they disappear. Going higher temperatures, the alpha laths started to grow (1173K) until decomposition of martensite is accomplished at 1273K, producing even a thicker lath. These results are similar to the 100 $s^{-1}$ reported in section 5.2.2, however due to low strain rate (Figure 6.4), hence longer time of residence in the machine, the resulted microstructure at 1273 K displayed higher lath thickness compared to 100 $s^{-1}$ condition.

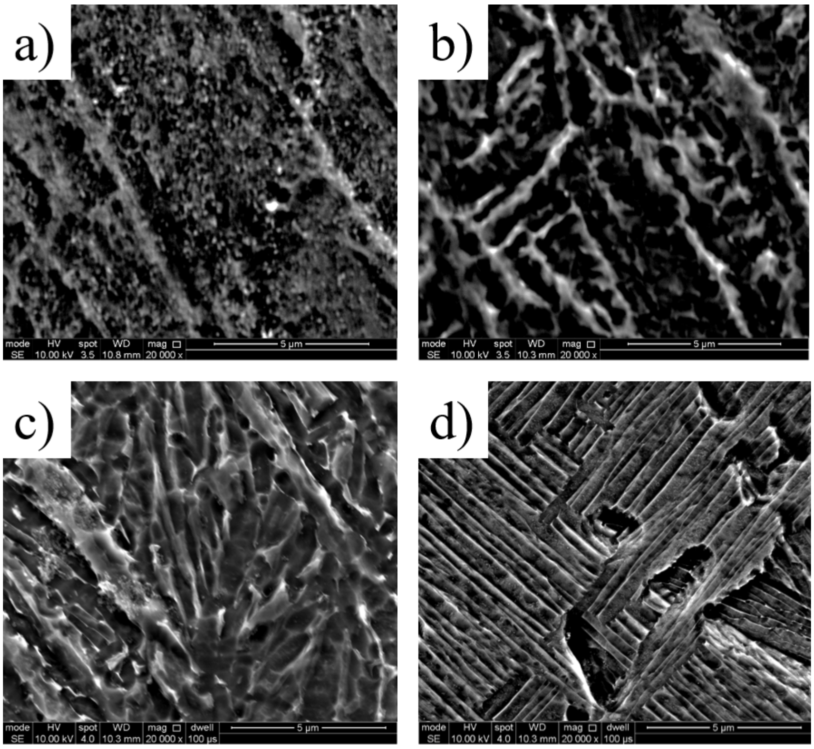


Figure 6.4 SEM micrographs during hot deformation at 1 $s^{-1}$ at: a,) 973K, b)1073K, c)1173K and d)1273K

Figure 6.5 shows the last condition considered at a strain rate of 10 $s^{-1}$ and temperatures of a) 973K, b)1073K, c)1173K and d)1273K. As can be seen, the 973K temperatures displays again white particles within the alpha laths, whereas 1073 and 1173K displayed grain growth with no apparent evidence of white particles. Surprisingly at 1273K, particles appeared again, even coarser. Therefore, it was used higher magnification to study the 10 $s^{-1}$ and 1273K condition.

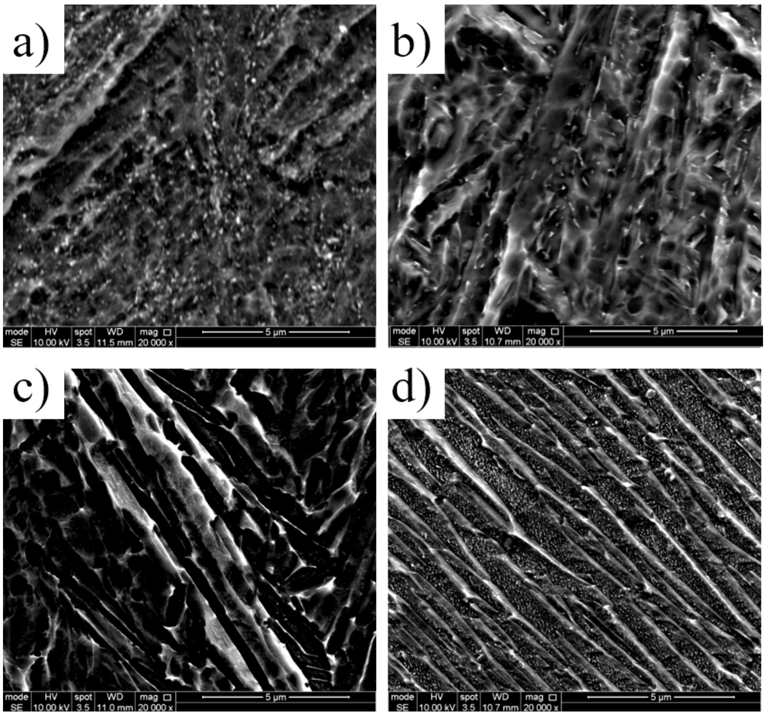


Figure 6.5 SEM micrographs during hot deformation at 10 $s^{-1}$ at: a,) 973K, b)1073K, c)1173K and d)1273K

Figure 6.6 shows a higher magnification of a) 60,000x and b) 214,815x for 10 $s^{-1}$ and 1273K deformation condition. As can be seen from micrograph in Figure 6.6b; the increase of the white precipitates completely filled the alpha laths, creating a different microstructure compared to other deformation conditions. The white precipitates ranging from 20 to 50 nm provided drastic increase of material's strength as shown in Figure 6.6c (dotted red square). Worth to mention that this condition displayed the highest strength and conversely the lowest ductility for the twelve deformation conditions.

It has been reported by Ivasishin et al. [3, 220], that α' decompose through aging creating the orthorhombic α'' martensite phase in binary Ti-7%Mo alloys, creating a drastic increase in yield strength. Authors described the phenomenon as disordered, solute rich zones becoming stronger obstacles to dislocation motion. Also, due to drastic increase of volume fraction of these precipitates, the material suffers low ductility on a macroscopic point of view.

The early report from the 50's during that time was found with limited relevant to commercial titanium alloys, however due to the development of AM technologies is becoming more and more relevant the study of mechanism of martensite formation in titanium alloys and its relationship to mechanical properties.

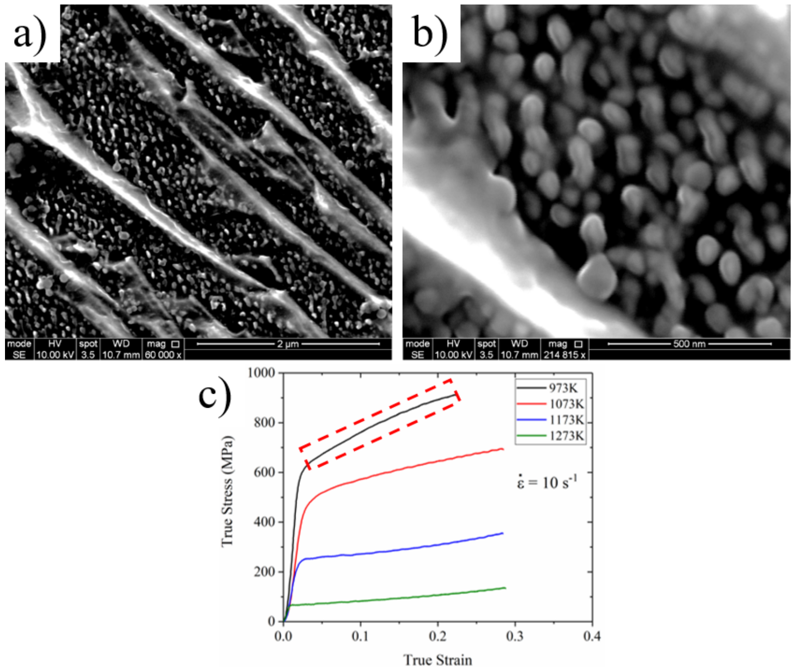


Figure 6.6 Precipitation hardening: a and b) SEM micrographs at 10 $s^{-1}$ and 1273K, c) mechanical response (dotted red square)

With the compiled data of the four temperatures and three strain rates, Figure 6.7 presents the processing map of SLM-Ti-64 during hot deformation. In the horizontal axis is presented temperature and on the vertical axis strain rate. Together with the SEM micrographs for all the conditions tested. Also, it is shown the micrographs surrounded by red and blue squares, where red colour shows the conditions where precipitation takes place and in blue displays the conditions where the material suffered from martensite decomposition and grain growth.

In total, five conditions were found with precipitated, with four of them prevailing at the lowest temperature (973K), whereas the extreme precipitation effect was found at isolated case of 1073 K and 10 $s^{-1}$, this shows clearly a competence of effects between martensite phase decomposition and precipitation of beta phase displaying a totally modulated microstructure.

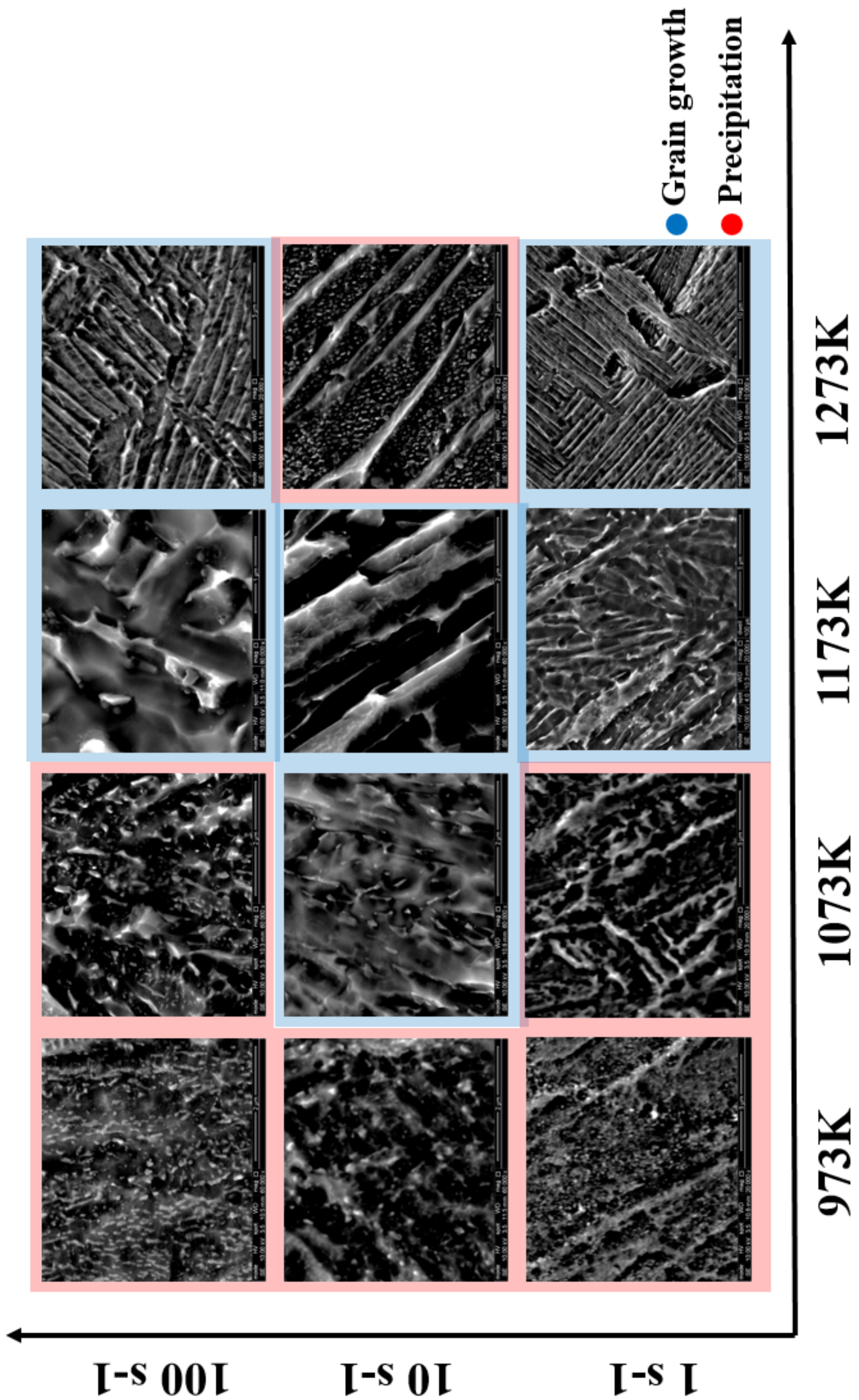


Figure 6.7 Process map of SLM ti-64 during hot deformation

### 6.3.2 Modelling results analysis

In order to incorporate precipitation effect in equation 4.22, it is removed the term of DRX, therefore only phase transformation is considered. Leading to the already presented equation 4.16, however instead of describe DRV effects into flow stress, it describes the precipitation effects, as follows:

$$\bar{\sigma}_{precip} = \left(\sigma_0^\alpha + \frac{k_{HP}}{\sqrt{D_\alpha}}\right) G_\alpha V_\alpha + \sigma_0^\beta G_\beta (1 - V_\alpha) + 0.3M\mu b\left[\left(\frac{k_1}{bf_{DRV}}\left(\frac{k_1}{bf_{DRV}} - \sqrt{\rho_0}\right)\right) e^{-\frac{1}{2} f_{DRV}\varepsilon}\right]$$

Equation 6.1

Worth noting that Equation 6.1 is the same as Equation 4.16, however in order to avoid confusion it has been changed the resulted flow stress for $\bar{\sigma}_{precip}$. Where, Taylor's equation describes the hardening behaviour due to dislocation evolution and the first (Hall-Petch-type) describes the phase transformation.

In order to predict accurately yield strength of Ti-64 SLM during hot deformation (first term on Equation 6.1), it was required to calibrate the activation energies for both phases ($G_\alpha$ $G_\beta$) presented in Equations 4.23 and 4.24 respectively, where $\kappa_\alpha$ and $n_\alpha$ are materials constants related to $\alpha$ phase contribution and were adjusted to hot deformation of Ti-64 experimental data reported in [23, 88, 212] giving values of 0.4 and 0.23, respectively. $\kappa_\beta$ and $n_\beta$ are materials constants related to $\beta$ phase contribution.

These constants were adjusted using hot deformation experimental data for four near-$\beta$ alloys (Ti-5Al—5M0-5V-1Cr-1Fe, Ti-1300, Ti-40, Ti-10AV-2Fe-3Al) reported in [34, 213-215] giving $\kappa_\beta$ and $n_\beta$ values of 2.8 and 0.088, respectively. The trigger function used to predict the instantaneous volume fraction value was determined by Equation 4. 26.

After calibrating the model, it was compared the prediction results against the experimental data. Figure 6.8 shows the experimental yield strength against its prediction. The twelve deformation conditions are predicted within the ±5% error (dotted red line in the centre of the plot). As can be seen from this figure, the model successfully predicts the precipitation behaviour due to increase of temperature, therefore, the next step was to compare the flow stress predictions against the experimental data.

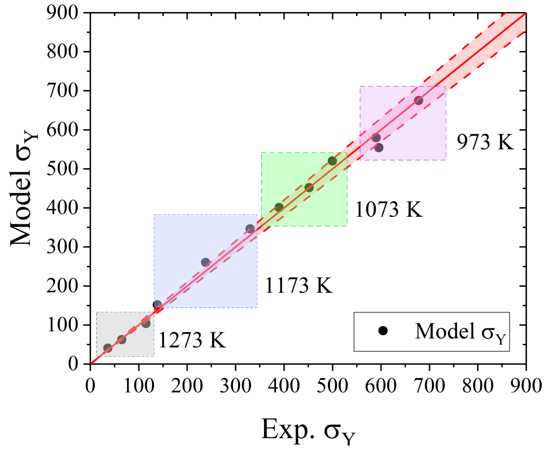


Figure 6.8 Yield strength prediction against experimental data during hot deformation of Ti-64 SLM

The flow stress predictions for Equation 6.1 are presented in Figure 6.9 for strain rates of a) 1 b) 10 and c) 100 $s^{-1}$ and the four tested temperatures. Also, it is presented coloured areas representing the ±5 % error.

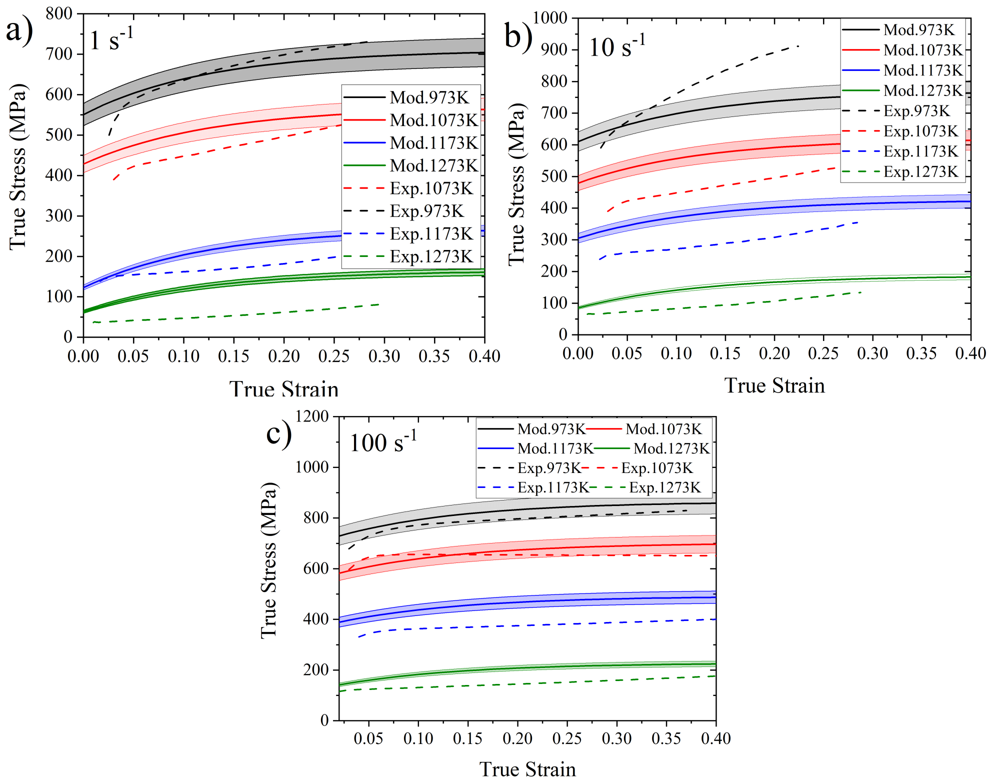


Figure 6.9 $\bar{\sigma}_{precip}$ prediction for: a) 1, b) 10 and c) 100 $s^{-1}$ at 973 up to 1273K

The closest $\bar{\sigma}_{precip}$ predictions were achieved during the highest strain rate (100 $s^{-1}$), whereas the highest mismatch with experimental data was presented during 10 $s^{-1}$. This could be explained as the trigger function (Equation 4.26) updates the volume fraction of the constitutive phases by only considering temperature, whereas in reality phase transformation also requires time for diffusion-nucleation and finally growth.

That is why during 100 $s^{-1}$, the event occurs so fast that there is no drastic evolution in the microstructure during deformation, whereas during 1 $s^{-1}$ the model is capable to capture the hardening effect at 973 and 1073, however at higher temperatures, the material displayed a hardening behaviour ~0.15 strain, this could be related to first martensite decomposition at the beginning of plastic deformation, once the material reaches ~0.15 strain,  precipitation occurs within the fresh alpha phase plates, hence the model updates volume fraction faster than in reality is happening.

Similar results were achieved for 10 $s^{-1}$ condition, the model predicts higher yield strength during 1073, 1173 and 1273K, as the model only considers temperature and not time, however at 973K, the model predicted the closest value for yield strength for this condition, this could be attributed to the high-volume fraction of precipitation in the material, this is confirmed as for all strain rates at 973K precipitates were present in all samples.

These results shown that the performance of the model is effective at the highest and lowest strain rates, whereas the intermediate strain rate (10 $s^{-1}$) displays high discrepancy compared with the experimental results. Specifically, at this strain rate the SLM Ti-64 alloy displayed a competence between precipitation and martensite decomposition (as shown in the processing map in Figure 6.7), as result the model suffers from a delay on the prediction of the constitutive phases during hot deformation.

The modified model, $\bar{\sigma}_{precip}$was implemented into VUMAT subroutine in Abaqus to study the distribution of phases through the deformed samples. Also, the numerical simulations were tested against the force-displacement curves acquired from experimental results.

Figure 6.10 shows the predictions of PRECIP-VUMAT. As expected, the best results were achieved during 100 $s^{-1}$ during the four temperatures (Figure 6.10c), whereas for 1 $s^{-1}$ condition (Figure 6.10a), at temperatures of 973 and 1073K, the PRECIP-VUMAT predicts reasonable correct, while 1173K, there is the highest discrepancy of not only this strain rate but for all simulations, this could be explained due to the adiabatic heating effect implemented in the model; by increasing the mechanical work, the temperature will increase, hence the trigger function of alpha phase updates the volume fraction automatically as result the model will predict higher volume fraction of precipitates, hence higher strength as shown in Figure 6.10a.

Also, at the same strain rate, at 1273K, the model predicts reasonable correct at the beginning of plastic deformation, however through displacement the error increases, as the model again predicts higher volume fraction of precipitates, whereas in reality the material suffers from martensite decomposition and grain growth, hence the level of stresses maintains constant adjusting the strain energy itself.

Surprisingly, the numerical results for 10 $s^{-1}$ strain. rate displayed better results than the calibrated flow stress curves used to develop the model in Figure 6.9. This may be explained due to adiabatic effect incorporated in the PRECIP-VUMAT, as explained previously the model predicts the updated volume fraction as a function of temperature only, which in this case the simulation s reflects more reliable results due to faster rate of precipitates generation.

Worth noting at the end of the simulations (displacement 5.25 mm) during 973 and 1073K the subroutine creates a peak of force, exactly the same as the actual flow stress curves of the experiments (both samples failed before 4 and 5 mm respectively). This could be attributed due to premature failure of the material at the actual experiments creating cracks in the material, however as the current state of the subroutine does not consider failure, hence the model crashes just at the end of the simulation as the levels of stresses are too high.

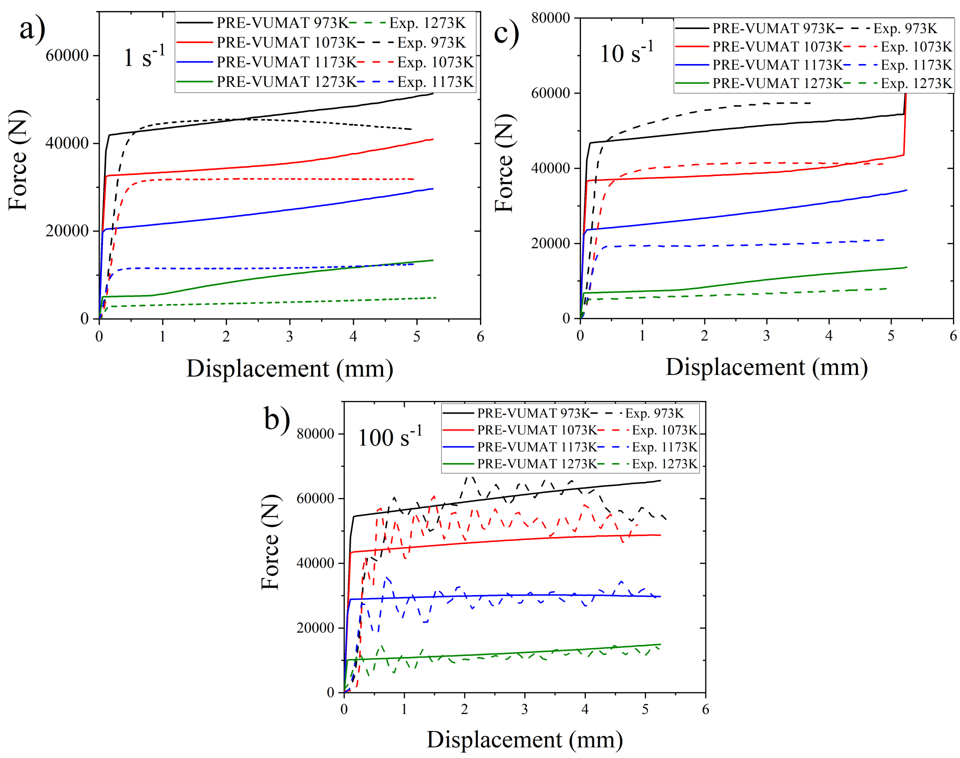


Figure 6.10 PRECIP-VUMAT predictions compared with experiments at: a)1, b)10 and c)100 $s^{-1}$.

Figure 6.11 shows an example of the simulated distribution of the deformed sample at 100 $s^{-1}$ and 973K. Figure 6.11a shows the Von Mises stresses distribution in Pascals, displaying the lowest distribution of stresses in the centre of the sample (roughly 469 MPa).

Figure 6.11b shows the PEEQ distribution, where the highest strains are found in the both end corners of the sample (1.06), whereas in the centre is around 0.8. Figure 6.11c shows the distribution of stress due to dislocation evolution in MPa, displaying the maximum values of roughly 35.2 MPa, on top surfaces of the sample whereas in the centre displaying a maximum of 26.1 MPa. As can be seen from the last image, the contribution to strength due to dislocation evolution is very low compared to SHPB simulations.

Figure 6.11d the increase of temperature in Kelvin degrees due to adiabatic heating effects, as it is shown in this figure, the maximum temperature increase was found in the centre of the sample giving 1170K (~200K increase). Due to this increase on temperature, the volume fraction of alfa in percentage evolved as shown in Figure 6.11e through the deformed sample.

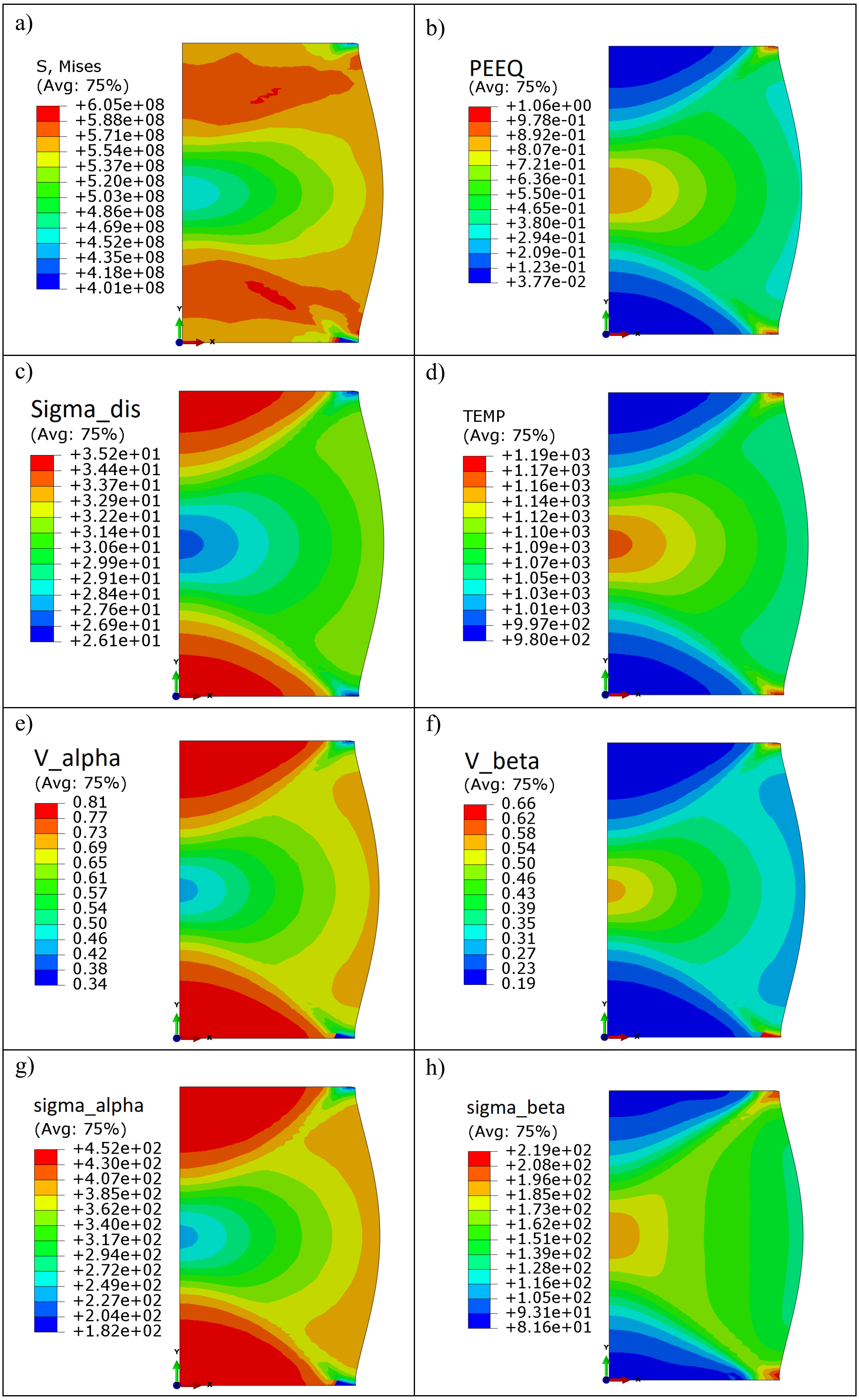


Figure 6.11 PRECIP-VUMAT simulated distribution at 973K and 100 $s^{-1}$

Similarly, Figure 6.11f shows the instantaneous volume fraction of beta in percentage, as can be seen from both images, there is an equilibrium of both phases in the centre (roughly 50% each phase). The solid solution contribution of both phases ($\sigma_0^\alpha$ $\sigma_0^\beta$) to Ti-64 SLM strength and in MPa are presented in Figures 6.11g and h respectively. As can be seen from both figures, at the centre of the sample both phases contribute with similar values, i.e. alpha phase with 250 MPa whereas beta phase 196 MPa.

To understand the evolution of constitutive phases through time, Figure 6.12 shows a plot of time (horizontal axis) against time (left vertical axis in the left side), PEEQ (green vertical axis in the right side), volume of alpha (blue vertical axis in the right side) and volume of beta (magenta vertical axis in the right side).

As can be seen from this plot, when temperature increases (red line), alpha phase decreases rapidly (blue), while beta phase increases at the same rate (magenta line). For instance, at the time 0.00025s the model predicts a temperature of 985K, PEEQ of 0.05188, volume of alpha 80% and beta 19.6% and as plastic deformation occurs during time, just in the middle of the simulation (or 2.7 mm displacement) the model predicts a temperature of 1080K, a PEEQ of 0.48, volume alpha and beta 65% and 35% respectively. Until the deformation is completed at 0.0035 seconds the resulted values were presented in Figure 6.12.

.

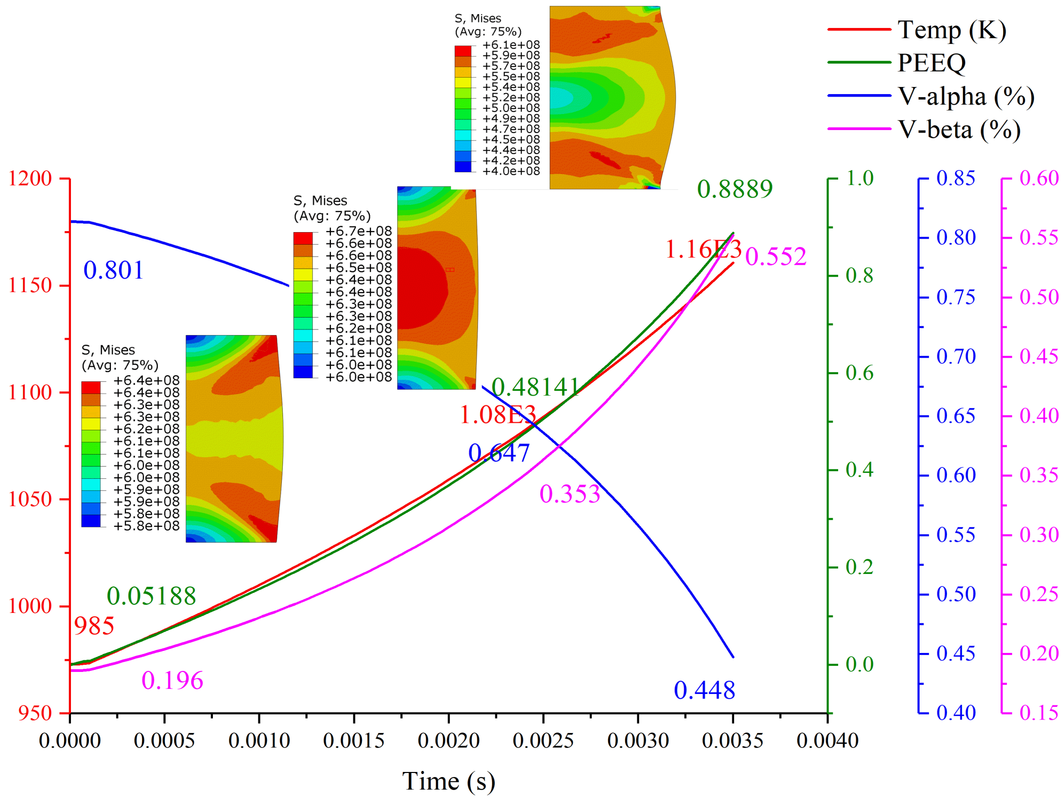


Figure 6.12 Phase transformation through time during 973K and 100 $s^{-1}$

In order to develop a single expression that could describe both, C&W and SLM Ti-64 plastic deformation at high temperatures, it was modified Equation 4.22 (DRV+DRX), where instead of only consider DRV effects, also phase transformation occurs simultaneously, therefore combining Equation 4.22 and 6.1 gives the new expression for C&W deformation as follows:

$$\bar{\sigma} = \bar{\sigma}_{precip}(1 - V_{REX}) + \bar{\sigma}_{DRX}V_{REX}$$

Equation 6.2

The new expression considers DRV, DRX and phase transformation effects occurring simultaneously. A new subroutine (DRX2-VUMAT) was developed in order to validate it against the experimental data reported for hot compression tests of a Ti64 alloy with lamellar, equiaxed and martensitic microstructures subjected to different deformation conditions reported by Zhang et al. [88].

Authors studied two temperatures (1073 and 1123K) and five strain rates ranging from 0.001 up to 1 $s^{-1}$. The FE axisymmetric hot compression tests were modelled for cylindrical samples with 8mm diameter and 12mm height.

The samples were modelled with 4000 axisymmetric quadrilateral elements (CAX4R) in a thermally coupled model, whereas the two anvils were considered as analytical rigid bodies. A surface-to-surface kinematic contact together with the Coulomb friction model and a coefficient of 0.1 [21] was also implemented. The mechanical properties for FE simulations are the same as previous simulations shown in Table 5.3, whereas, Table 6.1 shows the microstructural properties of the tested samples which were used to predict the flow stress of the material.

Table 6.1 Microstructural features as reported by Zhang et al.[88]

| Type | Mean alpha grain size ($D_\alpha$) | Mean lath thickness ($W_\alpha$) | Volume fraction of alpha ($V_\alpha$) |
|---|---|---|---|
| Equiaxed | 100 | - | 0.9 |
| Lamellar | - | 10 | 0.8 |
| Martensite | - | 0.6 | 1 |

Figure 6.13 shows the solid curves for predicted flow stress of each microstructure and the colour markers represent the experimental results at a given strain rate. The experimental and modelling results are illustrated using similar colours for the sake of better comparison.

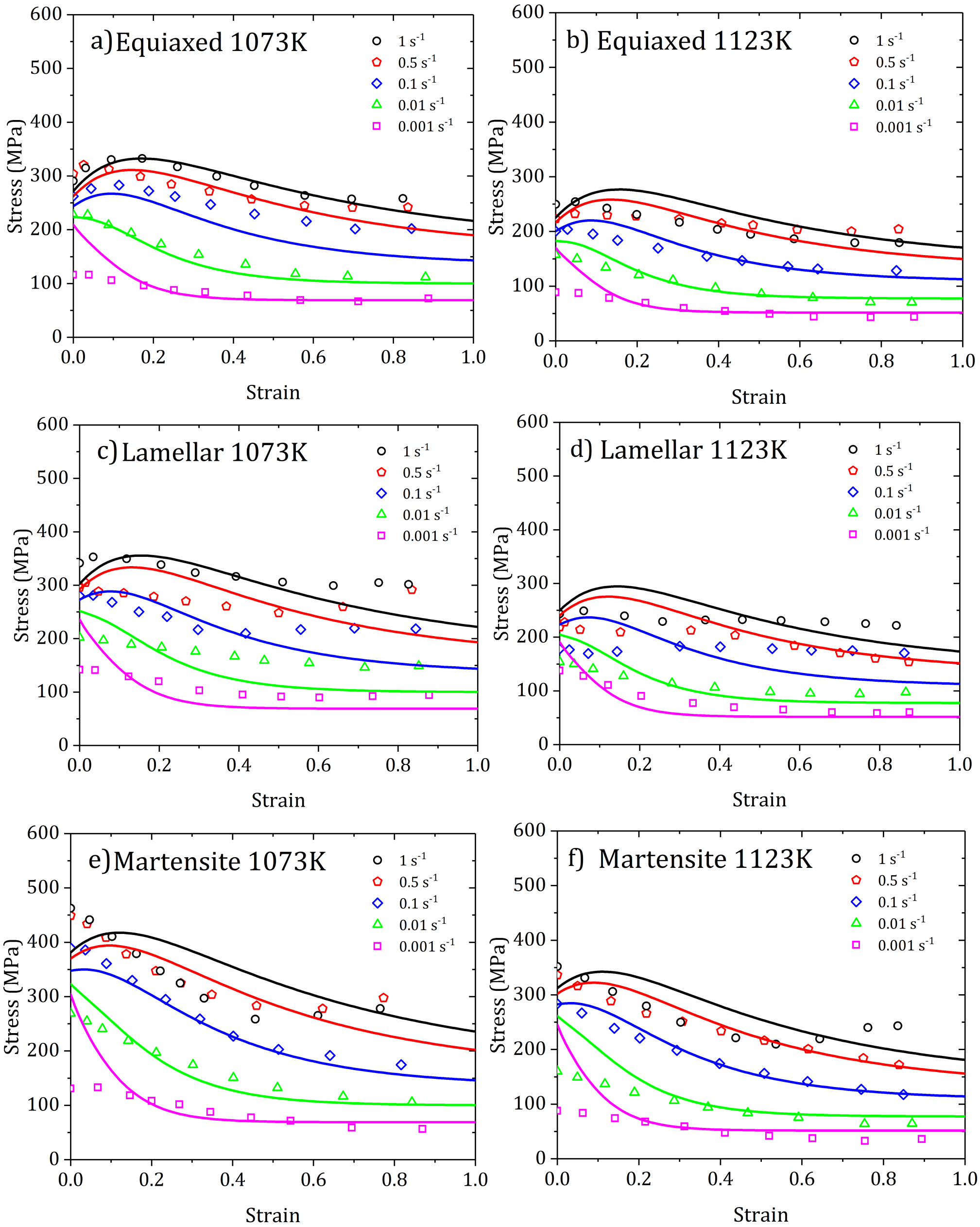


Figure 6.13 Predicted flow curves with the given experimental data for hot compression of Ti-64 with equiaxed (a,b), lamellar (c,d) and martensitic (e,f) microstructures at 1073K and 1123K and strain rates from 0.001up to 1 $s^{-1}$

The results shown in Figure 6.13 shown a great improvement compared to previous model (Equation 4.22), however drawbacks need to be pointed out; for equiaxed structures (a and b), the model easily follows the trend of the flow softening for both temperatures, specially at 1 and 0.5 $s^{-1}$, however at the lowest strain rate (0.001), the model over predicts the yield strength of the material and after 0.4 strain, the model follows reasonability correct the trends. Similarly, to previous model ($\bar{\sigma}_{precip}$), the factor time to transform from the beta regime to alpha is highly crucial and as the model considers this automatically gives inaccurate results.

The experimental data for lamellar structures (c and d) presented lower softening effect due to DRX at 1 and 0.5 $s^{-1}$, and by decreasing the strain rate the material somehow maintain the level of strength, while model predicts higher softening for the first three strain rates creates high different values, nonetheless at the lowest strain rate the model follows reasonably correct the flow trend.

The most surprisingly result was achieved with the C&W martensitic microstructure, as this microstructure is the closest it can be to SLM martensitic microstructures and could be used as benchmark for the results. The new model predicts reasonable correct for both temperatures and 1, 0.5 and 0.1 conditions, whereas for the last strain rates (0.01 and 0.001) the model over overpredicts yield strength, however through strain evolution the model follows well the flow trends. This could be explained due to a delay of time to decompose martensite and diffusion starts to show before nucleate to beta phase.

The experimental data shows a softening effect due to DRX, whereas the SLM structures displayed a hardening effect. From this outcome it could be pointed out that C&W and SLM martensitic structures behave mechanical different, for instance, Zhang et al [88] reported that the material does present DRX grains creating a drastic drop in strength. From this outcome, it is clear that despite both are the same alloys, the processing route (C&W and AM) plays a key factor for the performance of Ti-64.

Figure 6.14 shows an example of the simulated distribution of the deformed sample at 1 $s^{-1}$ and 1073K (Figure 6.14a calibrated model). Figure 6.14a shows the Von Mises stresses distribution in Pascals, displaying the highest distribution of stresses in top and bottom faces with around 321 MPa. Figure 6.14b shows the PEEQ distribution, where the highest strains are found in the centre of the sample (3.34).

Figure 6.14c shows the temperature distribution at the end of the deformation, displaying in the centre of sample the highest temperatures (an increase of 245K). Figure 6.14d shows the strength due to DRV, whereas Figure 6.14e shows the strength due to DRX both in in Pa. From these two figures could be seen the competence occurring, as the higher values for DRV are present, DRX has minimum contribution to Ti-64 strength exactly in the same areas.

Another phenomenon occurring is the competence between alpha and beta phases (Figure 6.14f and g respectively) through the full process. Finally Figure 6.14h shows the final volume recrystallised grains of alpha phase. Comparing Figures 6.14a and h, it could be found a correlation of stresses and alpha volume recrystallised distribution, these figures give a better understanding of the phenomena occurring simultaneously through the complex process.

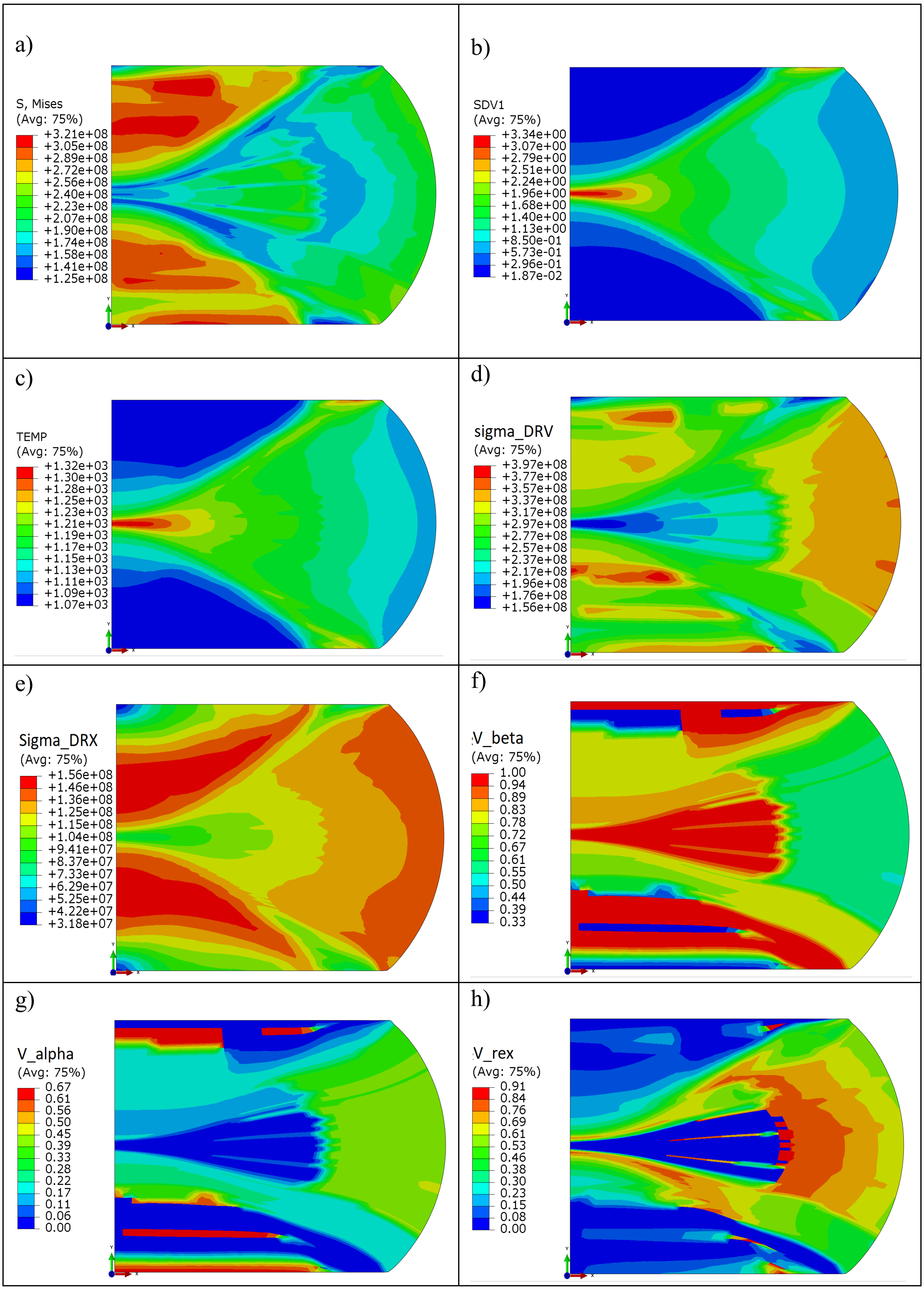


Figure 6.14 DRX2-VUMAT distribution for equiaxed structure at 1073K and 1 $s^{-1}$

To understand the evolution of volume of alpha recrystallised through time, Figure 6.15 shows a plot of time (horizontal axis) against time (left vertical axis in the left side), PEEQ (green vertical axis in the right side), volume of alpha (blue vertical axis in the right side) and volume of alpha phase recrystallised (magenta vertical axis in the right side).

As can be seen from this plot, when temperature increases (red line), alpha phase decreases rapidly (blue), simultaneously the volume of alpha phase suffers from recrystallisation almost at the same rate (magenta line) than alpha. For instance, at the time 0.3s the model predicts a temperature of 1120K, PEEQ of 0.41, volume of alpha 57% and within this percentage, the average volume recrystallised of alpha phase is about half (46%). Whereas at the time around 0.45s, the maximum value of recrystallised phase is achieved (75%) followed by a drop of alpha phase as the temperature reaches the transus temperature from alpha to beta phase (1263K). This result is achieved through the exponential function presented in Equation 4.26. Until the deformation is completed at 0.6 seconds, the resulted the model predicted values were presented in Figure 6.15.

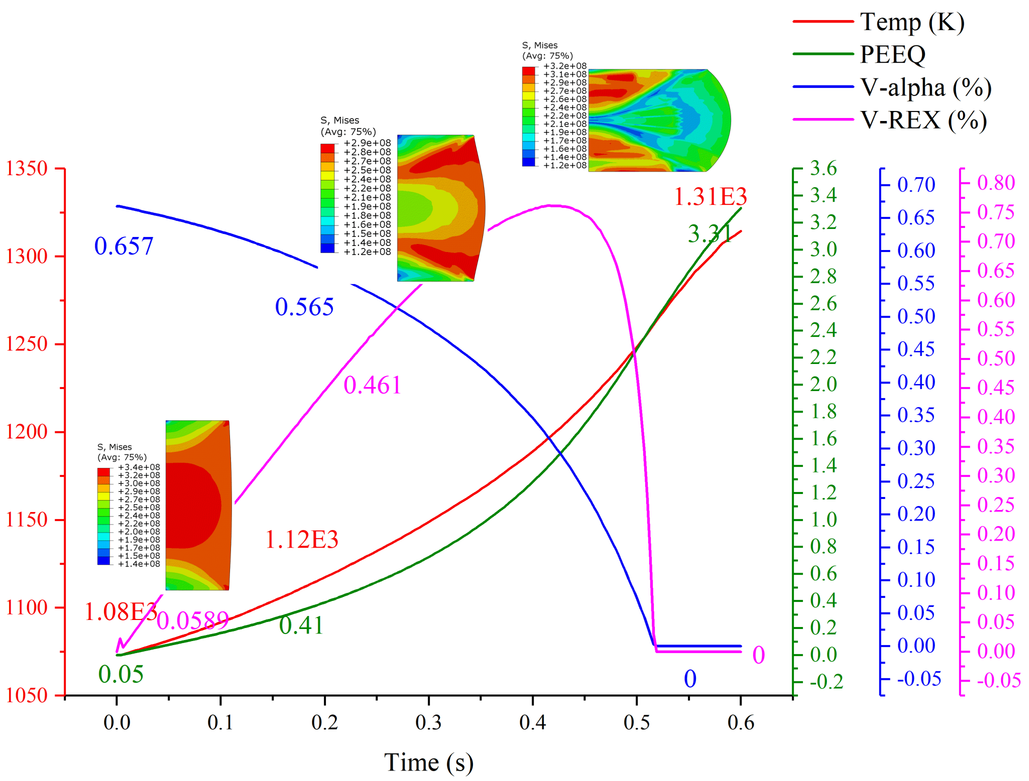


Figure 6.15 Phase transformation through time during 1073K and 1 $s^{-1}$

# 7. Conclusions & future work

## 7.1 Conclusions

The current work has covered modelling and experimental approaches to describe plastic deformation of Ti-64 through conventional processing such as Cast and Wrought technologies also for additive manufacturing processing including Selective Laser Melting.

The experimental approach consisted in two mechanical testing methods, Split-Hopkinson Pressure Bar testing (section 3.3) and axisymmetric hot compression tests (section 3.4) and orthogonal machining tests (section 3.5). The major outcomes of the conducted experiments can be summarised as follows:

SHPB tests (section 5.2.1):

- Through high strain rates tests, SLM Ti-64 displayed roughly half of the ductility than the conventional processed Ti-64 reported within the literature.
- Ti-64 SLM displayed a strain rate hardening effect, for instance at the highest strain rate tested (2000 $s^{-1}$), the material displayed the highest strength followed by 1500 $s^{-1}$ and 1000 $s^{-1}$.

Axisymmetric hot compression tests (section 5.2.2):

- It was found that SLM martensitic structure $\alpha'$ presents a complex evolution from martensite to $\alpha + \beta$ regime, by decomposing first in orthorhombic martensite ($\alpha''$), then it decomposes in solute lean and solute rich regions just before $\beta$ phase precipitates within $\alpha$ phase creating a $\alpha + \beta$ structure. The described sequence can be summarised as: $\alpha' \Rightarrow \alpha'' \Rightarrow \alpha"_{lean} + \alpha"_{rich} \Rightarrow \alpha + \beta$.
- This evolution was verified by SEM microscopy showing that martensite decomposition starts at 973K and finishes the process around 1173K.
- During hot deformation, SLM Ti-64 displayed an increase of strength, contrary what is reported for C&W Ti-64 which displays softening due to dynamic recrystallisation. The increase of strength of Ti-64 was attributed to precipitation of beta phase within alpha laths

Orthogonal machining tests (section 5.2.3):

- The new proposed orthogonal machining rig proved consistency and good repeatability during the machining tests. As result, the successfully implemented rig significantly reduced the costs of trials in comparison with conventional orthogonal machining of tubes.
- Within the three Ti-64 tested (two SLM built vertically and horizontally and one C&W), SLM built horizontally displayed the highest cutting and thrust forces, followed by SLM built vertically and C&W alloy. This was found to be related to the microstructural state of tested materials. As SLM components possess martensitic structure, commercial C&W components own well defined $\alpha + \beta$ phases. Martensite gives to SLM components an increase of strength; hence they produce higher machining forces. Whereas for the difference of forces between SLM samples tested was related to building direction in other words texture.

Whereas for the modelling a work, two main areas can be distinguished; verification and validation of the new physically-based model proposed and the implementation into FE techniques. The major outcomes of the modelling work could be summarised as follows:

New physically-based model (section 5.3.1 & section 5.3.2):

- The physically-based was capable of linking microstructural relevant features such as volume fraction of constitutive phases, mean grain size and type with Ti-64's strength, after predicting yield strength of different Ti-64 alloys in a wide range of deformation conditions, the model successfully predicted flow stress due to dynamic recovery, dynamic recrystallisation, precipitation/phase transformation.
- For high strain rate conditions, it was found that DRV is the principal mechanism occurring due to plastic deformation in SLM and C&W components.
- The model was capable to describe hot deformation for both, C&W and SLM components, which was found that C&W presents DRX softening whereas SLM precipitation hardening, hence it was presented two different equations for the mechanisms occurring during hot deformation.

Finite Element simulations (section 5.4):

- The DRV-VUMAT shown to be effective for SHPB FE model, whereas PRECIP-VUMAT shown relatively good results with the experimental data produced in this thesis (section 6.3.2). Whereas the modified DRX2-VUMAT shown good agreement with experimental data within the literature.

- For the phase transformation effect implemented in PRECIP and DRX2 VUMATs, it was found that model overpredicts strength due to the proposed function fitted within experimental results within the literature for Ti-64 phase transformation during hot deformation. The proposed function only considers temperature effects; however, phase transformation phenomenon also requires time, however overall results shown good agreement with experimental data (section 6.3.2).
- The implementation of three VUMATs aided to study in more detail the distribution of the mechanisms occurring simultaneously within the samples during plastic deformation at high strain rates and hot deformation regimes. Moreover, the use of subroutines enables the opportunity to study the evolution through time of the constitutive phases, dislocations, DRV and DRX during deformation.
- The chip formation FE model shown that is capable to predict accurately the serrated chip morphologies found in machining Ti-64 and difficult-to-cut materials. However, the model underpredicted the cutting and thrust forces in all cutting conditions. The error on the prediction of cutting forces was attributed to the material constitutive model used (Johnson-Cook) which does not describe softening due to DRX occurring during the adiabatic shear bands produced within the chips. Also, the failure initiation criterion (JC) shown that is not suitable for machining operations, whereas the error on the thrust forces was related to the friction behaviour used (Coulomb law).

Through the course of this research several new major contributions have been done in order to understand plastic deformation of Ti-64 in a wide range of processing route. The contribution of this work can be broken into two main areas, modelling of plasticity and experimental work

The work presented in this thesis has developed a new approach for hot forming and machining research communities, one that describes plastic deformation with physics-based modelling based in relevant microstructural features of Ti-64 irrespectively of the processing route performed. For hot forming, the proposed model could be used to design and optimize C&W processing routes of Ti-64 for desired specific mechanical properties. Also, the model could be used for AM post heat treatments for tailoring final microstructures hence, mechanical properties. Lastly, since the model is sensitive to chemical composition, the model could be implemented for designing Ti-based alloys not only for the $\alpha + \beta$ family, but also for other families.

On the experimental side, it was developed a novel machining rig capable of measuring cutting forces in an economic fashion, compared to traditional orthogonal machining rigs. The bespoke rig not only reduced costs but also aided to study in more detail the mechanics of chip formation, as the chips samples were easily acquired for further characterisation, compared to traditional tests rigs where it is required to trim long chips or even difficult to take them out of big lathe machines.

## 7.2 Future Work

The future work can be broken into two main areas, orthogonal machining tests and modelling. With regard with the machining trials, the main area of improvement is the development of a stiffer fixture used to hold the samples, as during titanium alloys cutting forces are expected to be high specially at low speeds as the one tested in this work. The main purpose of designing a stiffer fixture is because it was recorded high amount of out of plane forces compromising the orthogonal condition. Despite the rig recorded for the out of plane forces less than 5% of the cutting forces maintaining the orthogonal condition, the fixture has to be improved, in order to test higher cutting speeds and depth of cuts.

On the modelling side several recommendations are proposed. The new physically-based model could be improved by modifying the phase transformation function by adding time variable to it so it could predict more accurately. Additionally, the model could be expanded first to other $\alpha + \beta$ titanium alloys, followed by other Ti-families.

VUMATs could be improved by adding damage initiation criterion, together with element deletion in Abaqus so that could be used for chip formation simulations. So, it could be studied the combined mechanisms due to plastic deformation within the chips generated in numerical simulations. Another suggestion is the implementation of the new model in a user subroutine UMAT for low deformation ranges during hot deformation.

# References


[1] W. J. C. Lütjering G., *Titanium*. Berlin: Springer, 2003.

[2] L. C. a. M. Peters, Ed. *Titanium and Titanium Alloys. Fundamentals and Applications*. Wiley-VCH GmbH & Co. KGaA, 2003.

[3] J. R. I. a. B. H. M., *Titanium Science and Technology*. Springer, 1973.

[4] C. W. D. Jr., *Materials Science and Engineering: An Introduction*. John Wiley & Sons Inc., 2007.

[5] H. Matsumoto *et al.*, "Room-temperature ductility of Ti–6Al–4V alloy with α′ martensite microstructure," *Materials Science and Engineering: A,* vol. 528, no. 3, pp. 1512-1520, 2011/01/25/ 2011, doi: http://dx.doi.org/10.1016/j.msea.2010.10.070.

[6] V. N. Moiseev, É. V. Polyak, and A. Y. Sokolova, "Martensite strengthening of titanium alloys," *Metal Science and Heat Treatment,* journal article vol. 17, no. 8, pp. 687-691, August 01 1975, doi: 10.1007/bf00664318.

[7] I. Bantounas, D. Dye, and T. C. Lindley, "The role of microtexture on the faceted fracture morphology in Ti–6Al–4V subjected to high-cycle fatigue," *Acta Materialia,* vol. 58, no. 11, pp. 3908-3918, 2010, doi: https://doi.org/10.1016/j.actamat.2010.03.036.

[8] G. Lütjering, "Influence of processing on microstructure and mechanical properties of (α+β) titanium alloys," *Materials Science and Engineering: A,* vol. 243, no. 1–2, pp. 32-45, 3/15/ 1998, doi: http://dx.doi.org/10.1016/S0921-5093(97)00778-8.

[9] S. L. Semiatin, V. Seetharaman, and I. Weiss, "Flow behavior and globularization kinetics during hot working of Ti–6Al–4V with a colony alpha microstructure," *Materials Science and Engineering: A,* vol. 263, no. 2, pp. 257-271, 5/15/ 1999, doi: http://dx.doi.org/10.1016/S0921-5093(98)01156-3.

[10] "Effect of phase transformations on laser forming of Ti–6Al–4V alloy," *Journal of Applied Physics,* vol. 98, no. 1, p. 013518, 2005, doi: 10.1063/1.1944202.

[11] S. L. Semiatin, V. Seetharaman, and I. Weiss, "The thermomechanical processing of alpha/beta titanium alloys," *JOM,* journal article vol. 49, no. 6, pp. 33-39, June 01 1997, doi: 10.1007/bf02914711.

[12] I. Weiss and S. L. Semiatin, "Thermomechanical processing of beta titanium alloys—an overview," *Materials Science and Engineering: A,* vol. 243, no. 1, pp. 46-65, 1998, doi: https://doi.org/10.1016/S0921-5093(97)00783-1.

[13] N. Stefansson and S. L. Semiatin, "Mechanisms of globularization of Ti-6Al-4V during static heat treatment," *Metallurgical and Materials Transactions A,* journal article vol. 34, no. 3, pp. 691-698, March 01 2003, doi: 10.1007/s11661-003-0103-3.

[14] L. Guo, X. Fan, G. Yu, and H. Yang, "Microstructure control techniques in primary hot working of titanium alloy bars: A review," *Chinese Journal of Aeronautics,* vol. 29, no. 1, pp. 30-40, 2016/02/01/ 2016, doi: https://doi.org/10.1016/j.cja.2015.07.011.

[15] G.-z. Quan, G.-c. Luo, J.-t. Liang, D.-s. Wu, A. Mao, and Q. Liu, "Modelling for the dynamic recrystallization evolution of Ti–6Al–4V alloy in two-phase temperature range and a wide strain rate range," *Computational Materials Science,* vol. 97, pp. 136-147, 2015, doi: https://doi.org/10.1016/j.commatsci.2014.10.009.

[16] H.-W. Song, S.-H. Zhang, and M. Cheng, "Dynamic globularization kinetics during hot working of a two phase titanium alloy with a colony alpha microstructure," *Journal of Alloys and Compounds,* vol. 480, no. 2, pp. 922-927, 2009, doi: https://doi.org/10.1016/j.jallcom.2009.02.059.

[17] C. H. Park, J. H. Kim, Y.-T. Hyun, J.-T. Yeom, and N. S. Reddy, "The origins of flow softening during high-temperature deformation of a Ti–6Al–4V alloy with a lamellar microstructure," *Journal of Alloys and Compounds,* vol. 582, pp. 126-129, 2014, doi: https://doi.org/10.1016/j.jallcom.2013.08.041.

[18] J. Xiao, D. S. Li, X. Q. Li, and T. S. Deng, "Constitutive modeling and microstructure change of Ti–6Al–4V during the hot tensile deformation," *Journal of Alloys and Compounds,* vol. 541, pp. 346-352, 2012/11/15/ 2012, doi: https://doi.org/10.1016/j.jallcom.2012.07.048.

[19] https://www.intechopen.com/books/recent-developments-in-the-study-of-recrystallization/characterization-for-dynamic-recrystallization-kinetics-based-on-stress-strain-curves. "characterization of dynamic recovery and recrystallization." (accessed.

[20] R. Ding and Z. X. Guo, "Microstructural evolution of a Ti–6Al–4V alloy during β-phase processing: experimental and simulative investigations," *Materials Science and Engineering: A,* vol. 365, no. 1, pp. 172-179, 2004, doi: https://doi.org/10.1016/j.msea.2003.09.024.

[21] G.-Z. Quan, J. Pan, and Z.-h. Zhang, "Phase transformation and recrystallization kinetics in space–time domain during isothermal compressions for Ti–6Al–4V analyzed by multi-field and multi-scale coupling FEM," *Materials & Design,* vol. 94, pp. 523-535, 2016.

[22] N. Stefansson, S. L. Semiatin, and D. Eylon, "The kinetics of static globularization of Ti-6Al-4V," *Metallurgical and Materials Transactions A,* journal article vol. 33, no. 11, pp. 3527-3534, November 01 2002, doi: 10.1007/s11661-002-0340-x.

[23] S. L. Semiatin and T. R. Bieler, "The effect of alpha platelet thickness on plastic flow during hot working of TI–6Al–4V with a transformed microstructure," *Acta Materialia,* vol. 49, no. 17, pp. 3565-3573, 2001/10/09/ 2001, doi: http://dx.doi.org/10.1016/S1359-6454(01)00236-1.

[24] E. B. Shell and S. L. Semiatin, "Effect of initial microstructure on plastic flow and dynamic globularization during hot working of Ti-6Al-4V," *Metallurgical and Materials Transactions A,* journal article vol. 30, no. 12, pp. 3219-3229, December 01 1999, doi: 10.1007/s11661-999-0232-4.

[25] S. L. Semiatin, S. L. Knisley, P. N. Fagin, D. R. Barker, and F. Zhang, "Microstructure evolution during alpha-beta heat treatment of Ti-6Al-4V," *Metallurgical and Materials Transactions A,* journal article vol. 34, no. 10, pp. 2377-2386, October 01 2003, doi: 10.1007/s11661-003-0300-0.

[26] P. S. Follansbee and G. T. Gray, "An analysis of the low temperature, low and high strain-rate deformation of Ti−6Al−4V," *Metallurgical Transactions A,* journal article vol. 20, no. 5, pp. 863-874, 1989, doi: 10.1007/bf02651653.

[27] U. F. Kocks and H. Mecking, "Physics and phenomenology of strain hardening: the FCC case," *Progress in Materials Science,* vol. 48, no. 3, pp. 171-273, 2003/01/01/ 2003, doi: http://dx.doi.org/10.1016/S0079-6425(02)00003-8.

[28] N. Kotkunde, A. D. Deole, A. K. Gupta, and S. K. Singh, "Comparative study of constitutive modeling for Ti–6Al–4V alloy at low strain rates and elevated temperatures," *Materials & Design,* vol. 55, pp. 999-1005, 2014/03/01/ 2014, doi: https://doi.org/10.1016/j.matdes.2013.10.089.

[29] B. Babu and L.-E. Lindgren, "Dislocation density based model for plastic deformation and globularization of Ti-6Al-4V," *International Journal of Plasticity,* vol. 50, pp. 94-108, 2013/11/01/ 2013, doi: https://doi.org/10.1016/j.ijplas.2013.04.003.

[30] S. Nemat-Nasser, W.-G. Guo, V. F. Nesterenko, S. S. Indrakanti, and Y.-B. Gu, "Dynamic response of conventional and hot isostatically pressed Ti–6Al–4V alloys: experiments and modeling," *Mechanics of Materials,* vol. 33, no. 8, pp. 425-439, 2001/08/01/ 2001, doi: http://dx.doi.org/10.1016/S0167-6636(01)00063-1.

[31] W. Roberts and B. Ahlblom, "A nucleation criterion for dynamic recrystallization during hot working," *Acta Metallurgica,* vol. 26, no. 5, pp. 801-813, 1978.

[32] W. Read, "WT Read and W. Shockley, Phys. Rev. 78, 275 (1950)," *Phys. Rev.,* vol. 78, p. 275, 1950.

[33] Y. Sun *et al.*, "Modeling the correlation between microstructure and the properties of the Ti–6Al–4V alloy based on an artificial neural network," *Materials Science and Engineering: A,* vol. 528, no. 29, pp. 8757-8764, 2011/11/15/ 2011, doi: https://doi.org/10.1016/j.msea.2011.08.059.

[34] Y. Sun, W. Zeng, Y. Zhao, X. Zhang, Y. Shu, and Y. Zhou, "Research on the hot deformation behavior of Ti40 alloy using processing map," *Materials Science and Engineering: A,* vol. 528, no. 3, pp. 1205-1211, 2011.

[35] W. Yu, M. Q. Li, J. Luo, S. Su, and C. Li, "Prediction of the mechanical properties of the post-forged Ti–6Al–4V alloy using fuzzy neural network," *Materials & Design,* vol. 31, no. 7, pp. 3282-3288, 2010/08/01/ 2010, doi: https://doi.org/10.1016/j.matdes.2010.02.009.

[36] M. Zhang, J. Zhang, and D. L. McDowell, "Microstructure-based crystal plasticity modeling of cyclic deformation of Ti–6Al–4V," *International Journal of Plasticity,* vol. 23, no. 8, pp. 1328-1348, 2007, doi: https://doi.org/10.1016/j.ijplas.2006.11.009.

[37] C. Zener and J. H. Hollomon, "Effect of strain rate upon plastic flow of steel," *Journal of Applied physics,* vol. 15, no. 1, pp. 22-32, 1944.

[38] C. M. Sellars and W. McTegart, "On the mechanism of hot deformation," *Acta Metallurgica,* vol. 14, no. 9, pp. 1136-1138, 1966.

[39] D. Samantaray, S. Mandal, A. Bhaduri, and P. Sivaprasad, "An overview on constitutive modelling to predict elevated temperature flow behaviour of fast reactor structural materials," *Transactions of the Indian Institute of Metals,* vol. 63, no. 6, pp. 823-831, 2010.

[40] M. Li, S. Cheng, A. Xiong, H. Wang, S. Su, and L. Sun, "Acquiring a novel constitutive equation of a TC6 alloy at high-temperature deformation," *Journal of materials engineering and performance,* vol. 14, no. 2, pp. 263-266, 2005.

[41] S. M. Abbasi and A. Momeni, "Effect of hot working and post-deformation heat treatment on microstructure and tensile properties of Ti-6Al-4V alloy," *Transactions of Nonferrous Metals Society of China,* vol. 21, no. 8, pp. 1728-1734, 2011, doi: https://doi.org/10.1016/S1003-6326(11)60922-9.

[42] A. Momeni and S. M. Abbasi, "Effect of hot working on flow behavior of Ti–6Al–4V alloy in single phase and two phase regions," *Materials & Design,* vol. 31, no. 8, pp. 3599-3604, 2010, doi: https://doi.org/10.1016/j.matdes.2010.01.060.

[43] C. Zhang, X.-q. Li, D.-s. Li, C.-h. Jin, and J.-j. Xiao, "Modelization and comparison of Norton-Hoff and Arrhenius constitutive laws to predict hot tensile behavior of Ti–6Al–4V alloy," *Transactions of Nonferrous Metals Society of China,* vol. 22, pp. s457-s464, 2012/12/01/ 2012, doi: https://doi.org/10.1016/S1003-6326(12)61746-4.

[44] M. A. Shafaat, H. Omidvar, and B. Fallah, "Prediction of hot compression flow curves of Ti–6Al–4V alloy in α+β phase region," *Materials & Design,* vol. 32, no. 10, pp. 4689-4695, 2011/12/01/ 2011, doi: https://doi.org/10.1016/j.matdes.2011.06.048.

[45] J. William and R. Mehl, "Reaction kinetics in processes of nucleation and growth," *Trans. Metall. Soc. AIME,* vol. 135, pp. 416-442, 1939.

[46] M. Avrami, "Kinetics of phase change. I General theory," *The Journal of chemical physics,* vol. 7, no. 12, pp. 1103-1112, 1939.

[47] M. Avrami, "Kinetics of phase change. II transformation-time relations for random distribution of nuclei," *The Journal of chemical physics,* vol. 8, no. 2, pp. 212-224, 1940.

[48] M. Avrami, "Kinetics of phase change. III: granulation, phase change and microstructure," *Journal of chemical physics,* vol. 9, pp. 177-184, 1941.

[49] A. N. Kolmogorov, "On the statistical theory of the crystallization of metals," *Bull. Acad. Sci. USSR, Math. Ser,* vol. 1, no. 3, pp. 355-359, 1937.

[50] G. Ruitenberg, A. K. Petford-Long, and R. C. Doole, "Determination of the isothermal nucleation and growth parameters for the crystallization of thin Ge2Sb2Te5 films," *Journal of Applied Physics,* vol. 92, no. 6, pp. 3116-3123, 2002, doi: 10.1063/1.1503166.

[51] Y.-p. Yi, X. Fu, J.-d. Cui, and H. Chen, "Prediction of grain size for large-sized aluminium alloy 7050 forging during hot forming," *Journal of Central South University of Technology,* journal article vol. 15, no. 1, pp. 1-5, February 01 2008, doi: 10.1007/s11771-008-0001-3.

[52] J. H. Kim, S. L. Semiatin, Y. H. Lee, and C. S. Lee, "A Self-Consistent Approach for Modeling the Flow Behavior of the Alpha and Beta Phases in Ti-6Al-4V," *Metallurgical*

*and Materials Transactions A,* journal article vol. 42, no. 7, pp. 1805-1814, July 01 2011, doi: 10.1007/s11661-010-0567-x.

[53] A. Gebhardt, "Basics, Definitions, and Application Levels," in *Understanding Additive Manufacturing*: Hanser, 2011, pp. 1-29.

[54] F. Froes, "Titanium alloys: properties and applications," 2001.

[55] F. H. Froes, I. Chang, and Y. Zhao, "8 - Powder metallurgy of titanium alloys," in *Advances in Powder Metallurgy*: Woodhead Publishing, 2013, pp. 202-240.

[56] B. Dutta and F. H. Froes, "The Additive Manufacturing (AM) of titanium alloys," *Metal Powder Report,* vol. 72, no. 2, pp. 96-106, 2017, doi: https://doi.org/10.1016/j.mprp.2016.12.062.

[57] D. Whittaker, F. H. Froes, and M. Qian, "30 - Future prospects for titanium powder metallurgy markets," in *Titanium Powder Metallurgy*. Boston: Butterworth-Heinemann, 2015, pp. 579-600.

[58] C. F. Yolton, F. H. Froes, and M. Qian, "2 - Conventional titanium powder production," in *Titanium Powder Metallurgy*. Boston: Butterworth-Heinemann, 2015, pp. 21-32.

[59] C. Zopp, S. Blümer, F. Schubert, and L. Kroll, "Processing of a metastable titanium alloy (Ti-5553) by selective laser melting," *Ain Shams Engineering Journal,* vol. 8, no. 3, pp. 475-479, 2017/09/01/ 2017, doi: https://doi.org/10.1016/j.asej.2016.11.004.

[60] B. Dutta and F. H. Froes, "Chapter 6 - Markets, Applications, and Costs," in *Additive Manufacturing of Titanium Alloys*: Butterworth-Heinemann, 2016, pp. 61-73.

[61] A. Gebhardt, "Layer Manufacturing Processes," in *Understanding Additive Manufacturing*: Hanser, 2011, pp. 31-63.

[62] C. Baykasoglu, O. Akyildiz, D. Candemir, Q. Yang, and A. C. To, "Predicting Microstructure Evolution During Directed Energy Deposition Additive Manufacturing of Ti-6Al-4V," *Journal of Manufacturing Science and Engineering,* vol. 140, no. 5, pp. 051003-051003-11, 2018, doi: 10.1115/1.4038894.

[63] B. Dutta and F. H. Froes, "Chapter 1 - The Additive Manufacturing of Titanium Alloys," in *Additive Manufacturing of Titanium Alloys*: Butterworth-Heinemann, 2016, pp. 1-10.

[64] P. Edwards and M. Ramulu, "Fatigue performance evaluation of selective laser melted Ti–6Al–4V," *Materials Science and Engineering: A,* vol. 598, pp. 327-337, 3/26/ 2014, doi: http://dx.doi.org/10.1016/j.msea.2014.01.041.

[65] T. DebRoy *et al.*, "Additive manufacturing of metallic components – Process, structure and properties," *Progress in Materials Science,* vol. 92, pp. 112-224, 2018, doi: https://doi.org/10.1016/j.pmatsci.2017.10.001.

[66] S. Hällgren, L. Pejryd, and J. Ekengren, "Additive Manufacturing and High Speed Machining -cost Comparison of short Lead Time Manufacturing Methods," *Procedia CIRP,* vol. 50, pp. 384-389, 2016, doi: https://doi.org/10.1016/j.procir.2016.05.049.

[67] M. Galindo-Fernandez, K. A. Mumtaz, P. E. J. Rivera-Diaz-del-Castillo, E. I. Galindo-Nava, and H. Ghadbeigi, "A microstructure sensitive model for deformation of Ti-6Al-4V describing Cast-and-Wrought and Additive Manufacturing morphologies," *Materials and Design,* 09/15 2018, doi: 10.1016/j.matdes.2018.09.028.

[68] H. Gong, K. Rafi, H. Gu, G. D. Janaki Ram, T. Starr, and B. Stucker, "Influence of defects on mechanical properties of Ti–6Al–4 V components produced by selective laser melting and electron beam melting," *Materials & Design,* vol. 86, pp. 545-554, 12/5/ 2015, doi: http://dx.doi.org/10.1016/j.matdes.2015.07.147.

[69] B. Vayssette, N. Saintier, C. Brugger, M. Elmay, and E. Pessard, "Surface roughness of Ti-6Al-4V parts obtained by SLM and EBM: Effect on the High Cycle Fatigue life," *Procedia Engineering,* vol. 213, pp. 89-97, 2018/01/01/ 2018, doi: https://doi.org/10.1016/j.proeng.2018.02.010.

[70] X. Zhao *et al.*, "Comparison of the microstructures and mechanical properties of Ti–6Al–4V fabricated by selective laser melting and electron beam melting," *Materials & Design,* vol. 95, pp. 21-31, 2016/04/05/ 2016, doi: http://dx.doi.org/10.1016/j.matdes.2015.12.135.

[71] A. International, *Standard terminology for additive manufacturing technologies : designation F2792-12a*. West Conshohocken, PA: ASTM International (in English), 2012.

[72] B. Dutta and F. H. Froes, "Chapter 2 - Raw Materials for Additive Manufacturing of Titanium," in *Additive Manufacturing of Titanium Alloys*: Butterworth-Heinemann, 2016, pp. 11-23.

[73] B. Dutta and F. H. Froes, "Chapter 5 - Comparison of Titanium AM Technologies," in *Additive Manufacturing of Titanium Alloys*: Butterworth-Heinemann, 2016, pp. 51-59.

[74] "http://www.sciaky.com/additive-manufacturing/wire-am-vs-powder-am." (accessed 24/05/2017.

[75] H. Ali, L. Ma, H. Ghadbeigi, and K. Mumtaz, "In-situ residual stress reduction, martensitic decomposition and mechanical properties enhancement through high temperature powder bed pre-heating of Selective Laser Melted Ti6Al4V," *Materials Science and Engineering: A,* vol. 695, pp. 211-220, 2017/05/17/ 2017, doi: http://dx.doi.org/10.1016/j.msea.2017.04.033.

[76] F. Luca, M. Emanuele, R. Pierfrancesco, M. Alberto, H. Simon, and W. Konrad, "Ductility of a Ti-6Al-4V alloy produced by selective laser melting of prealloyed powders," *Rapid Prototyping Journal,* vol. 16, no. 6, pp. 450-459, 2010, doi: doi:10.1108/13552541011083371.

[77] G. Kasperovich and J. Hausmann, "Improvement of fatigue resistance and ductility of TiAl6V4 processed by selective laser melting," *Journal of Materials Processing Technology,* vol. 220, pp. 202-214, 6// 2015, doi: http://dx.doi.org/10.1016/j.jmatprotec.2015.01.025.

[78] S. Leuders *et al.*, "On the mechanical behaviour of titanium alloy TiAl6V4 manufactured by selective laser melting: Fatigue resistance and crack growth performance,"

*International Journal of Fatigue,* vol. 48, pp. 300-307, 3// 2013, doi: http://dx.doi.org/10.1016/j.ijfatigue.2012.11.011.

[79] B. J. Hayes *et al.*, "Predicting tensile properties of Ti-6Al-4V produced via directed energy deposition," *Acta Materialia,* vol. 133, pp. 120-133, 2017/07/01/ 2017, doi: http://dx.doi.org/10.1016/j.actamat.2017.05.025.

[80] X. Tan *et al.*, "Revealing martensitic transformation and α/β interface evolution in electron beam melting three-dimensional-printed Ti-6Al-4V," Article vol. 6, p. 26039, 05/17/online 2016, doi: 10.1038/srep26039 https://www.nature.com/articles/srep26039#supplementary-information.

[81] W. Xu *et al.*, "Additive manufacturing of strong and ductile Ti–6Al–4V by selective laser melting via in situ martensite decomposition," *Acta Materialia,* vol. 85, pp. 74-84, 2/15/ 2015, doi: http://dx.doi.org/10.1016/j.actamat.2014.11.028.

[82] W. Xu, S. Sun, J. Elambasseril, Q. Liu, M. Brandt, and M. Qian, "Ti-6Al-4V Additively Manufactured by Selective Laser Melting with Superior Mechanical Properties," *JOM,* journal article vol. 67, no. 3, pp. 668-673, 2015, doi: 10.1007/s11837-015-1297-8.

[83] R. K.D., *Ductility improvement due to martensite 'α decomposition in porous Ti-6Al-4V parts produced by selective laser melting for orthopaedic implants*. Department of the Air force, Wright-Patterson Air force Base, Ohio, USA, 2015.

[84] T. Vilaro, C. Colin, and J. D. Bartout, "As-Fabricated and Heat-Treated Microstructures of the Ti-6Al-4V Alloy Processed by Selective Laser Melting," *Metallurgical and Materials Transactions A,* journal article vol. 42, no. 10, pp. 3190-3199, 2011, doi: 10.1007/s11661-011-0731-y.

[85] E. Sallica-Leva, R. Caram, A. L. Jardini, and J. B. Fogagnolo, "Ductility improvement due to martensite α′ decomposition in porous Ti–6Al–4V parts produced by selective laser melting for orthopedic implants," *Journal of the Mechanical Behavior of Biomedical Materials,* vol. 54, pp. 149-158, 2// 2016, doi: http://dx.doi.org/10.1016/j.jmbbm.2015.09.020.

[86] C. H. Park, Y. I. Son, and C. S. Lee, "Constitutive analysis of compressive deformation behavior of ELI-grade Ti–6Al–4V with different microstructures," *Journal of Materials Science,* journal article vol. 47, no. 7, pp. 3115-3124, 2012, doi: 10.1007/s10853-011-6145-9.

[87] C. Zheng *et al.*, "Effect of microstructures on ballistic impact property of Ti–6Al–4V targets," *Materials Science and Engineering: A,* vol. 608, pp. 53-62, 7/1/ 2014, doi: http://dx.doi.org/10.1016/j.msea.2014.04.032.

[88] Z. X. Zhang, S. J. Qu, A. H. Feng, J. Shen, and D. L. Chen, "Hot deformation behavior of Ti-6Al-4V alloy: Effect of initial microstructure," *Journal of Alloys and Compounds,* vol. 718, pp. 170-181, 2017/09/25/ 2017, doi: https://doi.org/10.1016/j.jallcom.2017.05.097.

[89] C. H. Park, Y. G. Ko, J.-W. Park, and C. S. Lee, "Enhanced superplasticity utilizing dynamic globularization of Ti–6Al–4V alloy," vol. 496, no. 1, pp. 150-158, 2008.

[90] A. S. Khan, Y. Sung Suh, and R. Kazmi, "Quasi-static and dynamic loading responses and constitutive modeling of titanium alloys," *International Journal of Plasticity,* vol. 20, no. 12, pp. 2233-2248, 12// 2004, doi: http://dx.doi.org/10.1016/j.ijplas.2003.06.005.

[91] A. S. Khan and R. Liang, "Behaviors of three BCC metal over a wide range of strain rates and temperatures: experiments and modeling," *International Journal of Plasticity,* vol. 15, no. 10, pp. 1089-1109, 1999/01/01/ 1999, doi: https://doi.org/10.1016/S0749-6419(99)00030-3.

[92] D.-G. Lee, S. Lee, C. S. Lee, and S. Hur, "Effects of microstructural factors on quasi-static and dynamic deformation behaviors of Ti-6Al-4V alloys with widmanstätten structures," *Metallurgical and Materials Transactions A,* journal article vol. 34, no. 11, p. 2541, November 01 2003, doi: 10.1007/s11661-003-0013-4.

[93] W.-S. Lee and C.-F. Lin, "High-temperature deformation behaviour of Ti6Al4V alloy evaluated by high strain-rate compression tests," *Journal of Materials Processing Technology,* vol. 75, no. 1–3, pp. 127-136, 3/1/ 1998, doi: http://dx.doi.org/10.1016/S0924-0136(97)00302-6.

[94] J. P. Davim, *Machining: fundamentals and recent advances*. Springer Science & Business Media, 2008.

[95] J. P. Davim, *Machining of titanium alloys*. Springer, 2014.

[96] M. A. P., *Finite Element Method in Machining Processes*. Springer, 2013.

[97] N. L. de Lacalle and A. L. Mentxaka, *Machine tools for high performance machining*. Springer Science & Business Media, 2008.

[98] Y. Altintas, *Manufacturing automation, Metal cutting mechanics, machine tool vibrations, and CNC design*, second ed. Cambridge University Press, 2012.

[99] V. A. Balogun and P. T. Mativenga, "Impact of un-deformed chip thickness on specific energy in mechanical machining processes," *Journal of Cleaner Production,* vol. 69, pp. 260-268, 2014, doi: https://doi.org/10.1016/j.jclepro.2014.01.036.

[100] Z. N.N, "Interrelationship between shear processes occurring along tool face and on shear plane in metal cutting," *Proceedings of the international research in production engineering conference, ASME,* pp. 42–49, 1963.

[101] D. Ulutan and T. Özel, "Methodology to Determine Friction in Orthogonal Cutting With Application to Machining Titanium and Nickel Based Alloys," no. 54990 C2 - International Manufacturing Science and Engineering Conference, pp. 327-334
C1 - ASME 2012 International Manufacturing Science and Engineering Conference, 2012.

[102] J. M. Huang and J. T. Black, "An Evaluation of Chip Separation Criteria for the FEM Simulation of Machining," *Journal of Manufacturing Science and Engineering,* vol. 118, no. 4, pp. 545-554, 1996.

[103] S. N. Melkote *et al.*, "Advances in material and friction data for modelling of metal machining," *CIRP Annals,* vol. 66, no. 2, pp. 731-754, 2017, doi: https://doi.org/10.1016/j.cirp.2017.05.002.

[104] F. Zhou, "A new analytical tool-chip friction model in dry cutting," *The International Journal of Advanced Manufacturing Technology,* vol. 70, no. 1, pp. 309-319, 2014, doi: 10.1007/s00170-013-5271-8.

[105] M. Sima and T. Özel, "Modified material constitutive models for serrated chip formation simulations and experimental validation in machining of titanium alloy Ti–6Al–4V," *International Journal of Machine Tools and Manufacture,* vol. 50, no. 11, pp. 943-960, 11// 2010, doi: http://dx.doi.org/10.1016/j.ijmachtools.2010.08.004.

[106] T. Özel, "The influence of friction models on finite element simulations of machining," *International Journal of Machine Tools and Manufacture,* vol. 46, no. 5, pp. 518-530, 2006, doi: https://doi.org/10.1016/j.ijmachtools.2005.07.001.

[107] W. König, R. Komanduri, H. K. Tönshoff, and G. Ackershott, "Machining of Hard Materials," *CIRP Annals,* vol. 33, no. 2, pp. 417-427, 1984, doi: https://doi.org/10.1016/S0007-8506(16)30164-0.

[108] E. O. Ezugwu and Z. M. Wang, "Titanium alloys and their machinability—a review," *Journal of Materials Processing Technology,* vol. 68, no. 3, pp. 262-274, 1997, doi: https://doi.org/10.1016/S0924-0136(96)00030-1.

[109] J. P. Davim, *Machining of Hard Materials*. Springer, 2011.

[110] D. J. P. a. L. A. J. R. Veiga C., "Review on machinability of titanium alloys: the process perspective," *Rev. Adv. Mater. Sci,* vol. 34, pp. 148-164, 2013 2013.

[111] K. Rana *et al.*, "2D FE Prediction of Surface Alteration of Inconel 718 under Machining Condition," *Procedia CIRP,* vol. 45, pp. 227-230, 2016/01/01/ 2016, doi: https://doi.org/10.1016/j.procir.2016.02.346.

[112] A. Pramanik, "Problems and solutions in machining of titanium alloys," *The International Journal of Advanced Manufacturing Technology,* journal article vol. 70, no. 5, pp. 919-928, 2014, doi: 10.1007/s00170-013-5326-x.

[113] X. Yang and C. Richard Liu, "MACHINING TITANIUM AND ITS ALLOYS," *Machining Science and Technology,* vol. 3, no. 1, pp. 107-139, 1999/01/01 1999, doi: 10.1080/10940349908945686.

[114] F. Wang, J. Zhao, A. Li, and J. Zhao, "Experimental Study on Cutting Forces and Surface Integrity in High-Speed Side Milling of Ti-6Al-4V Titanium Alloy," *Machining Science and Technology,* vol. 18, no. 3, pp. 448-463, 2014/07/03 2014, doi: 10.1080/10910344.2014.926690.

[115] P. J. Arrazola, A. Garay, L. M. Iriarte, M. Armendia, S. Marya, and F. Le Maître, "Machinability of titanium alloys (Ti6Al4V and Ti555.3)," *Journal of Materials Processing Technology,* vol. 209, no. 5, pp. 2223-2230, 3/1/ 2009, doi: http://dx.doi.org/10.1016/j.jmatprotec.2008.06.020.

[116] M. Armendia, A. Garay, L. M. Iriarte, and P. J. Arrazola, "Comparison of the machinabilities of Ti6Al4V and TIMETAL® 54M using uncoated WC–Co tools," *Journal of Materials Processing Technology,* vol. 210, no. 2, pp. 197-203, 1/19/ 2010, doi: http://dx.doi.org/10.1016/j.jmatprotec.2009.08.026.

[117] R. Komanduri, "Some clarifications on the mechanics of chip formation when machining titanium alloys," *Wear,* vol. 76, no. 1, pp. 15-34, 1982, doi: https://doi.org/10.1016/0043-1648(82)90113-2.

[118] P. A. a. L. G., "Machining of titanium alloy (Ti-6Al-4V), Theory to application," *Machining Sci. and Tech.,* vol. 19, pp. 1-49, 2015.

[119] M. V. Ribeiro, M. R. V. Moreira, and J. R. Ferreira, "Optimization of titanium alloy (6Al–4V) machining," *Journal of Materials Processing Technology,* vol. 143–144, pp. 458-463, 12/20/ 2003, doi: http://dx.doi.org/10.1016/S0924-0136(03)00457-6.

[120] J. D. Puerta Velásquez, B. Bolle, P. Chevrier, G. Geandier, and A. Tidu, "Metallurgical study on chips obtained by high speed machining of a Ti–6 wt.%Al–4 wt.%V alloy," *Materials Science and Engineering: A,* vol. 452–453, pp. 469-474, 4/15/ 2007, doi: http://dx.doi.org/10.1016/j.msea.2006.10.090.

[121] J. D. P. Velásquez, A. Tidu, B. Bolle, P. Chevrier, and J. J. Fundenberger, "Sub-surface and surface analysis of high speed machined Ti–6Al–4V alloy," *Materials Science and Engineering: A,* vol. 527, no. 10–11, pp. 2572-2578, 4/25/ 2010, doi: http://dx.doi.org/10.1016/j.msea.2009.12.018.

[122] A. E. Bayoumi and J. Q. Xie, "Some metallurgical aspects of chip formation in cutting Ti-6wt.%Al-4wt.%V alloy," *Materials Science and Engineering: A,* vol. 190, no. 1, pp. 173-180, 1995, doi: https://doi.org/10.1016/0921-5093(94)09595-N.

[123] J. Barry, G. Byrne, and D. Lennon, "Observations on chip formation and acoustic emission in machining Ti–6Al–4V alloy," *International Journal of Machine Tools and Manufacture,* vol. 41, no. 7, pp. 1055-1070, 2001, doi: https://doi.org/10.1016/S0890-6955(00)00096-1.

[124] M. Calamaz, M. Nouari, D. Géhin, and F. Girot, "Damage modes of straight tungsten carbide in dry machining of titanium alloy TA6V," *J. Phys. IV France,* vol. 134, pp. 1265-1271, 2006.

[125] H. G. Prengel, W. R. Pfouts, and A. T. Santhanam, "State of the art in hard coatings for carbide cutting tools," *Surface and Coatings Technology,* vol. 102, no. 3, pp. 183-190, 1998, doi: https://doi.org/10.1016/S0257-8972(96)03061-7.

[126] K. A. Venugopal, S. Paul, and A. B. Chattopadhyay, "Tool wear in cryogenic turning of Ti-6Al-4V alloy," *Cryogenics,* vol. 47, no. 1, pp. 12-18, 2007, doi: https://doi.org/10.1016/j.cryogenics.2006.08.011.

[127] S. Joshi, P. Pawar, A. Tewari, and S. S. Joshi, "Influence of β phase fraction on deformation of grains in and around shear bands in machining of titanium alloys," *Materials Science and Engineering: A,* vol. 618, pp. 71-85, 11/17/ 2014, doi: http://dx.doi.org/10.1016/j.msea.2014.08.076.

[128] D. Yameogo, B. Haddag, H. Makich, and M. Nouari, "A physical behavior model including dynamic recrystallization and damage mechanisms for cutting process simulation of the titanium alloy Ti-6Al-4V," *The International Journal of Advanced Manufacturing Technology,* 2018/09/24 2018, doi: 10.1007/s00170-018-2663-9.

[129] H. Wu and S. To, "Serrated chip formation and their adiabatic analysis by using the constitutive model of titanium alloy in high speed cutting," *Journal of Alloys and Compounds,* vol. 629, pp. 368-373, 4/25/ 2015, doi: http://dx.doi.org/10.1016/j.jallcom.2014.12.230.

[130] G. G. Ye, S. F. Xue, M. Q. Jiang, X. H. Tong, and L. H. Dai, "Modeling periodic adiabatic shear band evolution during high speed machining Ti-6Al-4V alloy," *International Journal of Plasticity,* vol. 40, pp. 39-55, 1// 2013, doi: http://dx.doi.org/10.1016/j.ijplas.2012.07.001.

[131] V. P. Astakhov, *Tribology of metal cutting*. Elsevier, 2006.

[132] S. Athavale and J. Strenkowski, "Finite element modeling of machining: from proof-of-concept to engineering applications," *Machining Science and Technology,* vol. 2, no. 2, pp. 317-342, 1998.

[133] P. J. Arrazola, T. Özel, D. Umbrello, M. Davies, and I. S. Jawahir, "Recent advances in modelling of metal machining processes," *CIRP Annals - Manufacturing Technology,* vol. 62, no. 2, pp. 695-718, // 2013, doi: http://dx.doi.org/10.1016/j.cirp.2013.05.006.

[134] P. Oxley, "Introducing strain-rate dependent work material properties into the analysis of orthogonal cutting," *CIRP,* vol. 13, no. 2, pp. 127-138, 1966.

[135] P. L. B. Oxley and M. C. Shaw, "Mechanics of Machining: An Analytical Approach to Assessing Machinability," *Journal of Applied Mechanics,* vol. 57, no. 1, pp. 253-253, 1990, doi: 10.1115/1.2888318.

[136] E. Usui, T. Shirakashi, and T. Kitagawa, "Analytical prediction of cutting tool wear," *Wear,* vol. 100, no. 1, pp. 129-151, 1984/12/01 1984, doi: http://dx.doi.org/10.1016/0043-1648(84)90010-3.

[137] S. T. Maekawa K., Usui E., "Process modeling of orthogonal cutting by the rigid plastic finite element method.," *ASME J. Eng. Ind.,* vol. 106, pp. 132–138, 1984.

[138] F. J. Zerilli and R. W. Armstrong, "Dislocation-mechanics-based constitutive relations for material dynamics calculations," *Journal of Applied Physics,* vol. 61, no. 5, pp. 1816-1825, 1987, doi: 10.1063/1.338024.

[139] J. G. R. C. W.H, "A constitutive model and data for metals subjected to large strains, high strain rates and high temperatures.," *Proceedings of the 7th international symposium on ballistics,* no. 61, pp. 1816–1825, 1983.

[140] M. Calamaz, D. Coupard, and F. Girot, "A new material model for 2D numerical simulation of serrated chip formation when machining titanium alloy Ti–6Al–4V," *International Journal of Machine Tools and Manufacture,* vol. 48, no. 3–4, pp. 275-288, 3// 2008, doi: http://dx.doi.org/10.1016/j.ijmachtools.2007.10.014.

[141] Y. M. Arısoy and T. Özel, "Prediction of machining induced microstructure in Ti–6Al–4V alloy using 3-D FE-based simulations: Effects of tool micro-geometry, coating and cutting conditions," *Journal of Materials Processing Technology,* vol. 220, pp. 1-26, 2015/06/01/ 2015, doi: https://doi.org/10.1016/j.jmatprotec.2014.11.002.

[142] T. Özel and Y. Karpat, "Identification of Constitutive Material Model Parameters for High-Strain Rate Metal Cutting Conditions Using Evolutionary Computational Algorithms," *Materials & Manufacturing Processes,* Article vol. 22, no. 5, pp. 659-667, 2007, doi: 10.1080/10426910701323631.

[143] V. Schulze, Y. Zhang, J. C. Outeiro, and T. Mabrouki, "15th CIRP Conference on Modelling of Machining Operations (15th CMMO)On the Selection of Johnson-cook Constitutive Model Parameters for Ti-6Al-4V Using Three Types of Numerical Models of Orthogonal Cutting," *Procedia CIRP,* vol. 31, pp. 112-117, 2015/01/01 2015, doi: http://dx.doi.org/10.1016/j.procir.2015.03.052.

[144] Y. Zhang, J. C. Outeiro, and T. Mabrouki, "On the Selection of Johnson-cook Constitutive Model Parameters for Ti-6Al-4V Using Three Types of Numerical Models of Orthogonal Cutting," *Procedia CIRP,* vol. 31, pp. 112-117, 2015, doi: https://doi.org/10.1016/j.procir.2015.03.052.

[145] A. Shrot and M. Bäker, "Determination of Johnson–Cook parameters from machining simulations," *Computational Materials Science,* vol. 52, no. 1, pp. 298-304, 2012, doi: https://doi.org/10.1016/j.commatsci.2011.07.035.

[146] K. S. Vijay Sekar and M. Pradeep Kumar, "Finite element simulations of Ti6Al4V titanium alloy machining to assess material model parameters of the Johnson-Cook constitutive equation," *Journal of the Brazilian Society of Mechanical Sciences and Engineering,* vol. 33, pp. 203-211, 2011.

[147] S. N. Melkote, R. Liu, P. Fernandez-Zelaia, and T. Marusich, "A physically based constitutive model for simulation of segmented chip formation in orthogonal cutting of commercially pure titanium," *CIRP Annals - Manufacturing Technology,* vol. 64, no. 1, pp. 65-68, // 2015, doi: http://dx.doi.org/10.1016/j.cirp.2015.04.060.

[148] T. Ozel, I. Llanos, J. Soriano, and P. J. Arrazola, "3D FINITE ELEMENT MODELLING OF CHIP FORMATION PROCESS FOR MACHINING INCONEL 718: COMPARISON OF FE SOFTWARE PREDICTIONS," *Machining Science and Technology,* vol. 15, no. 1, pp. 21-46, 2011/04/13 2011, doi: 10.1080/10910344.2011.557950.

[149] T. Özel, Y. M. Arısoy, and C. Guo, "Identification of Microstructural Model Parameters for 3D Finite Element Simulation of Machining Inconel 100 Alloy," *Procedia CIRP,* vol. 46, pp. 549-554, 2016/01/01/ 2016, doi: https://doi.org/10.1016/j.procir.2016.04.021.

[150] F. Jafarian, M. Imaz Ciaran, D. Umbrello, P. J. Arrazola, L. Filice, and H. Amirabadi, "Finite element simulation of machining Inconel 718 alloy including microstructure changes," *International Journal of Mechanical Sciences,* vol. 88, pp. 110-121, 2014/11/01/ 2014, doi: https://doi.org/10.1016/j.ijmecsci.2014.08.007.

[151] R. Liu, M. Salahshoor, S. N. Melkote, and T. Marusich, "A unified material model including dislocation drag and its application to simulation of orthogonal cutting of OFHC Copper," *Journal of Materials Processing Technology,* vol. 216, pp. 328-338, 2015/02/01/ 2015, doi: https://doi.org/10.1016/j.jmatprotec.2014.09.021.

[152] G. Chen, C. Ren, X. Yang, X. Jin, and T. Guo, "Finite element simulation of high-speed machining of titanium alloy (Ti–6Al–4V) based on ductile failure model," *The*

*International Journal of Advanced Manufacturing Technology,* journal article vol. 56, no. 9, pp. 1027-1038, 2011, doi: 10.1007/s00170-011-3233-6.

[153] S. Seo, O. Min, and H. Yang, "Constitutive equation for Ti–6Al–4V at high temperatures measured using the SHPB technique," *International Journal of Impact Engineering,* vol. 31, no. 6, pp. 735-754, 7// 2005, doi: http://dx.doi.org/10.1016/j.ijimpeng.2004.04.010.

[154] U. F. Kocks, "Laws for Work-Hardening and Low-Temperature Creep," *Journal of Engineering Materials and Technology,* vol. 98, no. 1, pp. 76-85, 1976, doi: 10.1115/1.3443340.

[155] M. Huang, P. E. J. Rivera-Díaz-del-Castillo, O. Bouaziz, and S. van der Zwaag, "A constitutive model for high strain rate deformation in FCC metals based on irreversible thermodynamics," *Mechanics of Materials,* vol. 41, no. 9, pp. 982-988, 9// 2009, doi: http://dx.doi.org/10.1016/j.mechmat.2009.05.007.

[156] E. I. Galindo-Nava and P. E. J. Rivera-Díaz-del-Castillo, "A thermostatistical theory of low and high temperature deformation in metals," *Materials Science and Engineering: A,* vol. 543, pp. 110-116, 5/1/ 2012, doi: http://dx.doi.org/10.1016/j.msea.2012.02.055.

[157] S. Anurag and Y. B. Guo, "A modified micromechanical approach to determine flow stress of work materials experiencing complex deformation histories in manufacturing processes," *International Journal of Mechanical Sciences,* vol. 49, no. 7, pp. 909-918, 2007/09/01/ 2007, doi: https://doi.org/10.1016/j.ijmecsci.2006.11.010.

[158] Y. Bergström, "The plastic deformation of metals - A dislocation model and its applicability," *Rev. Powder Metall. Phys. Ceram.,* vol. 2, no. 3, pp. 79-265, 1983.

[159] P.-H. Li, W.-G. Guo, W.-D. Huang, Y. Su, X. Lin, and K.-B. Yuan, "Thermomechanical response of 3D laser-deposited Ti–6Al–4V alloy over a wide range of strain rates and temperatures," *Materials Science and Engineering: A,* vol. 647, pp. 34-42, 10/28/ 2015, doi: http://dx.doi.org/10.1016/j.msea.2015.08.043.

[160] K. H. Jung, H. W. Lee, and Y. T. Im, "A microstructure evolution model for numerical prediction of austenite grain size distribution," *International Journal of Mechanical Sciences,* vol. 52, no. 9, pp. 1136-1144, 2010, doi: https://doi.org/10.1016/j.ijmecsci.2009.09.010.

[161] T. Udagawa, E. Kropp, and T. Altan, "Investigation of metal flow and temperatures by FEM in the extrusion of Ti-6Al-4V tubes," *Journal of Materials Processing Technology,* vol. 33, no. 1, pp. 155-174, 1992, doi: https://doi.org/10.1016/0924-0136(92)90317-L.

[162] E.-L. Odenberger, M. Schill, and M. Oldenburg, "Thermo-mechanical sheet metal forming of aero engine components in Ti-6Al-4V—PART 2: Constitutive modelling and validation," *International Journal of Material Forming,* journal article vol. 6, no. 3, pp. 403-416, September 01 2013, doi: 10.1007/s12289-012-1094-7.

[163] T. R. Prabhu, "Simulations and Experiments of the Nonisothermal Forging Process of a Ti-6Al-4V Impeller," *Journal of Materials Engineering and Performance,* journal article vol. 25, no. 9, pp. 3627-3637, September 01 2016, doi: 10.1007/s11665-016-2186-1.

[164] Y. Zhu, W. Zeng, X. Ma, Q. Tai, Z. Li, and X. Li, "Determination of the friction factor of Ti-6Al-4V titanium alloy in hot forging by means of ring-compression test using

FEM," *Tribology International,* vol. 44, no. 12, pp. 2074-2080, 2011, doi: https://doi.org/10.1016/j.triboint.2011.07.001.

[165] H. Matsumoto and V. Velay, "Mesoscale modeling of dynamic recrystallization behavior, grain size evolution, dislocation density, processing map characteristic, and room temperature strength of Ti-6Al-4V alloy forged in the (α+β) region," *Journal of Alloys and Compounds,* vol. 708, pp. 404-413, 2017, doi: https://doi.org/10.1016/j.jallcom.2017.02.285.

[166] M. E. Merchant, "Basic mechanics of the metal-cutting process," *ASME J. of Applied Mechanics,* vol. 11, p. A168, 1944.

[167] R. Hill, "The mechanics of machining: A new approach," *Journal of the Mechanics and Physics of Solids,* vol. 3, no. 1, pp. 47-53, 1954, doi: https://doi.org/10.1016/0022-5096(54)90038-1.

[168] W. B. Palmer and P. L. B. Oxley, "Mechanics of Orthogonal Machining," *Proceedings of the Institution of Mechanical Engineers,* vol. 173, no. 1, pp. 623-654, 1959, doi: 10.1243/pime_proc_1959_173_053_02.

[169] R. N. Roth and P. L. B. Oxley, "Slip-Line Field Analysis for Orthogonal Machining Based upon Experimental Flow Fields," *Journal of Mechanical Engineering Science,* vol. 14, no. 2, pp. 85-97, 1972, doi: 10.1243/jmes_jour_1972_014_015_02.

[170] N. Fang, I. S. Jawahir, and P. L. B. Oxley, "A universal slip-line model with non-unique solutions for machining with curled chip formation and a restricted contact tool," *International Journal of Mechanical Sciences,* vol. 43, no. 2, pp. 557-580, 2001, doi: https://doi.org/10.1016/S0020-7403(99)00117-4.

[171] N. Fang and I. S. Jawahir, "Analytical predictions and experimental validation of cutting force ratio, chip thickness, and chip back-flow angle in restricted contact machining using the universal slip-line model," *International Journal of Machine Tools and Manufacture,* vol. 42, no. 6, pp. 681-694, 2002, doi: https://doi.org/10.1016/S0890-6955(02)00006-8.

[172] T. Matsumura and S. Tamura, "Cutting Simulation of Titanium Alloy Drilling with Energy Analysis and FEM," *Procedia CIRP,* vol. 31, pp. 252-257, 2015, doi: https://doi.org/10.1016/j.procir.2015.03.045.

[173] O. Isbilir and E. Ghassemieh, "Finite Element Analysis of Drilling of Titanium Alloy," *Procedia Engineering,* vol. 10, pp. 1877-1882, 2011, doi: https://doi.org/10.1016/j.proeng.2011.04.312.

[174] M. Sadeghifar, R. Sedaghati, W. Jomaa, and V. Songmene, "A comprehensive review of finite element modeling of orthogonal machining process: chip formation and surface integrity predictions," *The International Journal of Advanced Manufacturing Technology,* journal article vol. 96, no. 9, pp. 3747-3791, June 01 2018, doi: 10.1007/s00170-018-1759-6.

[175] A. J. Shih, "Finite element analysis of the rake angle effects in orthogonal metal cutting," *International Journal of Mechanical Sciences,* vol. 38, no. 1, pp. 1-17, 1995/01/01 1995, doi: http://dx.doi.org/10.1016/0020-7403(95)00036-W.

[176] T. D. Marusich and M. Ortiz, "Modelling and simulation of high-speed machining," *International Journal for Numerical Methods in Engineering,* vol. 38, no. 21, pp. 3675-3694, 1995, doi: doi:10.1002/nme.1620382108.

[177] C. Gao and L. Zhang, "EFFECT OF CUTTING CONDITIONS ON THE SERRATED CHIP FORMATION IN HIGH-SPEED CUTTING," *Machining Science and Technology,* vol. 17, no. 1, pp. 26-40, 2013/01/01 2013, doi: 10.1080/10910344.2012.747887.

[178] Q. Zhang *et al.*, "Modeling and Optimal Design of Machining-Induced Residual Stresses in Aluminium Alloys Using a Fast Hierarchical Multiobjective Optimization Algorithm," *Materials and Manufacturing Processes,* vol. 26, no. 3, pp. 508-520, 2011, doi: 10.1080/10426914.2010.537421.

[179] M. H. Dirikolu, T. H. C. Childs, and K. Maekawa, "Finite element simulation of chip flow in metal machining," *International Journal of Mechanical Sciences,* vol. 43, no. 11, pp. 2699-2713, 2001, doi: https://doi.org/10.1016/S0020-7403(01)00047-9.

[180] E. Ceretti, P. Fallböhmer, W. T. Wu, and T. Altan, "Application of 2D FEM to chip formation in orthogonal cutting," *Journal of Materials Processing Technology,* vol. 59, no. 1, pp. 169-180, 1996, doi: https://doi.org/10.1016/0924-0136(96)02296-0.

[181] E. Ceretti, M. Lucchi, and T. Altan, "FEM simulation of orthogonal cutting: serrated chip formation," *Journal of Materials Processing Technology,* vol. 95, no. 1, pp. 17-26, 1999, doi: https://doi.org/10.1016/S0924-0136(99)00261-7.

[182] E.-G. Ng, T. I. El-Wardany, M. Dumitrescu, and M. A. Elbestawi, "PHYSICS-BASED SIMULATION OF HIGH SPEED MACHINING," *Machining Science and Technology,* vol. 6, no. 3, pp. 301-329, 2002, doi: 10.1081/MST-120016248.

[183] G. R. Johnson and W. H. Cook, "Fracture characteristics of three metals subjected to various strains, strain rates, temperatures and pressures," *Engineering Fracture Mechanics,* vol. 21, no. 1, pp. 31-48, 1985, doi: https://doi.org/10.1016/0013-7944(85)90052-9.

[184] W. W. Chen and B. Song, *Split Hopkinson (Kolsky) bar: design, testing and applications*. Springer Science & Business Media, 2010.

[185] H. Kolsky, *Stress waves in solids*. Courier Corporation, 1963.

[186] B. Song, W. Chen, and V. Luk, "Impact compressive response of dry sand," *Mechanics of Materials,* vol. 41, no. 6, pp. 777-785, 2009, doi: https://doi.org/10.1016/j.mechmat.2009.01.003.

[187] H. Matsumoto, H. Yoneda, D. Fabregue, E. Maire, A. Chiba, and F. Gejima, "Mechanical behaviors of Ti–V–(Al, Sn) alloys with α′ martensite microstructure," *Journal of Alloys and Compounds,* vol. 509, no. 6, pp. 2684-2692, 2011/02/10/ 2011, doi: http://dx.doi.org/10.1016/j.jallcom.2010.11.089.

[188] A. Molinari, C. Musquar, and G. Sutter, "Adiabatic shear banding in high speed machining of Ti–6Al–4V: experiments and modeling," *International Journal of Plasticity,* vol. 18, no. 4, pp. 443-459, 2002, doi: https://doi.org/10.1016/S0749-6419(01)00003-1.

[189] F. Ducobu, E. Rivière-Lorphèvre, and E. Filippi, "Experimental contribution to the study of the Ti6Al4V chip formation in orthogonal cutting on a milling machine," *International Journal of Material Forming,* journal article vol. 8, no. 3, pp. 455-468, 2015, doi: 10.1007/s12289-014-1189-4.

[190] M. Shunmugavel, M. Goldberg, A. Polishetty, J. Nomani, S. Sun, and G. Littlefair, "Chip formation characteristics of selective laser melted Ti–6Al–4V," *Australian Journal of Mechanical Engineering,* pp. 1-18, 2017, doi: 10.1080/14484846.2017.1364833.

[191] S. Sun, M. Brandt, and M. S. Dargusch, "Characteristics of cutting forces and chip formation in machining of titanium alloys," *International Journal of Machine Tools and Manufacture,* vol. 49, no. 7, pp. 561-568, 2009, doi: https://doi.org/10.1016/j.ijmachtools.2009.02.008.

[192] G. G. Ye, Y. Chen, S. F. Xue, and L. H. Dai, "Critical cutting speed for onset of serrated chip flow in high speed machining," *International Journal of Machine Tools and Manufacture,* vol. 86, pp. 18-33, 2014, doi: https://doi.org/10.1016/j.ijmachtools.2014.06.006.

[193] E. O. Hall, "The Deformation and Ageing of Mild Steel: III Discussion of Results," *Proceedings of the Physical Society. Section B,* vol. 64, no. 9, p. 747, 1951.

[194] C.-Y. Hyun and H.-K. Kim, "The comparison of yield and fatigue strength dependence on grain size of pure Ti produced by severe plastic deformation," *Rev. Adv. Mater. Sci,* vol. 28, pp. 69-73, 2011.

[195] C. Y. H. a. H. K. Kim, "The comparison of yield and fatigue strength dependence on grain size of pure ti produced by severe plastic deformation," *Adv. Mat. Sci,* vol. 28, pp. 69-73, 2011.

[196] H. W. Rosenberg and W. D. Nix, "Solid solution strengthening in Ti-Al alloys," *Metallurgical Transactions,* journal article vol. 4, no. 5, pp. 1333-1338, May 01 1973, doi: 10.1007/bf02644529.

[197] A. Akhtar and E. Teghtsoonian, "Prismatic slip in α-titanium single crystals," *Metallurgical and Materials Transactions A,* journal article vol. 6, no. 12, p. 2201, December 01 1975, doi: 10.1007/bf02818644.

[198] "Mechanical properties of age-hardened titanium-aluminum alloys," *Acta Metallurgica,* vol. 18, no. 7, pp. 785 - 795, 1970, doi: https://doi.org/10.1016/0001-6160(70)90043-X.

[199] E. I. Galindo-Nava, L. D. Connor, and C. M. F. Rae, "On the prediction of the yield stress of unimodal and multimodal γ′ Nickel-base superalloys," *Acta Materialia,* vol. 98, pp. 377-390, 2015/10/01/ 2015, doi: http://dx.doi.org/10.1016/j.actamat.2015.07.048.

[200] R. Labusch, "A Statistical Theory of Solid Solution Hardening," *physica status solidi (b),* vol. 41, no. 2, pp. 659-669, 1970, doi: 10.1002/pssb.19700410221.

[201] D. P, "CRC Handbook of Chemistry and Physics," *Journal of Molecular Structure,* vol. 268, no. 1, p. 320, 1992/04/01/ 1992, doi: http://dx.doi.org/10.1016/0022-2860(92)85083-S.

[202] D. N. Williams, R. A. Wood, R. I. Jaffee, and H. R. Ogden, "The effects of zirconium in titanium-base alloys," *Journal of the Less Common Metals,* vol. 6, no. 3, pp. 219-225, 1964/03/01/ 1964, doi: http://dx.doi.org/10.1016/0022-5088(64)90102-X.

[203] T. Duerig and J. Williams, "Overview: microstructure and properties of beta titanium alloys," *Beta Titanium Alloys in the 1980's,* pp. 19-67, 1983.

[204] B. A. Welk, "Microstructural and property relationships in ϐ-Titanium alloy Ti-5553," Master's Materials Science and Engineering, The Ohio State University, Ohio, 2010.

[205] P. E. Markovsky and M. Ikeda, "Balancing of Mechanical Properties of Ti–4.5Fe–7.2Cr–3.0Al Using Thermomechanical Processing and Rapid Heat Treatment," *MATERIALS TRANSACTIONS,* vol. 46, no. 7, pp. 1515-1524, 2005, doi: 10.2320/matertrans.46.1515.

[206] W.-S. Lee and C.-F. Lin, "Plastic deformation and fracture behaviour of Ti–6Al–4V alloy loaded with high strain rate under various temperatures," *Materials Science and Engineering: A,* vol. 241, no. 1–2, pp. 48-59, 1// 1998, doi: http://dx.doi.org/10.1016/S0921-5093(97)00471-1.

[207] G. I. Taylor, "The mechanism of plastic deformation of crystals. Part I.—Theoretical," *Proceedings of the Royal Society of London. Series A, Containing Papers of a Mathematical and Physical Character,* vol. 145, no. 855, pp. 362-387, 1934.

[208] E. I. Galindo-Nava and C. M. F. Rae, "Microstructure-sensitive modelling of dislocation creep in polycrystalline FCC alloys: Orowan theory revisited," *Materials Science and Engineering: A,* vol. 651, pp. 116-126, 2016/01/10/ 2016, doi: https://doi.org/10.1016/j.msea.2015.10.088.

[209] E. I. Galindo-Nava, "On the prediction of martensite formation in metals," *Scripta Materialia,* vol. 138, pp. 6-11, 2017/09/01/ 2017, doi: http://dx.doi.org/10.1016/j.scriptamat.2017.05.026.

[210] E. I. Galindo-Nava and P. E. J. Rivera-Díaz-del-Castillo, "A model for the microstructure behaviour and strength evolution in lath martensite," *Acta Materialia,* vol. 98, pp. 81-93, 2015/10/01/ 2015, doi: http://dx.doi.org/10.1016/j.actamat.2015.07.018.

[211] E. Galindo-Nava and P. Rivera-Díaz-del-Castillo, "Thermostatistical modelling of hot deformation in FCC metals," *International Journal of Plasticity,* vol. 47, pp. 202-221, 2013.

[212] S. Semiatin, S. Knisley, P. Fagin, D. Barker, and F. Zhang, "Microstructure evolution during alpha-beta heat treatment of Ti-6Al-4V," *Metallurgical and Materials Transactions A,* vol. 34, no. 10, pp. 2377-2386, 2003.

[213] H. Z. Zhao, L. Xiao, P. Ge, J. Sun, and Z. P. Xi, "Hot deformation behavior and processing maps of Ti-1300 alloy," *Materials Science and Engineering: A,* vol. 604, pp. 111-116, 2014, doi: https://doi.org/10.1016/j.msea.2014.03.016.

[214] H. Liang, H. Guo, Y. Nan, C. Qin, X. Peng, and J. Zhang, "The construction of constitutive model and identification of dynamic softening mechanism of high-temperature deformation of Ti–5Al–5Mo–5V–1Cr–1Fe alloy," *Materials Science and*

*Engineering: A,* vol. 615, pp. 42-50, 2014, doi: https://doi.org/10.1016/j.msea.2014.07.050.

[215] F. Warchomicka, C. Poletti, and M. Stockinger, "Study of the hot deformation behaviour in Ti–5Al–5Mo–5V–3Cr–1Zr," *Materials Science and Engineering: A,* vol. 528, no. 28, pp. 8277-8285, 2011, doi: https://doi.org/10.1016/j.msea.2011.07.068.

[216] D. Bonorchis, "Implementation of material models for high strain rate applications as user-subroutines in abaqus/explicit," University of Cape Town, 2003.

[217] X. Fan, H. Yang, and P. Gao, "The mechanism of flow softening in subtransus hot working of two-phase titanium alloy with equiaxed structure," *Chinese Science Bulletin,* journal article vol. 59, no. 23, pp. 2859-2867, August 01 2014, doi: 10.1007/s11434-014-0332-4.

[218] H. J. Frost and M. F. Ashby, *Deformation mechanism maps: the plasticity and creep of metals and ceramics*. Pergamon press, 1982.

[219] L. Facchini, E. Magalini, P. Robotti, A. Molinari, S. Höges, and K. Wissenbach, "Ductility of a Ti-6Al-4V alloy produced by selective laser melting of prealloyed powders," *Rapid Prototyping Journal,* vol. 16, no. 6, pp. 450-459, 2010, doi: doi:10.1108/13552541011083371.

[220] R. I. Jaffee and N. E. Promisel, *The Science, Technology and Application of Titanium: Proceedings of an International Conference Organized by the Institute of Metals, the Metallurgical Society of Aime, and the American Society for Metals in Association with the Japan Institute of Metals and the Academy of Sciences, USSR, and Held at th.* Elsevier, 2013.

# Appendix A

## A.1 Engineering drawings

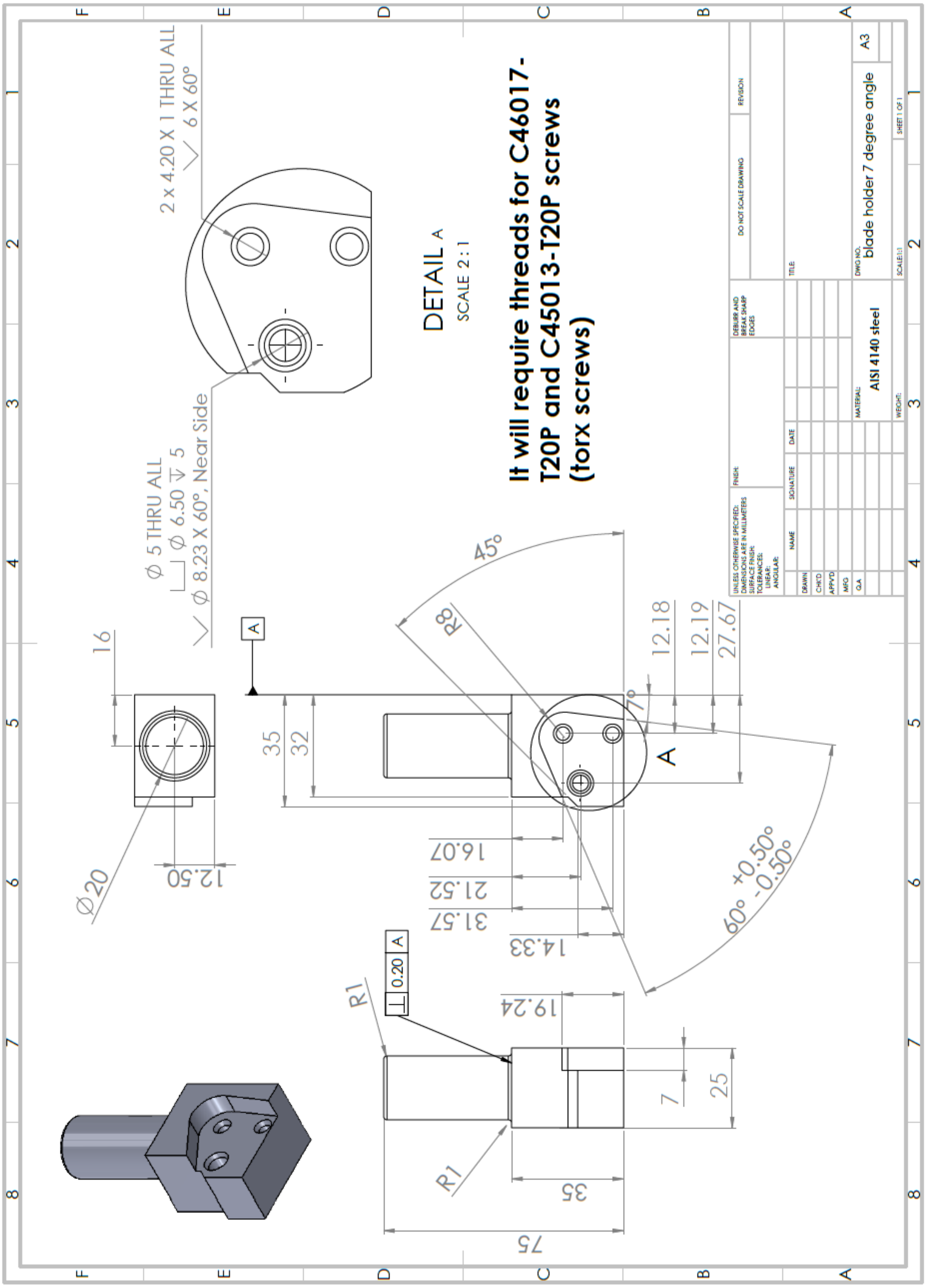

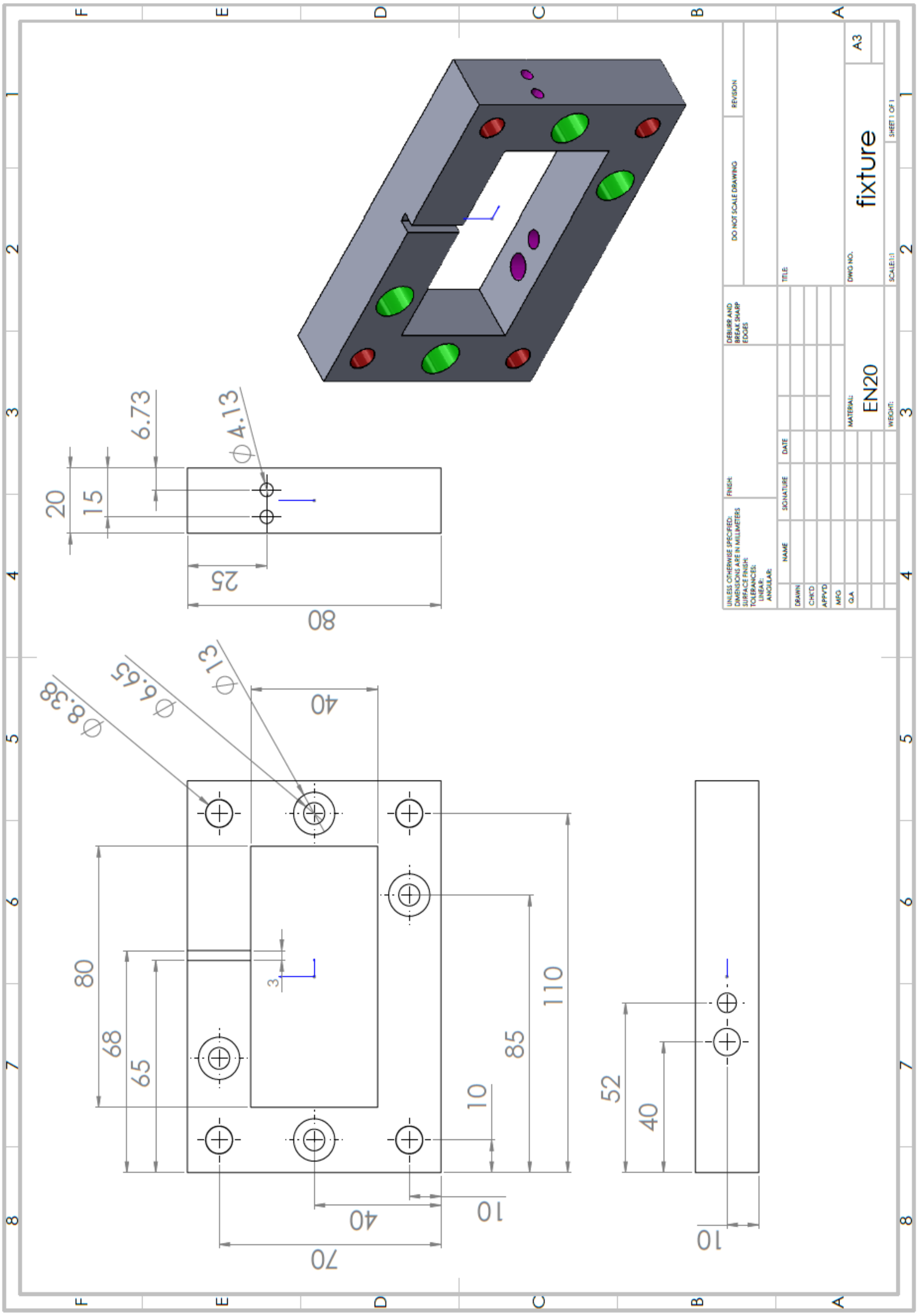
fixture
EN20
A3
DO NOT SCALE DRAWING
REVISION
TITLE:
DWG NO.
MATERIAL:
FINISH:
WEIGHT:
SCALE:1:1
SHEET 1 OF 1
DEBURR AND BREAK SHARP EDGES
UNLESS OTHERWISE SPECIFIED: DIMENSIONS ARE IN MILLIMETERS SURFACE FINISH: TOLERANCES: LINEAR: ANGULAR:
NAME
SIGNATURE
DATE
DRAWN
CHK'D
APPV'D
MFG
Q.A
Ø8.38
Ø6.65
Ø13
Ø4.13
6.73
20
15
25
80
40
80
68
65
3
110
85
10
40
10
70
52
40
10

# Appendix B

Microstructural features and deformation conditions tested in this work.

| Author | Alpha average grain size $D_{\alpha}$ (µm) | Alpha lamella width $W_{\alpha}$ (µm) | Total volume fraction alpha $V_{\alpha}$ | Volume fraction lamellar alpha $V_{\alpha}$ | Volume fraction of equiaxed alpha (Bimodal) $V_{\alpha}$ | Martensite average lath width $W_{\alpha'}$ (µm) | Volume fraction of martensite $V_{\alpha'}$ | Microstructure Type | Temperature (K) | Strain rate ($s^{-1}$) |
|---|---|---|---|---|---|---|---|---|---|---|
| Park et al.[32] | 9 | 0.6 | 0.72 | 0.28 | 0.85 | - | - | Bimodal | 298 | $10^{-3}$- 10 |
| Park et al.[32] | 13 | - | 0.85 | - | - | - | - | Equiaxed | 298 | $10^{-3}$- 10 |
| Park et al.[32] | - | 2.6 | - | 0.9 | - | - | - | Lamellar | 298 | $10^{-3}$- 10 |
| Zheng et al.[34] | 6 | 0.8 | 0.8 | 0.2 | .0.9 | - | - | Bimodal | 298 | 2600 |
| Zheng et al.[34] | 8 | - | 0.85 | - | - | - | - | Equiaxed | 298 | 2600 |
| Zheng et al.[34] | 9 | 2 | - | 0.9 | - | - | - | Lamellar | 298 | 2600 |
| Khan et al.[16] | 8 | - | 0.83 | - | - | - | - | Equiaxed | 298-755 | $10^{-6}$ - 3378 |
| Lee & Li[60] | 8 | - | 0.9 | - | - | - | - | Equiaxed | 298-1373 | 2000 |
| Li et al.[61] | - | - | - | - | - | 0.75 | 1 | PLD (α') | 298-1273 | 0.1 - 5000 |
| Kasperovich et al.[4] | 5 | - | 0.83 | - | - | - | - | Equiaxed | 298 | $10^{-3}$ |
| | - | - | - | - | - | 0.75 | 1 | SLM (α') | 298 | $10^{-3}$ |
| Kasperovich et al.[4] | 1.5 | - | .98 | - | - | - | - | SLM (α+β) | 298 | $10^{-3}$ |
| | 2 | - | .97 | - | - | - | - | SLM (α+β) | 298 | $10^{-3}$ |
| Kasperovich et al.[4] | 3 | - | .95 | - | - | - | - | SLM (α+β) | 298 | $10^{-3}$ |
| Kasperovich et al.[4] | | | | | | | | | | |

# Appendix C

## C.1 Single Element results for JC-VUMAT and JC-Abaqus

### C.1.1 Strain rates of 100 $s^{-1}$

Tensile single element test at $\dot{\varepsilon} = 100\ s^{-1}$

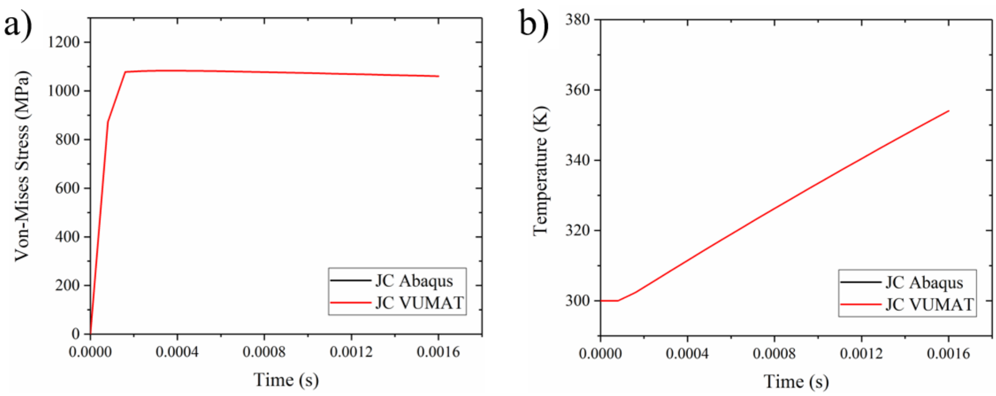


Compression single element test at $\dot{\varepsilon} = 100\ s^{-1}$

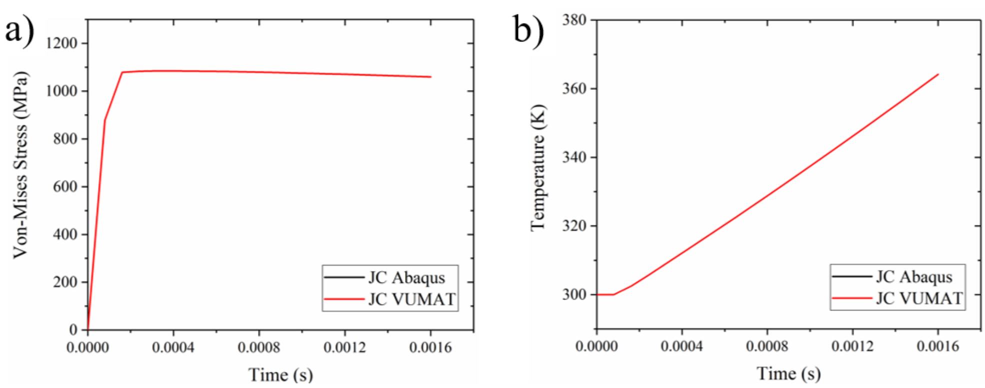


Shear single element test at $\dot{\varepsilon} = 100\ s^{-1}$

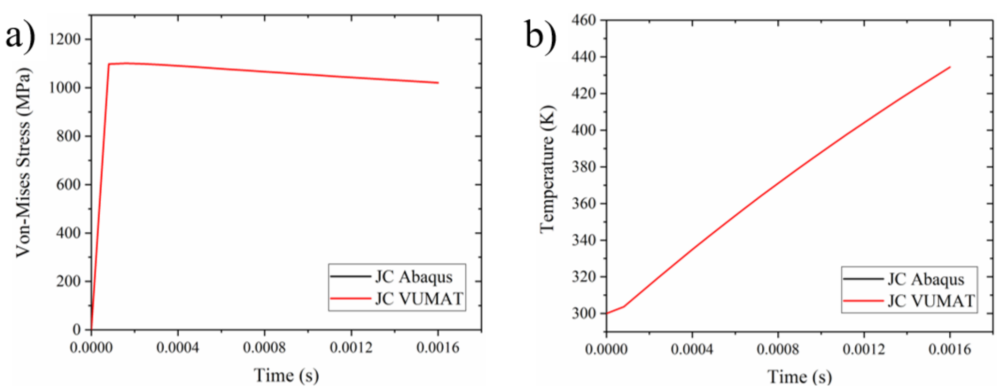

## C.1.2 Strain rates of 10 $s^{-1}$

Tensile single element test at $\dot{\varepsilon} = 10\ s^{-1}$

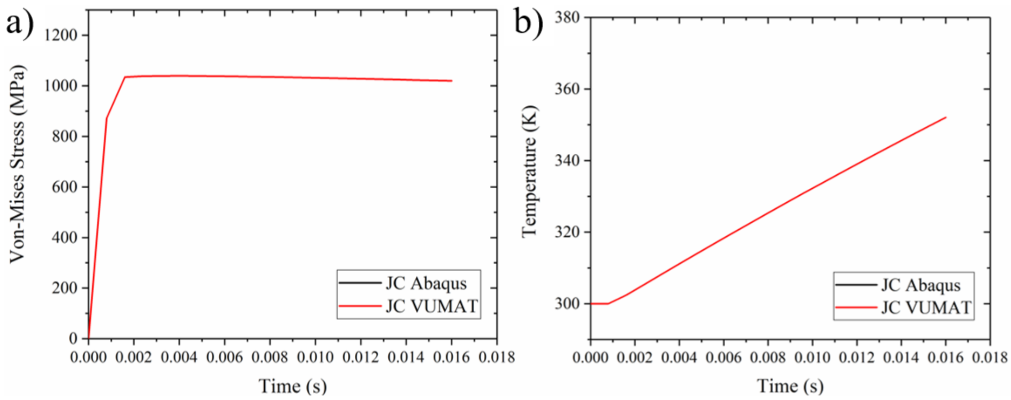


Compression single element test at $\dot{\varepsilon} = 10\ s^{-1}$

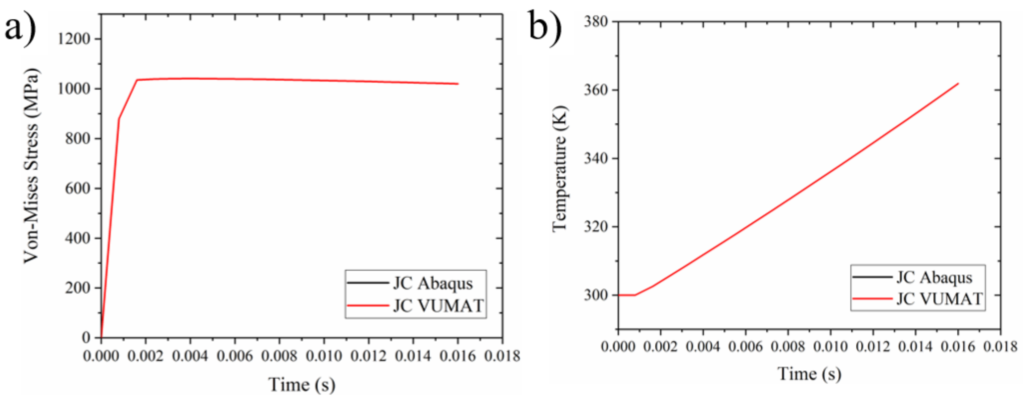


Shear single element test at $\dot{\varepsilon} = 10\ s^{-1}$

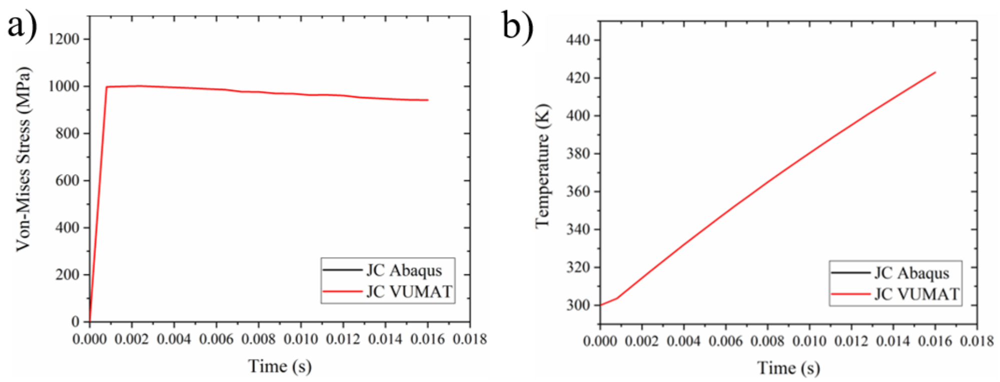

## C.2 125 Elements results for JC-VUMAT and JC-Abaqus

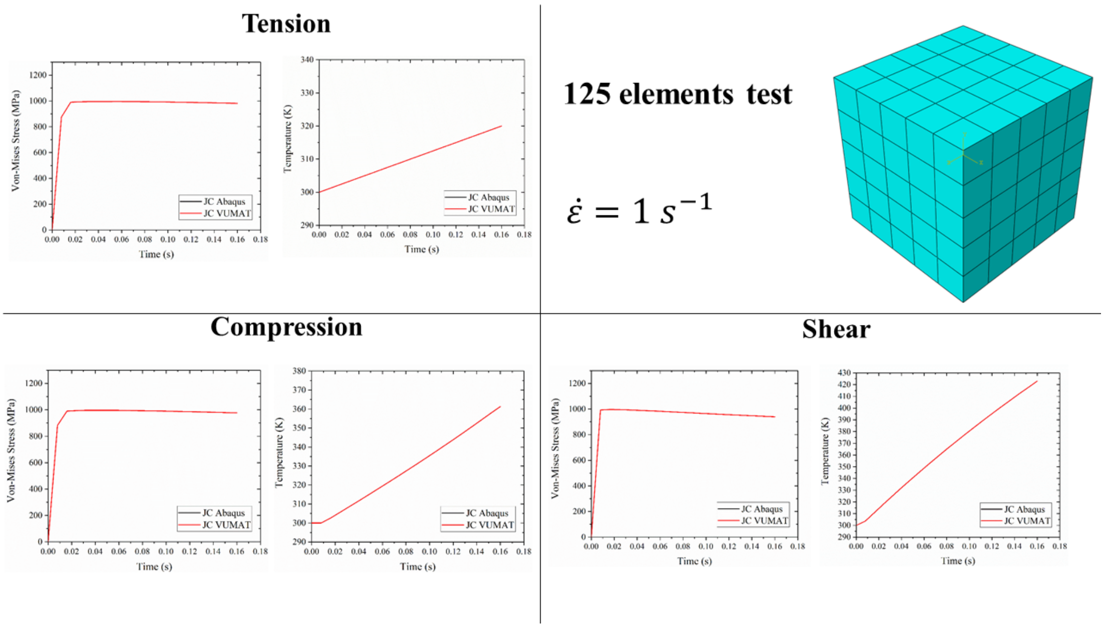


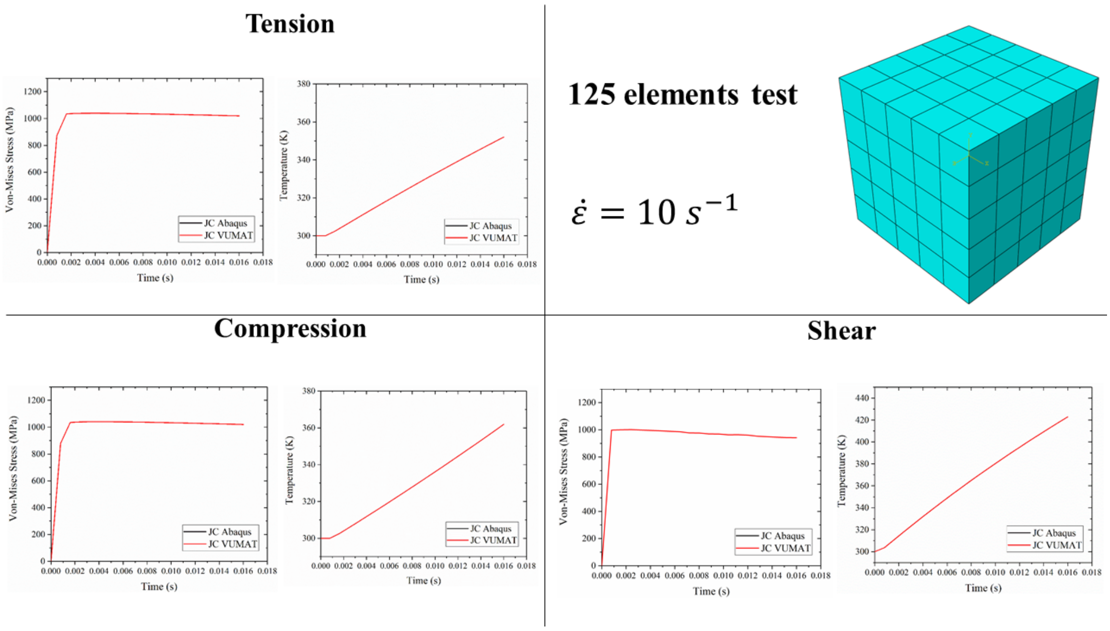

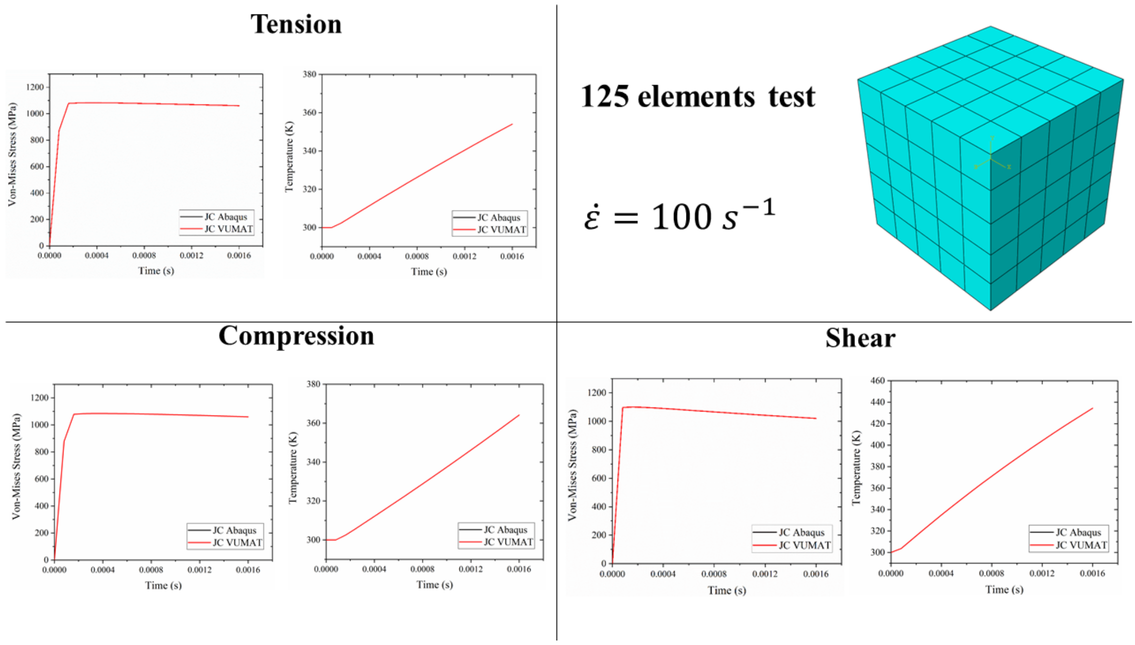
Tension
125 elements test
$\dot{\varepsilon} = 100\ s^{-1}$
Compression
Shear
Von-Mises Stress (MPa)
Temperature (K)
Time (s)
JC Abaqus
JC VUMAT

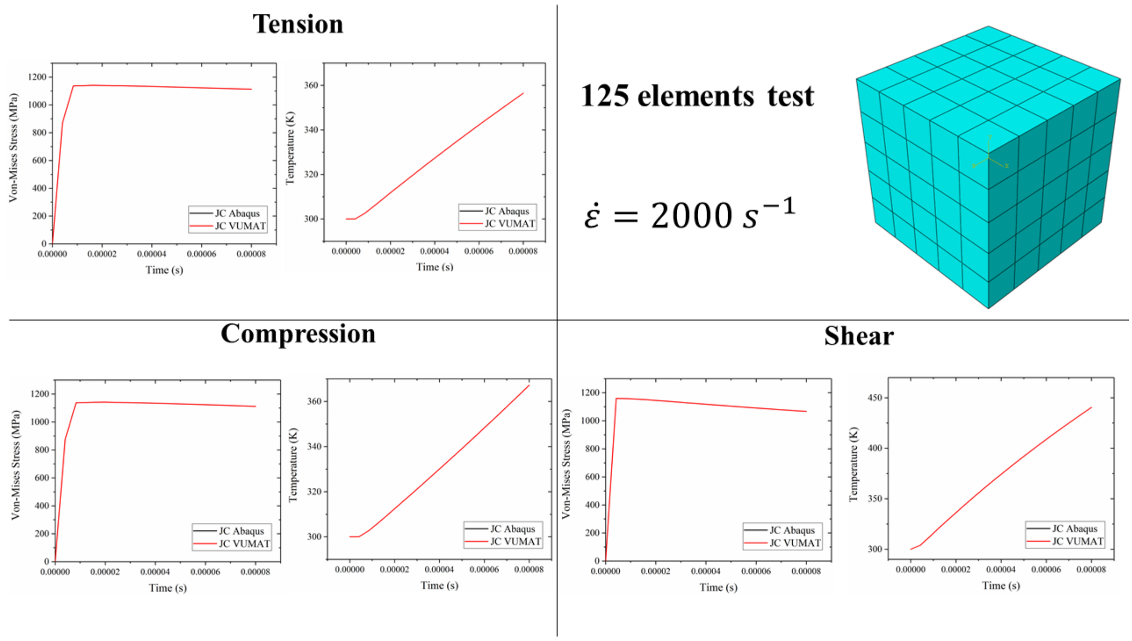
Tension
125 elements test
$\dot{\varepsilon} = 2000\ s^{-1}$
Compression
Shear
Von-Mises Stress (MPa)
Temperature (K)
Time (s)
JC Abaqus
JC VUMAT

# C.3 512 Elements results for JC-VUMAT and JC-Abaqus

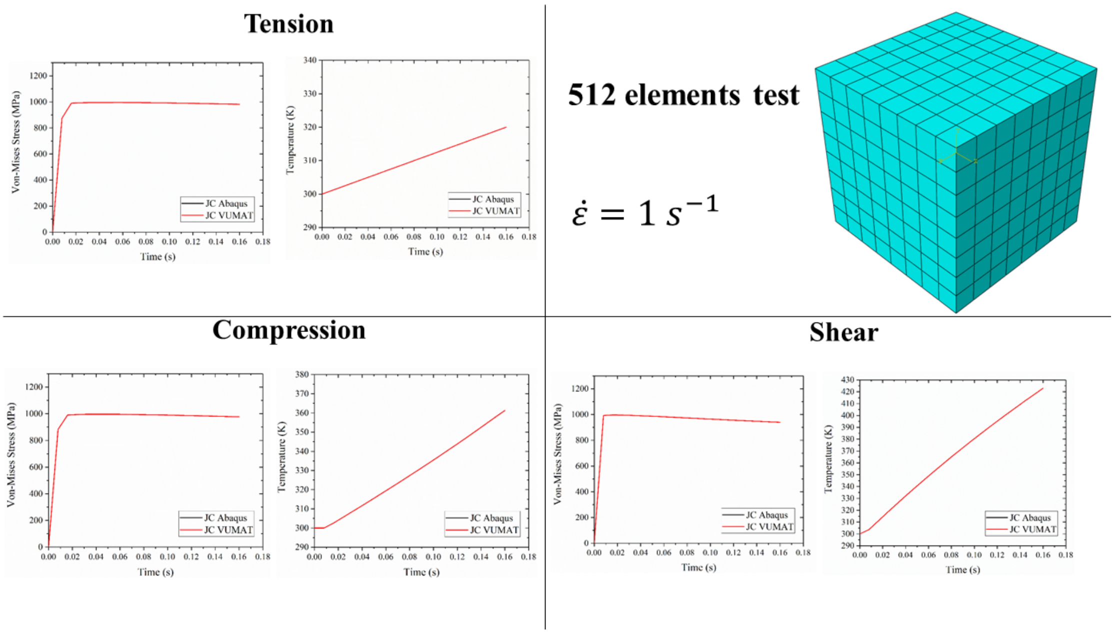


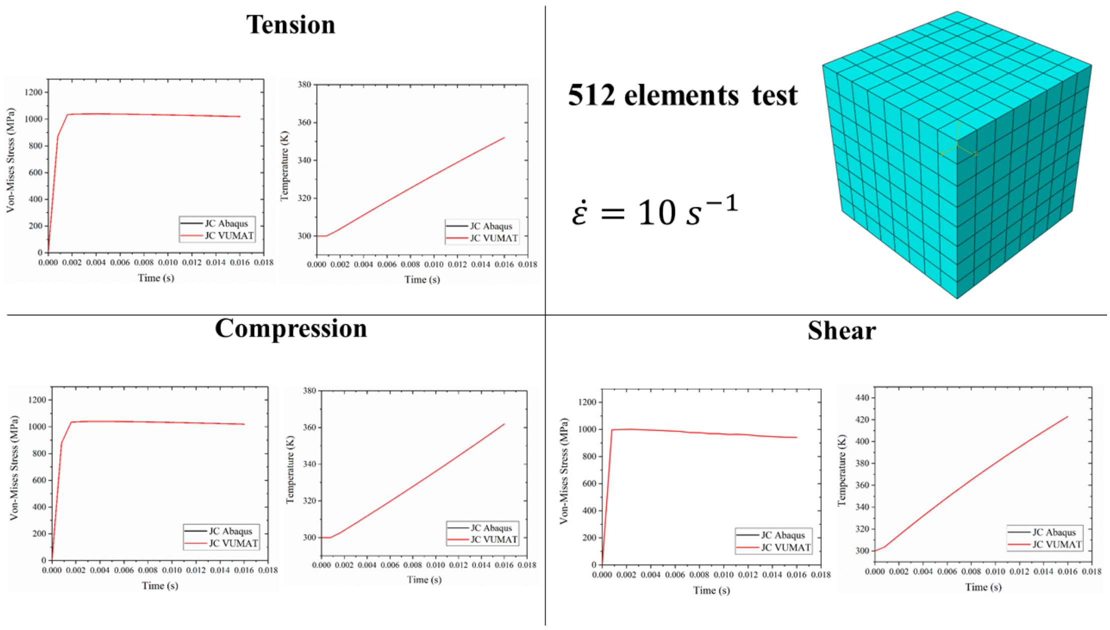

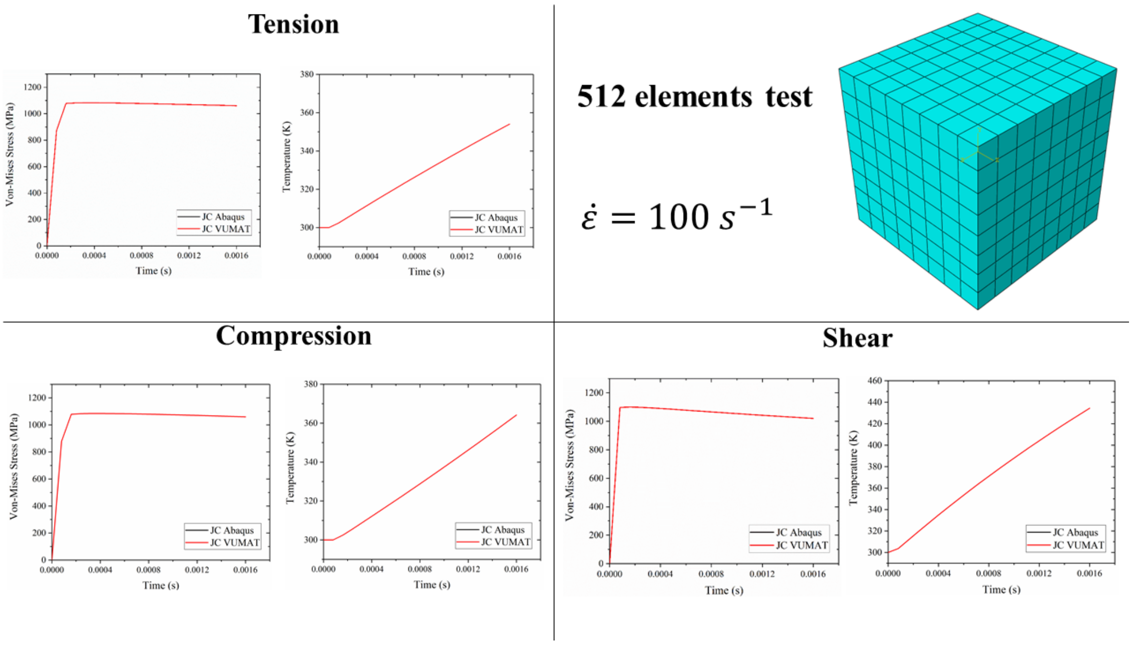
Tension
512 elements test
$\dot{\varepsilon} = 100\ s^{-1}$
Compression
Shear
Von-Mises Stress (MPa)
Temperature (K)
Time (s)
JC Abaqus
JC VUMAT

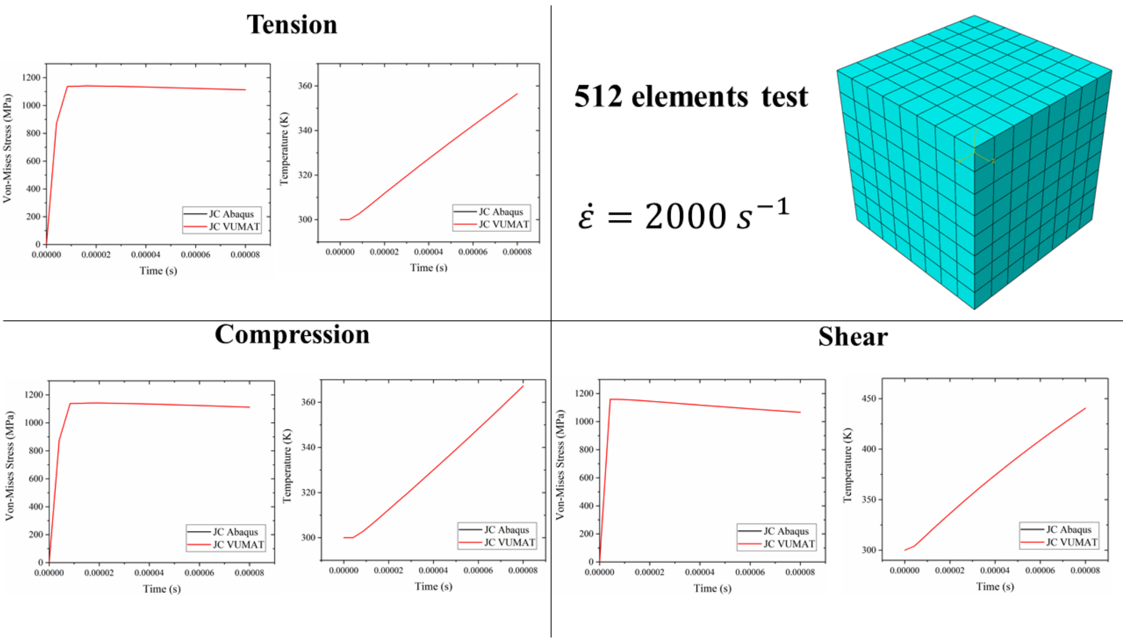
Tension
512 elements test
$\dot{\varepsilon} = 2000\ s^{-1}$
Compression
Shear
Von-Mises Stress (MPa)
Temperature (K)
Time (s)
JC Abaqus
JC VUMAT